SEISMIC ANALYSIS OF SUBMARINE SLOPES: RETROGRESSIVE AND THREE-DIMENSIONAL EFFECTS

ALIREZA AZIZIAN

Your file Votre référence
ISBN: 0-612-99028-1
Our file Notre référence
ISBN: 0-612-99028-1

Seismic Analysis of Submarine Slopes: Retrogressive and Three-Dimensional Effects

By:

© Alireza Azizian, B.Sc., M.Sc.

A thesis submitted to the
School of Graduate Studies
in partial fulfillment of the requirements for the degree of

Doctor of Philosophy
in
Civil Engineering

Faculty of Engineering & Applied Science
Memorial University of Newfoundland
St. John's, NL, Canada
January 2004

To my lovely wife

and our devoting parents...

ABSTRACT

Failures of submarine slopes, caused by earthquakes, rapid sedimentation, storm waves, etc., have resulted in significant damage near- and off-shore, in many areas of the world. High costs of off-shore projects, such as oil exploration projects, necessitate using accurate methods for assessing slope resistance and possible extent of slope failures due to rare events such as earthquakes that may lead to considerable devastations.

The stability analyses of submarine slopes, to this date, are mostly based on the classical methods of slope stability analysis such as the limit equilibrium method. While appropriate for static slope stability analysis, those methods have some limitations when used in seismic analysis of saturated soil slopes involving soil liquefaction. This study aims at filling some gaps in the current approach by using a state-of-the-art method for effective stress, seismic analysis of submarine slopes. The method proposed here implements a fully coupled, dynamic, finite element approach and a multi-yield surface plasticity model for simulating non-linear soil behaviour under dynamic loads.

According to the geological and geophysical investigations of past submarine failures, an important phenomenon observed in such events is the significant retrogression of failure, initiated as a slope failure and extending back to a long distance in a nearly flat seabed. Accurate prediction of the extent of retrogression is of crucial importance when assessing the safety of seabed facilities. In addition, seabed images showing crescent-shaped escarpments of failures indicate significant three-dimensional (3D) characteristics of such failures. Most slope stability analysis methods, and in particular those for dynamic analysis, are based on the two-dimensional, plane strain simplifying assumption. Assessment of 3D effects in seismic slope stability analysis is therefore essential for obtaining relatively more accurate numerical results. Moreover, geotechnical investigation in submarine environment is much more costly than on land. Geotechnical data regarding submarine soils are rather scarce and insufficient for stability analyses

where vulnerability to liquefaction is of great importance. Obtaining best estimates of soil properties from such scarce data based on some statistical methods is of great importance for numerical predictions.

The objectives of this research are aimed at addressing the needs of geotechnical practice: (1) to provide a procedure for analyzing seismically induced retrogressive slope failures and to use this procedure for explaining the mechanisms and identifying the main factors affecting the extent of those slope failures; (2) to assess the three-dimensional effects in seismic analysis of submarine slopes, in order to provide geotechnical practitioners with a reliable tool for extrapolating the results of manageable 2D seismic analyses to real 3D configurations; and (3) to design a procedure for constitutive model parameter calibration based on liquefaction strength analysis, using limited amount of experimental data and accounting for uncertainties in soil properties.

To the author's knowledge, the two aspects of slope stability analysis addressed here, namely, simulation of retrogressive slope failures and 3D seismic analysis of saturated soil slopes, have not been investigated in a consistent manner so far.

By modelling the retrogressive failures, the study highlights the importance of accounting for the potential of retrogression in regions that are seemingly safe but can be affected by such phenomenon. Risk assessment of infrastructures (e.g. pipelines) located on such seemingly safe zones should include estimation of retrogression distance. This is similar to accounting for the potential hazard of debris run-out for infrastructures located below the potentially unstable slopes. In this part of the study, a new method is introduced for simulating successive failures due to loss of support. For the various configurations of seabed slopes analyzed here for assessing the effects of gentle seafloor slope and presence of a layer with low permeability, it was found that the final linear extent of retrogressive failures are 5 to 20 times larger than those of the initial failure, which is usually the only stage of failure accounted for in practice.

Three-dimensional effects are assessed by comparing results of two- and three-dimensional analyses, in terms of predicted displacements, shear strains, and excess pore water pressure ratios. Limits of applicability of the 2D, plane strain analysis assumptions are quantitatively assessed. Some regression models are also presented that express ratios of 3D to 2D predictions as a function of slope width/height ratio and earthquake peak acceleration. The results of the present dynamic, fully coupled, non-linear analyses are also compared with those of static slope stability analyses. The comparison indicates that the trend of decrease in the ratio of 3D/2D response as a function of slope width/height ratio is very similar for both approaches. However, the applicability limit of the 2D assumption is found to be slightly lower in dynamic analysis (width/height ratio of about 3 – 5, with larger values corresponding to larger seismic accelerations) than in static analysis (width/height ratio of about 5) for the same level of tolerance (15%). Moreover, for B/H > 6 – 7, the differences between 3D analysis predictions on the symmetry plane of the slope and 2D analysis predictions are found to be insignificant.

Soil constitutive model parameters used in the analyses are obtained and calibrated for two types of sand, namely Nevada and Fraser River sands in a loose state, using available information from the literature as well as results of some recently performed laboratory soil tests.

Response Surface Methodology is used in several parts of this study for the efficient identification of the most important parameters (or factors) that affect analysis results (or responses). It is used for soil parameter calibration where some specific information regarding soil behaviour is not available, yet a set of parameters can be estimated that can re-produce the observed behaviour of soil as indicated by liquefaction strength analysis. This methodology is also used for identifying the significant factors, and then obtaining regression models, to quantify the 3D effects.

ACKNOWLEDGMENT

The author wishes to express his appreciation to his supervisor, Dr. Radu Popescu, for his comments, suggestions, and help. The author is also thankful to his co-supervisors, Drs. Leonard Lye and Ryan Phillips, for their guidance. Their recommendations have certainly improved the quality of the thesis.

The financial support provided by the Natural Sciences and Engineering Research Council of Canada (NSERC), through the Collaborative Research project COSTA–Canada, a Canadian contribution to the study of continental slope stability, is acknowledged. The Graduate Fellowship provided by the School of Graduate Studies, Memorial University of Newfoundland, is also acknowledged.

The author is indebted to Professor Jean H. Prevost, Princeton University, for providing the finite element code used in this study. The permission and training given by Dr. L. Lye for using the Design-Expert software is very much appreciated. Laboratory results provided by a research group involved in the study of "Damage Mitigation from Soil Liquefaction", at the University of British Columbia, are also acknowledged.

My wonderful parents have always encouraged and inspired me to pursue higher education and have constantly provided me with everything I needed. I thank God for giving me the ability to please their hearts and I ask Him all the best for them.

Countless thanks to my lovely wife, Mrs. Neda Zangeneh, for her devotion, support, and encouragement during her own graduate studies. Everything she did, during past three years of research and study, is unique and beyond description. May God bless her and her passionate parents, who always give us confidence in our future.

And for all the blessings, endless thanks to our Lord—God, the Almighty—who gives us knowledge, strength, and hope to discover the unknowns and serve the humankind.

Table of Contents

ABSTRACT iii

ACKNOWLEDGMENT vi

CHAPTER 1 - RESEARCH PURPOSE 1
1.1 INTRODUCTION 1
1.2 COSTA-CANADA OBJECTIVES 4
1.3 RESEARCH TOOLS 6
1.4 ORIGINAL CONTRIBUTIONS 7
1.5 OUTLINE OF THE THESIS 8

CHAPTER 2 - LITERATURE REVIEW 9
2.1 INTRODUCTION 9
2.2 SUBMARINE SLOPE FAILURES 9
2.2.1 Soil Investigation Techniques *9*
2.2.2 Seafloor Topography *13*
2.2.3 Causes and Mechanisms of Seabed Failures *14*
2.2.4 Submarine Retrogressive Failures *18*
2.3 SLOPE STABILITY ANALYSIS 28
2.3.1 Introduction *28*
2.3.2 State-of-Practice in Seismic Analysis of Earth Slopes *31*
2.3.3 Finite Element Analysis of Slopes *36*
2.3.4 Three- vs. Two-Dimensional Analysis of Earth Slopes *48*
2.3.5 Boundary Conditions *55*
2.4 RESPONSE SURFACE METHODOLOGY (RSM) 63
2.4.1 Introduction *63*
2.4.2 Overview of RSM *63*

CHAPTER 3 - NUMERICAL MODEL 69
3.1 INTRODUCTION 69
3.2 FINITE ELEMENT CODE: DYNAFLOW 70
3.3 ANALYSIS CHARACTERISTICS 71
3.3.1 Solid-Fluid Coupled-Field Analysis *71*
3.3.2 Analysis Procedure *71*
3.3.3 Input Motion *72*
3.3.4 Boundary Conditions *73*
3.4 MULTI-YIELD SURFACE PLASTICITY MODEL 75
3.4.1 Soil Constitutive Model Parameters *79*
3.4.2 Model Validation *84*
3.5 NEVADA SAND PROPERTIES 85
3.5.1 Constitutive Experiment (Element Test) *86*
3.5.2 Replication of VELACS, Model #2 Centrifuge Test *87*
3.6 FRASER RIVER SAND PROPERTIES 92

3.6.1 Estimation of Soil Properties 93
3.6.2 Procedure for Parameter Calibration 108

CHAPTER 4 - RETROGRESSIVE FAILURES 113
4.1 INTRODUCTION 113
4.2 FINITE ELEMENT MODEL 114
4.2.1 Finite Element Mesh 114
4.2.2 Material Properties 115
4.2.3 Boundary Conditions and Earthquake Loading 117
4.3 ANALYSIS PROCEDURE 118
4.4 ANALYSIS RESULTS 119
4.4.1 Case 1: Uniform Sand, Flat Seafloor ($\beta = 0^o$) 120
4.4.2 Case 2: Sand Overlain by Silt layer, Flat Seafloor ($\beta = 0^O$) 129
4.4.3 Case 3: Uniform Sand, Sloping Seafloor ($\beta = 2^O$) 133
4.4.4 Case 4: Sand Overlain by Silt Layer, Sloping Seafloor ($\beta = 2^O$) 135
4.4.5 Effect of Mesh Refinement 136
4.5 LIMITATIONS OF THE STUDY 139
4.6 CONCLUSIONS 140

CHAPTER 5 - THREE-DIMENSIONAL EFFECTS 142
5.1 INTRODUCTION 142
5.2 FINITE ELEMENT MODEL 144
5.2.1 Finite element mesh 144
5.2.2 Boundary conditions and earthquake loading 145
5.2.3 Material properties 148
5.3 FACTORS AND RESPONSES 149
5.4 NUMERICAL ANALYSIS ASPECTS 151
5.4.1 Screening by RSM 151
5.4.2 Lateral boundary effects 153
5.5 THREE-DIMENSIONAL EFFECTS 163
5.5.1 Analysis results 163
5.5.2 RSM regression models 173
5.5.3 Effect of slope angle 178
5.5.4 Updated Material Properties 178
5.5.5 Effect of Transverse Loading 179
5.5.6 Comparison with previous studies 183
5.6 CONCLUSION 188

CHAPTER 6 - CONCLUDING REMARKS 192
6.1 SUMMARY AND CONCLUSIONS 192
6.2 FUTURE WORK 197

REFERENCES 198

List of Figures

Figure 2-1. SAR mosaic showing slump scars in one of the source areas of the 1929 Grand Banks event (after Piper et al., 1992). Photo obtained from Mulder and Cochonat (1996)..... 17
Figure 2-2. Shaded relief image of multibeam bathymetric data from the slide scar 1, Karmsundet and Skudenesfjorden, Norway (Boe et al., 2000)..... 17
Figure 2-3. Side scan image of small- and large-scale rotational slumps on St. Pierre Slope, Grand Banks, Newfoundland, after the 1929 earthquake (Piper et al., 1999). 19
Figure 2-4. Classification of successive submarine slumps or slides (Mulder and Cochonat, 1996)..... 20
Figure 2-5. Seismic-reflection profile of retrogressive features in the Humboldt Slide (Gardner et al., 1999b) showing the main body of the slide with folded and back-rotated slide blocks. Black lines show the shear surfaces..... 21
Figure 2-6. Detailed illustration of retrogression mechanism by factor-of-safety obtained from limit equilibrium method (Haug et al., 1976). Note that the factor of safety on the horizontal failure zone is 1.82. The slide is located near South Saskatchewan River, Canada..... 23
Figure 2-7. Finite element analysis of a slope of normally consolidated clay resting on a sensitive clay layer (strain softening) over a strong base (Kvalstad et al., 2002)..... 27
Figure 2-8. Simulation of run-out by a Computational Fluid Dynamics program (Kvalstad et al., 2002) 27
Figure 2-9. Steady state line concept with two possible conditions under which flow liquefaction can, or cannot take place. Graph obtained from Hampton et al. (1996). 35
Figure 2-10. Constitutive model showing different phases of contraction, dilation and liquefaction-induced perfectly plastic deformations (Elgamal et al., 2002)..... 46
Figure 2-11. UBCSAND model (after Byrne et al., 1993): a) yield loci and direction of plastic strains; and b) hyperbolic relationship between stress ratio and plastic shear strain..... 47
Figure 2-12. Ratio of 3D/2D factors of safety (Arellano and Stark, 2000). 50
Figure 2-13. Plan view of horizontal displacements of Storvass dam crest (Martin, 1978). 51
Figure 2-14. Out-of-plane curvature of slope (Jeremic, 2000). 52
Figure 2-15. Comparison of surface acceleration time histories from low-intensity reversed-spike input motion with different boundary conditions: a) reversed-spiked input motion, b) shallow transmitting boundary; c) deep transmitting boundary; d) rigid base Chen (1985)..... 62
Figure 3-1. Main features of the multi-yield plasticity soil constitutive model: a) yield surfaces; b. plastic flow rule; c. hardening rule; d. numerical integration (Popescu, 1995). 77
Figure 3-2. Cyclic simple shear test: a) field of yield surfaces, b) loading-reverse loading stress-strain curves (Prevost, 1977). 78
Figure 3-3. Cyclic triaxial test: a) field of yield surfaces, b) loading-reverse loading stress-strain curves (Prevost, 1977). 78

Figure 3-4. Mohr-Coulomb (hexagonal) yield surface: a) nested surfaces in principal stress space, and, b) concept of rounded surface in π-plane. 79
Figure 3-5. Presentation of Drucker-Prager, Mohr-Coulomb, and Rounded Mohr-Coulomb yield surface on π-plane for friction angle values of a) 31°, and b) 36°. .. 83
Figure 3-6. Recorded (solid line) and predicted (dashed line) excess pore water pressure. VELACS, Nevada Sand, Dr = 40%, Effective Consolidation Pressure = 80 kPa, Cyclic Deviator Stress = 28.8 kPa, Frequency = 1 Hz, Number of Cycles to Liquefaction = 3.2 (http://geoinfo.usc.edu/gees/velacs/) 87
Figure 3-7. VELACS Model #2 Configuration (http://geoinfo.usc.edu/gees/velacs/). 89
Figure 3-8. VELACS Model # 2 predicted and recorded (dashed line) deformed shape, and contours of excess pore water pressure ratio at t = 8.34 s. Deformation magnification scale = 5. 89
Figure 3-9. Comparison between recorded and predicted excess pore water pressure at P1. 90
Figure 3-10. Comparison between recorded and predicted excess pore water pressure at P2. 90
Figure 3-11. Comparison between recorded and predicted excess pore water pressure at P3. 90
Figure 3-12. Comparison between recorded and predicted excess pore water pressure at P4. 91
Figure 3-13. Comparison between recorded and predicted displacements at LVDT3. 91
Figure 3-14. Comparison between recorded and predicted displacements at LVDT4. 91
Figure 3-15. Comparison between recorded and predicted displacements at LVDT5. 92
Figure 3-16. Comparison between recorded and predicted displacements at LVDT6. 92
Figure 3-17. Results of monotonic triaxial test in a) compression, and b) extension, Vaid et al. (2001). 95
Figure 3-18. Effective stress states at quasi-steady state (in strain-softening specimens), or phase transformation (in dilative specimens), Vaid et al. (2001). 96
Figure 3-19. Idealization of different states of soil deformation under monotonic undrained loading (modified after Yoshimine et al., 1999). 97
Figure 3-20. Liquefaction strength curve obtained by calibrating X_{pp} using Vaid et al. (2001) tests. 105
Figure 3-21. Liquefaction strength curve for Fraser River sand: laboratory and simulation results. 107
Figure 3-22. The ratio of cyclic resistance under simple shear and triaxial stress conditions (Vaid and Sivathayalan, 1996). 107
Figure 3-23. Comparison between stress paths recorded in laboratory (Vaid et al., 2001) and predicted by element test for isotropically consolidated, cyclic triaxial test with CSR = 0.145, on Fraser River sand at Dr = 40%. 108
Figure 3-24. Comparison between stress paths recorded in laboratory (provided by UBC) and predicted by element test for cyclic simple shear test on Fraser River sand at Dr = 40%. 108
Figure 3-25. Relative significance of soil properties, influencing the number of cycles to liquefaction: a) normalized effects, b) Normal probability plot method. 112
Figure 4-1. General form of the finite element meshes used in this study: a) standard, and b) fine mesh 115

Figure 4-2. Stress path predicted by element test for cyclic triaxial test using the sand properties listed in Table 4-1. 117
Figure 4-3. Acceleration time history with 0.3g peak ground acceleration. 118
Figure 4-4. Contours of predicted maximum shear strain (γ_{max}) and excess pore pressure ratio (r_u) at selected time instants in case 1. Removal times are t = 15, 115, and 165 s. 121
Figure 4-5. Case 1, element E (near slope): a) horizontal shear stress vs. vertical stress, b) horizontal shear stress vs. horizontal shear strain, low-strain part, c) horizontal shear stress vs. horizontal shear strain, large-strain part, d) excess pore pressure ratio... 124
Figure 4-6. Case 1, element B (free field): a) horizontal shear stress vs. vertical stress, b) horizontal shear stress vs. horizontal shear strain, low-strain part, c) horizontal shear stress vs. horizontal shear strain, large-strain part, d) excess pore pressure ratio... 125
Figure 4-7. Horizontal shear strength of element F with and without removal of the first group at t = 15 s. 127
Figure 4-8. Contours of γ_{max} and r_u at selected time instants in case 2. Note that the first and second removal times are t = 15 and 165 s in this analysis. 130
Figure 4-9. Predicted profile at the end of retrogression for case 2, showing the five stages of element removal. Removal times are t = 15, 165, 240, 340, and 390 s... 131
Figure 4-10. Variation of excess pore pressure ratio (r_u) with time and depth in cases 1 and 2. Locations of elements A to D are shown in Figure 4-1. In (b), elements A – C belong to the second group removed at t = 165 s in case 2. 131
Figure 4-11. Variation of excess pore pressure ratio (r_u) with time and depth in cases 1 and 2 during the earthquake shaking. Locations of elements A to D are shown in Figure 4-1. In (b), elements A – C belong to the second group removed at t = 165 s in case 2. 132
Figure 4-12. Case 2, element B (second removed group): a) horizontal shear stress vs. vertical stress, b) horizontal shear stress vs. horizontal shear strain, low-strain part, c) horizontal shear stress vs. horizontal shear strain, large-strain part, d) excess pore pressure ratio. 133
Figure 4-13. Contours of γ_{max} at selected time instants in case 3. Removal time is t = 15 s. 134
Figure 4-14. Variation of r_u with depth at the end of shaking in cases 3 and 4, and the limit value of r_u required for infinite slope failure. 135
Figure 4-15. Contours of γ_{max} at selected time instants in case 4. Removal time is t = 15 s. 136
Figure 4-16. Contours of γ_{max} and r_u at selected time instants in case 5. Removal times are t = 15, 90, 115, and 165 s. 137
Figure 4-17. Variation of r_u with depth in free-field elements in Case 2 at: a) t = 5 s (during shaking), b) t = 15 s (end of shaking), c) t = 100 s (long after end of shaking), predicted using the fine and standard meshes. 138
Figure 5-1. 3D (finite curved) versus 2D (infinite cylindrical) assumptions of the shape of failure surface 143
Figure 5-2. The finite element meshes used in this study: a) 3D, b) 2D coarse, and c) 2D fine meshes 145
Figure 5-3. Boundary conditions of the 3D model. The boundary condition codes are according to the definitions given in Table 5-1, with the following order: x, y, z

components of solid phase motion, and x, y, z components of fluid phase motion. 147
Figure 5-4. Acceleration time history with 0.3g peak ground acceleration (a_{max})..... 148
Figure 5-5. Selected elements for calculating: a) shear strain, and b) r_u indices. 151
Figure 5-6. Half Normal Probability plot of the effects—a tool for identifying significant effects. 152
Figure 5-7. Effect of lateral boundaries: Crest displacement ratio for various model widths and a_{max}. 154
Figure 5-8. Predicted deformed shape of the crest at t = 15 s, for various model widths and a_{max} = 0.1g. 154
Figure 5-9. Predicted deformed shape of the crest at t = 15 s, for various model widths and a_{max} = 0.3g. 155
Figure 5-10. Predicted deformed shape of the crest at t = 15 s, for a_{max} = 0.5g. 155
Figure 5-11. Reflection of a single pulse from a fixed end in a rod. 156
Figure 5-12. Standing wave caused by interference of incident and reflected waves. ... 156
Figure 5-13. Comparison of crest profiles of the models with different boundary conditions (BC) for B/2 = 40 m and a_{max} = 0.1g: a) no transmitting BC; b) with transmitting BC, $\rho C = (\rho C)_i$; c) with transmitting BC, $\rho C = 10 \cdot (\rho C)_i$; d) with transmitting BC, $\rho C = (\rho C)_i / 10$. 160
Figure 5-14. Crest profile of the model with B/2 = 100 and transmitting boundaries.... 161
Figure 5-15. Contours of predicted displacement (m): a) without, and b) with transmitting boundary conditions for B/2 = 70 m and a_{max} = 0.1g at t = 15 s. Deformation magnification scale = 10. 162
Figure 5-16. Analysis results and a schematic best-fit curve for crest displacement ratio (R_d) for a_{max} = 0.1g: a) using 3D model with B/2 = 100 m, and b) using 2D model. 162
Figure 5-17. Contours of total displacement (m) in 3D (B/H = 3.2) and 2D, at t = 15 s, for a_{max} = 0.1g. Deformation magnification scale is 2. 165
Figure 5-18. Contours of total displacement (m) in 3D (B/H = 3.2) and 2D, at t = 15 s, for a_{max} = 0.3g. Deformation magnification scale is 2. 166
Figure 5-19. Contours of total displacement (m) in 3D (B/H = 3.2) and 2D, at t = 15 s, for a_{max} = 0.5g. Deformation magnification scale is 2. 166
Figure 5-20. Contours of maximum shear strain in 3D (B/H = 3.2) and 2D, at t = 15 s, for a_{max} = 0.1g. Deformation magnification scale is 2. 167
Figure 5-21. Contours of maximum shear strain in 3D (B/H = 3.2) and 2D, at t = 15 s, for a_{max} = 0.3g. Deformation magnification scale is 2. 167
Figure 5-22. Contours of maximum shear strain in 3D (B/H = 3.2) and 2D, at t = 15 s, for a_{max} = 0.5g. Deformation magnification scale is 2. 168
Figure 5-23. Contours of excess pore pressure ratio (r_u) in 3D (B/H = 3.2m) and 2D, at t = 15 s, for a_{max} = 0.1g. Deformation magnification scale is 2. 168
Figure 5-24. Contours of excess pore pressure ratio (r_u) in 3D (B/H = 3.2m) and 2D, at t = 15 s, for a_{max} = 0.3g. Deformation magnification scale is 2. 169
Figure 5-25. Contours of excess pore pressure ratio (r_u) in 3D (B/H = 3.2m) and 2D, at t = 15 s, for a_{max} = 0.5g. Deformation magnification scale is 2. 169

Figure 5-26. Shear stress (τ_{xy}) vs. effective vertical stress (σ_y) for elements A and B, shown in Figure 5-2b, in the model with B/H = 3.2, for a_{max} = 0.1g. Element A is near the slope and element B is in the free-field..... 170
Figure 5-27. Variation of r_u with time for elements A and B shown in Figure 5-2b, in the model with B/H = 3.2, for a_{max} = 0.1g. Element A is near the slope and element B is in the free-field..... 170
Figure 5-28. Shear stress (τ_{xy}) vs. effective vertical stress (σ_y) for element A (shown in Figure 5-2b) in the model with B/H = 3.2, obtained from the analyses where a_{max} is: a) 0.1g, b) 0.3g, and c) 0.5g. 171
Figure 5-29. Variation of r_u with time for element A (shown in Figure 5-2b), in the model with B/H = 3.2, obtained from the analyses where a_{max} = 0.1g, 0.3 and 0.5g. 172
Figure 5-30. Stress path in 3D principal stress space for element A (shown in Figure 5-2b), in the model with B/H = 3.2, obtained from the analysis where a_{max} = 0.5g. 172
Figure 5-31. Crest displacement ratio (R_d): RSM model and analysis results for all values of a_{max}..... 174
Figure 5-32. Shear strain index ratio (R_s): RSM model and analysis results for all values of a_{max}..... 176
Figure 5-33. 3D presentation of the response surface for shear strain index ratio (R_s).. 176
Figure 5-34. r_u index ratio (R_r): RSM model and analysis results for all values of a_{max}. 177
Figure 5-35. Boundary conditions of the 3D model subject to transverse loading. The boundary condition codes are according to the definitions given in Table 5-1, with the following order: x, y, z components of solid phase motion, and x, y, z components of fluid phase motion..... 180
Figure 5-36. Contours of total displacement (m) induced by transverse loading for B/H = 2 and 8, and a_{max} = 0.3g at t = 15 s. Deformation magnification scale is 2. 181
Figure 5-37. Contours of maximum shear strain induced by transverse loading for B/H = 2 and 8, and a_{max} = 0.3g at t = 15 s. Deformation magnification scale is 2. 181
Figure 5-38. Contours of excess pore pressure ratio (r_u) induced by transverse loading for B/H = 2 and 8, and a_{max} = 0.3g at t = 15 s. Deformation magnification scale is 2. 182
Figure 5-39. Comparison with a previous study (Arellano and Stark, 2000)..... 187
Figure 5-40. 3D Geometry of the slope studied by Arellano and Stark (2000)..... 187

List of Tables

Table 2-1. Various methods of analysis and corresponding theoretical solution conditions (Potts and Zdravkovic, 1999) 28
Table 2-2. Equations characterizing transmitting boundaries (Kausel, 1988) 60
Table 3-1. The parameters of the multi-yield plasticity model (Popescu, 2001) 80
Table 3-2. Material properties of Fraser River sand. (See Section 3.6.1 for the descriptions of the parameters.) 93
Table 3-3. Results of general soil tests for Fraser River sand. 94
Table 3-4. Ranges of Poisson's ratio for different types of soils. 98
Table 3-5. Liquefaction strength data (Vaid et al., 2001) and the estimated dialtion parameter, X_{pp}. 104
Table 3-6. Significance of soil parameters influencing liquefaction strength. 110
Table 4-1. Soil properties used in simulation of retrogressive failures. 116
Table 4-2. Cases analyzed in this study and predicted lengths of retrogression 120
Table 5-1. Description of boundary condition codes (Prevost, 2002). 147
Table 5-2. Material properties 149
Table 5-3. Analyses combinations. 152
Table 5-4. Effect of slope angle 178
Table 5-5. Comparison between 3D/2D ratios of responses (for B/H = 2, and a_{max} = 0.3g) calculated from cases of parallel and transverse loading. 182
Table 5-6. Comparison with some previous studies. 188

List of Symbols and Abbreviations

1D: one-dimensional
2D: two-dimensional
3D: three-dimensional
a: attraction
a_{max}: peak ground acceleration
$\mathbf{a}^s$: solid acceleration
$\mathbf{b}$: body force
B: slope width
B_0: low strain elastic shear modulus
B_f: fluid bulk modulus
c: cohesion
C: shear wave speed
c_d: dilatational-wave speed
C_r: ratio of cyclic resistance under simple shear and triaxial stress conditions
CRR: cyclic resistance ratio
$CRR_{7.5}$: cyclic resistance ratio for magnitude 7.5 earthquake
c_s: shear-wave speed
CSR: cyclic stress ratio
c_u: undrained shear strength
C_u: coefficient of uniformity
D_{10}: effective grain size
D_{50}: median grain size
DOE: Design of Experiment
D_r: relative density
e: void ratio
E: elastic Young's modulus
EPWP: Excess Pore Water Pressure
e_{max}: maximum void ratio
e_{min}: minimum void ratio
F_{2D}: two-dimensional safety factor
F_{3D}: three- dimensional safety factor
Fs: factor of safety
g: acceleration of gravity
$g(\theta)$: function of the shape of the cross-section of failure surface on the deviatoric plane
G: shear modulus
G_0: low strain elastic shear modulus
G_{max}: maximum shear modulus
G_s: specific gravity
h: slope height
H: slope height
$I = I(t)$: arbitrary function presenting incident motion
$\bar{J}_2$: second invariant of $\bar{\mathbf{s}}$ tensor
$\bar{J}_3$: third invariant of $\bar{\mathbf{s}}$ stress tensor
k: hydraulic conductivity
$\bar{k}$: parameter for yield surface size
k_0: coefficient of lateral stress
K_α: Correction factor for the effect of static shear stress on liquefaction susceptibility
$K_{\alpha\sigma}$: Combined correction factor for the effects of overburden pressure and static shear stress on liquefaction susceptibility
K_σ: Correction factor for the effect of overburden pressure on liquefaction susceptibility
L: length
M_k: material parameters determining the shape of failure surface
MSF: Magnitude Scaling Factor
n: power exponent
N: arbitrarily-shaped wave moving in the negative x-direction
N_{Liq}: number of cycles to liquefaction
N_s: stability number
n^w: porosity
p: mean (effective) stress
P: arbitrarily-shaped wave moving in the positive x- direction
$\mathbf{P}$: symmetric second-order tensor of plastic deformations direction

$\bar{p}$: difference between the mean stress and attraction ($\bar{p} = p - a$)

p_0': reference effective mean stress

p_a: atmospheric pressure (100 kPa)

p^w: pore fluid pressure

$R = R(t)$: arbitrary function presenting reflected motion

r_d: stress reduction factor

R_d: 3D/2D crest displacement ratio

R_r: 3D/2D r_u index ratio

R_s: 3D/2D shear strain index ratio

RSM: Response Surface Methodology

r_u: excess pore water pressure ratio with respect to initial vertical effective stress

s: multiplier for incident motion

$\mathbf{s}$: deviatoric stress tensor

$\bar{\mathbf{s}}$: transformed deviator stress tensor ($\bar{\mathbf{s}} = \mathbf{s} - \bar{p}\mathbf{a}$)

t: time

T: wave period

$u = u(t)$: associated displacement motion at the node

u_e: excess pore water pressure

u_j: displacement in y-direction (at t_j)

v: displacement in y-direction

v_j: displacement in y-direction (at t_j)

v^s: solid velocity

v^w: fluid velocity

x, y, z: spatial coordinates

X_1: level of quantitative factor ξ_1

X_{pp}: dilation parameter

$\hat{Y}$: approximate/ predicted response

$\mathbf{a}$: tensor of coordinates of the center of the yield surface

α: stress-strain curve coefficient

α_c: ratio of in-situ to triaxial stress conditions

α_N: Newmark algorithm parameter

β: slope angle of seafloor

β_{ij}: regression coefficients

β_N: Newmark algorithm parameter

$\mathbf{d}$: Kronecker delta tensor

ε_c: maximum deviator strain in compression

ε_t: maximum deviator strain in extension

ε_{dev}^{max}: maximum deviator strain

ε_v^p: plastic volumetric strain

ϕ: friction angle at failure

ϕ_{cv}: constant-volume friction angle

ϕ_d: developed (mobilized) friction angle

$\phi_{QSS/SS}$: mobilized friction angle at quasi-steady state or steady state

$\Phi(X_1, X_2, ..., X_k)$: true response function of levels Xi

γ: unit weight

γ_{max}: maximum shear strain

γ^p: plastic shear strain

γ_w: fluid unit weight

γ_{xy}: horizontal shear strain

η: stress ratio

$\bar{\eta}$: normalized stress ratio

η_ψ: dilation stress ratio

λ: wavelength

ν: Poisson's ratio

θ: Lode angle

ρ: mass density

ρ_s: solid particles mass density

ρ_w: fluid mass density

$\mathbf{s}$: normal (effective) stress tensor

σ_{bd}: applied-at-boundary normal stress

$\sigma_{d,cyc}$: cyclic deviator stress

σ_{in}: incident normal stress

σ_m: average confining pressure

σ_{v0}: initial total vertical overburden stress
σ': effective normal stress
σ'_{3c}: initial effective all-round pressure (triaxial)
σ'_h: horizontal effective stress
σ'_{nc}: initial consolidation pressure
σ'^{s}: solid effective stress
σ'_v: vertical effective stress
σ'_{v0}: initial effective vertical overburden stress
σ'_{vc}: initial effective vertical stress (simple shear)
τ: shear stress
τ_{bd}: applied-at-boundary shear stress
τ_{cyc}: cyclic shear stress
τ_e: shear stress applied during earthquake
τ_{in}: incident shear stress
τ_{xy}: horizontal shear stress (in xy-plane)
ξ_1: quantitative factor
ψ: dilation angle
ζ: true response

Chapter 1 - RESEARCH PURPOSE

1.1 Introduction

Most landslides on the seafloor have occurred unobserved or during prehistoric times. A few slides, however, have been documented directly (e.g. Hampton et al., 1996). Earthquakes, rapid sedimentation, tidal and storm waves, tsunami draw-downs, gas hydrates, and glacial loading are the known causes of submarine landslides (e.g. Locat and Lee, 2002). Some famous submarine failures near Canada in areas such as Grand Banks (NL), Scotian Shelf (NS), Saguenay Fjord (Quebec), Vancouver Island (BC), Kitimat Arm (BC), Fraser River Delta (BC), Valdez (Alaska), and Humboldt (northern California) were all triggered by earthquakes and resulted in tsunamis, turbidity currents, or debris flows. These landslides have been and continue to be a serious potential hazard to human life and economical resources on- and offshore. The 1929 Grand Banks failure, for instance, which was triggered by an earthquake, severed trans-Atlantic telegraph cables and killed 27 people onshore (Piper et al., 1999).

Such evidence, in addition to a large number of other submarine landslides worldwide, have raised the importance of considering causes and mechanisms of seafloor failures in more detail using rigorous methodologies, especially owing to current increasing economic activities along Canada's continental margins and coastlines such as offshore oil explorations.

Some features of submarine landslides can be recognized from seafloor images and profiles. These features are in some cases very different from terrestrial landslides. Submarine slides typically involve much larger amounts of mass movement. Submarine

failures occurring on very flat slopes are more frequent than terrestrial landslides. Three-dimensional shapes of escarpments in submarine slope failures are similar to terrestrial failures but much more extensive. In addition, the retrogression linear and aerial extent of submarine failures is usually much greater than on land, and retrogressive failures have been known to extend up to 20 km in length.

To this date, most of the studies on submarine landslides have been carried out from geological and geophysical points of view; and geotechnical analysis of such failures, associated with earthquake-induced instabilities in particular, have been mostly carried out using simple methods that are based on a series of simplified assumptions.

It is thus of great importance to better understand the mechanisms and reliably predict the extent of seismically induced submarine slope failures so that losses can be minimized.

This research has two primary objectives:

- To provide a tool for analyzing seismically induced ***retrogressive*** slope failures and to use this tool for explaining the mechanisms and identifying the main factors affecting the extension of those slope failures*;*
- To assess the ***three-dimensional*** (3D) effects in seismic analysis of submarine slopes, in order to provide geotechnical practitioners with a reliable tool for extrapolating the results of manageable 2D seismic analyses to real 3D configurations.

Based on the results obtained in the study, quantitative and qualitative guidelines for geotechnical practice are provided, for the range of slope geometries and soil characteristics addressed here. These guidelines are provided in two areas of soil

dynamics that have not been explored in a consistent manner in the past: (1) seismically induced retrogressive slope failures, and (2) effective stress, dynamic, nonlinear 3D analysis of saturated slopes.

Another objective of the study, related to the scarcity of geotechnical data on submarine soils, is:

- To design a procedure for constitutive model parameter ***calibration*** based on liquefaction strength analysis, using Response Surface Methodology and accounting for uncertainties in soil properties.

These objectives are achieved by using rigorous methodologies, specifically, numerical modelling by the finite element method, which can account for the important aspects of soil dynamic behaviour. In particular, since submarine soils are saturated, liquefaction potential may be significant in seabed deposits. Simulating the liquefaction phenomenon requires sophisticated methodologies, such as coupled-field analysis of two-phase media, in addition to using advanced constitutive models. These require more parameters and input data, which as mentioned earlier, are scarce for seismic analysis of submarine slopes. For such analysis, other sources of uncertainty in addition to soil parameters include the initial (pre-failure) geometry of slope and characteristics of loading such as earthquake magnitude, frequency content, and maximum acceleration. However, the main purpose of this study is to understand and explain the mechanisms generally involved in seismically induced submarine failures rather than to perform a site-specific analysis; therefore, soil properties, slope geometries, and earthquake loadings as close as possible to those addressed in the literature are used for this purpose.

This research also addresses some of the objectives of the COSTA-Canada project, a Canadian contribution to the study of Continental Slope Stability, aimed at increasing the reliability of economic activities along Canada's continental margin and coastline. The objectives of this international project are described in Section 1.2.

Accurate simulation of soil behaviour under cyclic loading and the full coupling between solid and fluid particles allows more accurate prediction of liquefaction phenomenon. The two- and three-dimensional seismic analyses of submarine slopes performed herein are carried out using a state-of-the-art finite element program for the static and transient response analysis of linear and nonlinear, two- and three-dimensional systems.

The numerical model is used to identify and explain the triggering mechanisms of seismically induced retrogressive failures, showing how submarine failures propagate to very long distances. It is also used to assess the significance of 3D effects on seismic stability of slopes with an emphasis on boundary conditions effects.

1.2 COSTA-Canada Objectives

COSTA-Canada (Locat et al., 2001), a Canadian contribution to the study of Continental Slope Stability, is an integrated approach to the study of submarine mass movements, from its initiation to the formation of the final deposit (see COSTA-Canada, 2000).

The project is aimed at increasing the safety and reliability of developing economic activities along Canada's continental margin in various fields including natural resources (oil and gas), transportation (port development), electrical transmission, and communication (cables). COSTA-Canada is a contribution to COSTA-Europe, which

brings together several researchers and scientists in different fields of geology, geophysics, and geotechnique from countries such as Norway, France, Italy, and UK. Five Canadian universities participate in the COSTA-Canada project, which has started in April 2000. From Memorial University, the participants in the project study different aspects of submarine slope failures such as numerical and experimental (centrifuge) analysis of initiation of submarine slopes.

Long-term and short-term objectives of the project are as follows (COSTA-Canada, 2000):

a) Long-term objectives are related to these fundamental questions that persist on the continental slope stability and seafloor failures:

1. What are the triggering mechanisms of slope failures on the continental margins?
2. What is the variability from one site to the next?
3. Why will one region of seafloor fail while neighbouring regions remain stable?
4. What are the factors that determine where a slope failure will occur?
5. What determines the location of the slip planes?
6. What is the role of gas hydrates in slope stability?

b) COSTA-Canada project has identified the following short-term objectives:

1. Assessment of historical records of slope instability, slope parameters, seismicity, and tectonic setting.
2. Understanding of seafloor failure dynamics through 3D imaging of sediment architecture and geometry of slope failures.

3. Understanding of sediment physical, mechanical and elastic properties of slip planes and areas prone to slope sliding.
4. Determination of presence of gas hydrate and its significance for slope stability.
5. Modelling of forces and mechanical processes that control the initiation of slope instabilities (release mechanisms), flow dynamics and initiation of tsunamis.
6. Assessment of risk-fields related to slope stability.

The results of the present research contribute to some of the major objectives of COSTA-Canada project from a geotechnical point of view, especially, objectives a.1, a.3, a.4, a.5, b.3, and b.5 with regard to seismic trigger. It should be emphasized that the focus is on pre-failure or initiation of the failure in submarine slopes. Issues such as post-failure or run-out distances are not addressed herein and are out of the scope of this research.

1.3 Research Tools

This research involves nonlinear dynamic finite element analysis using the finite element program, Dynaflow; and processing of laboratory soil test results for calibrating the numerical model parameters. The following software with the listed license information are used:

- Dynaflow, Version 2002, Release 02.A, Copyright © 1998, Princeton University, NJ, USA.
- FEMGV 6.2, Release 01, Copyright © 2000 Femsys Limited, UK, Licensed to Memorial University: as pre- and post-processor for Dynaflow.
- Design-Expert®, Licensed to Dr. L. Lye and available by his kind permission for calculations pertaining to the Design of Experiments and Response Surface Methodology.

Some other programs such as MATLAB, Excel, etc. have been used through the computer network of the Faculty of Engineering, at Memorial University of Newfoundland.

1.4 Original Contributions

The original contributions of this doctoral research, related to applying a state-of-the-art method of numerical modelling of dynamic soil behaviour to the analysis of submarine slopes subjected to seismic loading, are:

1. Introducing a procedure for simulating earthquake-induced retrogressive failures of submarine slopes: using the proposed procedure, the mechanisms of retrogression are explained and predictions of retrogression distance accounting for the effects of some geo-morphological factors are provided for geotechnical practice.
2. A study for quantifying three-dimensional (3D) effects in seismic slope stability analysis of submarine slopes susceptible to liquefaction: to the author's knowledge this is the first study using dynamic, effective stress, fully coupled, non-linear finite element analyses in the general area of slope stability analysis.
3. Introducing a method for soil parameter calibration, using limited laboratory information and based on liquefaction strength analysis, by applying a set of statistical tools and techniques provided in the context of Response Surface Methodology (RSM).

1.5 Outline of the Thesis

This thesis has five chapters. The objectives of the research have been described in this chapter. In addition, how the present study ties in with an international effort (i.e. COSTA-Canada and Europe) on understanding the submarine, continental slope stability was highlighted. In Chapter 2, the literature pertinent to the present study is reviewed. This is followed, in Chapter 3, by a detailed description of the numerical model, the finite element code used, and the procedure for soil parameter estimation. Chapter 4 presents the procedure for simulation of retrogressive failures, and the initiation and propagation mechanisms of such failures, to emphasize the importance of accounting for this effect in off-shore structures risk assessment. Finally, Chapter 5 presents a comparison between three- and two-dimensional analyses, quantifying the 3D effects, resulting in practical guidelines for extrapolating 2D analysis results to 3D situations.

Chapter 2 - LITERATURE REVIEW

2.1 Introduction

The main topics of this research are finite element simulation of submarine retrogressive failures, and assessment of the three-dimensional effects in slope stability analysis. The published literature related to the above topics covers the broad areas of submarine geology/geophysics, soil characterization, finite element analysis, soil constitutive laws, and seismic loading. The literature review presented here covers only the studies that are reasonably useful as background and/or comparison basis for particular phenomena analyzed in this study. Since in the comparison of the 3D and 2D effects, transmitting boundary conditions are implemented, this topic is also included in the review. An overview of Response Surface Methodology (RSM) and Design of Experiments is also given, since these techniques were also used for various aspects of the research.

2.2 Submarine Slope Failures

2.2.1 Soil Investigation Techniques

Review of existing data and planning is the first step in a marine geotechnical investigation program (Poulos, 1988). It can take up to 2% of total cost of investigation, but can play an important role. Other phases are related to:

- Geophysical survey
- Oceanographic data collection
- Laboratory (including on-board and on-shore), and in-situ soil testing

Offshore investigation cost is about 79% of total cost of investigation, which is much more than any other phase, even laboratory tests (8%) or engineering analysis (11%). However, each project may require a different amount of site investigation. Design of a platform foundation, for example, may require a great amount of detailed geophysical investigation (including 3D seismic profiling and in-situ testing) at a particular location, whereas design of a pipeline may only require seafloor mapping along the pipeline route with limited in-situ testing.

Geophysical surveys are very efficient in site investigation both economically and technically. Common techniques are (e.g. Williams and Aurora, 1982; Poulos, 1988):

- Bathymetry: Water depth is measured by high-precision echo sounders to produce a seabed contour map.
- Seafloor topography: Images of surficial physiographic features of seafloor are obtained by side-scan sonar 'fish' transmitters.
- Vertical profiling: Two- and three-dimensional profiles of seabed in depth are obtained by energy sparker systems.

In the past decade, high-resolution multibeam mapping systems have been largely developed and implemented in offshore site investigations. According to Locat and Lee (2002), with the development of multibeam techniques and Differential Global Positioning Systems (DGPS), precise bathymetric maps of near air-photograph quality can be produced. Seafloor images of this kind clearly show morphological features of seafloor mass movements. Samples of seafloor images and seismic profiles are shown in the following sections showing examples of submarine slope failures. The most recent improvements may be found in Hughes Clarke (1996), Gardner et al. (1999a), and Locat

and Lee (2002). Of great interest are new trends in geophysical investigations using Biomedical Imaging Modalities (Rack, 2000), such as Digital X-Ray and Nuclear Magnetic Resonance Imaging (NMR and MRI).

These techniques will allow non-destructive determination of geophysical characteristics of sediments. Geotechnical properties will then be estimated using geophysical-geotechnical correlations.

Cone Penetration Test (CPT) is the most widely used technique of seabed in-situ geotechnical characterization. Moran (1993) discusses difficulties encountered in offshore investigations near Canada: Scotian Shelf, Grand Banks of Newfoundland, Beaufort Shelf, and Cascadian Margin. For instance, interruption of CPT profile with large boulders, and health risk due to gas hydrates in soil samples, e.g. by standard (gravity) piston corer, from Cascadia margin are among issues addressed.

Standard laboratory tests, including tests for basic classification of soils (such as grain size distribution analysis and water content measurement) and tests for determining shear resistance of soils (such as triaxial, simple shear, and consolidation tests) are also common for submarine soils (Williams and Aurora, 1982).

A classification system is presented by Noorany (1989) to extend the existing Unified System of terrestrial soil classification for submarine sediments. Criteria of this classification are based on some major and minor categories such as: origin of the soil (namely, lithogenous, hydrogenous, biogenous), and location (namely, Neretic: shelf zone, Hemipelagic: combined slope and rise zone, Pelagic: deep-sea zone, and Terrigenous: originated from terrestrial materials.)

The most difficult task for performing laboratory tests on submarine soils is to preserve the in-situ condition of samples by collecting so-called undisturbed samples (Clark and Guigne, 1988). This is especially difficult for samples of highly overconsolidated layers of clay (with over-consolidation ratios as high as 8 – 12) in depths of 5 – 10 m below seafloor, samples with dissolved gas, and those that are very soft (e.g. Christian and Morgenstern, 1986, Canadian Beaufort Sea; Morin and Dawe, 1986, Labrador Sea).

Cyclic triaxial and simple shear tests can be used for laboratory evaluation of liquefaction strength of submarine sands (see e.g. Locat and Lee, 2002). Again, the reliability of such test results to present real in-situ strength is under question due to sample disturbance. Moreover, liquefaction resistance of re-constituted sand samples (and in general the undrained response of sands) has also been found to be sensitive to factors such as various pluviation methods, e.g. water- and air-pluviation techniques (Vaid et al., 1999).

According to Noorany (1984), two major differences exist between marine and terrestrial soils: (1) Salinity: seawater has more dissolved salt (typically up to 4%); and (2) Gas: high pressure at great depths maintains considerable amount of gas dissolved in seawater (see also Grozic, 1999). Traditional phase relationships in soil mechanics do not consider dissolved salt in water, and dissolved gas in air, thus, leading to systematic error in computations. This error can be in order of about 10% for water content and void ratio calculations, to about 2% in calculating porosity. In general, the larger the porosity the larger the error of calculation (of all parameters) will be.

State-of-the-art techniques in remote sensing, robotics, artificial neural network, and other expert systems are now employed to reduce sampling and laboratory testing efforts (Clark and Guigne, 1988; Rack 2000).

In this study, results of cyclic triaxial and simple shear tests are used for liquefaction strength analysis. Such test results are obtained from: (1) published studies in the literature (e.g. Vaid et al., 2001; Vaid and Sivathayalan, 1999; Howie et al., 2000, etc.); (2) research projects web sites, including "VErification of Liquefaction Analysis by Centrifuge Studies" project (VELACS: http://geoinfo.usc.edu/gees/velacs/); and "Earthquake Induced Damage Mitigation from Soil Liquefaction" (http://www.civil.ubc.ca/liquefaction). Also, the centrifuge experimental results of one of the VELACS tests are used for validation of the model parameters. The particular test results used in this research and their sources are addressed in the particular sections that the relevant calculations are reported (see Section 3.5).

2.2.2 Seafloor Topography

Seafloor topographical features common to all oceans are (Poulos, 1988):

- Continental margins: including continental shelf, continental slope, and continental rise. Continental margins form 21% of oceans area, and are of great interest for offshore oil explorations. Slope gradients of continental slopes are usually about 2^{o} and may reach 6^{o}.
- Deep ocean-basin floor: including everything seaward from the continental margin except oceanic ridges. Abyssal plains are very flat and connected by canyons to landward sources of sediments.

- Major oceanic ridge systems: including seamounts and guyots forming a series of connected topographical high areas.

In this research, seafloor failures in deep ocean floors and oceanic ridges are excluded, as only failures on continental slope/shelf are the focus of the study.

2.2.3 Causes and Mechanisms of Seabed Failures

A large amount of evidence is now available on instability of submarine slopes in various offshore environments ranging from near-shore areas to continental slopes, and to the ocean deeps. According to Prior and Coleman (1984), these forms of instabilities were defined first by Heim in 1908 as 'subsolifluction or subaqueous solifluction'. Submarine landslides commonly involve large volumes of material, often far greater than in terrestrial slides (Cotecchia, 1987), and they can take place on very flat slopes with an angle of only 0.5^{o} (Prior and Coleman, 1984). On land, the largest landslides involved about 20 – 30 km^3 of mass movement, whereas submarine slides typically involve 4,000 – 5,000 km^3, even up to 20,000 km^3 of mass movement (Hampton et al., 1996).

Most landslides on the seafloor have occurred unobserved or in prehistoric times (Hampton et al., 1996). Only a few slides have been documented directly, including those that occurred near shore and retrogressed back to coastline (1888 Trondheim Harbor slide, Norway, Andersen and Bjerrum, 1967), those that caused disastrous tsunamis (Kitimat Arm, BC, Canada, Prior et al., 1982) and the Grand Banks failure that severed trans-Atlantic telegraph cable (Piper et al., 1999).

Essential features of submarine landslides, i.e. rupture surface (failure surface), headwall scarp, and displaced mass are visible in reflection profiles and sonar images (Hampton et al., 1996).

Hampton et al. (1996) and Mulder and Cochonat (1996), among others, give a very comprehensive list of references reporting failures and their possible mechanisms in five submarine environments:

- Fjords
- Active river deltas on continental margin
- Submarine canyon-fan systems
- Open continental slope, and
- Oceanic volcanic islands and ridges.

Failure mechanisms involved in these environments include (see also Locat and Lee, 2002; Grozic et al., 2000):

- Tectonic activity: earthquake, over-steepening, etc.
- Rapid sedimentation
- Low tidal levels
- Storm waves
- Tsunami draw down
- Gas hydrates
- Seepage
- Glacial loading

Notable examples of earthquake-induced instabilities are (see also Chillarige et al., 1997a; Seed, 1968):

- 1929 Grand Banks Slide, Newfoundland, Canada (Piper et al., 1999); Figure 2-1
- 1946 Vancouver Island, BC, Canada (Mosher et al., 2001)

- 1964 Alaska Earthquake, Valdez, (Lemke, 1967)
- Saguenay Fjord, Quebec, Canada (Urgeles et al., 2001)
- Storegga Slide, Norway (e.g. Bugge et al., 1987)
- Karmsundet and Skudenesfjorden, Norway, (Boe et al., 2000); Figure 2-2
- Humboldt Slide, northern California, US (Gardner et al., 1999b)

Two major modes of submarine slope failures are rotational slumps and translational slides. Referring to a failure as a slump or slide depends upon the ratio between the depth, h, and length, l, of the failure surface (Skempton and Hutchinson, 1969). If h/l is less than 0.15, the failure is called 'slide' (or translational slide) and if it is greater than 0.33, the failure is called 'slump' (or rotational slump). Most submarine failures appear to be translational slides (Prior and Coleman, 1984).

Liquefaction, including flow (static) liquefaction and cyclic liquefaction, has been inferred in submarine failures. Failures occurred in the following areas (among some others) are attributed to cyclic liquefaction due to earthquakes (Mulder and Cochonat, 1996):

- Storegga Slide
- Grand Banks
- Fraser River Delta

Chaney and Fang (1991) have given a list of significant number of seismic liquefaction case histories in coastal environments around the world, explaining site characteristics (such as slope degree, soil type) and observations such as sand boiling, development of cracks, etc.

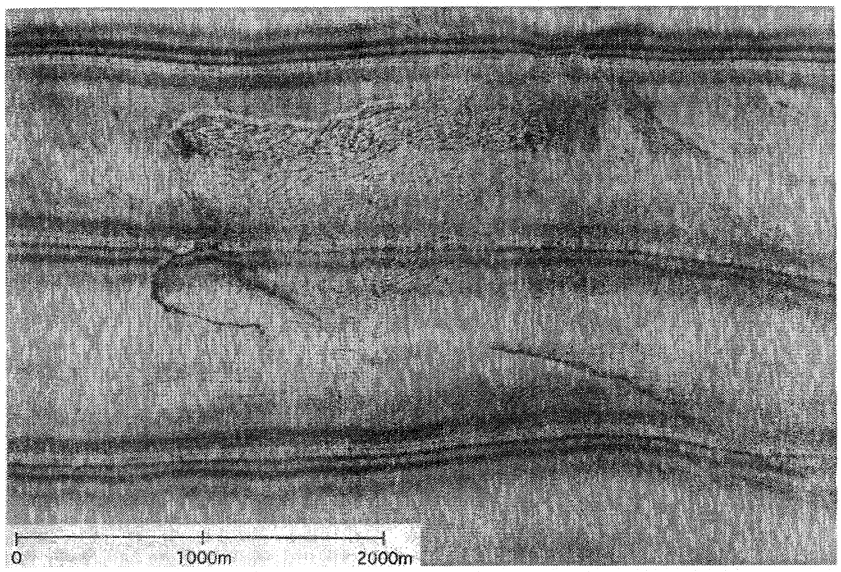

Figure 2-1. SAR mosaic showing slump scars in one of the source areas of the 1929 Grand Banks event (after Piper et al., 1992). Photo obtained from Mulder and Cochonat (1996).

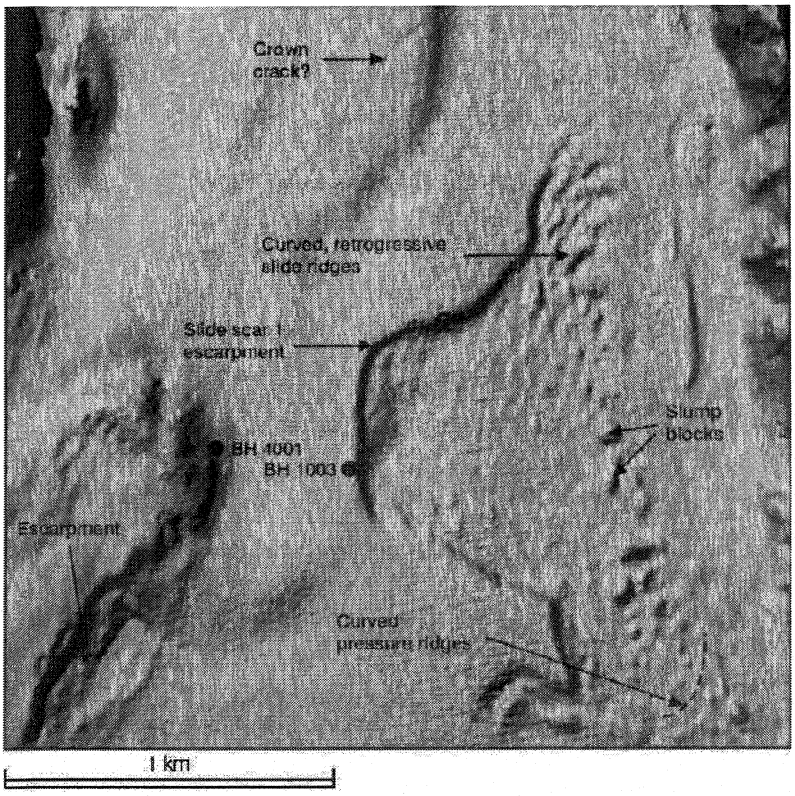

Figure 2-2. Shaded relief image of multibeam bathymetric data from the slide scar 1, Karmsundet and Skudenesfjorden, Norway (Boe et al., 2000).

2.2.4 *Submarine Retrogressive Failures*

According to Hampton et al. (1996), sliding that occurs serially as numerous adjacent failures that progress upslope is termed "retrogressive". Some unique characteristics of submarine slides, such as huge volumes of mass movement, vast scars, very long displacement of slide blocks, considerable travel distances of debris or mudflows, and development of the slide on nearly flat surfaces are believed to be caused, at least in part, by retrogression effects (Edwards et al., 1995; Hampton et al., 1996; Mulder and Cochonat, 1996).

Retrogressive slides have occurred in both offshore (continental margin and deep ocean) and near-shore environments. Some recent slides originated near-shore and retrogressed back across the shoreline. Examples of such failures are the catastrophic slides in Seward and Valdez, during 1964 Alaska earthquake (Lemke, 1967), and 1888 Trondheim Harbor slide, Norway (Andersen and Bjerrum, 1967). On land, such failures have been reported and documented in many areas, especially in Scandinavia and eastern Canada in extra sensitive quick clays (Terzaghi et al., 1996).

Flow failures in submarine loose sand, silt, and sensitive clays are often retrogressive. Some adjacent flow failures are very common in loose sandy and silty deposits in the Finnish and Norwegian Fjords (Bjerrum, 1954; Terzaghi, 1956; Andersen and Bjerrum, 1967) as well as Atlantic and Pacific margins of Canada and USA (Hampton et al., 1996; Piper et al, 1999). Some of these failures seem linked to low tides, when degree of saturation is below 1, the excess pore pressure generated during high tide does not have enough time to dissipate during the ebb (Andersen and Bjerrum, 1967). In Alaska, Fraser River Delta, and Grand Banks, retrogressive failures were triggered by earthquakes (e.g.

Chillarige et al. 1997a; Piper et al, 1999). The 1929 Grand Banks failure (Figure 2-3) is one of the most extensive retrogressive failures triggered by an earthquake (Piper et al., 1992, 1999). Rapid sedimentation is a triggering mechanism in Mississippi River Delta, which has resulted in numerous retrogressive slides (Prior and Coleman, 1978). In addition, other environmental processes such as gas hydrates can contribute to the initiation and acceleration of retrogression (e.g. Hampton et al., 1996).

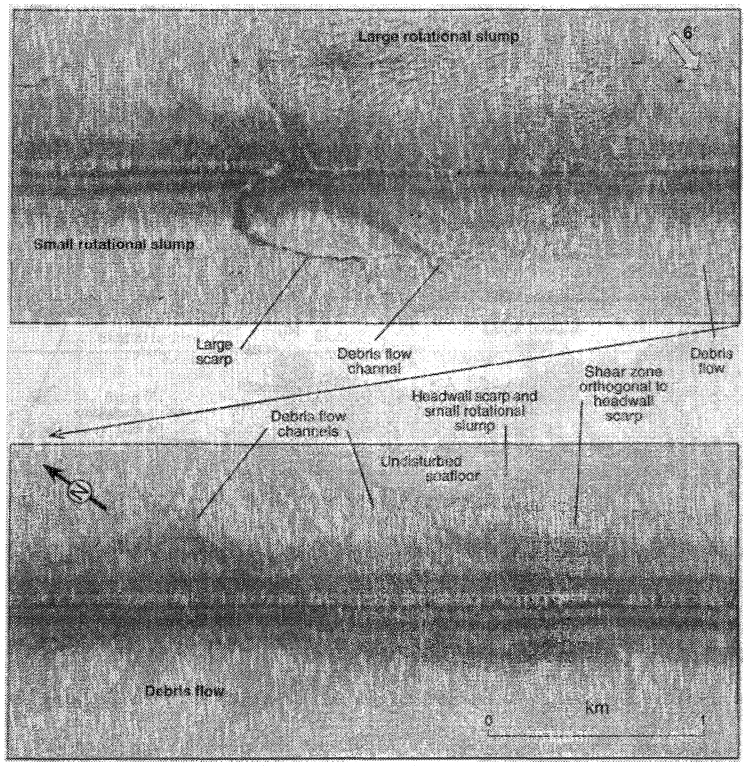

Figure 2-3. Side scan image of small- and large-scale rotational slumps on St. Pierre Slope, Grand Banks, Newfoundland, after the 1929 earthquake (Piper et al., 1999).

Based on observations on numerous landslides worldwide, Mulder and Cochonat (1996) classified retrogressive failures (also termed as progressive or complex slumps or slides) as follows (Figure 2-4):

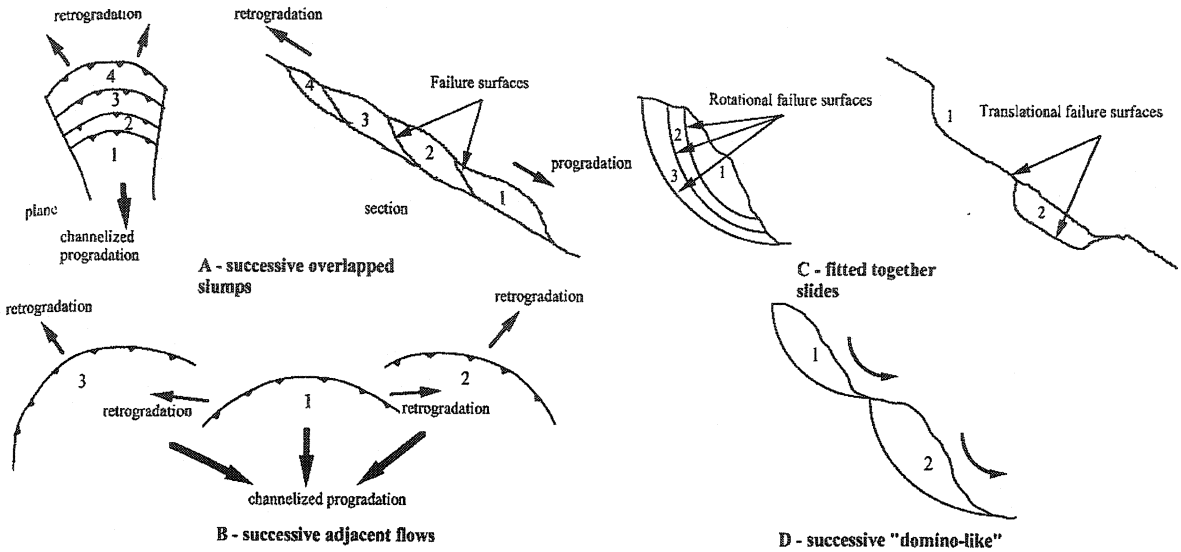

Figure 2-4. Classification of successive submarine slumps or slides (Mulder and Cochonat, 1996).

A) Successive overlapped: if the failure surface of the main body (i.e. initial failure) is merged with the failure surfaces of the following failures;

B) Adjacent: if the main body triggers the instability along the whole perimeter of the scar; this type of failure is not so frequent;

C) Fitted together (or additive): if the failure surface of the main body is not merged with the failure surfaces of the following failures. This type is also termed as 'additive' failure. These slides are unique because retrogression occurs at the bottom of the first slide rather than at the top scarp;

D) Domino-like: if a topographically high mass of sediment fails and induces mobility in an underlying second material mass; this type is infrequent.

Many examples of such successive failures are presented by Mulder and Cochonat (1996); however, it seems that the term 'retrogressive' is sometimes used instead of 'successive'. As was mentioned previously, retrogression is the propagation of the failure in the upslope direction. Obviously, only types (A) and (B) can be referred to as

retrogressive failures in accordance with other researchers' definitions (e.g. Hampton et al., 1996).

Presence of surficial ridges, inclined, truncated seismic reflections, rotated blocks, basal and internal shear surfaces, distal sediment compression, etc, are all typical characteristics and visual features of submarine retrogressive slides (Piper et al, 1992; Gardner et al., 1999b; Boe et al., 2000, Locat and Lee, 2002; among others). Such features are visible in seafloor images (Figure 2-1 and Figure 2-2) and seismic reflection profiles (Figure 2-5).

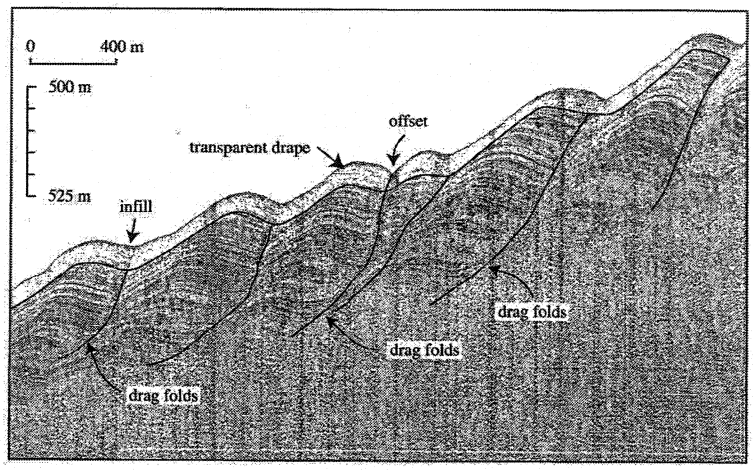

Figure 2-5. Seismic-reflection profile of retrogressive features in the Humboldt Slide (Gardner et al., 1999b) showing the main body of the slide with folded and back-rotated slide blocks. Black lines show the shear surfaces.

Limitation (i.e. stop of retrogression) mechanisms proposed in different sources (Andersen and Bjerrum, 1967; Piper et al., 1999; Chillarige et al., 1997a; Carson and Lajoie, 1981; Prior and Coleman, 1984; Anderson and Richards, 1987, etc) include various factors, such as:

a) Topographic: constraints due to volume of the receiving valley, channel, etc.; shape of the scar; upslope gradient change; stable back scarp angle;

b) Geomechanical: existence of dense sands with dilative post-yield behaviour, overconsolidated non-sensitive clays, and more permeable soils that allow rapid drainage.

Based on these studies, submarine retrogression typically extends to distances of the order of 0.5 – 7 km and in extreme cases up to 20 km.

From geotechnical point of view, some researchers have explained the mechanism of retrogressive failures, triggered by causes other than earthquakes. These studies include:

- Haug et al. (1976) for a failure near Saskatchewan River, triggered by movement or unloading at the toe of the slope, using the limit equilibrium method (factor of safety approach): In this study it is shown that if one failure surface is assumed for the failed mass, the factor of safety is well above one (Fs = 1.8 in Figure 2-6), which cannot explain the occurrence of failure. However, the occurrence of failure as a multiple retrogressive failure is explained by locating the individual failure surfaces shown in Figure 2-6 by examination of borehole samples in the field and calculating the factors of safety for each failure surface (which are well below one).

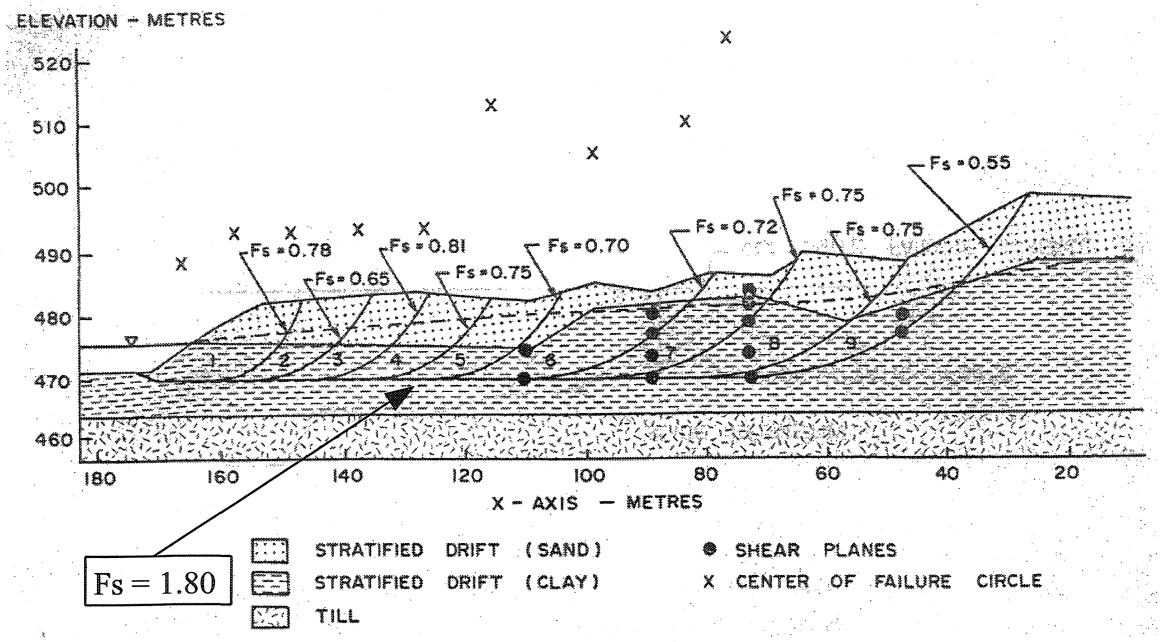

Figure 2-6. Detailed illustration of retrogression mechanism by factor-of-safety obtained from limit equilibrium method (Haug et al., 1976). Note that the factor of safety on the horizontal failure zone is 1.82. The slide is located near South Saskatchewan River, Canada.

- Sladen et al. (1985b) for the Nerlerk Berm submarine failure using the collapse surface concept: The slides were triggered by hydraulic sand placement, which caused static liquefaction in the underlying sand. According to this study, a sudden drop in strength associated with liquefaction leads to the removal of the failed mass and leaves over-steepened head scarp which itself can lead to another liquefaction failure. Factors of safety close to unity are calculated for the initial and subsequent failure surfaces, which altogether, form the final bowl-shaped crests.
- Mitchell and Markell (1974) and Leroueil et al. (1996), among others, based on classical undrained slope stability analysis using the stability number for clays: According to the former study, in (terrestrial) clays of eastern Canada, significant retrogression happens if the stability number $N_s = \gamma h/c_u$ (where, γ = unit weight, h = slope height, and c_u = undrained shear strength) is larger than

5.5; however, the latter relates the phenomenon to the plasticity index as well based on the remolding characteristics of clays.

- Chillarige et al. (1997a) using a state boundary surface concept for Fraser River delta submarine failures of sand deposits: In this study, the retrogressive flow slides of the Fraser River Delta sediments are attributed to the undrained stress redistribution after pore pressure changes due to low tides. After low tides that result in some initial flow failures, sediments that have already experienced some partially drained residual pore pressures can undergo stress redistributions, which can be sufficient to bring the state of the sediments on to the 'contractant state boundary surface (CSB)'. This is a surface in $p'-q-e$ space that controls the behaviour of purely contractant sands at large strains, and envelopes all the undrained effective stress paths of such soils (Sasitharan et al., 1993). The redistribution can cause strain softening of the remaining unsupported sediments, which results in another flow slide, and hence, retrogression of failure. Such slides cease to progress when a denser soil deposit or a stable back scarp is encountered.
- Kvalstad et al. (2003) using a Finite Element Analysis and a Computational Fluid Dynamics program (CFX4 code, AEA Technology 1999), for a headwall scarp left by the Storegga slide (off Norway, occurred ca. 8000 years ago) involving clay deposits: In this study, to evaluate the effect of sensitivity and brittleness on the development of progressive failure, the Finite Element Method is used for modelling the initiation of failure in a slope with 30° inclination of a normally consolidated clay resting on a sensitive clay layer

over a strong base (Figure 2-7). The general slope of the seafloor is about 1° over a distance of about 20 km down to the edge of the headwall (i.e. the slope of the seafloor to the right of the slope in Figure 2-7 is about 1°). A non-linear strain softening material model is applied for the stability analysis of the slope material. The triggering mechanism is not specified, however, the seismic trigger is shown to be not enough to initiate such a failure because it only induces very small strains. In addition, the run-out distance analysis is carried out by the CFX4 program, modelling soil as a Bingham fluid with intact and residual yield strength and a strength degradation model controlling the reduction in strength as a function of strain. As illustrated in Figure 2-7, the mechanism of retrogression is as follows (summarized after Kvalstad et al., 2002):

- an initial slide is developed in the lower part of the slope with sensitive clay layers which reduces the pressure against the headwall
- the unloading of the headwall causes undrained expansion of the soil towards the scar and strain concentrations in the toe area
- the strain concentrations cause strain softening in the base layer and progressive failure develops as indicated by the shear bands (Figure 2-7) predicted by a finite element analysis.
- the factor of safety decreases and the failing soil mass accelerates into the existing slide scar under gravity loading leaving a new headwall.
- the reduction in strength gives sufficient mobility (acceleration) to unload the next headwall and the process repeats itself until soil

strength parameters, layering or geometry change sufficiently to reduce mobility and decelerate the sliding process.

According to Kvalstad et al. (2002), reduction in strength below failure limit and softening towards remoulded strength "leads to run out and separation of out-runner block." Also, the simulation of run-out carried out by the Computational Fluid Dynamics program CFX4, indicates that the material travels up to several hundred meters (see e.g. Figure 2-8, where the debris profile is displayed at a time instant that the debris frontier is about 800 m away from the initial location of slope toe.)

De Blasio et al. (2003) and Issler et al. (2003) have also performed numerical simulations of the debris flow occurred in the large Storegga slide (phase 1) and a particular location of the slide (Ormen Lange), respectively. In these studies, a Bingham (visco-plastic) model is used for the clay material to assess effects of such parameters as the shear resistance between the debris flow and the seabed on run-out distance. Since the numerical simulation results in run-out distances much smaller than the observed typical run-out distance in the Ormen Lange area (15 – 20 km), Issler et al. (2003) explain how some processes such as remolding, wetting and hydroplaning can reduce the shear resistance and thus lead to re-producing a profile that is in agreement with the observed post-failure profile of debris deposition.

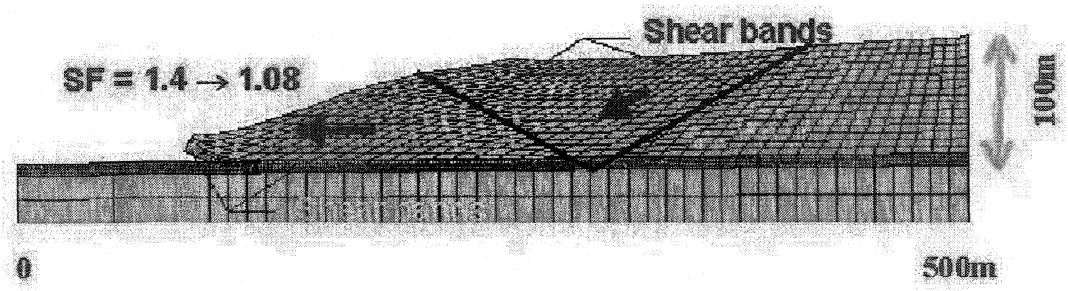

Figure 2-7. Finite element analysis of a slope of normally consolidated clay resting on a sensitive clay layer (strain softening) over a strong base (Kvalstad et al., 2002).

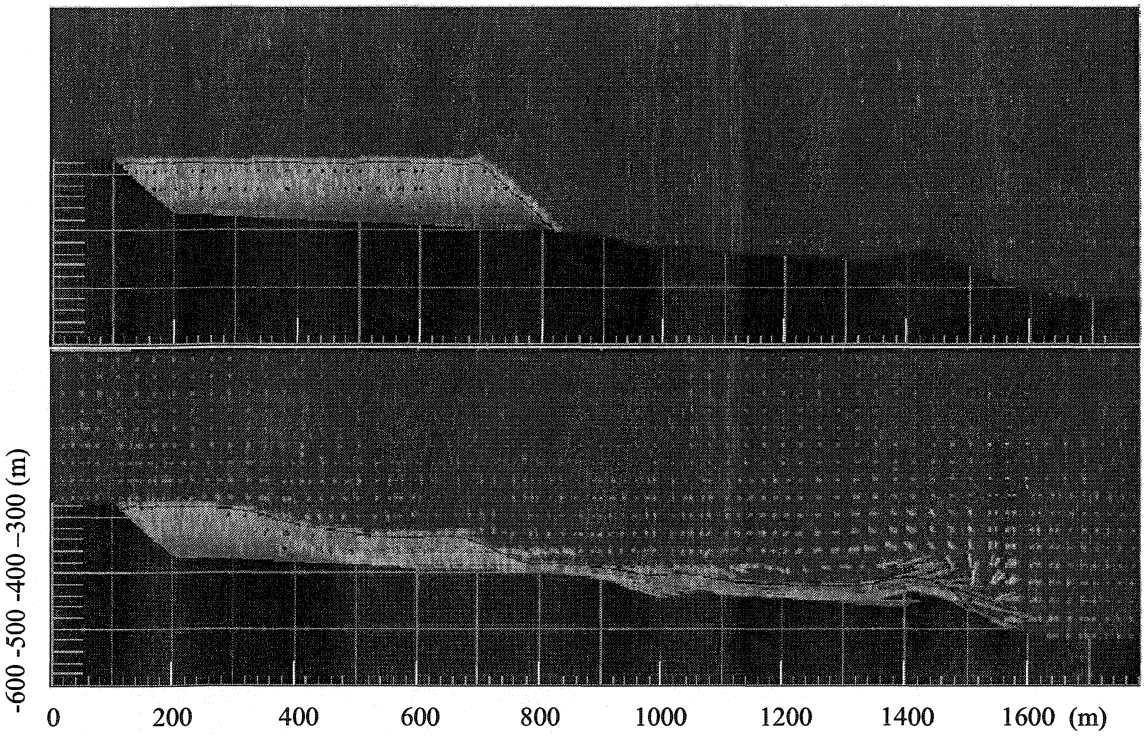

Figure 2-8. Simulation of run-out by a Computational Fluid Dynamics program (Kvalstad et al., 2002)

Certainly, ignoring the possibility of retrogression mechanism will result in neglecting a considerable risk of damage for coastal or offshore infrastructures. In a complete landslide hazard analysis, the susceptibility classes should consider gently sloping or even flat seabed above and below unstable slopes, where the hazard may be increased owing to retrogressive failures and debris run-out, respectively (Hansen, 1984).

2.3 Slope Stability Analysis

2.3.1 Introduction

Generally, four conditions must be satisfied in a complete theoretical solution of a continuum mechanics system: *equilibrium*, *compatibility*, *constitutive behaviour*, and *boundary conditions* of force and displacement (see, for example; Zienkiewics and Taylor, 1989). To solve a system of simultaneous governing equations, equal number of unknowns and equations must exist:

Unknowns (15) = Stresses (6) + Strains (6) + Displacements (3)

Equations (15) = Equilibrium (3) + Compatibility (6) + Constitutive Relationships (6)

Constitutive relationships relate stresses and strains in a material and in fact describe the behaviour of the material. The most common methods of analysis for slopes are: limit (or limiting) equilibrium, limit analysis (upper and lower bound theorems), and numerical methods such as finite element, and finite difference methods.

One of the main differences among all above-mentioned methods is in the way they satisfy the four conditions of a complete solution. Table 2-1 summarizes these aspects showing what conditions are satisfied.

Table 2-1. Various methods of analysis and corresponding theoretical solution conditions (Potts and Zdravkovic, 1999).

Analysis Method		Equilibrium	Compatibility	Constitutive Model	Boundary Conditions	
					Force	Displacement
Limit Equilibrium		Yes	No	Rigid & Failure Criterion	Yes	No
Limit Analysis	Lower Bound	Yes	No	Ideal Plasticity & Associated Flow Rule	Yes	No
	Upper Bound	No	Yes		No	Yes
Numerical Methods (e.g. Finite Element)		Yes[1]	Yes	Any	Yes	Yes

[1]Local equilibrium is satisfied to the extent of correctness of selected approximating functions.

Obviously, excepting for modern numerical methods such as Finite Element Method (FEM), at least one major condition is not satisfied in other methods, which consequently leads to the inaccuracy of the solution. The error caused is greater in case of dynamic analysis due to complexity of dynamic soil behaviour, dynamic loading, and failure mechanisms. For example, in these analyses it is assumed that soil is a rigid-perfectly plastic material that does not deform until failure occurs and leads to indefinite deformation, whereas there is a gradual deformation of soil according to its elasto-plastic behaviour. The rigid body assumption also affects the correct simulation of seismic waves propagation. In a highly non-linear medium such as soil, seismic response characteristics of a site can change the characteristics of loading (amplitude, frequency, etc.) transmitted from the source of loading to the area of interest. Such aspects, and many more, are not accounted for in limit equilibrium or limit analysis methods.

Several comprehensive and comparative studies have been performed to show the capabilities and limitations of conventional methods (including limit equilibrium and limit analysis), for example: Chang et al. (1984), Anderson and Richards (1987), Yu et al. (1998). Despite the limitations of these methods (see Table 2-1), since the results of these methods have been calibrated against field observations, and because of their simplicity and ease of use, they can be applied in the first stages of study in order to have a general approximate estimate of the stability. Yu et al. (1998), for example, conclude that different methods of limit equilibrium and limit analysis of drained or undrained slope stability give results within 5 – 10% tolerance, which means that the results are not very different.

In the limit equilibrium method an arbitrary failure surface (linear, multi-linear or curved) is assumed and global equilibrium conditions between the failing block and boundary forces are considered, assuming that the failure criterion holds everywhere along the failure surface. Global equilibrium means that the internal distribution of forces (or stresses) is not taken into account; however, in many instances the stress equilibrium along the failure surface is considered. Majority of classical methods of slope stability analysis fall into this category, for example: Bishop (1955), Morgenstern and Price (1965), Chen and Morgenstern (1983), Leshchinsky (1990), etc. (see Fredlund and Krahn, 1977).

In the limit analysis approach, upper and lower bounds of collapse loads are approximated using the upper- and lower- bound theorems of the ideal plasticity theory. If the upper and lower values are equal, the solution is exact (of course, in the limit analysis sense). In stability analyses, the lower bound of collapse load is more important, obviously because it can provide a safe limit. Both theorems provide infinite number of solutions because either equilibrium or compatibility is not satisfied in upper- and lower-bound theorems, respectively (e.g. Chen, 1975; Atkinson, 1981); however, only the minimum of the upper-bound and the maximum of the lower-bound solutions are taken into account.

None of the above methods provides any information on magnitude of displacements, and thus, serviceability of slopes after earthquakes. Factor-of-safety approach only gives a limited image of slope performance at a certain moment during or after earthquake loading. Numerical seismic analysis methods, on the other hand, are aimed at estimating displacements, stresses/strains, and pore water pressures from the beginning of

earthquake loading to any time after. In general, as pointed out by Finn (2000), displacement criteria are much more cost-effective than those based on the factor of safety approach.

Major methods of numerical analysis in geotechnical engineering are Finite Element, Finite Difference, Boundary Element, and Discrete Element Methods. Finite Element Method (FEM) is the most popular method in the stability and especially deformation analysis of earth structures and natural slopes. The main advantage of FEM as compared to the conventional methods of slope analysis (i.e. limit equilibrium and limit analysis) is that no postulated failure mechanism or *a priori* assumption of soil behaviour mode is required (Griffiths and Lane, 1999) as these are predicted by the analysis.

2.3.2 *State-of-Practice in Seismic Analysis of Earth Slopes*

The state-of-practice in seismic analysis of earth slopes addresses the necessity of estimating both earthquake-induced displacements and excess pore water pressures, using simplified procedures that can be employed in engineering practice. The following sections give an overview of the frequently used methods that are essentially introduced to overcome some of the limitations of the classical methods (e.g. limit equilibrium) discussed earlier.

2.3.2.1 Newmark Method of Displacement Analysis

Newmark (1965) introduced the importance of displacement analysis of slopes due to earthquakes and proposed a simple procedure to calculate permanent displacement caused by earthquake shaking. It is possible that the pseudo-static factor of safety becomes less than one several times during an earthquake although it does not lead to slope collapse, i.e. infinite deformations. Newmark's analytical procedure comprises two

main steps: first, obtaining a yield (or critical) acceleration, which is a threshold value of acceleration that causes pseudo-static instability of slope, and second, double integrating that portion of the acceleration time history that exceeds the yield acceleration to estimate slope displacements.

Chang et al. (1984) and Urgeles et al. (2001), among many others, have applied the method to show that for some slope angles and earthquake magnitudes/accelerations, a pseudo-static factor of safety lower than one is equivalent to a Newmark displacement of a few centimeters that is acceptable in most engineering projects.

However, there are some limitations in the application of Newmark method in seismic analysis of submarine slopes, especially because of vulnerability of submarine deposits to liquefaction. A comparison between results of Newmark displacement analysis integrated with the simplified procedure of estimation of excess pore water pressure build-up (Seed et al., 1975) and those obtained in an effective stress, finite element analysis was carried out by Azizian and Popescu (2001), and showed the importance of modelling the dissipation phase. A modification of the model accounting for the both effects, i.e. pore water pressure build-up and dissipation, is proposed by Zangeneh and Popescu (2003). Verification of the results with some centrifuge test results (VELACS, Arulandan and Scott, 1993 & 1994) showed that the procedure is promising.

2.3.2.2 Simplified Procedure of Liquefaction Potential Assessment

The simplified procedure of liquefaction analysis is due to Professor Harry Seed and his co-workers at the University of California, Berkeley. From the early works, e.g. Seed and Idriss (1971), to the latest reviews and conclusions by Youd et al. (2001), many advances have been made in the original framework of comparing earthquake-induced

cyclic stress ratio (CSR) and cyclic resistance ratio (CRR) of the soil. According to the latest recommendations of the NCEER 1996 Workshop (Youd et al., 2001), the factor of safety against triggering liquefaction can be computed as:

$$F_s = \left(\frac{CRR_{7.5}}{CSR}\right).MSF.K_\sigma.K_\alpha \qquad (2\text{-}1)$$

$CRR_{7.5}$ is the cyclic resistance ratio for magnitude 7.5 earthquakes and may be obtained from correlations based on in-situ tests such as SPT, CPT or shear wave velocity. The SPT- and the CPT-based liquefaction assessment charts are the preferred means of evaluating liquefaction potential as they are the most reliable ones because they are supported by the largest database (Finn, 2002). CPT correlations proposed by Robertson and Wride (1998) are recommended by the NCEER 1996 Workshop. Other CPT correlations include Shibata and Teparaksa (1988), and Stark and Olson (1995), among others.

CSR is the cyclic stress ratio induced by earthquake, which is calculated as (after Seed and Idriss, 1971):

$$CSR = \frac{\tau_{\max}}{\sigma'_{vo}} = 0.65\frac{a_{\max}}{g}\frac{\sigma_{v0}}{\sigma'_{v0}}r_d \qquad (2\text{-}2)$$

where, σ_{v0} and σ'_{v0} are the total and effective vertical overburden stresses at the depth in question, $a_{\max}$ is the peak horizontal ground surface acceleration, g is the acceleration due to gravity, and r_d is the stress reduction factor that provides an approximate correction for flexibility of the soil profile.

In liquefaction assessment of submarine slopes, for calculating the ratio of total to effective stresses, since hydrodynamic effects of water are neglected and no shear stress

is applied to the soil by water, the ratio of total to effective stress is equal to the ratio between saturated and buoyant unit weights.

Since CRR and CSR are computed for magnitude 7.5 earthquakes, a correction factor, MSF, is taken into account. Different values of this factor have been proposed by various researchers. Values recommended by the NCEER 1996 Workshop are reported by Youd et al. (2001).

Correction factors K_σ and K_α account for the effects of overburden pressure and static shear stress on liquefaction susceptibility. There still exists a variety of proposed values for these two factors. The latter is more controversial. The NCEER committee has recommended a relationship for K_σ, but no such recommendation is provided for the evaluation of K_α except that engineers are referred to Harder and Boulanger (1997) who have summarized previously published curves. Current state-of-practice is mainly based on values proposed by Seed and Harder (1990). Vaid et al. (2001) have recently introduced a combined factor $K_{\alpha\sigma}$ directly measured from laboratory tests to compare empirical values with laboratory results. According to this study, the degree of conservatism of empirical methods is high.

Mosher et al. (2001) have applied this method to back-analyze the 1946 earthquake-induced landslides at Goose Spit, Vancouver Island, using CPT data. The procedure could very well explain the possibility of liquefaction failure mechanism during the event, which is in accordance with the observations and recorded data.

2.3.2.3 Steady-State Line Approach to Liquefaction Potential Assessment

The steady-state-line approach (Poulos, 1981) seems to be more prevalent among geophysicists in interpreting and classifying submarine liquefaction failures (see, for example, Mulder and Cochonat, 1996).

A soil that has reached to initial liquefaction is still capable of sustaining a shear stress at constant volume. This shear stress is termed by Poulos (1981) as the steady state strength, by Terzaghi et al. (1996) as the undrained critical strength, and by Seed (1987) as residual strength. On a semi-log graph of void ratio (or water content or liquidity index) versus effective confining (or consolidation) pressure (Figure 2-9), the points representing the steady state condition of soil fall on a straight line that is known as the 'steady state line' (Poulos, 1981).

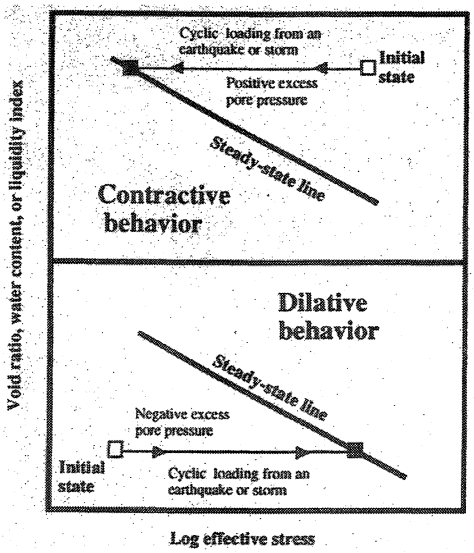

Figure 2-9. Steady state line concept with two possible conditions under which flow liquefaction can, or cannot take place. Graph obtained from Hampton et al. (1996).

According to this methodology, all combinations of void ratio and consolidation pressure located above the steady state line represent conditions that result in a post-yield contractive response. If the initial state of soil is above the steady state line, the pore

pressure will increase during undrained shearing of the soil and the effective stress will decrease (Figure 2-9). The shear strength will then drop to a much lower value and thus the soil can flow. Dense sands, on the other hand, have a tendency to dilate after yielding; hence, the effective stress and undrained shear strength increase and arrest further deformation. This approach is used for both static (flow) and cyclic liquefaction.

Collapse surface concept (Sladen et al., 1985a) and its extended model, i.e. contractant state boundary surface (CSB) (Sasitharan et al., 1993) are newer extensions of the methodology that are somewhat similar to critical state concept (Roscoe et al., 1958). These have been applied to liquefaction analysis of earth structures (e.g. lower San Fernando Dam, Gu et al., 1993), level ground (e.g. Wildlife Site, Imperial Valley, Gu et al, 1994), as well as submarine slopes (e.g. Fraser River Delta, Chillarige et al., 1997a).

State-parameter approach (Been and Jefferies, 1985) is another extension of the steady-state line approach, which has been used in liquefaction analysis (e.g. Been et al., 1987).

2.3.3 Finite Element Analysis of Slopes

2.3.3.1 Introduction

According to Duncan (1996), the finite element method was introduced to the geotechnical engineering profession by Clough and Woodward (1967), where they used a non-linear stress-strain relationship for the analysis of an embankment dam. Duncan (1996) also presents an interesting discussion and a list of many studies of deformation analysis of earth dams. Later studies are mostly concentrated on developing techniques that can implement relatively more advanced constitutive models. However, all these studies are mostly focused on dams rather than on natural slopes. Fewer deformation

analyses have been performed on natural slopes, perhaps because of the sufficiency of conventional stability analysis. Zienkiewics et al. (1975), and Griffith and Lane (1999), for example, have applied FEM to the stability analysis of slopes and have compared the results with the conventional analyses. Griffith and Lane (1999) conclude that the method is a reliable and robust method, and widespread use of it should be seriously considered by geotechnical practitioner as a more powerful alternative to traditional limit equilibrium methods.

2.3.3.2 Dynamic FEM Analysis

The dynamic response analysis of earth structures and soil sites is still largely based on the technology developed in the 1970s (Finn 2000), when the first analyses were done in terms of total stresses by equivalent linear procedures, which appear to work quite well provided the behaviour of the structure is not strongly non-linear and significant pore pressures do not develop. Such analyses represent the current state-of-practice and are neither fundamental nor likely to improve our basic understanding of the liquefaction process (Byrne et al., 2003).

A class of the state-of-the-art methods in seismic evaluation of earth structures is represented by finite element programs such as TARA-3 (Finn et al., 1986). The stress-strain relationships are expressed using nonlinear models such as the hyperbolic model proposed by Duncan and Chang (1970). The excess pore water pressure (EPWP) is updated during the analysis based on empirical relations (e.g. Martin et al., 1975). The reduction of soil shear strength is introduced by accounting for reduction in effective stress (e.g. Finn, 1990), or, using a triggering criterion to switch the strength of any liquefiable element to residual strength at the proper time (as in TARA-3FL, Finn and

Yogendrakumar, 1989). The direct (empirical) soil constitutive models used require relatively complicated regression analysis procedures for parameter calibration. Moreover, validity of these constitutive models is only guaranteed for the conditions under which experimental observations were made (see e.g. Dafalias, 1994) and therefore they may not capture the plastic dilation behaviour under arbitrary 3D stress states. As for the post-liquefaction analysis, the focus is on assigning a value of the residual strength. It does not directly provide the actual dynamic response of the structure, including continuous yielding of the material induced by EPWP build-up, and gradual strengthening after the shaking, following the pore water pressure dissipation. Also, according to Finn (1991), the computed deformations are highly dependent on the specified residual strength.

Another class of the state-of-the-art methods in seismic evaluation of earth structures is represented by finite element programs such as Dynaflow (Prevost, 1981 – 2002), which is used in the present study and will be described in detail in Chapter 3. The methodology is one of the first ones successfully applied to the analysis of liquefiable soils by implementing a relatively simple plasticity theory (Prevost, 1985) and performing effective stress analysis based on fluid-solid coupled field equations (Biot, 1962). This numerical model provided reasonable predictions of the centrifuge test results performed in the VELACS project in early 1990's (Arulanandan and Scott, 1993, 1994, see also Section 3.4.2). At that time, a very limited number of numerical models were successful in accomplishing this task (Byrne et al., 2003). Popescu and Prevost (1995) present a comparison between all VELACS numerical class-A predictions and the centrifuge experimental results.

In the recent years, a similar approach has been followed for providing better predictions of the behaviour of liquefiable soils subject to earthquake loading. Centrifuge facilities equipped with earthquake simulators (shakers) are now being used more frequently than before (see e.g. Phillips, 2001; Taboada-Urtuzuastegui et al., 2002) to provide geotechnical practice and numerical modellers with more experimental evidence on liquefaction-induced (and post-liquefaction) deformations. Several numerical models have been validated using centrifuge experiments, and have shown a good promise for providing reliable predictions of soil dynamic (cyclic) behaviour under relatively complex situations. (e.g. Byrne et al., 2003; Elgamal et al., 2002)

This approach may also have some disadvantages, as stated by Finn (2000). First, such procedures make heavy demands on computing time and resources. Second, the quality of response predictions is strongly path dependent, that is, as the loading path deviates from the calibration path, the prediction becomes less reliable.

The following are two examples of such recent studies on evaluating the liquefaction potential of sands:

Byrne et al. (2003) present numerical analysis of some centrifuge tests, using the finite difference program FLAC (Fast Lagrangian Analysis of Continua, see Itasca), with an emphasis on the effects of partial saturation of sand and densification of lower layers caused by confining stresses induced in the centrifuge during spin-up. The constitutive model used is the UBCSAND model (described later in Section 2.3.3.3) and the material used in the tests is Nevada sand. It is concluded that the initial degree of saturation can have a very large effect on pore pressure rise and liquefaction response. A slight reduction in the degree of saturation can result in significantly lower pore pressure

predictions. Also, the fact that some current numerical analysis procedures predict liquefaction to occur first at the base, in contrast to centrifuge tests that show liquefaction of layers close to the surface, is attributed to the stress densification phenomenon occurring during centrifuge spin-up. The increase in the relative density of sand (which is significant at higher depths and insignificant near the surface) combined with the presence of high confining pressures is believed to highly increase the liquefaction resistance of the sand. The predictions of the model are in good agreement with the measurements as they can particularly explain the effects of the degree of saturation and densification.

Elgamal et al. (2002) have presented a back-analysis of the VELACS models #1 and #2, which represent an infinite, uniform layer of saturated sand (Nevada sand, Dr = 40%), one horizontal and one inclined at an angle of 2^{o} with horizontal, respectively. The latter angle is modified to a 4^{o} angle in the numerical analysis due to the effect of unbalanced hydrostatic water pressure in the centrifuge box (after Dobry and Taboada, 1994). The constitutive model developed for the study is basically the multi-yield surface plasticity model originally proposed by Prevost (1985), with some changes related to dilation and compaction of sand by introducing some coefficients characterizing its behaviour. The model is implemented in a solid-fluid coupled-field finite element program, to simulate the cyclic mobility effects associated with liquefaction-induced shear deformations, and also, to illustrate the effects of frequency content of earthquake motion on deformations. It is concluded that for the mildly sloping soil, as opposed to the flat one, the effect of cyclic mobility is significant in inducing large shear strain accumulations, although it may prevent unbounded flow failure because dilation of the sand causes the soil to regain

its shear strength. Also, the motion with lower frequency content is found to induce larger displacements as well as acceleration amplifications at the ground surface because the lower frequency allows accumulation of more shear strains in each cycle of loading. The predictions of the model, including those of excess pore pressures, displacements, and accelerations, are in excellent agreement with the measurements. Although the predictions were performed long after the centrifuge tests, they show the strong ability of elasto-plastic models in reproducing the seismic liquefaction phenomenon.

2.3.3.3 Constitutive Models

Soil behaviour is non-linear (e.g. Chen and Baladi, 1985). Simple linear elastic theories of material behaviour do not fit the real behaviour of soils. Soil behaviour is also so complex that no single constitutive model can predict or describe all aspects of the behaviour of all types of soils. Advancement of constitutive models is one of the challenging fields of geotechnical engineering and various models have been introduced in the literature. The following is a brief review of some models that have been verified and are currently being used in numerical analysis software. Comprehensive discussions and extensive historical reviews may be found in Scott (1985), Chen and Baladi (1985), Zienkiewics and Taylor (1989), Dafalias (1994), Ishihara (1996), Potts and Zdravkovicz (1999), etc.

Non-linear Elastic Models: Linear isotropic elastic models that need only two parameters to describe soil behaviour were first improved by accounting for the dependence of material parameters on stress and/or strain levels. The hyperbolic model introduced by Duncan and Chang (1970) was originally proposed to fit undrained triaxial test results. Further refinements of the method increased the number of model parameters.

The model has been extensively used; however, it cannot capture the changes in soil stiffness due to changes in strain. Thus, a class of models, known as small strain stiffness models, was proposed (e.g. Jardine et al., 1986; Puzrin and Burland, 1998) to overcome this deficiency, in the domain of loadings that cause small strains and material still remains elastic. With these models, no failure mechanism can be reproduced and more importantly they cannot reproduce volume changes due to shearing (Potts and Zdravkovicz, 1999).

Elastic-Plastic Models: Elastic-plastic models are based on three fundamental ingredients (e.g. Chen and Han, 1988):

a) Yield Surface: A surface is defined in the stress space as a criterion for yielding of the material. The common yield surfaces are: Tresca (hexagonal prism), Von-Mises (cylinder), Mohr-Columb (hexagonal pyramid) and Drucker-Prager (cone). The Mohr-Columb and Drucker-Prager shapes account for the dependency of shear strength on mean effective normal stress. Von-Mises and Drucker-Prager yield surfaces can be considered only as some approximations of Tresca and Mohr-Columb surfaces to overcome difficulties encountered in numerical procedures due to the corners of the hexagonal yield surfaces.

b) Flow Rule: Direction of the plastic strain in space is obtained by means of a plastic potential function. A flow rule specifies the direction and magnitude of plastic flow as a function of hardening/softening characteristics of the material. It is assumed that the principal directions of accumulated stress and incremental plastic strains coincide. Two main classes of plasticity models originate at this point: with associated flow rule, when the plastic potential function is assumed the same as the yield function; and, with non-

associated flow rule, when the plastic potential function and the yield function are described by two different expressions. According to the associated flow rule, the direction of the plastic strain vector is normal to the yield surface (known as normality condition). It has been shown that associative flow rules highly overestimate the volume changes of soils during shearing (e.g. Chen and Baladi, 1985).

c) Hardening/Softening Rule: Size, shape, and location of the yield surface are not constant and depend on some factors such as stress history. Major types of hardening rules are: isotropic (when the yield surface changes in size), kinematic (when the yield surface translates in the stress space), local (when shape of the yield surface changes locally), or combinations of those.

Prevalent Elastic-Plastic Models: A detailed discussion of prevalent constitutive models, i.e. those that have been used more frequently than the others in numerical geotechnical analysis, is beyond the scope of this research. Moreover, since the main goal of this research is to use the state-of-the-art finite element software, Dynaflow, that implements multi-yield plasticity model (Prevost, 1985) for seismic analysis of submarine slopes, it is not intended to include a comparative study of different models with different yield surfaces, flow rules or hardening/softening relationships. However, a general knowledge of some widely used models is believed to be helpful in better understanding the applied model. Hereafter is a list of such models:

- Cam Clay models are based on the concepts of the critical state. Roscoe and his coworkers at the University of Cambridge (e.g. Roscoe and Schofield, 1963) developed a model that was modified later by Roscoe and Burland (1968) and is known as Cam Clay model. It was the first (and simplest)

modern elasto-plastc constitutive soil model (Prevost, 1998). Other models such as Mutsouka and Nakai (1974) and Lade and Duncan (1975) are some extensions in the framework of the Cam Clay Model, where the main difference is in the shape of the yield surface in deviatoric plane. Another extension of the Cam Clay model, known as Cap Model, was first proposed by Di Maggio and Sandler (1971). A series of models were developed later to capture rate effects and anistropic behaviour within the yield surface and viscoplastic behaviour during yielding. Chen and Baladi (1975) have also presented some numerical procedures for applying the method. According to Prevost (1985), there are two obvious limitations of these models: 1) they do not adequately model soil stress-induced anisotropy, and 2) they are not applicable to cyclic loading conditions. These limitations are generally valid for models without kinematic hardening rule.

- Multi-yield surface model (Prevost, 1985) is based on the concept of nested yield surfaces (Iwan, 1967; Mroz, 1967) with a kinematic hardening rule, and non-associative flow rule in its volumetric strain (dilatational) component. Detailed descriptions are provided in the next Chapter (see Section 3.4). As noted before, an extension of this model is introduced by Elgamal et al. (2002) and is implemented in a finite element program (performing coupled-field analysis based on Biot's theory) for numerical modeling of cyclic mobility. In this model, some modifications are made regarding dilative/contractive behaviour of sand (Figure 2-10), which requires calibration of some more parameters. It is assumed that there are two contractive phases: one during

shear loading inside phase-transformation (PT) surface (phase 0 – 1 in Figure 2-10) and the other during shear unloading starting outside PT surface until p'_D (phase 3 – 4 in Figure 2-10). Also, there is a dilative phase during shear loading outside PT surface, (phase 2 – 3 in Figure 2-10). Another parameter is also required that describes liquefaction-induced perfectly plastic deformation of sand during shear loading (phase 1 – 2 in Figure 2-10).

- UBCSAND: Beaty and Byrne (1998) present the key features of the model, with examples of prediction of field behaviour, as well as monotonic and cyclic behaviour of sand in simple shear test, which are all in good agreement with the measurements and records. The model is implemented in the finite difference program FLAC (see Itasca). This elasto-plastic model is intended primarily for simulating liquefaction response of sand. The yield surface is described by a line of constant stress ratio: $\tau / \sigma' = \tan(\phi_d)$, where τ = shear stress, σ' = effective normal stress, and ϕ_d = developed (mobilized) friction angle (Figure 2-11a). A hyperbolic relationship is assumed between stress ratio and plastic shear strain (Figure 2-11b). The rate of movement of yield surface is a function of the hyperbolic hardening relation. Plastic shear strain increment is defined to occur in the direction of the principal shear stress. A kinematic hardening rule and a non-associative flow rule are defined assuming that there is a unique stress ratio corresponding to constant-volume shearing of sand (corresponding to ϕ_{cv}, Figure 2-11a), below which the soil exhibits contractive behaviour and above which it dilates. The vectors shown in Figure 2-11a also illustrate that any positive increment in plastic shear strain ($d\gamma^p$)

results in: 1) positive plastic volumetric strain ($d\varepsilon_v^p$), or contraction, below the phase transformation (PT) line (corresponding to ϕ_{cv}); 2) no $d\varepsilon_v^p$ on the PT line; and 3) negative $d\varepsilon_v^p$, or dilation, above the PT line. Additionally, the effect of pore fluid is accounted for by volumetric stiffness of the pore fluid, that is, to simulate undrained laboratory tests, for example, infinite stiffness is assumed for the pore fluid.

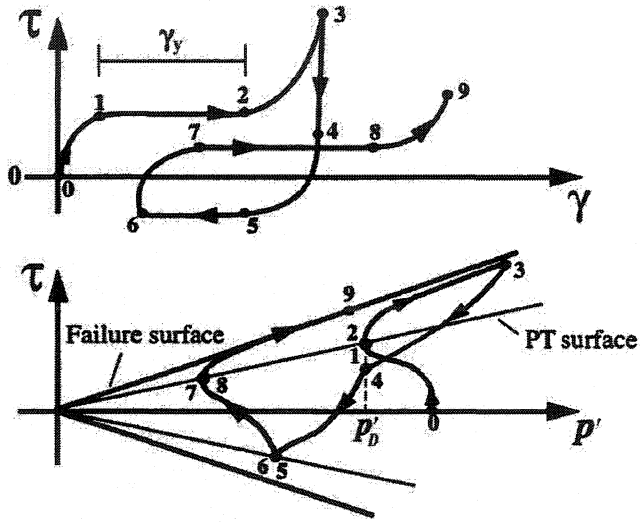

Figure 2-10. Constitutive model showing different phases of contraction, dilation and liquefaction-induced perfectly plastic deformations (Elgamal et al., 2002).

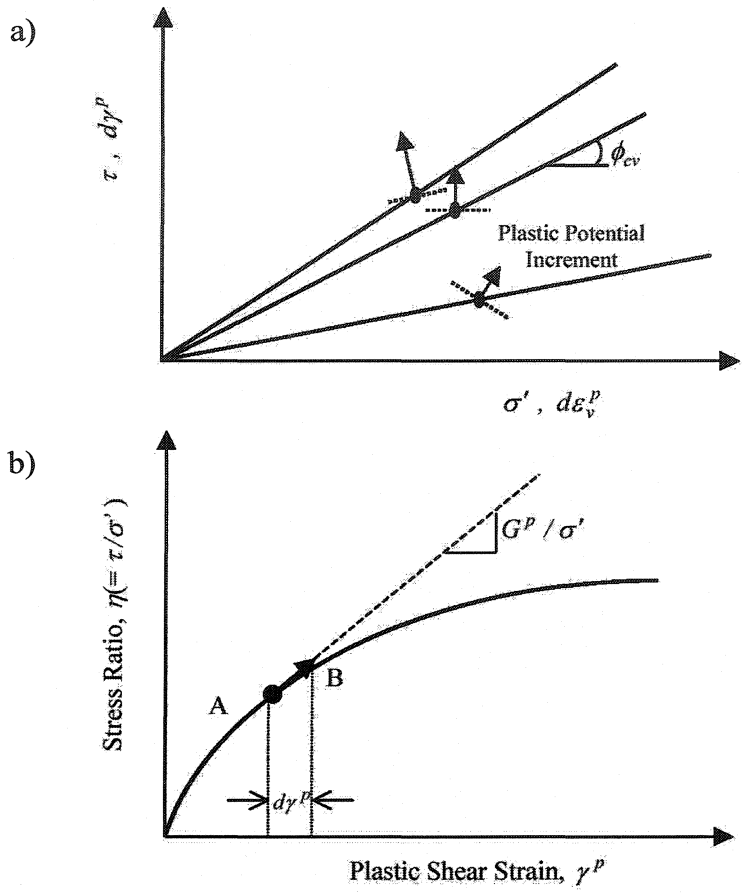

Figure 2-11. UBCSAND model (after Byrne et al., 1993): a) yield loci and direction of plastic strains; and b) hyperbolic relationship between stress ratio and plastic shear strain.

- Bounding surface model has been introduced by Dafalias and Popov (1975) originally for metals, and developed later for soils. Dafalias and Herrmann (1982), for example, have discussed the basics of bounding surface model. The model is a more fundamental framework that is applicable to monotonic or cyclic, drained or undrained or any other form of loading conditions in order to be of value for the analysis of soils under complex loading. According to Dafalias (1994), the outstanding feature of the model is that for stress points inside the bounding surface, plastic yielding occurs at a magnitude depending

on the distance of the actual stress from an image stress on the surface. As such, plastic volumetric and deviator strains can be simulated during cyclic loading when the stress path is within the surface, which is very important for the simulation of pore water pressure build-up under undrained cyclic loading. In the classical plasticity theory, since it is assumed that the behaviour is purely elastic inside the yield surface, no change in plastic modulus is allowed as long as the stress state is inside the yield surface. The bounding surface is somewhat similar to the outermost yield surface in multi-yield surface models (e.g. Prevost ,1985).

- Some other constitutive models, such as endochronic model, which have some fundamental differences with the above-mentioned models, have also been introduced in the literature. A discussion on endochronic models may be found in Valanis and Read (1982). According to Finn (1982), this concept is useful in describing the earthquake-induced volume changes and pore pressures.

2.3.4 Three- vs. Two-Dimensional Analysis of Earth Slopes

Jeremic (2000), Stark and Eid (1998), Byrne et al. (1992), Justo and Saura (1983), among many others, have studied the importance of considering 3D effects in the analysis of slopes.

Duncan (1996) cites over 20 studies (since 1960s) concluding that in the factor-of-safety approach, two-dimensional analysis yields conservative results compared to three-dimensional analysis, i.e. $F_{2D} < F_{3D}$ provided that F_{2D} is calculated for the most critical 2D section. There are a few exceptions, e.g. Chen and Chameau (1983), which have obtained reverse results in some cases. Cavounidis (1987) states that these studies either

compare inappropriate factors or more probably contain simplifying assumptions, such as neglecting normal stresses on vertical surfaces or not satisfying conditions of equilibrium.

Since $F_{2D} < F_{3D}$, Leshchinsky and Huang (1992) emphasize that in order to obtain post-failure in-situ shear strength of soils by back-analysis of slope failures, 3D analysis should be avoided so that shear strength (to be used in 2D analysis) is not overestimated (see also Duncan and Stark, 1992).

Effect of failure mechanism is also significant. Stark and Eid (1998), for instance, have shown that in a translational mode of failure that usually occurs in flat slopes, the mobilized shear strength along back scarp and sides of the slide mass are significantly different from those along the base. Arellano and Stark (2000) present several curves (Figure 2-12) showing the ratio of 3D to 2D factor of safety for different width/height ratios and slope angles, with translational failure mechanism. These curves show, for example, that the 3D to 2D factors of safety ratio for a 3H:1V slope is greater than 1.05 if the width/height ratio is less than 4.

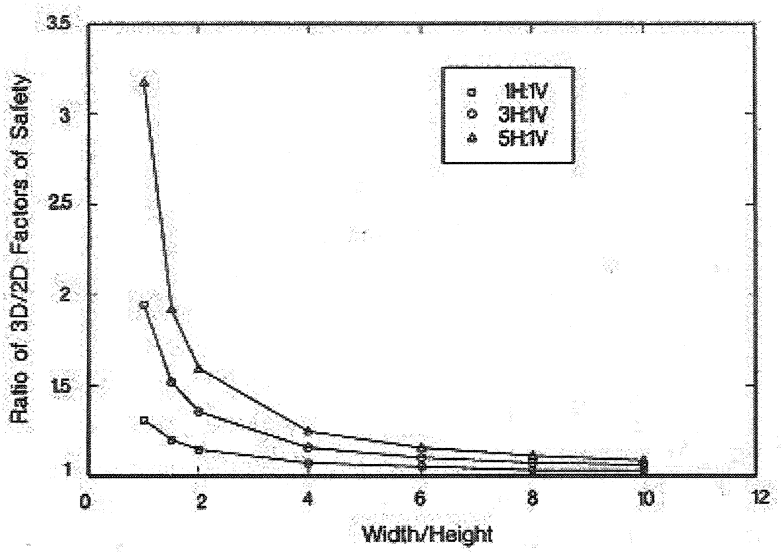

Figure 2-12. Ratio of 3D/2D factors of safety (Arellano and Stark, 2000).

In deformation analysis approach to the analysis of slopes, Lefebvre et al. (1973) found that 2D analysis can significantly overestimate movements of a dam in a V-shaped steep-wall valley because the effects of cross-valley arching are ignored in 2D analysis. They performed 3D finite element analyses for dams in V-shaped valleys with three different valley wall (or abutments) slopes, using linear elastic material properties and simulating construction of dams. The dam fill slope was 2.5:1. Both 2D plane stress and plane strain analyses were carried out on the maximum longitudinal and transverse sections, respectively. Analyses of the transverse sections showed that if the valley walls slopes were 1:1 or steeper, plane strain results would be significantly inaccurate, as a result of cross-valley arching. 2D/3D ratios of principal stresses, maximum shear stress, and displacements are presented. For example, average 2D/3D ratio of horizontal displacement for 1:1 wall is 2.68, whereas that for 6:1 wall is 1.05.

Duncan (1996), after comparing 2D and 3D analysis results of finite element analysis of New Melones dam, states that the 2D results could have been adjusted to provide reasonable estimates of the 3D behaviour. For this dam, the steep valley walls have

average slopes of about 1.2H:1V, with a height of 190.5m and crest length of about 500m, i.e. B/H = 2.5. No quantitative information is given as to how such adjustment could be done.

Martin (1978) presents a 3D deformation analysis of a dam during reservoir filling. The dam is 80m high. Its longitudinal profile is somewhat L-shaped, i.e. two lines at an angle of about 135°. The lengths of the two parts are approximately 700 and 350 m. Unfortunately, no comparison with 2D analysis is made in the study; however, according to the presented plan view of horizontal displacements of the dam crest (Figure 2-13), the crest displacement has less variation within a section that is about 180 m away from the right abutment.

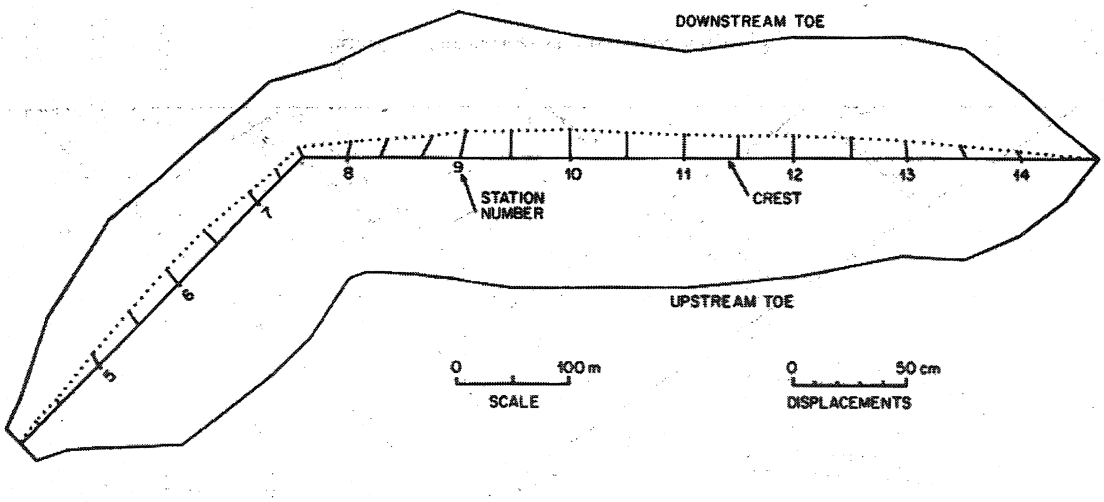

Figure 2-13. Plan view of horizontal displacements of Storvass dam crest (Martin, 1978).

Similarly, in the observed (measured) crest displacements of another dam during water rise (Justo and Saura, 1983), with 180 m height, it can be seen that points farther than 70 – 80 m from the abutments have almost the same displacements.

Jeremic (2000) presents a 3D finite element approach for static large-deformation analysis of slopes, for capturing continuous localization of deformations. The soil

behaviour is modeled by a hyperelastic-plastic nonlinear model with hierarchical set of rounded Mohr-Coulomb yield surfaces, plastic potential surfaces, and hardening-softening laws. The factor of safety can be significantly reduced if the slope is curved out of plane in a convex fashion (Figure 2-14), from 2.0 for 2D to 1.65 and 1.38 for 45° and 90° out of plane curvatures, respectively. Although this may seem in contrary to other 3D studies, one should note that other studies have not taken into account such a significant out of plane curvature as considered by Jeremic (2000).

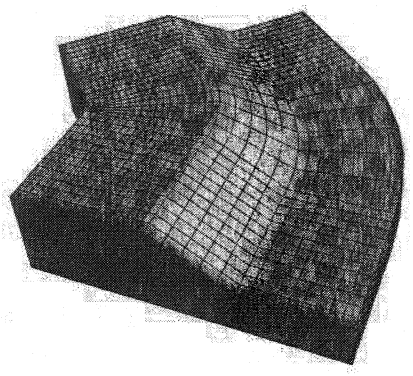

Figure 2-14. Out-of-plane curvature of slope (Jeremic, 2000).

Prevost et al. (1985) performed 2D and 3D total stress, dynamic FE analysis of Santa Felicia earth dam using nonlinear multi-surface plasticity model and compared the measured and computed earthquake responses. Their analysis showed that the first 10 frequencies of the 3D model all fall within the first 2 frequencies of the 2D model, indicating that more intermediate modal configurations are generated, despite the fact that the dam is a relatively long dam and 3D effects should not be significant. The study demonstrates the importance of 3D effects more pronounced for strong shaking, in terms of crest acceleration and permanent deformations. In case of strong shaking, the 3D horizontal crest acceleration response is significantly lower than the 2D one due to significant contributions from higher modes of vibration. The authors finally conclude

that compared to recorded measurements, 3D analysis slightly overestimates the response, which indicates that other mechanisms may be present in a real dam than purely hysteretic energy dissipation.

Among other 3D studies, based on 3D and 2D modelling of train-track embankment on half-space subjected to dynamic loads, performed by coupled Boundary Element-Finite Element methods, Adam et al. (2002) conclude that a problem can be treated as a 2D case if the length to width ratio (L/B) is about three or more. For ratios less than 1.5, the 3D approach is essential.

Lai et al. (2002) present results of highly instrumented centrifuge experiments to study the linear and non-linear, 3D behaviour of dry, stiff soils during earthquake-like excitations. Two types of centrifuge containers are used: Flexible Shear Beam to simulate level ground conditions, and rigid to simulate ground response in a rigid basin. 3D finite element models are also analyzed (by the eigenvalue method of analysis) to explore the nature and extent of 3D effects. For the particular dry stiff soil used (Nevada sand at approximately 100% relative density), it is found that for the flexible boundary, the first lateral resonance is well isolated from subsequent higher resonances and that the fundamental mode shape of the soil deposit is similar to the first mode shape of a 1D shear beam, that is, the behaviour is predominantly 1D shear behaviour. On the other hand, the 3D effects are significant in the case of rigid box as no such isolation of the first mode from higher modes is observed.

The two-dimensional idealization is normally based on the following considerations:

Site Material Idealization: If non-homogeneity or anisotropy of the slope material, either small-scale or large-scale, in all three directions, is not negligible, then performing

2D analysis is not appropriate (see, e.g., Potts and Zdravkovic, 1999). In most cases, it is assumed that soil layering is perpendicular to the plane of interest and a cross section represents all sections.

Site Geometry Idealization: In numerical or analytical approaches toward many geotechnical problems, three main geometric idealizations (among others) are usually used that simplify and accelerate the analysis significantly (see, e.g., Zienkiewics and Taylor, 1989): plane strain, plane stress, and axi-symmetry. Almost all two-dimensional slope stability analyses use plane strain assumption, in which the value of the strain component perpendicular to the plane of interest is zero. This reduces the number of unknowns and simplifies the derivation of the constitutive relationships. Analysis time as well as necessary computational resources will decrease significantly, especially in a seismic step-by-step time-domain analysis (e.g., Prevost et al., 1985). However, all above assumptions are valid if there is one dimension very large in comparison with the other two. This implies either of these conditions:

- No curvature or corners exist in geometry of slope
- The slope deformation is not constrained significantly by a near lateral boundary, such as a dam in a narrow rock-walled valley.
- No curvature exists in the shape of (postulated) failure surface in the direction perpendicular to the plane of interest. That is, failure surface is the same in any cross section.

Loading Idealization: Design recommendations usually suggest that from three components of earthquake acceleration, only the larger horizontal acceleration would suffice for analysis purposes (see, e.g., Youd et al., 2001). Vertical and smaller horizontal

components of acceleration are then ignored. In the analysis of slopes, the horizontal acceleration is usually applied to the slope in its plane, that is, no instability due to perpendicular excitation is taken into account.

2.3.5 Boundary Conditions

2.3.5.1 Introduction

Boundary conditions have an important role in the analysis of slopes that are considered as initial boundary value problems (elliptic, parabolic, or hyperbolic, depending on the type of analysis) in the finite element analysis. Experimental evidence also confirms that the imposed boundary conditions can significantly change the behaviour of a soil deposit (e.g. Lai et al., 2002, see Section 2.3.4)

For finite element analysis of slopes, as opposed to the limit equilibrium approach, placing the boundaries beyond the extent of failure surface is not sufficient because boundary conditions should be specified at a distance where slope failure does not affect the stress-strain state. Specifying the boundary conditions for static analysis, either 2D or 3D, is an easier task since reasonable results can be obtained by only assuming rigid boundaries (base/walls) located far from the slope and potential failure surface (see e.g. Griffith and Lane, 1999; Chugh, 2003). For seismic analysis, however, because the earthquake loading is being applied at the boundaries of the analysis domain, the situation is more complex. Wave interference caused by multiple reflections of seismic waves from boundaries can change the nature of a problem, especially in the regions close to the boundaries. Interference of an incident motion with the reflected motion in some cases can cause a loading with greater magnitude; and thus, greater deformation than expected.

This necessitates the use of transmitting (non-reflecting) boundaries so that the real situation is simulated as accurately as possible.

An alternate approach to applying the input motion (e.g. acceleration) at the boundaries is to use free-field elements to input the free-field excitation, and thus to eliminate the need to transmit the seismic excitation through artificial boundaries (e.g. Bielak and Christiano, 1984; Cremonini et al., 1988). However, as pointed out by Bielak and Christiano (1984), in this case as well, satisfactory results can be obtained only if (1) the boundary is placed far from the region of interest, (2) a substantial amount of energy is dissipated in the interior region, and (3) one of the various types of absorbing (transmitting) boundaries are employed.

In the 3D analysis of this study, a comparison is made between the effects of rigid and transmitting boundary conditions (see Section 5.4.2). What follows is a review of common transmitting boundary condition definitions.

2.3.5.2 Types of Transmitting Boundaries

Transmitting, or as termed by others, non-reflecting (e.g., Steedman et al., 1989), absorbing (e.g., Engquiest and Madja, 1977), silent boundaries (e.g., Cohen and Jennings, 1983), or infinite elements (e.g., Wolf and Song, 1996), all developed for *elastic* media, have been subject of many studies in the past 30 years. The purpose of implementing these boundaries is to prevent wave reflections (or echoes) at the edges of the mathematical model, which, by necessity must remain finite in size.

The idea of a transmitting boundary is to introduce a differential equation, governing the boundary region, which transmits (or does not reflect) the incoming waves. For example, consider the one-dimensional form of the wave equation:

$$\frac{\partial^2 u}{\partial t^2} - c^2 \frac{\partial^2 u}{\partial x^2} = 0 \qquad (2\text{-}3)$$

where u = displacement, t = time, c = wave speed, and x = coordinate. This equation has the solution:

$$P(x - ct) + N(x + ct) = 0 \qquad (2\text{-}4)$$

where functions P and N represent arbitrarily-shaped waves moving in the positive and negative x-directions, respectively, with the speed c. If a differential equation is found that has only the P function as its solution, then it can be used as a boundary condition that transmits waves in the positive x-direction while it does not reflect waves in the negative x-direction. One such equation is:

$$\frac{\partial u}{\partial t} + c \frac{\partial u}{\partial x} = 0 \qquad (2\text{-}5)$$

which is proposed by Clayton and Engquist (1977). Another form considered by Cohen and Jennings (1983) is:

$$\frac{\partial^2 u}{\partial t^2} - c^2 \frac{\partial^2 u}{\partial t \partial x} = 0 \qquad (2\text{-}6)$$

which has the advantage of being dimensionally consistent with the wave equation.

Kausel (1988) gives an excellent review of local transmitting boundary approaches, showing how they are mathematically related to each other. The equations characterizing these boundaries are given in Table 2-2, some of which are explained hereafter. It should be noted that there are some other types of transmitting boundaries such as "consistent" boundaries (e.g. Lysmer and Waas, 1972) formulated by exact solutions. These boundaries that simulate an infinite succession of finite elements (such as used for the analysis of foundations on layered soils) are non-local in space and time. That is, they couple boundary points and are proper only for frequency-domain solutions. Therefore,

they are not suitable for nonlinear analysis using time-integration techniques. Other types addressed hereafter are local in space and time, and thus suitable for time-domain, non-linear analysis.

According to Kausel (1988), the first transmitting boundary was proposed by Lysmer and Kuhlemeyer (1969), which is known as viscous boundary since viscous dashpots are implemented. The idea is to apply boundary stresses to an otherwise free boundary, to cancel the stresses that are produced at the boundary by incoming waves. To cancel both dilatational- and shear-waves that are reaching the boundaries, normal and shear stresses (σ and τ) are applied to the boundaries, respectively, so that (see e.g. Cohen and Jennings, 1983):

$$\sigma_{in} + \sigma_{bd} \approx 0\,,\ \tau_{in} + \tau_{bd} \approx 0 \tag{2-7}$$

where, subscripts *in* and *bd* denote the incident and applied-at-boundary stresses. As such, the following stresses can be applied at boundaries:

$$\sigma = -\rho c_d \frac{\partial u}{\partial t}\,,\ \tau = -\rho c_s \frac{\partial v}{\partial t} \tag{2-8}$$

where ρ = density, c_d = dilatational-wave speed, c_s = shear-wave speed, v = displacement in y-direction.

In addition to several other boundaries proposed in the 70's, cited by Kausel (1985), including the boundary formulated by Ang and Newmark (1972) that involves a differential condition on the stresses (Table 2-2), an important type of absorbing boundaries, called para-axial (or paraxial), was proposed by Lindman (1973). Engquist and Madja (1977), and Clayton and Engquist (1977) proposed similar boundaries for both the scalar and elastic wave equations, respectively. The para-axial boundary is important because its formulation includes the viscous type, and more importantly, it absorbs not

only the waves with normal incidence (as viscous dashpots do) but also those with inclined incidence. The simplest forms of this boundary are Eqs. (2-5) and (2-6), presented at the beginning of this Section (see also Table 2-2).

Another scheme was originally proposed by Smith (1974) based on the concept of "cancelling the reflections as they occur." This approach is elsewhere (e.g., Steedman et al., 1989; Simons and Randolph, 1986) called as the superposition approach since it superposes the Dirichlet and Neumann boundary conditions (see, for example; Zienkiewics and Taylor, 1989). Neither the superposition nor the viscous boundary treatment can support a static load component, thus loadings with non-vanishing time averages must be treated with caution (Simons and Randolph, 1986).

Another type was proposed by Liao and Wong (1984) based on determining the motion at the boundary by extrapolating the motion at points in the neighborhood of the boundary at earlier times (see Table 2-2).

After showing that these formulations (Table 2-2) are not truly different and independent, Kausel (1988) concludes that the choice of method in a particular environment should be dictated by consideration on convenience, ease of implementation, accuracy, and stability. He continues that Liao-Wong (1984) boundary appears most convenient for finite element applications, although it may lead to dynamic instabilities for high-frequency excitations.

Table 2-2. Equations characterizing transmitting boundaries (Kausel, 1988).

Boundary	Equation (first-order)
Engquist-Madja (1977)	$\frac{1}{c}\frac{\partial u}{\partial t}+\frac{\partial u}{\partial x}=0$
Lysmer-Kuhlemeyer (1969)	$C=\rho c$ (viscous dashpot)
Ang-Newmark (1972)	$\frac{\partial \tau_{xy}}{\partial x}+\frac{\partial \tau_{yz}}{\partial z}+\frac{1}{c}\frac{\partial \tau_{xy}}{\partial t}=0$
Modified Smith (1974)	Two complementary conditions; Average solution after few steps
Liao-Wong (1984)	$u_{j+1}-v_j=0$

x, y, z: spatial coordinates (x, z: in-plane, y: out-of-plane)
c: shear-wave velocity
ρ: density
t: time
u_j: out-of-plane displacement (in y-direction) at $t = t_j$
τ_{xy}: shear stress in xy-plane
v_j: out-of-plane displacement (at t_j) of a nodal line very next to boundary line

Roesset and Ettouney (1977) evaluated some of these transmitting boundaries by comparing the results they produce in the amplification of seismic motions, the determination of foundation stiffness, and the structural response. Recommendations for placement of the boundaries for different loadings (earthquake-like, single frequency) are also given.

A different approach, in which only the geometry configuration of the boundary region is changed to increase the path length of wave propagation, is proposed and studied by Steedman, Madabhushi and Chan (1989). Also, to maximize the path length *and* to improve the receptivity of the boundary zone, 'Compound Parabolic Collectors' are used, in which the geometry of the boundary is modified to a parabolic shape. The latter approach is shown to be effective for both P- and S-wave propagation with a wide range of excitation frequencies.

A simple example given by Chen (1985) illustrates the importance of implementing transmitting boundaries. This study is a one-dimensional seismic response analysis of a horizontal soil deposit idealized as a lumped-mass system, with nonlinear soil behaviour model, having a Lysmer-Kuhlemeyer (1969) dashpot as transmitting boundary. In Figure 2-15, three types of seismic response (surface acceleration) to a simple input motion for different boundary conditions are presented. Results from the rigid-base case (part d) indicate that the effect of multiple reflections can be quite pronounced if a transmitting boundary is not considered. Such multiple reflections are depicted in Figure 2-15d as the continuation of motion (with both high and low frequencies), as opposed to the other two cases with transmitting boundaries (Figure 2-15b and c), in which the motion is attenuated much faster since the waves traveling downward are not reflected back upward towards the surface of the soil. Since these plots are obtained from analyses with low-intensity loading, no significant difference can be observed in the response of the two systems having the transmitting boundaries at shallow and deep depths; however, based on other analyses of high-intensity loading Chen (1985) recommends that the transmitting boundary should be located as deep as possible.

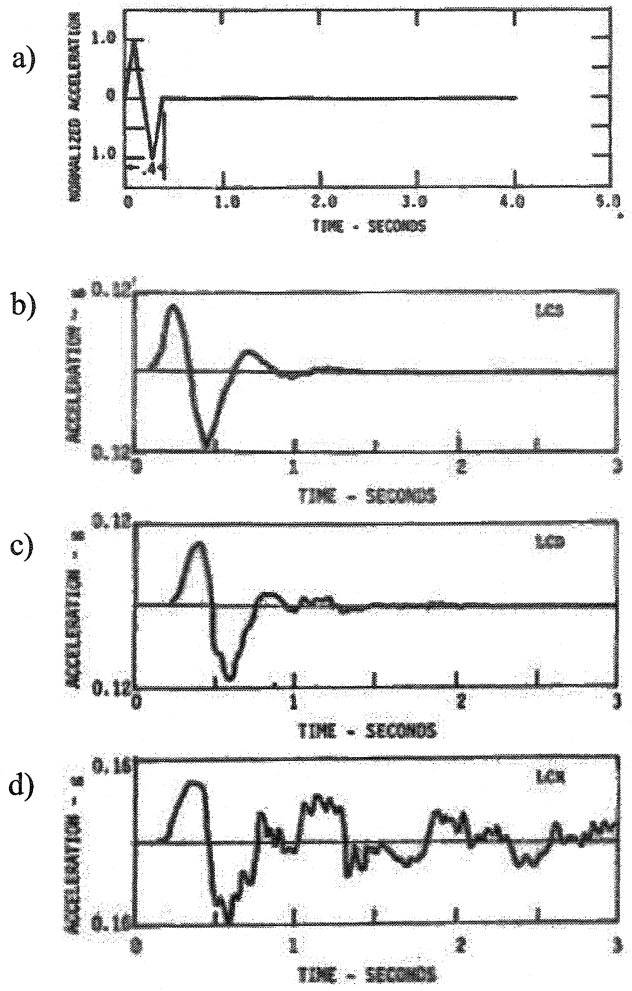

Figure 2-15. Comparison of surface acceleration time histories from low-intensity reversed-spike input motion with different boundary conditions: a) reversed-spiked input motion, b) shallow transmitting boundary; c) deep transmitting boundary; d) rigid base Chen (1985).

The transmitting boundary approach implemented in Dynaflow (Prevost, 2002), described in Section 3.3.4.1, is frequency independent, and is local in space and time, i.e. boundary points are not coupled and the boundary conditions are proper for time-domain analysis. This definition of boundary condition is similar to the Lysmer-Kuhlemeyer (1969) in the sense that a shear stress is applied at the boundary, and it generally belongs to the Engquist-Madja (1977) family of local transmitting boundaries (see Table 2-2).

2.4 Response Surface Methodology (RSM)

2.4.1 Introduction

Response surface methodology (RSM) is used in this research to minimize parametric studies involving dynamic, non-linear finite element analyses. The advantages of applying this methodology are:

- Reduction in the number of runs required for studying significance of the effects of different factors on a response of interest. Methods used are two-level factorial design, and especially fractional factorial design. This concept is used here for the calibration of soil properties, as well as in 3D analyses.
- Development of simplified relationships that can reduce the high costs of performing advanced numerical analyses. RSM used provides regression models that are useful for practical engineering purposes. Regression models are obtained in this study for quantifying the 3D effects. It is also used for parameter calibration because finding a set of parameters that yield a certain response by using an equation is much faster than by running the finite element code itself.

The following is an overview of the applications of the method and its advantages, and a brief explanation of the procedures involved.

2.4.2 Overview of RSM

Box and Wilson (1951) introduced the Response Surface Methodology (RSM) and others developed it for designing experiments and subsequent analysis of the experimental data. The method manipulates the techniques of the Design of Experiments (DOE, e.g. Montgomery, 1997), particularly Two-level Factorial Design, or in problems

where large number of input variables are involved Two-level *Fractional* Factorial Design (e.g. Cox and Baybutt, 1981).

In close relation with the RSM are regression analysis methods (e.g. Montgomery et al., 2000; Box and Draper, 1987), where RSM techniques are employed before, during, and after the regression analysis. Where applicable, a partial analysis (e.g. Sedov, 1993) may precede the RSM to reduce the number of input variables and generate necessary and sufficient dimensionless numbers.

RSM consists of a set of techniques used in the empirical study of relationships between one or more responses, and a group of variables (Cornell, 1990). RSM comprises of three techniques or methods (Myers and Montgomery, 1995):

- Statistical experimental design, in particular, two-level factorial or fractional factorial design of experiment methods
- Regression modelling techniques
- Optimization methods

Although it is usually referred to as the process of identifying and fitting an appropriate response surface model from experimental data, it can be applied to numerical modelling studies, where each run can be regarded as an experiment. An example of the efficiency of the method is given by Zangeneh et al. (2002), where the methodology is applied to the Newmark analysis of slopes.

RSM can be viewed from three major standpoints (Cornell, 1990):

- If the system response is rather well-discovered, RSM techniques are used to find the best (optimum) value of the response.

- If discovering the best value is beyond the available resources of the experiment, then RSM techniques are used to at least gain a better understanding of the overall response system.
- If obtaining the system response necessitates a very complicated analysis that requires hours of run-time and advanced computational resources for performing uncertainty analyses using methods such as Monte Carlo simulation (e.g. Firestone et al., 1997), then the original analysis may be replaced by a simplified equivalent response surface that reduces run-time significantly (e.g. Downing et al., 1985; Zangeneh et al., 2002)

According to Cox and Baybutt (1981), response surface methods of uncertainty analysis were developed to overcome the disadvantages of the Monte Carlo approach, and therefore the principal advantage of it is economy.

The method is particularly prevalent in Industrial Engineering (where quality control or product optimization is one of the main challenges), Chemistry, etc. (Myers and Montgomery, 1995). RSM has been applied to uncertainty analysis of, for example, nuclear reactor accidents (Baybutt et al., 1981).

The main limitation of the method is that RSM is a 'black box' approach. That is, estimating the accuracy of approximation, or in other words the magnitude of the approximation errors, is difficult (Cox and Baybutt, 1981).

The other limitation of the method is that it is a local analysis. The developed response surface is invalid for regions other than studied range of factors. For instance, displacement analysis of slopes under earthquake (this research) involves liquefaction phenomenon that may result in indefinite displacements. If response of interest is defined

as slope displacement at a given point, it may range from about zero to infinity. This will lead to non-applicability of the developed response surface in terms of displacement to liquefaction cases.

2.4.2.1 Basic Procedures

An excellent review of the basic procedures of the methodology and its advantages is given by Lye (2002 and 2003), where the pitfalls of the commonly used one-factor-at-a-time method of experimentation and the advantages of the two-level-factorial design are discussed, and an example of obtaining a regression model for ultimate capacity of a footing according to Terzaghi's theory, as a function of soil parameters is also explained.

The main idea is to replace a complicated response with an approximate function. A brief explanation of the basic procedures is as follows (Cornell, 1990):

Assume that the true response, ζ, of a system depends on the levels X_1, X_2, ..., X_k of k quantitative factors, ξ_1, ξ_2, ..., ξ_k, then there exists some mathematical function of X's that for any given combination of factor levels supplies the corresponding value of ζ:

$$\zeta = \Phi(X_1, X_2, ..., X_k) \tag{2-9}$$

The function Φ is called the true response function and is assumed a continuous function of X's. For two factors at two levels, a second-order polynomial approximation of the true response function is:

$$\zeta = \Phi(X_1, X_2) = \beta_0 + \beta_1 X_1 + \beta_2 X_2 + \beta_{12} X_1 X_2 + \beta_{11} X_1^2 + \beta_{22} X_2^2 + ... \tag{2-10}$$

where β_{ij} are called regression coefficients. In many instances, only the four first terms of the above equation can satisfactorily predict the response.

Response surfaces are not intended, and should not be expected, to model a system for a wide range of input variables. A polynomial approximation is a rational approach for replacing the true response with a simple first-order or second-order function in a specified range. The approximate or predicted response, $\hat{Y}$, of the system can be presented graphically, in three-dimensional or contour format, to show the behaviour visually.

A typical RSM analysis of this study involves the following steps:

Design of Experiment (DOE): Selection of the possibly effective factors, which should be controllable, is the first step of the analysis. Ranges of factors, i.e. low and high-level (or, minimum and maximum) values of factors can be selected according to the Central Composite Design (CCD), Box-Behnken and Face Center Cube (FCC) requirements. FCC is preferable for the purposes of this study since in the CCD star points may fall outside physically possible ranges.

In the context of Two-level Factorial Design of Experiments a special notation is used that can be described briefly as follows:

- Upper case letters denote both the factors and their effects. For example, A is the effect of factor A and AB is interaction effect of factors A and B.
- Lower case letters denote treatments, i.e. combinations of factor levels used in each run. For example, abd denotes a run in which high-level values of a, b, and d, and low-level values of other factors are used.

In an experiment with k factors, the Two-level Factorial analysis requires 2^k treatments (or runs). Two-level Fractional Factorial Design can be used to reduce the number of required runs. Half-fraction design, for example, makes the required number

of runs as half as the number of runs required for full design. The idea is based on neglecting high-order interaction effects, e.g. ABCDE, in a five-factor analysis.

Analysis of variance method (ANOVA) is used to determine significant factors. Normal probability plot may also be used for this purpose as a visual tool. On this plot, all significant effects, either main effect or interaction effect, fall outside a straight line formed by all non-significant effects.

Regression Analysis: Using only the identified significant effects, a regression model is developed. If the variance of residuals of the regression model is not uniformly distributed, the response should be transformed. For example, if the distribution is funnel-shaped, log transformation may give a uniform distribution. If the value of predicted R^2 is greater than 0.9 a satisfactorily good regression model that can very well replace the model is obtained.

The regression model represents a surface in a hyper-space formed by the significant factor. This surface is referred to as response surface. Significance of curvature of response surface is checked by testing center values, that is, comparing true response and the value obtained from the regression model at central points. Again, significance is determined using ANOVA table. If the curvature of the surface is significant, second-order terms should be introduced in the model; otherwise, the linear regression model is sufficient. To include second order terms, additional runs should be done.

Confirmation runs may be done to verify validity of the developed regression model for arbitrary points in the analysis domain. A plot of observed vs. predicted values can be used to visually confirm the goodness of fit.

Chapter 3 - NUMERICAL MODEL

3.1 Introduction

Compared to the classical methods, a full elasto-plastic analysis can more accurately predict the stress/strain state and excess pore water pressure (EPWP) changes, leading to a more realistic prediction of seismically induced displacements. To achieve such results, some aspects related to soil behaviour such as: shear-induced, plastic, volumetric strains (dilation/contraction) and subsequent changes in EPWP; continuous softening/hardening; observed nonlinear hysteretic behaviour; and shear stress-induced anisotropic effects should be taken into account.

All these aspects can be addressed by advanced elasto-plastic models implemented in Finite Element or Finite Difference codes. One of them is Dynaflow (Prevost, 2002), which belongs to a new generation of finite element programs, and is implemented with:

- Multi-yield plasticity constitutive model with a well-defined and robust methodology of calibrating the model parameters based on results of standard in-situ and/or laboratory soil tests.
- Coupled analysis in which solid and fluid coupled field equations (Biot, 1962) are used in a step-by-step dynamic effective-stress analysis to correctly capture the inertial and dissipative coupling terms.

The numerical model has been repeatedly validated in the past based on full- scale studies and centrifuge experimental results.

In the following sections, the relevant features of the software selected for this research (i.e. Dynaflow) are first described. Then general, common aspects and

characteristics of the analyses performed here are pointed out. An overview of the multi-yield surface plasticity model and the methodology to obtain and calibrate soil parameters for Nevada sand are described. Finally, the procedure for estimating material properties of the Fraser River sand from the literature, and updating them by the results of the tests performed at the University of British Columbia (UBC) is presented.

It should be noted that the parameter calibration for Nevada sand was done based on the available information from the VELACS project (see Section 3.5), before completion of UBC laboratory soil tests. The procedure was repeated in this study to calibrate soil parameters suitable for using Mohr-Coulomb yield surface rather than Drucker-Prager surface as used by Popescu and Prevost (1993a). These material properties were verified by replicating one of the VELACS centrifuge model tests. These properties are then used for the simulation of retrogressive failures with some changes to represent a very loose sand with relative density of 30 – 40%. For the study of 3D effects, however, the material properties of Fraser River sand (see Section 3.6), inferred from the literature and then updated by the information provided by UBC, are used.

3.2 Finite Element Code: Dynaflow

Dynaflow (Prevost, 2002) is a state-of-the-art general-purpose finite element analysis program for linear and non-linear, two- and three-dimensional systems. In particular, it offers transient analysis capabilities for both parabolic and hyperbolic initial value problems in solid, structural, and fluid mechanics. A multi-yield surface plasticity soil constitutive model is implemented in the program, in addition to some other models. Coupled analysis of porous media is performed for simulating the behaviour of saturated

soil materials under partially drained conditions by means of an extension of Biot's formulation in the non-linear regime.

3.3 Analysis Characteristics

3.3.1 Solid-Fluid Coupled-Field Analysis

State-of-the-art in dynamic analysis of saturated porous media employs solid-fluid coupled field equations introduced by Biot (e.g. Biot, 1962). This formulation, including the extension to the nonlinear regime and its implementation in Dynaflow, is presented in detail by Prevost (1993). In summary, the procedure of dynamic analysis of a porous saturated medium comprises of solution of the following coupled equations (Prevost, 1998):

$$\rho^s \boldsymbol{a}^s = \nabla.\sigma'^s - (1-n^w)\nabla p^w - \xi.(v^s - v^w) + \rho^s \boldsymbol{b} \qquad (3\text{-}1)$$

$$\rho^w (Dv^w / Dt) = \rho^w (v^s - v^w).\nabla v^w - n^w \nabla p^w + \xi.(v^s - v^w) + \rho^w \boldsymbol{b} \qquad (3\text{-}2)$$

where, σ'^s = solid effective stress, $\boldsymbol{a}^s$ = solid acceleration, $v^s (v^w)$ = solid (fluid) velocity, $\boldsymbol{b}$ = body force, p^w = pore fluid pressure, $\rho^s = (1-n^w)\rho_s$ and $\rho^w = n^w \rho_w$ with $\rho_s (\rho_w)$ = solid particles (fluid) mass density and n^w = porosity; $\xi = n^2 \gamma_w k^{-1}$ with k = hydraulic conductivity and γ_w = fluid unit weight, g = acceleration of gravity.

3.3.2 Analysis Procedure

The dynamic analysis of the present coupled porous continuum, according to Biot's theory of porous media, Eqs. (3-1) and (3-2) is treated as a Hyperbolic Initial Boundary Value problem. For time integration, the Newmark algorithm is selected, with $\alpha_N \geq 0.5$. Also, as the step-by-step implicit analysis is chosen, the time step size is dictated only by

the sampling time step used for the synthesized input motion (see Section 3.3.3). In addition for this type of analysis the Newmark parameter β_N is set internally to $(\alpha_N + 0.5)^2 / 4$.

For non-linear iterations the quasi-Newton BFGS method is selected because it provides faster solutions compared to other methods and it is sufficiently accurate. The details of BFGS updating formula can be found in Dynaflow manual (see Prevost, 2002).

Each finite element analysis of this study is performed in one run consisting of two phases. First, gravity loads are applied and the soil is allowed to fully consolidate. The consolidation phase is calculated dynamically, while the Newmark algorithm parameters in the integration scheme are set to α_N = 1.5 and β_N = 1. After consolidation is completed, the nodal displacements, velocities, and accelerations are zeroed, the time is reset to zero and the input acceleration is applied at the mesh boundaries. The Newmark parameters are chosen as α_N = 0.65 and $\beta_N = (\alpha_N + 0.5)^2 / 4$ = 0.33, to introduce a slight numerical damping and maximize high frequency numerical dissipation. No additional viscous physical damping is introduced. Post-earthquake analysis, including EPWP dissipation and, where applicable, post-liquefaction deformations, is simulated in the same phase, by continuing the analysis for the desired time period after the end of the seismic motion.

3.3.3 Input Motion

The seismic motion is prescribed as an acceleration time history at selected boundaries of the finite element mesh. The base of the analysis domain is usually extended to a more resistant soil layer, assumed rigid and impervious, and situated at a

certain depth, so that those assumptions do not significantly influence the calculation results. Recorded acceleration time histories as well as artificially generated time-histories may be applied as input motion. Dynaflow is also capable of generating spectrum-compatible motions, as described below.

3.3.3.1 Response Spectrum-Compatible Motions

The acceleration time history is generated according to an acceleration response spectrum (e.g. UBC, 1994). This algorithm, implemented in the computer package PRISM, is described by Popescu et al. (2000). The algorithm is based on a method for simulating non-stationary vector processes proposed by Deodatis (1996). The most recent application of the methodology is presented by Popescu (2002), in which effects of seismic loading rate (frequency content) on liquefaction are studied by generating time histories compatible with response spectra of different soil types (stiff, soft, etc.) proposed in Uniform Building Code (1994).

3.3.4 Boundary Conditions

In Dynaflow, several types of boundary conditions (BC) are available including the standard type of BC (i.e. prescribed displacement, velocity, or acceleration for solid and fluid phases), free-field BC, and transmitting BC. Boundary conditions for each analysis of this study are described in the corresponding Chapters (see Sections 4.2.3 and 5.2.2).

The following section presents details of the transmitting boundary conditions implemented in the finite element program Dynaflow and used in this study (see Sections 5.2.2 and 5.4.2).

3.3.4.1 Transmitting Boundary Conditions

The nodal transmitting element is used to provide a transmitting nodal boundary for incident propagating motions. The boundary is frequency independent, and is local in space and time (see also Section 2.3.5.2). It is exact for vertically propagating wave motions and linear systems only. At the boundary (Prevost, 2002):

$$\tau(t) = \rho C(2s\frac{\partial I}{\partial t} - \frac{\partial u}{\partial t}) \tag{3-3}$$

where $t =$ time, $\rho =$ mass density of underlying medium, $C =$ shear wave speed, $I = I(t) =$ incident motion, $u = u(t) =$ associated displacement motion at the node, and $s =$ multiplier. The incident motion $I(t)$ is the earthquake motion applied at the boundary. The wave speed is:

$$C = \sqrt{\frac{G}{\rho}} \tag{3-4}$$

where $G =$ shear modulus.

The above definition of transmitting boundary (as a shear stress on the boundary) is based on the solution of the equation of motion, as presented hereafter according to Prevost (2002), for vertical propagation of shear waves:

$$\rho u_{,tt} = G u_{,xx} \tag{3-5}$$

where $_{,tt}$ and $_{,xx}$ denote second-order partial derivative with respect to t and x, respectively. The fundamental solution of Eq. (3-5) can be expressed as:

$$u(x,\ t) = I\left(t - \frac{x}{C}\right) + R\left(t + \frac{x}{C}\right) \tag{3-6}$$

where I and R are two arbitrary functions presenting the incident and reflected motions. The following two identities apply:

$$I_{,x}+\frac{1}{C}I_{,t}=0 \tag{3-7}$$

$$R_{,x}-\frac{1}{C}R_{,t}=0 \tag{3-8}$$

and therefore, differentiating Eq. (3-6) with respect to x and t in turn yields:

$$u_{,x}=\frac{1}{C}\left(-I_{,t}+R_{,t}\right) \tag{3-9}$$

$$u_{,t}=I_{,t}+R_{,t} \tag{3-10}$$

The shear stress $\tau(x,\ t)$ can therefore be expressed as

$$\tau(x,t)=Gu_{,x}=\rho C\left(-I_{,t}+R_{,t}\right) \tag{3-11}$$

and upon elimination of $R_{,t}$ the following relation is obtained:

$$\tau(x,t)=\rho C\left(u_{,t}-2I_{,t}\right) \tag{3-12}$$

which is the same as Eq. (3-3) except that the multiplier s is applied for scaling the incident motion, and the two equations are opposite in sign because, as noted in Section 2.3.5.2, the applied shear stress at the boundary is for canceling the incident shear waves.

3.4 Multi-yield Surface Plasticity Model

The multi-yield plasticity model is a kinematic hardening model based on a relatively simple plasticity theory (Prevost 1985) and is applicable to both cohesive and cohesionless soils. The concept of a "field of work-hardening moduli" (Iwan 1967, Mroz 1967, Prevost 1977) is used by defining a collection of nested yield surfaces in the stress space (Figure 3-1a, Figure 3-2, and Figure 3-3). In this study, rounded Mohr-Coulomb yield surfaces (Figure 3-4) are employed, since using Mohr-Coulomb yield surface is

imperative for 3D analysis. This is because Drucker-Prager yield surface corresponds to different friction angles at failure on different stress paths.

The yield surfaces define regions of constant shear moduli in the stress space, and in this manner, the model discretizes the smooth elastic-plastic stress-strain curve into a number of linear segments (Figure 3-3). The outermost surface, i.e. failure surface, corresponds to zero shear modulus. The plastic flow rule is associative in its deviator component. To account for experimental evidence from tests on granular soil materials, a non-associative flow rule is used for the dilatational component (Figure 3-1b), which also reflects the dependency of plastic dilatancy on effective stress ratio (e.g. Byrne and McIntyre, 1994). The material hysteretic behaviour and shear stress-induced anisotropic effects are simulated by a purely kinematic hardening rule. Upon contact, the yield surfaces are translated in the stress space by the stress point, as illustrated in Figure 3-1c. The direction of translation is selected such that the yield surfaces do not overlap, but remain tangent to each other at the stress point. The constitutive equations are integrated numerically using a stress relaxation procedure (Figure 3-1d). The return mapping algorithm proposed by Simo and Ortiz (1985) is modified for the multi-yield plasticity case (Prevost 1993). Altogether, accurate simulation of shear-induced plastic dilation, hysteretic effects, and full solid-fluid coupling leads to a more precise calculation of excess pore water pressure (EPWP) build-up/dissipation as well as modelling gradual soil softening/hardening during and after the earthquake shaking.

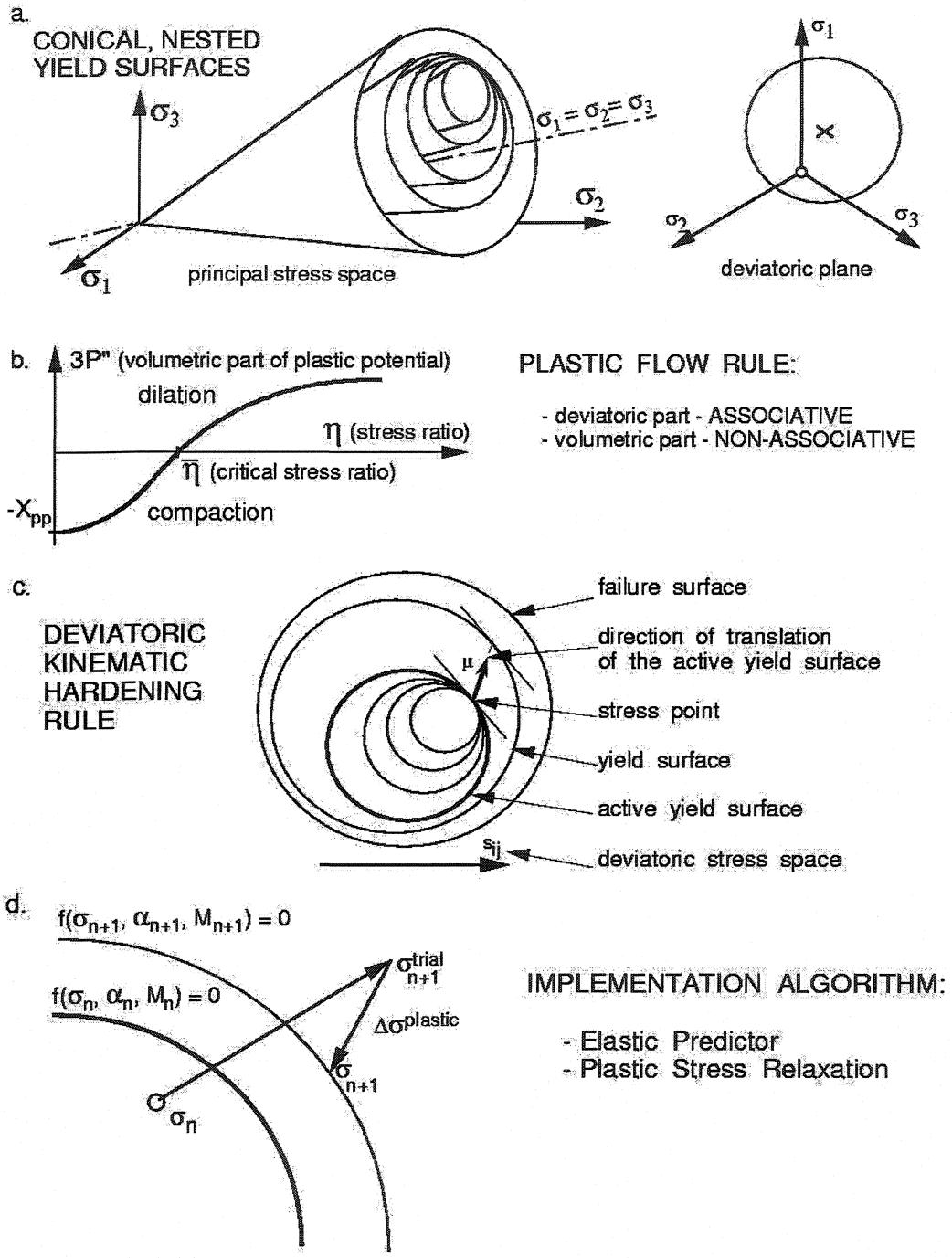

Figure 3-1. Main features of the multi-yield plasticity soil constitutive model: a) yield surfaces; b. plastic flow rule; c. hardening rule; d. numerical integration (Popescu, 1995).

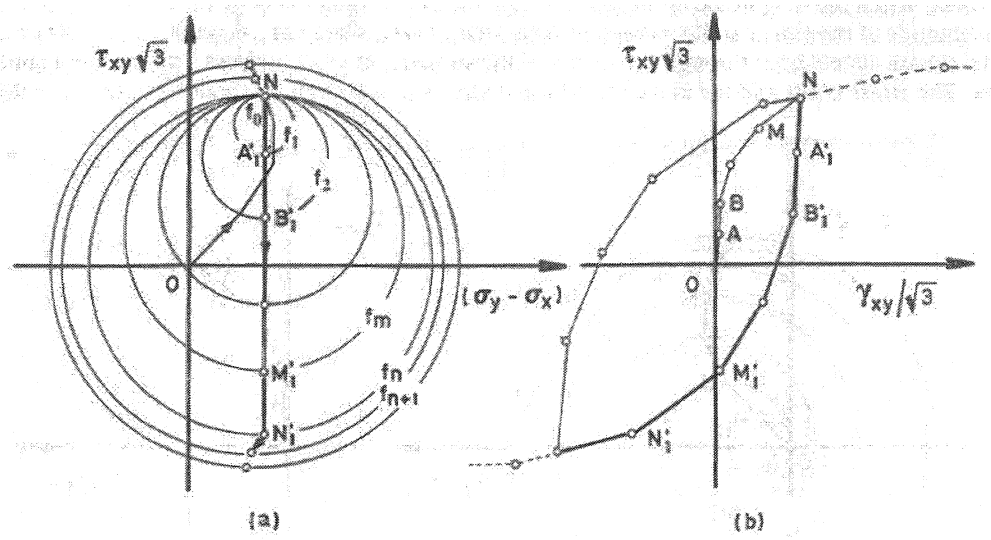

Figure 3-2. Cyclic simple shear test: a) field of yield surfaces, b) loading-reverse loading stress-strain curves (Prevost, 1977).

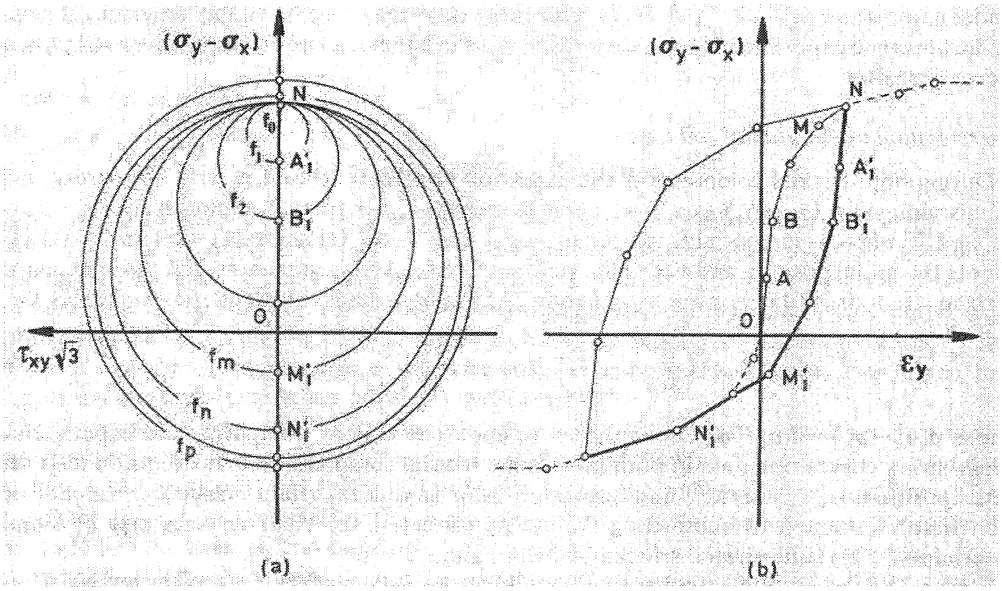

Figure 3-3. Cyclic triaxial test: a) field of yield surfaces, b) loading-reverse loading stress-strain curves (Prevost, 1977).

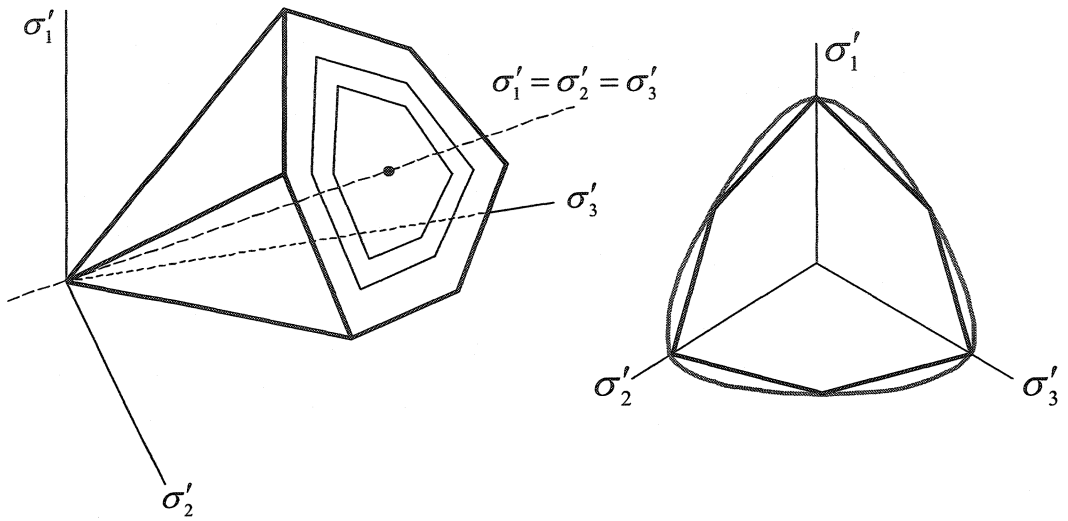

Figure 3-4. Mohr-Coulomb (hexagonal) yield surface: a) nested surfaces in principal stress space, and, b) rounded surface in π-plane.

3.4.1 Soil Constitutive Model Parameters

The required constitutive parameters of the multi-yield surface plasticity soil model are listed in Table 3-1. The yield and failure parameters are used to describe the initial position, size and plastic modulus corresponding to each yield surface. ϕ, ε_{dev}^{max}, k_0 *and* G_0, are included in a modified hyperbolic expression proposed by Prevost and Keane (1989) and Griffiths and Prevost (1990) describing a wide range of soil stress-strain relations. Hayashi et al (1992) proposed another expression using a hyperbola whose shape depends on the characteristics of the grain size distribution through the stress-strain curve coefficient α. They developed their model based on shear stress-strain curves obtained in a simple shear soil testing device, using soil specimens with a wide variety of grain size distributions tested under k_0 condition. Both models are implemented in Dynaflow.

Table 3-1. The parameters of the multi-yield plasticity model (Popescu, 2001)

Constitutive parameter	Symbol	Type
Mass density of solid	ρ_s	State
Porosity	n^w	parameters
Hydraulic conductivity	k	
Low strain elastic moduli	B_0, G_0	Low strain
Reference effective mean normal stress	p_0'	elastic
Power exponent	n	parameters
Friction angle at failure	ϕ	Yield and
Maximum deviator strain	ε_{dev}^{max}	failure
Coefficient of lateral stress	k_0	parameters
Stress-strain curve coefficient	α	
Dilation angle	ψ	Dilation
Dilation parameter	X_{pp}	Parameters

The dilation parameters are used in the plastic flow rule for calculating the dilation (shear-induced plastic volumetric strain). The dilation angle, ψ, is in fact the phase transformation angle, and the dilation parameter, X_{pp}, is a scale coefficient for plastic dilation, basically depending on relative density and soil type (fabric, grain size)—Popescu (1995).

From a general point of view, both categories of "yield and failure parameters" and "dilation parameters" are the plastic parameters of the model. Although only B_0 and G_0 are noted in Table 3-1 as the low-strain elastic parameters, in this study, G_0 and ν are used to describe the elastic behaviour of soil; therefore, other elastic parameters such as low-strain bulk modulus (B_0) can be computed as a function of G_0 and ν. All other parameters listed in Table 3-1 as "low-strain" and "state parameters" can be regarded as elastic parameters.

It should also be mentioned that the coefficient of earth pressure at rest, k_0, listed under "yield and failure parameters", is only used to generate the shear stress-strain curves necessary for defining the shear modulus for each yield surface. The initial state of stress is calculated by the program according to the value of Poisson's ratio.

According to Dynaflow manual (see Prevost, 2002), the yield function (Drucker-Prager or Mohr-Coulomb type) is defined as:

$$f = \left\{ \frac{3}{2} tr(\mathbf{s} - \bar{p}\mathbf{a})^2 \right\}^{1/2} + \bar{k}\bar{p}g(\theta) = 0 \tag{3-13}$$

where $\mathbf{s}$ is the deviatoric stress tensor, i.e.,

$$\boldsymbol{s} = \boldsymbol{s} - p\boldsymbol{d} \tag{3-14}$$

$$p = 1/3 tr\boldsymbol{s} \tag{3-15}$$

with $\boldsymbol{s}$ as the tensor of effective stresses. $\boldsymbol{a}$ is a tensor of coordinates of the center of the yield surface in the deviatoric stress space; $\bar{k}$ is the size of the yield surface; and:

$$\bar{p} = (p - a) \tag{3-16}$$

with a (attraction) = $c / \tan\phi$.

The function $g(\theta)$ determines the shape of the cross-section on the deviatoric plane:

$$g(\theta) = \frac{2M_k}{(1 + M_k) - (1 - M_k)\sin 3\theta} \tag{3-17}$$

in which

$$\sin 3\theta = -\sqrt{6}\bar{J}_3 / \bar{J}_2^{3/2} \tag{3-18}$$

$$\bar{J}_2 = tr\bar{\mathbf{s}}^2 \tag{3-19}$$

$$\bar{J}_3 = tr\bar{\mathbf{s}}^3 \tag{3-20}$$

$$\bar{\boldsymbol{s}} = \boldsymbol{s} - \bar{p}\boldsymbol{a} \tag{3-21}$$

and M_k material parameter. For a Drucker-Prager circular cone, $M_k = 1.0$, whereas for a round-cornered Mohr-Coulomb cone:

$$M_k = \frac{3 - \sin\phi}{3 + \sin\phi} \tag{3-22}$$

where ϕ = friction angle.

The dilation parameter X_{pp} is defined as follows to specify a non-associative flow rule for the dilatational component:

$$tr\mathbf{P} = X_{pp}(\overline{\eta}^2 - 1)/(\overline{\eta}^2 + 1) \tag{3-23}$$

in which, $\mathbf{P}$ is the symmetric second-order tensor of plastic deformations direction, $\overline{\eta}$ = normalized stress ratio, i.e.,

$$\overline{\eta} = \eta / \eta_{\psi} \tag{3-24}$$

$$\eta = \left\{ \frac{3}{2} trs^2 \right\}^{1/2} / \overline{p} \tag{3-25}$$

with η_{ψ} = dilation stress ratio (that is, the stress ratio at which phase transformation occurs, corresponding to phase transformation angle), and η is the mobilized stress ratio.

The Drucker-Prager, Mohr-Coulomb, and Rounded Mohr-Coulomb yield surfaces on π-plane are presented in Figure 3-5 for friction angle values of 31° and 36° used in this study (see Sections 4.2.2 and 5.2.3). The rounded surface is plotted using Eq. (3-13). These plots indicate that there is a slight concavity in the rounded surface at extension. It can be shown that this concavity exists for values larger than 22°. This is a limitation of the software; however, no non-convergence or numerical analysis problems were observed in the analyses presented in Chapters 4 and 5. Therefore, the effect of this slight concavity seems to have been insignificant in this study.

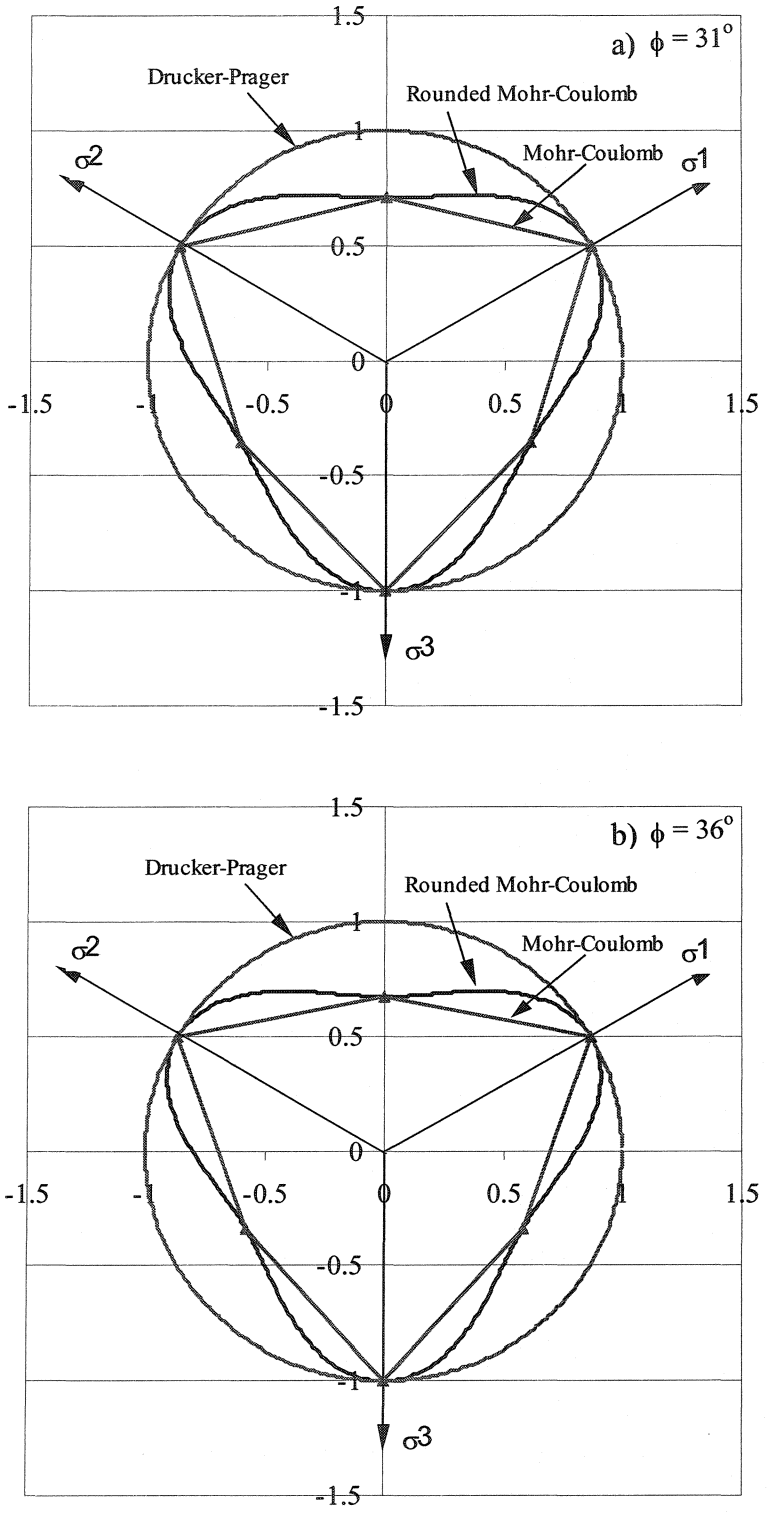

Figure 3-5. Presentation of Drucker-Prager, Mohr-Coulomb, and Rounded Mohr-Coulomb yield surface on π-plane for friction angle values of a) 31°, and b) 36°.

The required constitutive model parameters (except dilation parameter) can be derived from the results of conventional laboratory (triaxial, simple shear) and/or in-situ (cone penetration, standard penetration, wave velocity) soil tests and liquefaction strength analysis (see e.g. Popescu and Prevost 1993a, Popescu 1995). An example of parameter estimation from laboratory soil test data is presented by Popescu and Prevost (1993a). A method for constitutive model calibration, based on penetration test results (SPT or CPT), is proposed by Popescu (1995), and Prevost and Popescu (1996). The dilation parameter, X_{pp}, which controls the amount of plastic dilation, is evaluated based on the results of liquefaction strength analysis, as shown by Popescu and Prevost (1993a) and Popescu (1995, 2001).

3.4.2 Model Validation

The soil constitutive model, its implementation algorithm, and the methodology for estimating the constitutive model parameters have been repeatedly validated in the past for soil liquefaction computations, based on both full scale measurements and centrifuge experimental results (e.g. Keane & Prevost, 1989; Popescu and Prevost 1993a, b, 1995; Popescu et al. 1992, 1998).

The most comprehensive validation of the proposed model was carried out during the VELACS (Verification of Liquefaction Analysis by Centrifuge Studies) project (Arulanandan and Scott, 1993, 1994). This study was aimed at better understanding the mechanisms of soil liquefaction and at acquiring data for the verification of various analysis procedures. Nine centrifuge models (horizontal and sloping, homogeneous and non-homogeneous soil deposits, embankments, and structures on liquefiable soil) subjected to seismic motion were tested and duplicated at several centrifuge centers in

US and UK. The numerical predictions submitted by 20 groups of researchers were class 'A' predictions, and thus were made before the relevant experiments were performed. Those predictions were based on the results of conventional laboratory soil tests performed on the soil materials to be used in the centrifuge models. Class 'A' predictions using Dynaflow were submitted for all the nine centrifuge models. A summary comparison of the performance of all class 'A' predictions is presented by Popescu and Prevost (1995), and a detailed comparison, showing all recorded and predicted pore pressure, displacement and acceleration time histories, has been posted on the web at: http://cee.princeton.edu/~radu/soil/velacs/. It was found from these comparisons, as well as from studies presented by other authors (Arulanandan and Scott, 1994) that the VELACS project validated the mathematical model and methodology used here.

3.5 Nevada Sand Properties

As noted before (Section 3.1), material properties of two types of sand, namely, Nevada and Fraser River sands, are used for the analyses of retrogressive failures (Chapter 4) and 3D effects (Chapter 5), respectively. This is because when the analysis of retrogressive failures started, the results of laboratory tests on Fraser River sand (then to be provided by UBC) were not available. Since it was intended to perform the analyses using real soil parameters, it was decided to use Nevada sand properties. Nevada sand properties are estimated herein using the available information from the VELACS project, including laboratory tests reported by Arulmoli et al. (1992), the project web site (http://geoinfo.usc.edu/gees/velacs/), a previous study on numerical prediction of centrifuge test results (Popescu and Prevost, 1993a). The numerical model used in this study is different from the one used by Popescu and Prevost (1993a) because the rounded

Mohr-Coulomb yield surface is used rather than Drucker-Prager yield surface for better simulation of soil behaviour especially in 3D analysis. Therefore, to accommodate the changes in the constitutive model, the procedure for calibration of the dilation parameter (X_{pp}) for Nevada sand was repeated, and was then verified using VEACS Model #2 test results, as presented in the following Sections 3.5.1 and 3.5.2.

It should be emphasized, however, that for Nevada sand, only the procedure for performing constitutive experiment (element test) to calibrate X_{pp} is described and a full description of estimation of *all* material parameters is presented in Section 3.6 for Fraser River sand.

3.5.1 Constitutive Experiment (Element Test)

As noted before, all model parameters are based on traditional laboratory or in-situ test results, except for X_{pp} that can be estimated based on liquefaction strength analysis. Constitutive experiments (element tests) can be used for this purpose. The procedure consists of repeating a test on an element with known properties and changing the value of X_{pp} to obtain the same result as obtained in laboratory tests (either triaxial or simple shear cyclic tests). Test results are interpreted to be the same, if soil liquefaction occurs after the same number of stress cycles. The occurrence of initial liquefaction is considered as occurrence of 5% double amplitude axial strain, or unit excess pore pressure ratio (r_u), whichever occurs first.

Result of a sample constitutive experiment that replicates a cyclic triaxial test is shown in Figure 3-6. This experiment is for obtaining the value of X_{pp} for a soil specimen of Nevada Sand with Dr = 40% tested as part of the VELACS project. Values of other soil

parameters are obtained by Popescu and Prevost (1993a) based on laboratory soil test results (Arulmoli et al., 1992).

For this particular specimen, the value of X_{pp} is determined so that the element liquefies (r_u = 1) after the same number of stress cycles as recorded in laboratory (Figure 3-6).

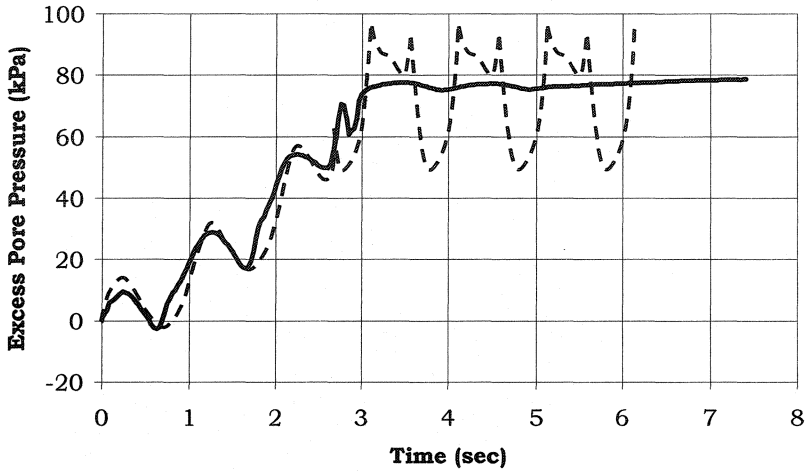

Figure 3-6. Recorded (solid line) and predicted (dashed line) excess pore water pressure. VELACS, Nevada Sand, Dr = 40%, Effective Consolidation Pressure = 80 kPa, Cyclic Deviator Stress = 28.8 kPa, Frequency = 1 Hz, Number of Cycles to Liquefaction = 3.2 (http://geoinfo.usc.edu/gees/velacs/)

3.5.2 Replication of VELACS, Model #2 Centrifuge Test

The above-calibrated X_{pp}, in addition to the other calculated soil parameters given by Popescu and Prevost (1993a) results in the following predictions of the VELACS Model #2 (see Figure 3-7 to Figure 3-16), replicated in this study using the latest version of the program used here, where Mohr-Coulomb yield surface is used rather than Drucker-Prager surface.

Using the estimated properties, the program provides close predictions of excess pore water pressures (Figure 3-9 to Figure 3-12). Predicted displacements at the end of

shaking, however, are about half the recorded displacements, except for LVDT3 located at the surface (Figure 3-13 to Figure 3-16). At this location, predicted displacement is double the recorded displacement. A comparison of the predicted and recorded displacement profiles at a time instant during strong shaking is also shown in Figure 3-8.

As stated by Finn (2000), soil models are strongly stress path dependent, that is, predictions are good if the same stress paths are used in loading and calibration phases of study. Otherwise, the predictions become less reliable. He then recommends that it is vitally important to calibrate the constitutive model for the job at hand: if the problem is shear on horizontal planes, then calibration is best done in terms of simple shear data, and if rocking is of prime concern then triaxial test data would be preferable. For the above analysis, since the slope failure is shear dominated, caused by propagation of earthquake shear waves, the best test that can represent in-situ conditions of loading is the simple shear test with initial static shear stress (or bias) applied during the consolidation phase of the test (resulting in anisotropic consolidation of the sample). It is believed that if such test results were used for parameter calibration, the predictions of displacements would enhance. Nonetheless, by performing curve-fitting exercise, one can modify the parameters for better prediction of the results of this specific test. This is not done here because the parameters are used for a rather qualitative study of retrogressive failures.

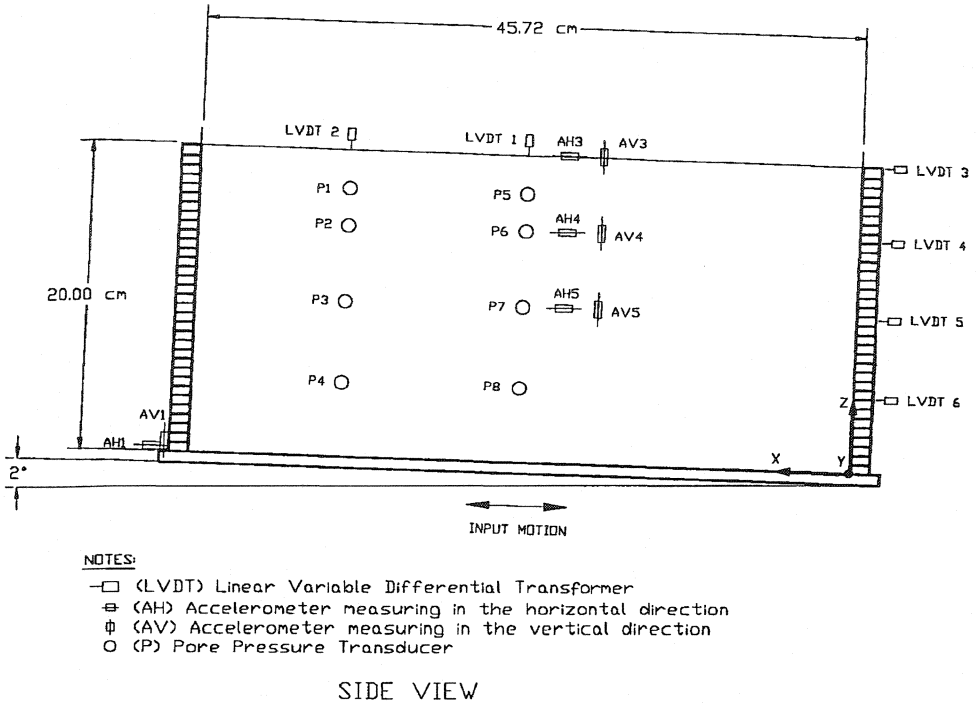

Figure 3-7. VELACS Model #2 Configuration (http://geoinfo.usc.edu/gees/velacs/).

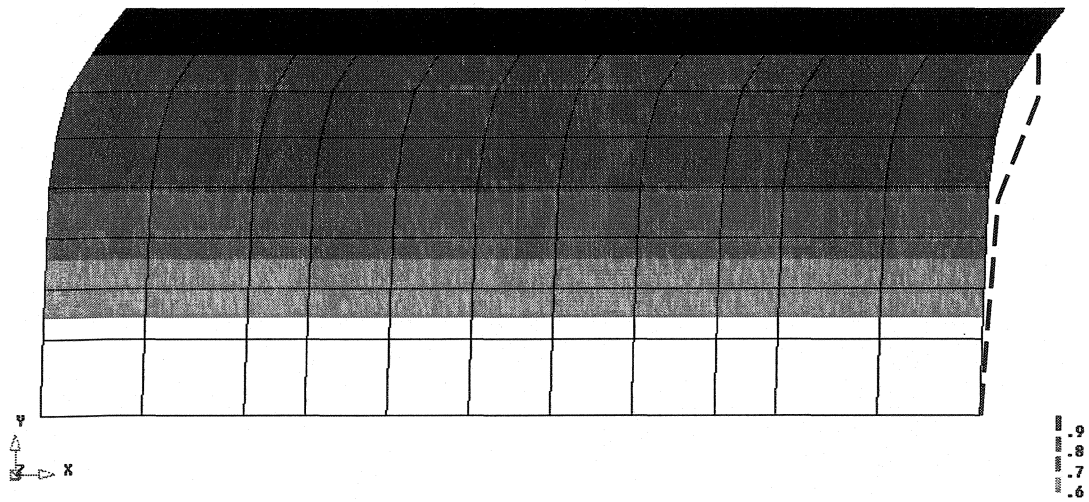

Figure 3-8. VELACS Model # 2 predicted and recorded (dashed line) deformed shape, and contours of excess pore water pressure ratio at t = 8.34 s. Deformation magnification scale = 5.

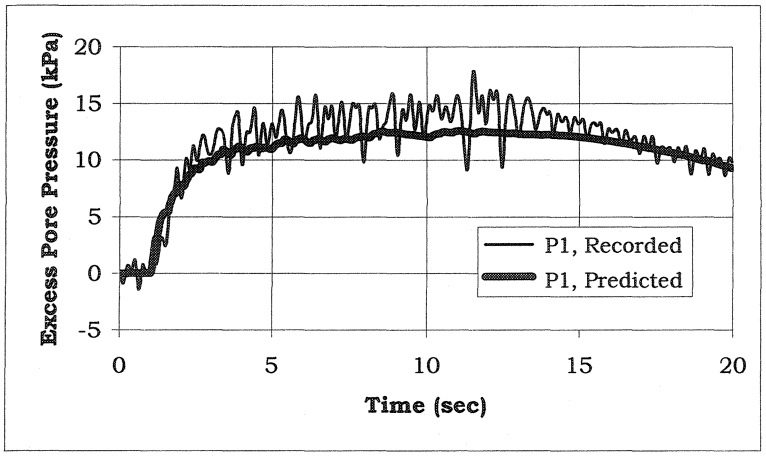

Figure 3-9. Comparison between recorded and predicted excess pore water pressure at P1.

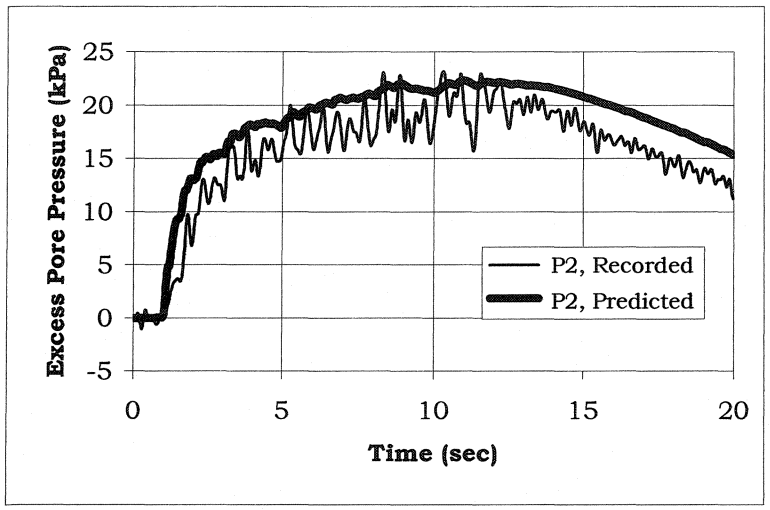

Figure 3-10. Comparison between recorded and predicted excess pore water pressure at P2.

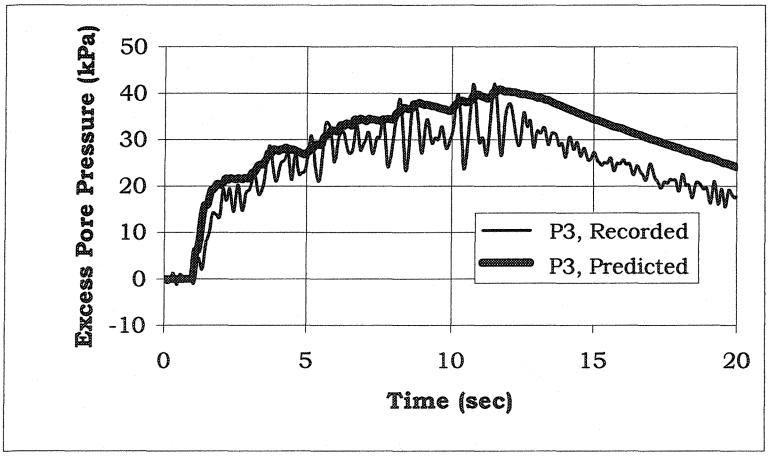

Figure 3-11. Comparison between recorded and predicted excess pore water pressure at P3.

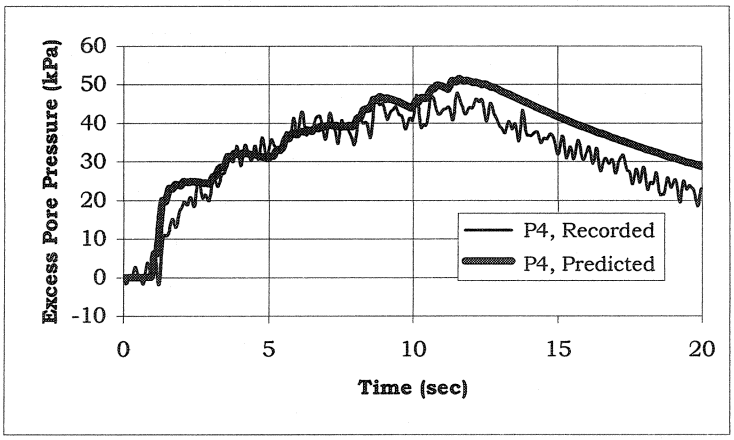

Figure 3-12. Comparison between recorded and predicted excess pore water pressure at P4.

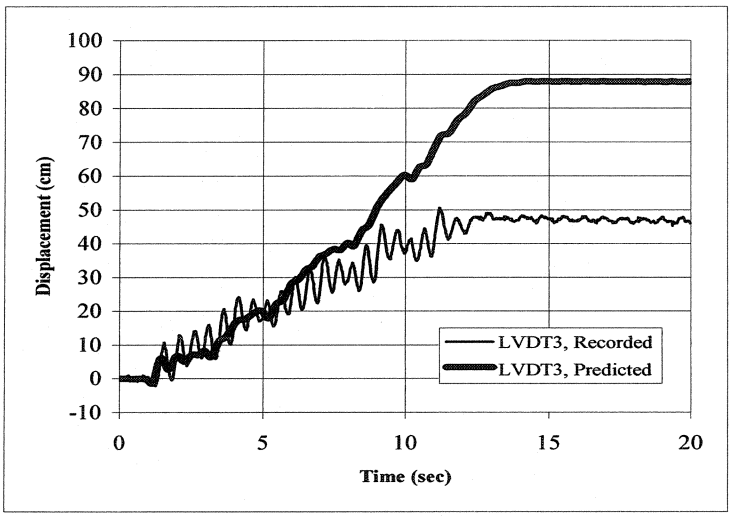

Figure 3-13. Comparison between recorded and predicted displacements at LVDT3.

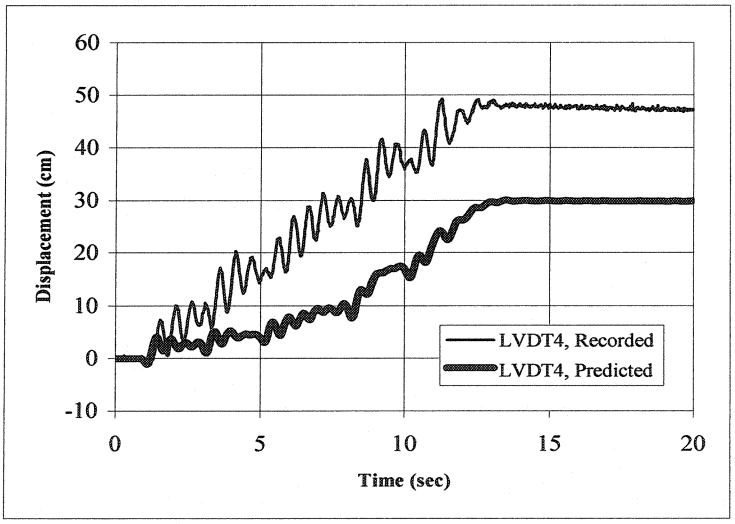

Figure 3-14. Comparison between recorded and predicted displacements at LVDT4.

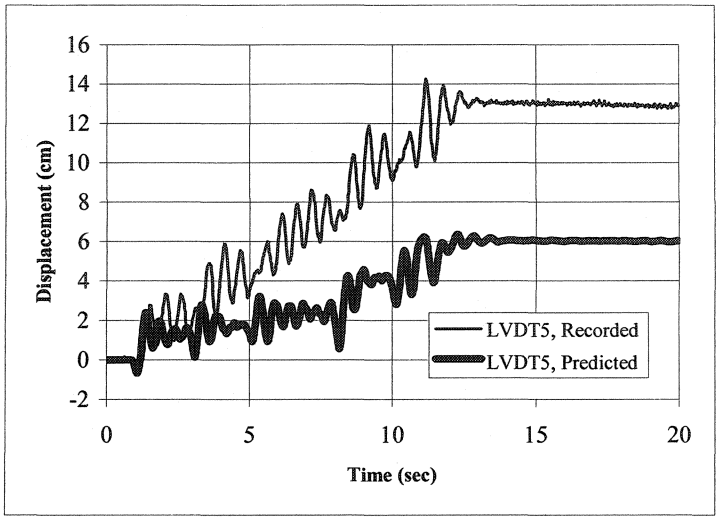

Figure 3-15. Comparison between recorded and predicted displacements at LVDT5.

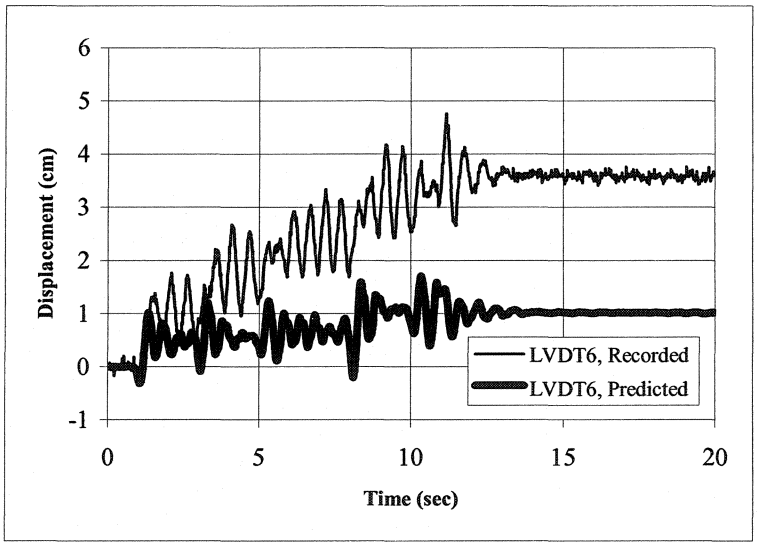

Figure 3-16. Comparison between recorded and predicted displacements at LVDT6.

3.6 Fraser River Sand Properties

The material properties used for evaluating the 3D effects in this study (Table 3-2) are estimated based on values reported in the literature for the Fraser River (BC, Canada) sand at D_r = 40%. The properties are updated and modified slightly after obtaining the results of cyclic simple shear tests performed at the University of British Columbia

(UBC), within the framework of "Earthquake Induced Damage Mitigation from Soil Liquefaction" project, (http://www.civil.ubc.ca/liquefaction/). The tests were conducted under the supervision of Dr. D. Wijewickreme.

Hereafter, the properties inferred from the literature are referred to as set #1, and the modified properties are referred to as set #2 (Table 3-2).

Table 3-2. Material properties of Fraser River sand. (See Section 3.6.1 for the descriptions of the parameters.)

Soil Property	Symbol	Set #1 (Literature)	Reference	Set #2 (UBC tests)
Mass density of solid (kg/m3)	ρ_s	2720	Howie et al. (2002)	2710
Porosity	n^w	0.45	Howie et al. (2002); Vaid et al. (2001), Sivathayalan and Vaid (2002)	0.45
Low-strain shear modulus (MPa)	G_0	40	Hardin and Richard (1963); Belloti et al. (1986); Vaid and Eliadorani (2000); Howie et al. (2002)	47
Poisson's Ratio	ν	0.3	e.g. Das (1998)	0.3
Reference mean effective normal stress (kPa)	p_0	100	-	100
Power exponent	n	0.5	Richart et al., 1970; Chillarige et al. (1997b)	0.5
Fluid bulk modulus (MPa)	B_f	2000	e.g. Nave (2000)	2000
Friction angle at failure	ϕ	36	Vaid and Chern (1985); Vaid et al., (1999); Vaid et al. (2001), Sivathayalan and Vaid (2002)	36
Cohesion (kPa)	c	0	-	0
Maximum deviator strain in compression/extension % (in p-constant triaxial test)	ε_{dev}^{max}	5/3	-	8/7
Dilation angle (phase transformation)	ψ	34	Vaid et al. (2001), Sivathayalan and Vaid (2002), Vaid and Sivathayalan (1996)	34
Dilation parameter	Xpp	0.2	Calibration using Vaid et al. (2001), [Vaid and Sivathayalan (1996): Cr = 0.78]	0.3
Hydraulic Conductivity (m/s)	k	$2.3*10^{-4}$	Shahabi et al. (1984)	$2.3*10^{-4}$

3.6.1 Estimation of Soil Properties

Hereafter, details of calculating the soil properties given in Table 3-2 are described. Results of general soil tests for Fraser River sand are given in Table 3-3.

Table 3-3. Results of general soil tests for Fraser River sand.

Soil properties	Howie et al. (2002)	Vaid et al. (2001)	UBC Tests
Specific gravity, G_s	2.72	-	2.71
Maximum void ratio, e_{max}	0.955	0.926	0.94
Minimum void ratio, e_{min}	0.627	0.605	0.62
Median grain size, D_{50} (mm)	0.27	0.30	~0.25
Effective grain size, D10 (mm)	0.16	-	~0.16
Coefficient of uniformity, C_u	1.9	1.8	-

Mass density: According to the first column of Table 3-3, the value of $G_s = 2.72$ is adopted. Hence, solid mass density is 2720 kg/m^3.

Porosity (n^w): Using the definition of relative density

$$D_r = \frac{e_{max} - e}{e_{max} - e_{min}} \tag{3-26}$$

the void ratio in terms of relative density can be obtained using

$$e = e_{max} - D_r(e_{max} - e_{min}) \tag{3-27}$$

The soil porosity can then be calculated using

$$n^w = \frac{e}{1+e} \tag{3-28}$$

An average value of $n^w = 0.45$ (corresponding to $e = 0.82$) is adopted based on the values of e_{max} and e_{min} given in Table 3-3.

Fiction angle at failure (ϕ) and dilation angle (ψ): The friction angle at failure (ϕ) and dilation angle (ψ, that corresponds to phase transformation state), in compression and extension, are obtained from the results of the monotonic triaxial compression and extension loading tests reported by Vaid et al. (2001) and shown in Figure 3-17.

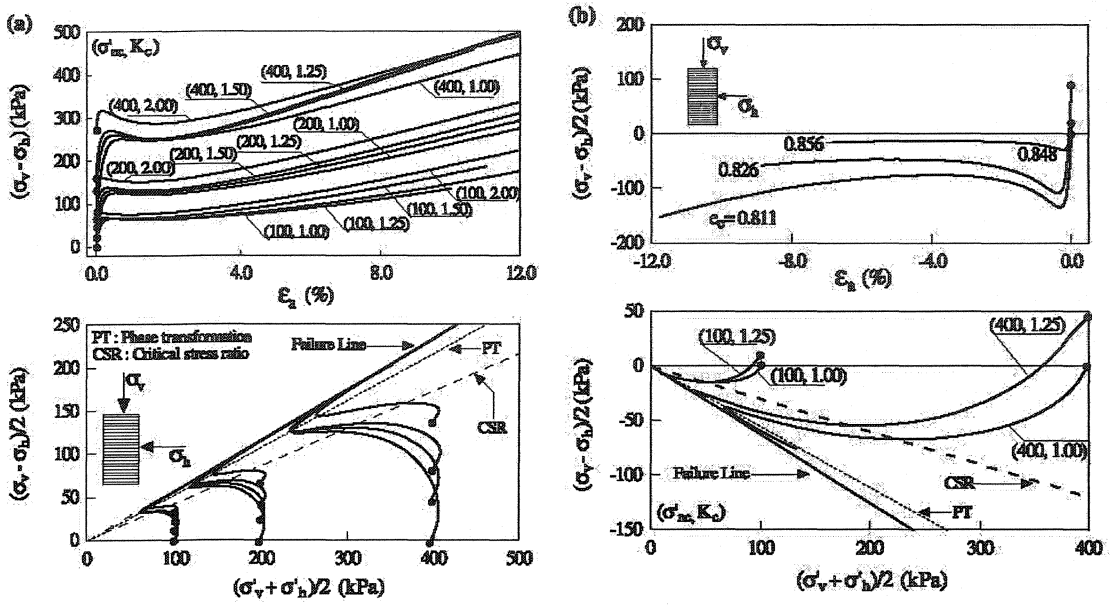

Figure 3-17. Results of monotonic triaxial test in a) compression, and b) extension, Vaid et al. (2001).

According to these graphs, in compression, the friction angle at failure and phase transformation states are approximately equal to 35.5° and 32.7°, respectively, using the following equation:

$$\sin(\phi) = \frac{\sigma'_v - \sigma'_h}{\sigma'_v + \sigma'_h} \tag{3-29}$$

where as shown in Figure 3-17, σ'_v = vertical effective stress, and σ'_h = horizontal effective stress. For calculating the friction angle at failure and the phase transformation angle (dilation angle), the vertical and horizontal stresses on the failure and the phase transformation (PT) lines, respectively, are used in the above relationship.

Based on a large number of experiments, Vaid et al (2001) have calculated the phase transformation angle—shown as $\phi_{QSS/SS}$ in Figure 3-18 denoting the mobilized friction angle at quasi-steady state (in strain-softening specimens), or phase transformation (in dilative specimens), see Figure 3-19—and reported a value equal to 34°. This angle is the same for both compression and extension modes (see also Vaid and Chern, 1985, Vaid et

al., 1999). The friction angle at failure in extension mode, according to the failure line plotted in Figure 3-17b is 39.4°, which seems to be higher than in compression. However, according to Mayne and Holtz (1985) and Nakase and Kamei (1988), the friction angle obtained from triaxial extension is on average about 22% larger than that obtained from triaxial compression, which shows that both values are in fair agreement. The value of friction angle at failure in extension will be taken equal to the value obtained for the compression mode of loading. Therefore, values of 36° and 34° are adopted for friction and dilation angles in both compression and extension.

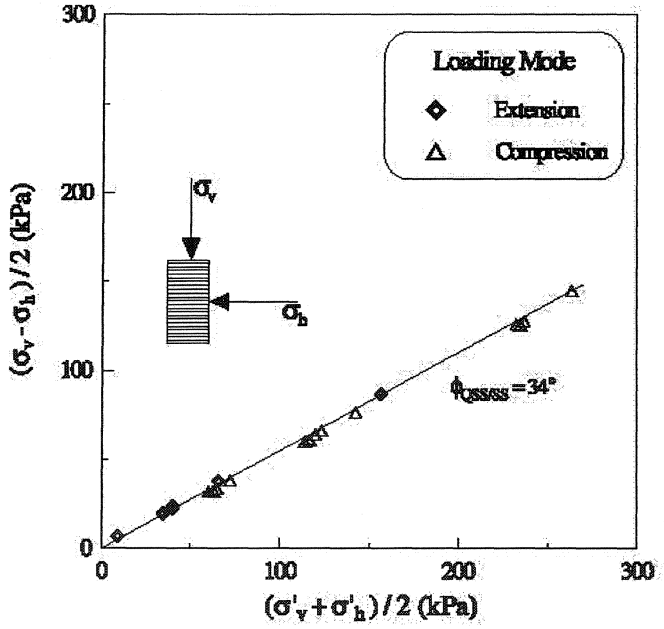

Figure 3-18. Effective stress states at quasi-steady state (in strain-softening specimens), or phase transformation (in dilative specimens), Vaid et al. (2001).

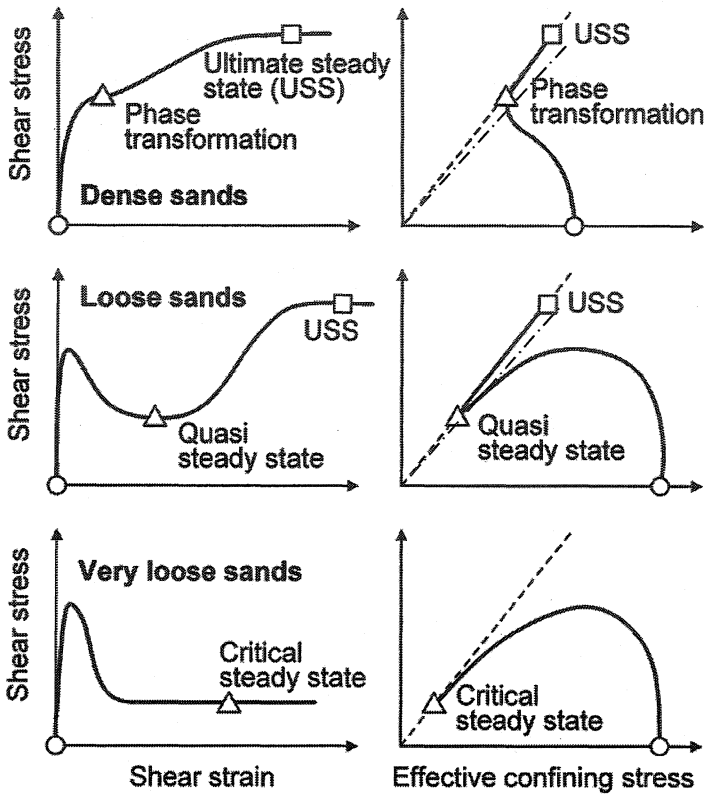

Figure 3-19. Idealization of different states of soil deformation under monotonic undrained loading (modified after Yoshimine et al., 1999).

The same values of $\phi = 36^\circ$ and ψ (or $\phi_{QSS/SS}$) $= 34^\circ$ can be calculated from the graphs presented by Sivathayalan and Vaid (2002). According to this study, $\phi_{QSS/SS}$ is essentially constant and is independent of void ratio, confining and static shear stress levels, and loading mode, which implies uniqueness of the quasi-steady state and steady state (see Figure 3-19) in the effective stress space. Since the phase transformation angle is independent of the loading mode, the simple shear, triaxial, and multiaxial (hollow cylinder torsional device) phase transformation angles are not different.

Chillarige et al. (1997b) have obtained a value of 35° for the friction angle at failure. This value is obtained by establishing the steady state line from the ultimate steady state points obtained from all the tests on the loose reconstituted samples of the Fraser River sand.

Poisson's ratio (ν): The ranges of Poisson's ratio for different types of soils are given in the Table 3-4 (Das, 1998):

Table 3-4. Ranges of Poisson's ratio for different types of soils.

Type of Soil	Poisson's ratio
Loose sand	0.2 – 0.4
Medium sand	0.25 – 0.4
Dense sand	0.3 – 0.45
Silty sand	0.2 – 0.4
Soft clay	0.15 – 0.25
Medium clay	0.2 – 0.5

Based on the range given for loose and medium dense sands, and the value used by Popescu and Prevost (1993a) for Nevada sand, the value of Poisson's ratio is selected as $\nu = 0.3$.

It is worth noting that the value of this parameter for very loose Fraser River sand, according to Howie et al. (2002), is between 0.07 and 0.13, depending on the time of sample confinement (1 – 1000 min.). Also, Byrne et al (2003), for Nevada sand at D_r = 40% have used a value of a soil parameter related to ν that implies $\nu = 0.1$, which lies in the range of 0 – 0.2 given by Hardin (1978).

Therefore, estimation of this parameter needs more consideration, which is presented later in Section 3.6.2.

Earth pressure at rest (k_0): This parameter can be estimated using the following well-known Jaky equation (see e.g. Craig, 1992):

$$k_0 = 1 - \sin\phi' \qquad (3\text{-}30)$$

Despite its simplicity, it is a widely used equation. For example, Chillarige et al. (1997b) have used this equation with the value of $\phi' = 35^\circ$ (refer to the sub-section on calculating the friction angle at failure in Section 3.6.1) for their evaluation of Fraser

River sand in-situ state. The value of k_0 corresponding to this friction angle is 0.43. For $\phi' = 36^o$, it results in $k_0 = 0.41$.

Additionally, for an elastic medium (low strains), k_0 can be calculated using:

$$k_0 = \frac{\nu}{1-\nu} \tag{3-31}$$

For $\nu = 0.3$, this equation results in $k_0 = 0.43$, which is very close to $k_0 = 0.41$ obtained from Jaky equation. For the 3D analyses of this study using Fraser sand properties, this option, i.e. calculating k_0 as a function of Poisson's ratio, is selected.

Power exponent (n): This parameter relates the low-strain shear modulus of the soil at reference mean effective stress, i.e. G_0 at p_0, to that at any given mean effective stress, G at p:

$$G = G_0\left(\frac{p}{p_0}\right)^n \tag{3-32}$$

A typical value of n = 0.5 is recommended for cohesionless soils when no further information (laboratory tests) is available (Richart et al., 1970). Chillarige et al. (1997b) have used the same value for their evaluation of in-situ state of Fraser River sand.

Low-strain shear modulus (G_0): This parameter is estimated by using different relationships corresponding to different strain levels, as follows. Hereafter, two different symbols are used for shear modulus: at *very* low strains (10^{-6} to 10^{-4}) it is denoted by G_{max} as the maximum shear strain which is usually estimated by resonant column test or in-situ shear-wave speed measurements, and at low strains (0.05 – 0.1%) it is denoted by G_0. The latter strain level, i.e. 0.05%, can be taken as a low strain corresponding to the assumed elastic range of soil behaviour within the first yield surface as modeled by the multi-yield surface model (corresponding to line segment OA in Figure 3-2).

The maximum shear modulus, G_{max}, can be estimated by the following equations using void ratio, e, (for very low strains smaller than 10^{-4} based on resonant column test results, Richart et al., 1970):

$$G_{\max} = \frac{2630(2.17-e)^2}{1+e}\sigma_m^{1/2} \tag{3-33}$$

for round-grained sands, and

$$G_{\max} = \frac{1230(2.97-e)^2}{1+e}\sigma_m^{1/2} \tag{3-34}$$

for angular-grained sands.

In the above equations, σ_m is the average effective confining pressure in psi.

Setting the reference effective mean stress, p_0, to 100 kPa or σ_m to 14.5 psi, and using the above equations with e = 0.82, results in G_{max} = 69 and 82 MPa for round- and angular-grained sands, respectively. According to Vaid et al. (2001), Fraser River sand grains are angular to sub-rounded. A value of G_{max} = 75 MPa can be assumed to correspond to sub-rounded sand.

Also, the following equation proposed by Belloti et al. (1986) for very low strains (i.e. 10^{-4}) results in G_{max} = 70 MPa, with D_r = 0.4 and p_a = 100 kPa:

$$G_{\max} = 400 p_a . \exp\{1.39 D_r\}\left(\frac{p'}{p_a}\right)^{0.43} \tag{3-35}$$

According to shear modulus degradation curves given by Ishibashi and Zhang (1993), the shear modulus at 0.05 – 0.1% strains is about 50 – 60% of that at 0.01% strain. Therefore, using the above-calculated values of G_{max} = 70 – 75 MPa, it can be inferred that G_0 ranges from 35 to 45 MPa.

According to Vaid and Eliadorani (2000), for isotropically consolidated samples of Fraser River sand at 30% relative density, the value of secant shear modulus corresponding to 0.05% shear strain (G_0) is approximately equal to 40 MPa. To extrapolate this value of G_0 to a value corresponding to D_r = 40%, one can use Equations (3-33) and (3-34) that relate maximum shear modulus to void ratio. As such, for angular-grained sand, for example, maximum shear modulus $(G_{max})_1$ and $(G_{max})_2$ corresponding to void ratios e_1 and e_2 are:

$$\frac{(G_{max})_1}{(G_{max})_2} = \frac{(2.97 - e_1)^2}{1 + e_1} \times \frac{1 + e_2}{(2.97 - e_2)^2} \tag{3-36}$$

Thus, shear modulus at D_r = 40% and 0.05% shear strain is 42 MPa.

Howie et al. (2002) have also shown that the stiffness of very loose Fraser River sand measured in triaxial compression is very dependent on the time of confinement prior to shearing and the stress ratio at which the sample is aged. For isotropically consolidated samples, E and ν (Young's modulus and Poisson's ratio) vary from 30 to 40 MPa and 0.07 to 0.13, respectively, depending on the time of confinement. These values correspond to 0.1% axial strain and are for a confining pressure of 100 kPa. Using the relationship between G, E and ν:

$$G = \frac{E}{2(1 + \nu)} \tag{3-37}$$

it can be found that G varies from 14 to 18 MPa (for very loose Fraser River sand). In addition, they state that the value of G_0 at 0.02% strain varies from 23 to 32 MPa, depending upon the time of confinement. It should be noted that the only information about the density of the samples used is that they are "very loose" and no quantitative information is available. If it is assumed that the very loose sand used in this study, has a

void ratio, e = 0.9, Equation (3-37) indicates that G_0 varies from 16 to 20 MPa, for 0.05% strain, and from 26 to 36 MPa for 0.02% strain (at confining pressure of 100 kPa).

Overall, more investigation is needed for a more reasonable estimation of this parameter as presented in Section 3.6.2; however, to proceed with the three-dimensional analyses of this research, G_0 = 40 MPa (at reference effective mean stress or confining pressure, p_0, equal to 100 kPa) is adopted that is within the range of values reported in the literature and is very close to the value given by Vaid and Eliadorani (2000) for 0.05% strain. It is also relatively close to the values used in previous studies on Nevada sand at the same relative density (Arulanandan and Scott, 1993, 1994).

Low-strain bulk modulus (B_0): The low-strain bulk modulus of soil is calculated by the following equation as a function of low-strain shear modulus and Poisson's ratio:

$$B_0 = \frac{2G_0(1+\nu)}{3(1-2\nu)} \tag{3-38}$$

Maximum deviator strain (ε_{dev}^{max}): The best way to determine this parameter is to perform a p-constant triaxial test. Unfortunately, no such test results were found for the specific soil at hand. However, the undrained tests reported by Vaid et al. (2001), Figure 3-17, indicate that the quasi-steady state (see Figure 3-19) of the loosest deposited Fraser River sand occur at axial strains (ε_a) about 1 – 3 %, depending upon initial density, confining pressure, etc. Since in an undrained triaxial test, ε_{dev} = 1.5 ε_a, the maximum deviator strain ranges from 1.5 – 4.5 %.

In addition, the maximum shear strain in compression according to the results of simple shear test provided by UBC is about 2.5% for air-pluviated and 1.5% for tapped samples.

These values are much lower than the value used in the previous studies: 8%, according to Popescu and Prevost (1993a) obtained from p-constant tests on Nevada sand (Arulmoli et al., 1992); or 7 and 4%, in compression and extension, according to Been et al. (1991) for Erksak sand (used for construction of artificial islands in the Canadian Beaufort Sea).

Therefore, similar to the low-strain shear modulus, more investigation is needed for a more reasonable estimation of this parameter, which is presented in Section 3.6.2. However, to proceed with the three-dimensional analyses of this research, finally adopted values are: maximum shear strain in compression = 5%, maximum shear strain in extension = 3%.

Permeability (k): The standard procedure for estimating permeability is to perform constant-head or falling-head permeability tests (e.g. Das, 1998). No such test results were found for the Fraser River sand in the literature. As such, the approximate value of permeability of the sand (for water) can be obtained using the well-known equation proposed by Hazen:

$$k = 10^{-2} D_{10}^2 \tag{3-39}$$

where k is in m/s and D_{10} is the soil effective size in mm. Therefore, the permeability of the soil, based on the value of D_{10} = 0.16 mm reported by Howie et al. (2002) is $2.6*10^{-4}$ m/s.

Additionally, this parameter may be evaluated using the equation proposed by Shahabi et al. (1984), to account for the effect of void ratio on permeability:

$$k = 1.2 C_u^{0.735} D_{10}^{0.89} \frac{e^3}{1+e} \tag{3-40}$$

For $n^w = 0.45$ (porosity), e = 0.82; and thus using $D_{10} = 0.16 \times 10^{-3}$ and $C_u = 1.8$, the estimated value of k is 2.3×10^{-4} m/s.

It is worth noting that the results of permeability tests posted on web in October 2003 (http://www.civil.ubc.ca/liquefaction/Index-Final.pdf), give the permeability of this sand at relative densities of 36% and 77% as 4.4×10^{-4} and 3.2×10^{-4} m/s. This indicates that the above-estimated permeability has the same order of magnitude as the measured ones and is about 55% of the corresponding value at $D_r = 40\%$, i.e. 4.3×10^{-4} m/s.

Dilation parameter (X_{pp}): The liquefaction strength data used here for calibration of the dilation parameter (X_{pp}) is obtained from the results given by Vaid et al. (2001), for Dr = 40%, and is given in Table 3-5, where, σ'_{nc} is the initial consolidation pressure, CSR is cyclic stress ratio ($\sigma_{d,cyc}$ / $2\sigma'_{nc}$) with $\sigma_{d,cyc}$ = deviator stress, and N_{Liq} is the number of cycles to liquefaction. The occurrence of initial liquefaction was considered as occurrence of 5% double amplitude axial strain, or unit excess pore pressure ratio, whichever occurred first (see also Section 3.5.1). The values of X_{pp} that correspond to each of these data points are also given in Table 3-5.

Table 3-5. Liquefaction strength data (Vaid et al., 2001) and the estimated dialtion parameter, X_{pp}.

Test No.	σ'_{nc} (kPa)	CSR	$N_{Liq.}$	X_{pp}
1	100	0.145	10	0.18
2	200	0.145	10	0.18
3	400	0.136	10	0.20

With the above soil parameters (Table 3-2, set #1, literature), the liquefaction strength curve of the sand, obtained from simulating isotropically consolidated, undrained cyclic triaxial test is as shown in Figure 3-20. A comparison of the recorded and predicted stress paths is also shown in Figure 3-23.

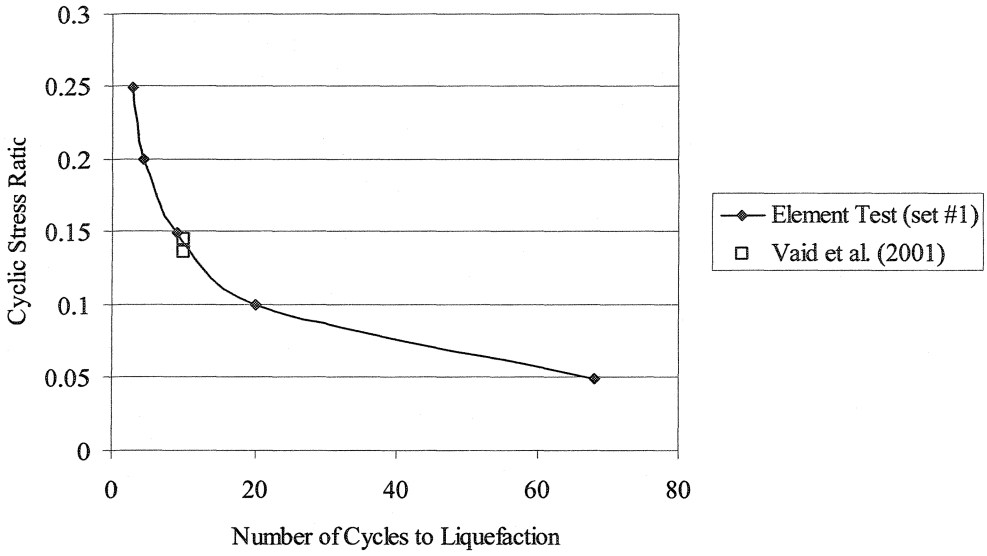

Figure 3-20. Liquefaction strength curve obtained by calibrating X_{pp} using Vaid et al. (2001) tests.

The material properties inferred from the literature (set #1) were updated using a new data set, provided by UBC, which consists of the results of three cyclic simple shear tests on Fraser Sand with $D_r = 40\%$. The liquefaction strength curve resulted from these tests is shown in Figure 3-21. The data points obtained with the new set of numerically calibrated parameters (set #2) are shown in Figure 3-21. Figure 3-24 shows the comparison between the recorded and predicted stress paths for one of the simple shear tests used in this calibration. For the purpose of parameter calibration, the RSM approach is applied for efficiently finding a set of soil parameters that best fit the experimental liquefaction strength curve obtained from the UBC tests. This procedure is explained in Section 3.6.2. Also shown on the graph are the data points used for calibrating X_{pp} according to cyclic triaxial tests reported by Vaid et al. (2001), and the resulted liquefaction strength curve as obtained from element tests (solid circle).

Vaid and Sivathayalan (1996) recommend a correction factor (C_r) as the ratio of cyclic resistance of Fraser Delta sand under simple shear (τ_{cyc}/σ'_{vc}) and triaxial ($\sigma_{dcyc}/2\sigma'_{3c}$) stress conditions (Figure 3-22):

$$(\tau_{cyc}/\sigma'_{vc})_{\text{simple shear}} = C_r.(\sigma_{dcy}/2\sigma'_{3c})_{triaxial} \qquad (3\text{-}41)$$

where, τ_{cyc} = cyclic shear stress, σ'_{vc} = initial effective vertical stress (simple shear), σ_{dcyc} = cyclic deviator stress, and σ'_{3c} = initial effective all-round pressure (triaxial).

For Dr = 40% this factor is C_r = 0.78. D_r = 40% is the only relative density for which C_r does not depend on initial confining pressure (σ'_{vc} or σ'_{3c}). The above-mentioned data points corrected by this factor are also shown in Figure 3-21.

Castro (1975) gives the following relation between the in-situ (during earthquake) and triaxial stress conditions, based on comparing the octahedral stresses:

$$(\tau_e/\sigma'_{vc})_{\text{in-situ}} = \alpha_C.(\sigma_{dcy}/2\sigma'_{3c})_{triaxial} \qquad (3\text{-}42)$$

with $\alpha_C = \dfrac{2(1+2k_0)}{3\sqrt{3}}$

where, τ_e = shear stress applied during earthquake, and k_0 = coefficient of at-rest earth pressure.

Such an in-situ stress condition during earthquake is assumed identical to simple shear test stress conditions. With k_0 = 0.3, 0.4 and 0.5, α_c = 0.62, 0.69, and 0.77. Thus, Castro recommends that α_c = 0.7 can be used for most sand deposits. According to Vaid and Sivathayalan (1996), a value of 0.6 is commonly adopted for the ratio (α_c or C_r) after Seed and Peacock (1971); however, since Vaid and Sivathayalan (1996) C_r is based on

the tests carried out on the Fraser sand, it is deemed more accurate for the present parameter calibration.

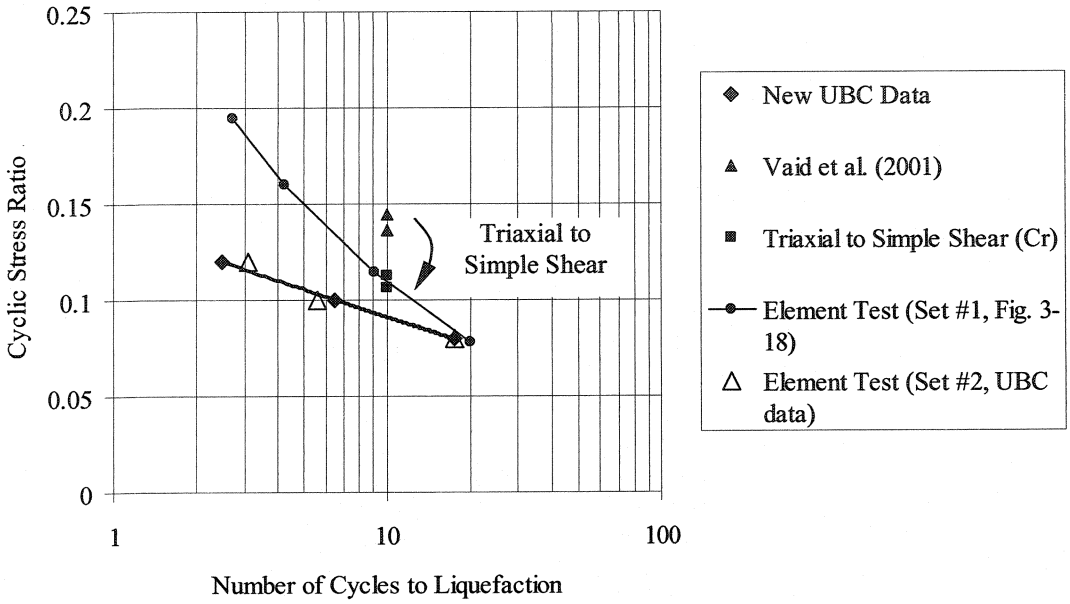

Figure 3-21. Liquefaction strength curve for Fraser River sand: laboratory and simulation results.

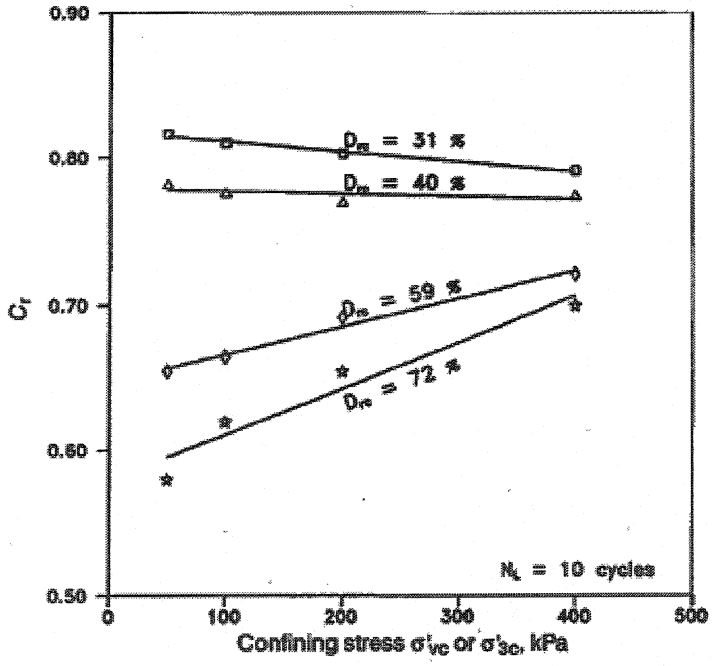

Figure 3-22. The ratio of cyclic resistance under simple shear and triaxial stress conditions (Vaid and Sivathayalan, 1996).

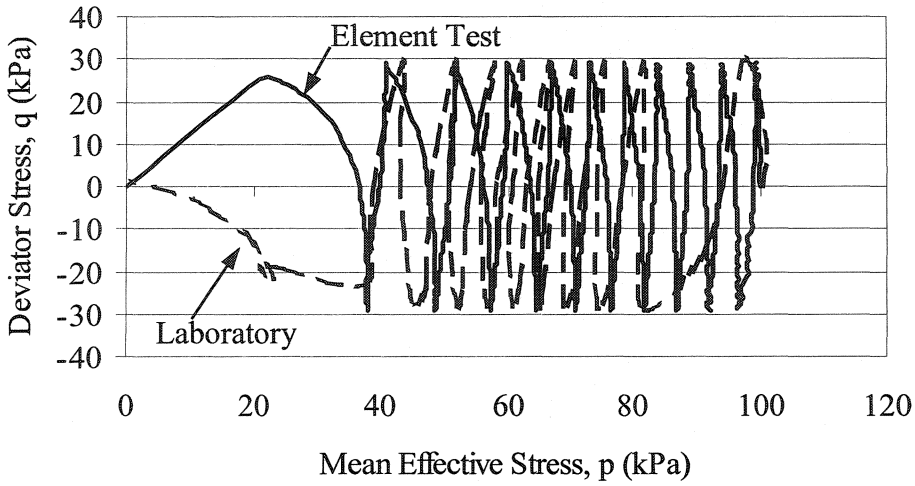

Figure 3-23. Comparison between stress paths recorded in laboratory (Vaid et al., 2001) and predicted by element test for isotropically consolidated, cyclic triaxial test with CSR = 0.145, on Fraser River sand at Dr = 40%.

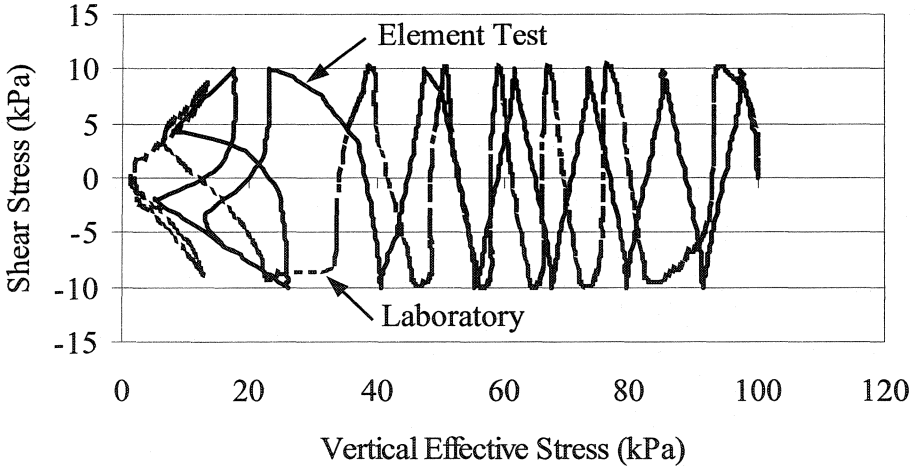

Figure 3-24. Comparison between stress paths recorded in simple shear laboratory test with CSR = 0.10 (provided by UBC) and predicted by element test for Fraser River sand at Dr = 40%.

3.6.2 Procedure for Parameter Calibration

As noted before, after obtaining the results of simple shear tests performed at UBC, some of the soil parameters, which were inferred from the literature, were updated so that they match better with the new measurements. Both set of parameters and their corresponding values are given in Table 3-2. Response Surface Methodology (RSM) is

used for this calibration. In this calibration, in addition to X_{pp}, which is always estimated from liquefaction strength analysis (simulation by element tests), some other parameters (such as low-strain shear modulus) are to be calibrated by following the same approach.

Four parameters, namely, low-strain shear modulus (G_0), Poisson's ratio (ν), dilation parameter (X_{pp}), and the maximum deviator strains in compression and extension ($\varepsilon_c/\varepsilon_t$) are calibrated in this section. This is done based on the position and slope of the liquefaction strength curve in a semi-log plot as shown in Figure 3-21. The obtained set of parameters may not be unique, however, the value are reasonably within the ranges inferred from the literature, as explained earlier.

As the first step of parameter calibration, a nine-factor, ¼-fraction, factorial design of experiment is set up to generally evaluate the relative significance of different soil parameters in terms of their influence on liquefaction resistance of the sand. The ranges selected for these parameters (factors) are based on the literature, and are somewhat wider to give more information about the effects. The response is the number of cycles to liquefaction.

The factors sorted by their relative significance are given in Table 3-6 (shown also in Figure 3-25). In addition to the soil properties given in Table 3-6, the cyclic stress ratio (CSR) is selected as a factor (a loading factor separate from material properties), which affects the response. In this case, CSR ranges from 0.05 to 0.25. It is mentioned here that CSR resulted among the significant factors affecting the number of cycles to liquefaction (N_{Liq}). However, CSR is not a soil property, but rather it reflects laboratory tests conditions, and therefore it is not a factor affecting liquefaction strength. Therefore, this is not shown in Table 3-6 and Figure 3-25.

No interaction effect turned out to be significant. Signs of the effects of significant factors are also given in Table 3-6. Negative sign indicates that with increase in the factor, the response decreases. For example, for the ranges of soil parameters considered in this study, with the increase in shear modulus the number of cycles to liquefaction decreases.

Table 3-6. Significance of soil parameters influencing liquefaction strength.

Factor	Symbol	Range	Significance (Main Effect)	Effect Sign
Dilation parameter	X_{pp}	0.05 – 0.35	Significant	Negative
Poisson's Ratio	ν	0.2 – 0.4	Significant	Negative
Shear modulus (MPa)	G_0	10 – 70	Significant	Negative
Friction angle (°)	ϕ	28 – 42	Significant	Positive
Difference between max. dev. strains in comp. and ext. (%)	$\varepsilon_c - \varepsilon_t$	0 – 2	Non-sig.	Positive
Maximum deviator strain in comp. (%)	ε_c	3 – 7	Non-sig.	Negative
Difference between friction and dilation angles (°)	$\phi - \psi$	0.5 – 3.5	Non-sig.	Positive
Power exponent	n	0.3 – 0.7	Non-sig.	Positive

Based on the results obtained from the nine-factor analysis, a five-factor, full factorial design is set up to calibrate the soil parameters which will reproduce the same liquefaction strength curve given by the UBC cyclic simple shear tests (Figure 3-21). The soil properties and their selected ranges are: G_0 (10 – 50 MPa), ν (0.25 – 0.35), X_{pp} (0.1 – 0.2), and $\varepsilon_c/\varepsilon_t$ (5/3 – 8/7%). Other parameters are set constant with values given in Table 3-2, which were estimated based on the information in the literature. In this case, the loading factor (CSR) varies from 0.08 to 0.12. It was found that the curvature of the response surface is significant, thus additional centre points are also analyzed, and a second-order polynomial regression model is obtained:

$$Log_{10}(N_{Liq}) = 11.460 - 23.771\ CSR + 6.922E\text{-}03\ G_0 - 47.631\ \nu - 3.054\ X_{pp} - 11.753\ \varepsilon_c + 2.848E\text{-}04\ G_0^2 + 67.073\ \nu^2 - 0.116\ CSR.G_0 + 51.729\ CSR.\nu - 0.089\ G_0.\nu + 0.245\ G_0.\varepsilon_c \quad (3\text{-}43)$$

The adjusted and predicted R-squared values are 0.96 and 0.94, respectively, indicating a very strong goodness-of-fit. Since this long equation is only applicable to the particular range of parameters used here, and represents only the simple shear test simulation by Dynaflow (with the multi-yield model), it should not be used for other purposes. The model is then used to fit the liquefaction strength curve, which is much easier and faster than replicating Dynaflow runs. An efficient way is to use MS Excel Solver to minimize the sum of square of residuals with changing three or four factors. This procedure resulted in G_0 = 44.4, ν = 0.33, X_{pp} = 0.32, $\varepsilon_c/\varepsilon_t$ = 8/7%. However, because of the slight difference between the regression model predictions and the actual results of Dynaflow simulation, the exact values of the parameters that result in the best-fit curve are finally calibrated by a few more element test trials. The final values of parameters are G_0 = 47.0 MPa, ν = 0.30, X_{pp} = 0.30, $\varepsilon_c/\varepsilon_t$ = 8/7%.

a)

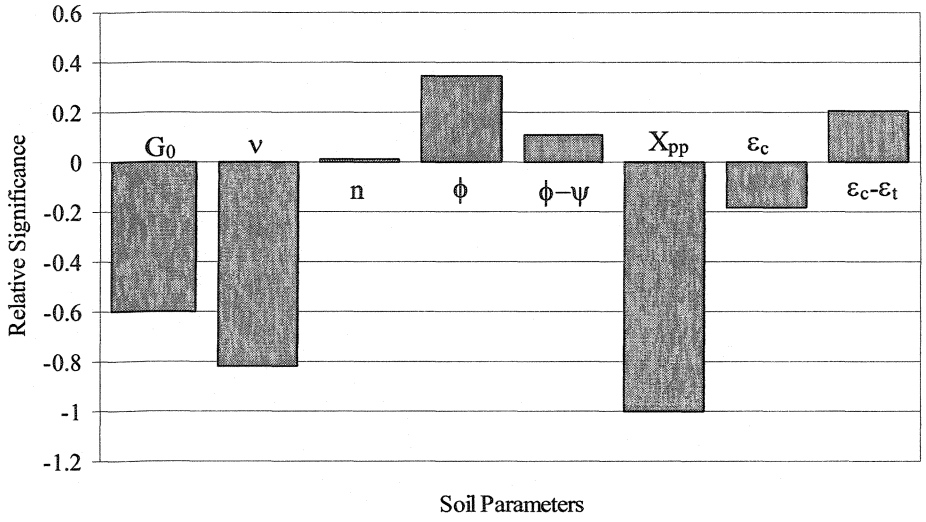

b)

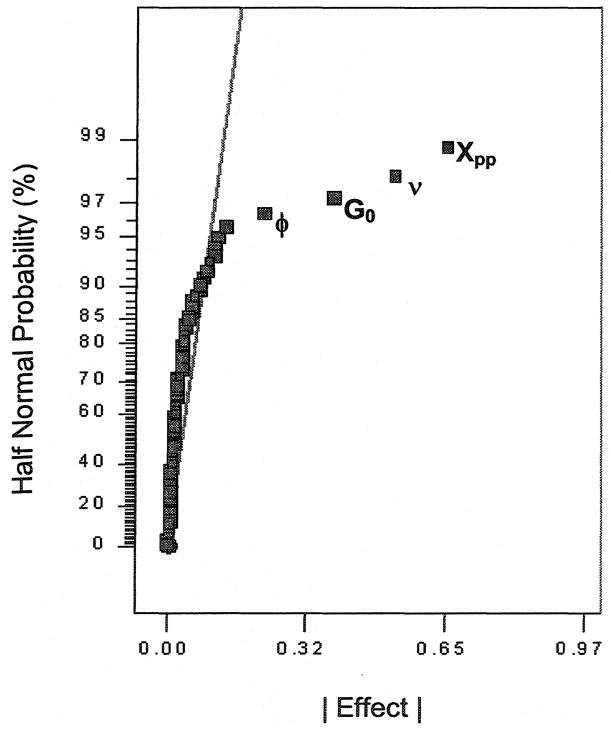

Figure 3-25. Relative significance of soil properties, influencing the number of cycles to liquefaction: a) normalized effects, b) Normal probability plot method.

Chapter 4 - RETROGRESSIVE FAILURES

4.1 Introduction

One of the key features of submarine landslides, especially those involving very huge scars and considerable travel distances of debris or mudflows, is a retrogressive pattern (Mulder and Cochonat, 1996). Retrogressive failures have had different impacts on offshore and coastal facilities. Such a mechanism can contribute to some unique characteristics of submarine slides, such as huge volumes of mass movement, very long displacement of slide blocks, and development of the slide on nearly flat surfaces (Hampton et al., 1996).

A first objective of this study is to introduce a method for simulating seismically induced retrogressive slope failures, using non-linear, dynamic finite element analysis, and to explain the basic mechanisms of such phenomena including the initial slope failure during or immediately after the earthquake, and subsequent failures of a flat seafloor. A second objective is to use the method for investigating the effects of a silt layer and of a gently sloping seafloor on the extension of retrogression in a sand deposit.

The analyses reported here, address only the seismic triggering mechanism of retrogressive failures. The importance of accounting for retrogression effect is illustrated for four cases with different soil profiles and seafloor slope conditions. The effects of mesh size are also investigated for one of those cases. It is shown that, for the type of finite element analysis performed in this study, the extent of failure, when the phenomenon of retrogression is simulated by removal of failed soil material, is much greater than that when no removal is performed. Such an analysis can provide a better

estimate of stability of a region, since ignoring the possibility of retrogression phenomenon may result in non-conservative predictions.

With reference to the classification of successive submarine slides given by Mulder and Cochonat (1996) and presented in Figure 2-4, retrogressive failures of type (a), i.e. successive overlapped, are simulated here.

4.2 Finite Element Model

4.2.1 Finite Element Mesh

Two-dimensional, plane strain finite element analyses are performed using the typical finite element mesh shown in Figure 4-1a, in which the 1:3 (V:H) front slope is followed by a flat or nearly flat seafloor. Hereafter, the term "slope" will be used for the 1:3 front slope, and "seafloor" will be used for the flat (or nearly flat) area situated to the left of the "slope". In all cases reported here, the "seafloor" is either flat ($\beta=0^o$) or gently sloped ($\beta=2^o$), and the "slope" is the same in all cases. The lateral boundaries are located 240 m and 90 m to the left and right of the slope crest and toe, respectively.

The selection of the slope angle (1V:3H) is according to the geometry of the slope to be analyzed by centrifuge experiments as part of the COSTA-Canada project (see COSTA-Canada, 2000). In this study, the purpose is to predict the extension of failure beyond the limits of the centrifuge box. Nonetheless, the geometry also resembles to some extent some field situations, e.g. the scarp left by the gigantic Storgga slide (see e.g. Kvalstad et al, 2002, Section 2.2.4).

To study the effect of mesh size, a finer mesh (Figure 4-1b) is also used, which is about 2.5 times finer (by length) than the mesh in Figure 4-1a. Hereafter, these two meshes will be referred to as the "standard" and the "fine" mesh.

The soil is discretized into four-node bilinear, quadrilateral finite elements with four degrees of freedom per node, corresponding to vertical and horizontal components of solid and fluid displacements. The standard and the fine meshes have 544 elements and 1275 elements, respectively.

a) Standard mesh

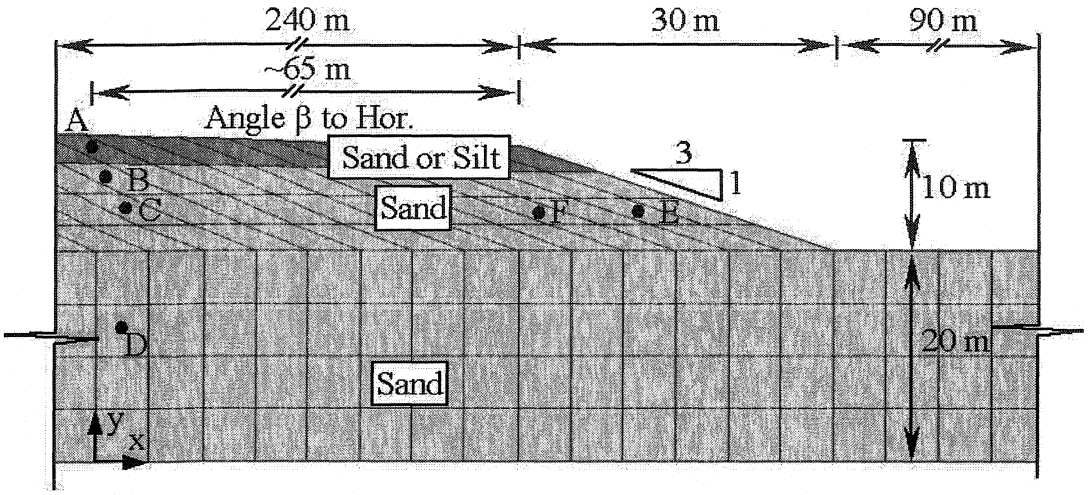

b) Fine mesh

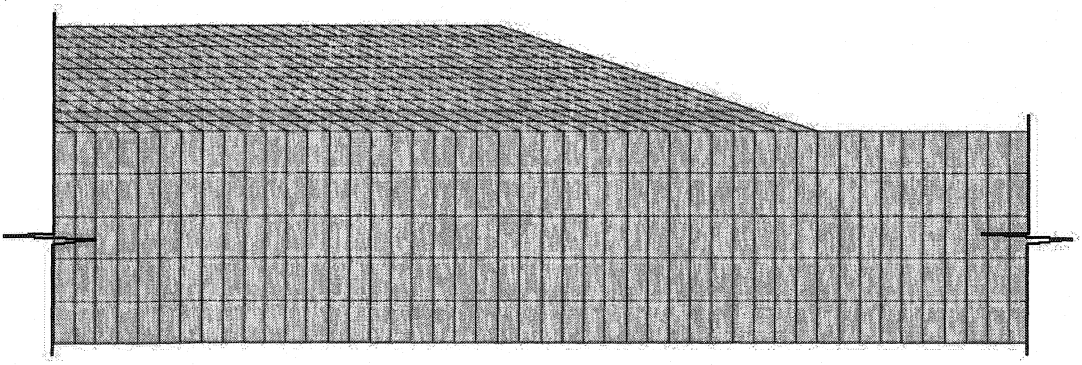

Figure 4-1. General form of the finite element meshes used in this study: a) standard, and b) fine mesh.

4.2.2 Material Properties

As shown in Figure 4-1, two types of soil are used in this study: loose sand, and silt. The soil properties, given in Table 4-1, are mainly based on the values calibrated using the results of VELACS laboratory soil tests for Nevada Sand at relative density $D_r = 40\%$

and Bonnie Silt. The predicted stress path based on the soil properties used here is shown in Figure 4-2.

A purely contractive behaviour is considered for both soils, i.e. the values of friction angle at failure and phase transformation angle are assumed equal. Such a purely contractive behaviour can be observed in very loose sands prepared in laboratory by moist tamping technique only where the friction angle at failure and the phase transformation angle are about the same. This type of material has been purposely selected in this study for illustrating the proposed method based on the evidence from the reported cases of retrogression in very loose sand (see Section 2.2.4).

Table 4-1. Soil properties used in simulation of retrogressive failures.

Soil Property	Sand	Silt
Mass density of solid (kg/m^3)	2670.0	2670.0
Porosity	0.424	0.44
Low-strain shear modulus (MPa)	25.0	7.5
Low-strain bulk modulus (MPa)	54.2	35.0
Reference mean effective normal stress (kPa)	100.0	40.0
Power exponent	0.7	1.0
Fluid bulk modulus (MPa)	2000.0	2000.0
Friction angle at failure	31.0	28.0
Cohesion (kPa)	0.0	0.0
Maximum deviator strain in comp/ext (%)	8.0/7.0	8.0/8.0
Dilation angle	31.0	28.0
Dilation parameter Xpp	0.1	0.04
Coefficient of earth pressure at rest	0.6	0.6
Permeability (m/s)	$2.1*10^{-4}$	$1.0*10^{-8}$

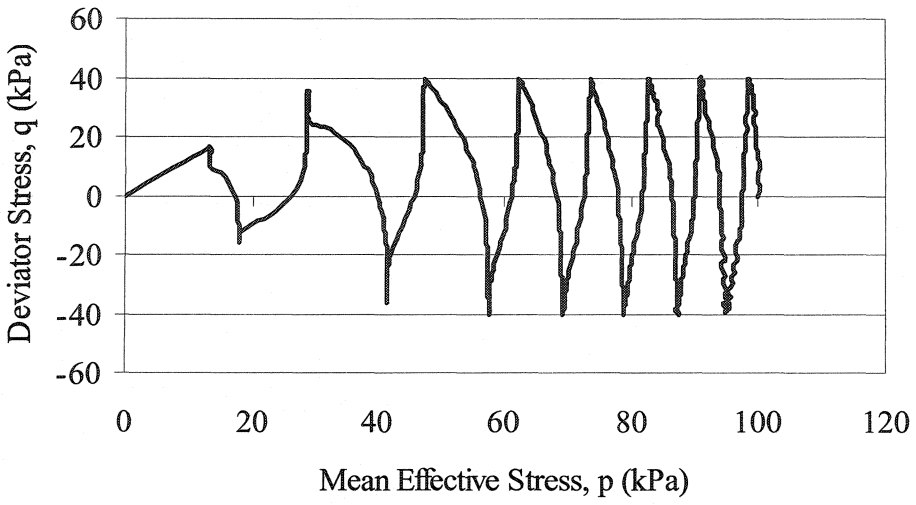

Figure 4-2. Stress path predicted by element test for cyclic triaxial test using the sand properties listed in Table 4-1.

4.2.3 Boundary Conditions and Earthquake Loading

The earthquake motion is applied at the base and at the two lateral boundaries of the analysis domain that are assumed rigid and are placed at a large distance from the slope. Specifically, boundary conditions at the base simulate the presence of a rigid, impervious bedrock, as follows: a) for the solid phase: prescribed horizontal acceleration, and fixed in vertical direction, b) for the fluid phase: free in horizontal direction and fixed in vertical direction. The boundary conditions at the lateral boundaries of the mesh are prescribed horizontal acceleration, and free vertical displacement for both solid and fluid phases. The earthquake motion is an acceleration time history generated according to the response spectrum for the soil type 3 (soft to medium clays and sands) recommended by the Uniform Building Code (1994). The peak ground acceleration is scaled to 0.30g and the duration of the strong motion is approximately 15 seconds (Figure 4-3). The analysis time is extended to 300 – 400 seconds to capture the end of retrogression. The time

increment selected for the analysis is equal to: 1) 0.01 during the application of earthquake motion (the first 15 sec.), and 2) 0.1 after the end of earthquake until the end of the analysis time.

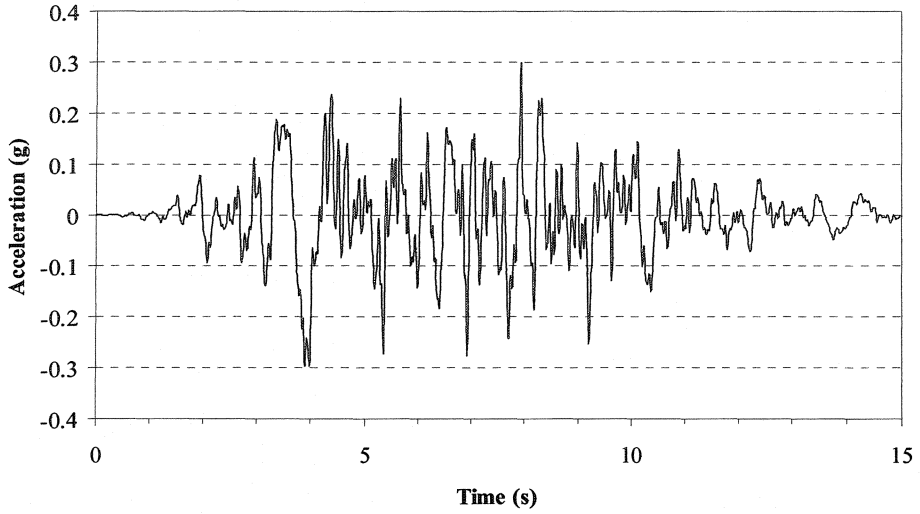

Figure 4-3. Acceleration time history with 0.3g peak ground acceleration.

4.3 Analysis Procedure

The main idea of the procedure is to remove one (or more) group(s) of elements at certain time instant(s), to simulate volumes of soil that fail and flow away, for example as parts of a debris flow. This is based on an important feature of submarine retrogressive failures, as described in Section 2.2.4, according to the studies by Kvalstad et al. (2002), De Blasio at al. (2003) and Issler et al. (2003), where very long run-out distances and separation of the out-runner block is inferred from the today's debris deposition. This also the basis for neglecting any surcharge or constraint effect imposed by debris accumulation.

The analysis procedure is iterative because the decision on element removal cannot be made interactively during the analysis. Based on the results predicted in the first analysis and the selected criterion of removing elements, the analysis is repeated from the very

first step, but one (or more) group(s) of elements is (are) set to be removed at certain time instant(s). This procedure is repeated several times until there is no zone that satisfies the criterion of element removal. In the beginning of each such analysis, the soil is allowed to consolidate and the seismic acceleration is then applied at the boundaries of the analysis domain.

The criterion for removal (or deactivation) of elements is selected based on the predicted maximum shear strain (γ_{max}), and slope failure is arbitrarily assumed for $\gamma_{max} >$ 100%. It is very important to note that without removal of elements, the extension of failure is very limited; however, after the removal of failed element groups, continuing failure can be predicted. This also contributed to the decision on the time instants at which element removal is performed. In all analyses performed in this study, there exists a certain time instant after which no significant increase in shear strains is predicted, i.e. the slope stabilizes to some extent. However, after removal, due to the loss of support and already developed EPWP, failure extends to a farther distance. The above steps are repeated until no further failure occurs (the criterion for element removal is no longer met).

4.4 Analysis Results

Four different situations are analyzed to explain the mechanism of retrogressive failure and to illustrate the effects of a top silt layer and of a very gentle slope angle on the extension of a retrogressive failure (Table 4-2). The silt layer has considerably smaller permeability than the sand and acts as a barrier layer for EPWP dissipation. The effects of mesh size on the computational results are assessed for one of those cases.

Table 4-2. Cases analyzed in this study and predicted lengths of retrogression.

Case	Soil materials	General slope of the seafloor	Mesh size	Predicted length of retrogression (m)
1	Uniform loose sand	Flat (β=0)	Standard	53
			Fine	55
2	Sand overlain by silt layer	Flat (β=0)	Standard	213
3	Uniform loose sand	Gently sloping ($\beta=2^0$)	Standard	160 and 300 (1)
4	Sand overlain by silt layer	Gently sloping ($\beta=2^0$)	Standard	To the boundary

(1) These distances depend on the location of the left lateral boundary. These values correspond to 240 and 400 m distance between the left lateral boundary and the crest of the slope.

4.4.1 Case 1: Uniform Sand, Flat Seafloor (β = 0°)

Three stages of retrogression are predicted in this analysis. Three groups of elements are removed at three different time instants, which are t = 15 s (roughly at the end of the earthquake), t = 115 and 165s. The time instants are selected based on the removal criterion described previously. Figure 4-4 shows contours of predicted maximum shear strain (γ_{max}) and excess pore water pressure (EPWP) ratio with respect to initial vertical effective stress (r_u) at selected time instants. Since in this case all stages of retrogressive failure are located near the slope, only a small part of the mesh is shown.

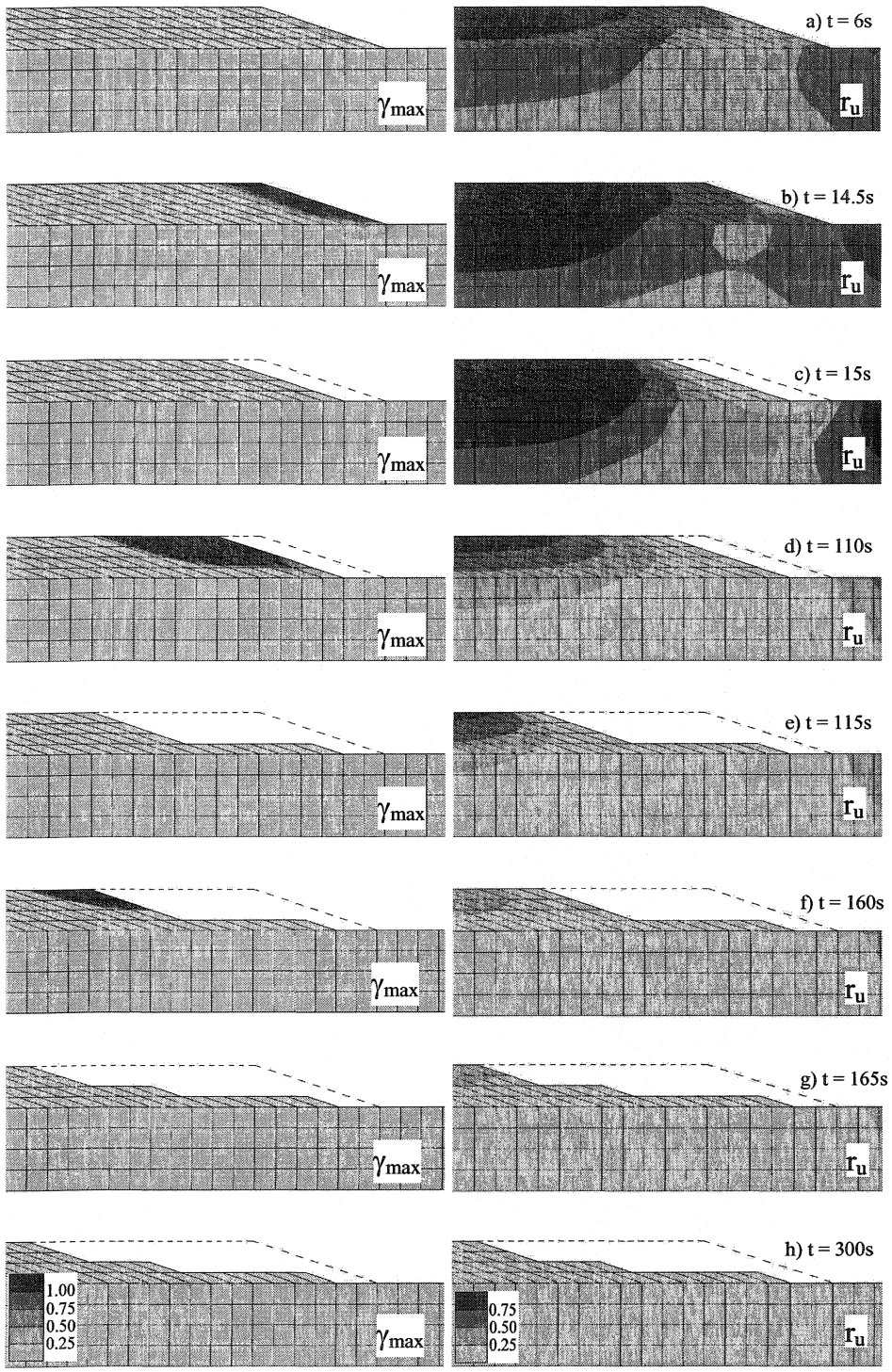

Figure 4-4. Contours of predicted maximum shear strain (γ_{max}) and excess pore pressure ratio (r_u) at selected time instants in case 1. Removal times are t = 15, 115, and 165 s.

At the beginning of the analysis, both the strains and the EPWP are zero in all elements. Gradually, EPWP increases, with maximum values in the free field near the soil surface. Owing to initial static shear stress, the numerical model predicts significantly lower EPWP immediately near the slope than in the free field, i.e. left of slope crest and right of slope toe. At t = 5 s, γ_{max} is still below 25%, however, after t = 6 s (Figure 4-4a) regions of γ_{max} > 25% start to develop from the midpoint of the slope. The general shape of the contours of γ_{max} is indicative of the location of failure surfaces encountered in classical slope stability analysis, especially those passing through the toe of the slope. Shear strains gradually increase with time near the slope (Figure 4-4b). At approximately t = 15 s, the first two columns of elements in the vicinity of the slope have undergone γ_{max} > 100%, i.e. these elements satisfy the removal criterion. It should be mentioned that if continuing the analysis with no element removal, the predicted shear strains would remain constant after the end of earthquake, and the predicted extension of slope failure would be about 10m from the slope crest.

After the first group of elements are removed at t = 15 s (Figure 4-4c), except for a very small area, there is no region with γ_{max} > 25%. Subsequently, regions of high γ_{max} start to develop gradually but with a smaller depth and greater lateral extension (Figure 4-4d) compared to those predicted in the first stage. Meanwhile, as the seismic motion has already ended, EPWP's are now dissipating as shown by the contours of r_u. Note that the marked decrease in r_u in the vicinity of slope, immediately after element removal, shown in Figure 4-4c, is only an artefact of presenting the contours of EPWP ratio with respect to the initial values of vertical effective stress. As explained later in this section, due to drop in overburden pressure after removal, the real EPWP ratio may increase in

this area. At t = 115 s, the second group of elements is removed (Figure 4-4e). After t = 115 s, regions of high γ_{max} develop with smaller depth and lateral extension (Figure 4-4f) compared to those predicted previously. This is mainly because most of the EPWP generated during strong ground motion have already dissipated. At t = 165 s, the third group of elements is removed (Figure 4-4g). By the end of the analysis period (t = 300 s), r_u < 25% over the entire analysis domain, and there are no regions with γ_{max} > 100% (Figure 4-4h). Total retrogression distance is approximately 55 m, which has occurred in three stages. The extensions of failure after the first two stages are about 10 and 40 m from the slope crest.

Some of the results predicted for elements B (free field) and E (near slope), as shown in Figure 4-1, are presented in Figure 4-5 and Figure 4-6. Element E belongs to the first group of elements removed at t = 15 s. Element B is located outside the area affected by retrogressive failure.

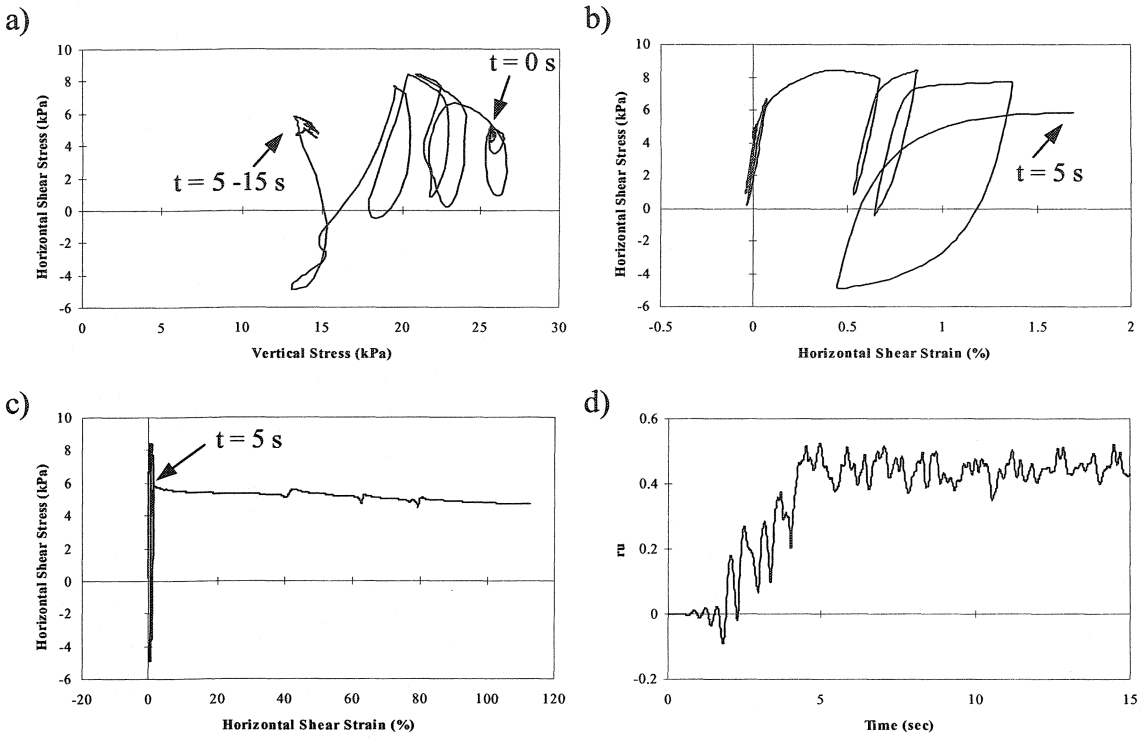

Figure 4-5. Case 1, element E (near slope): a) horizontal shear stress vs. vertical stress, b) horizontal shear stress vs. horizontal shear strain, low-strain part, c) horizontal shear stress vs. horizontal shear strain, large-strain part, d) excess pore pressure ratio.

Figure 4-5a and Figure 4-6a present predicted stress paths in terms of horizontal shear stress (τ_{xy}) vs. vertical effective stress (σ'_v). Horizontal shear stress (τ_{xy}) vs. horizontal shear strain (γ_{xy}) plots are presented in Figure 4-5b and Figure 4-6b for the small strains, and in Figure 4-5c and Figure 4-6c for the entire analysis, namely, until the removal of element E at t = 15s (Figure 4-5c), and until t = 300s for element B (Figure 4-6c). Finally, Figure 4-5d and Figure 4-6d present the evolution of EPWP ratio from the beginning to the removal of element E or end of analysis.

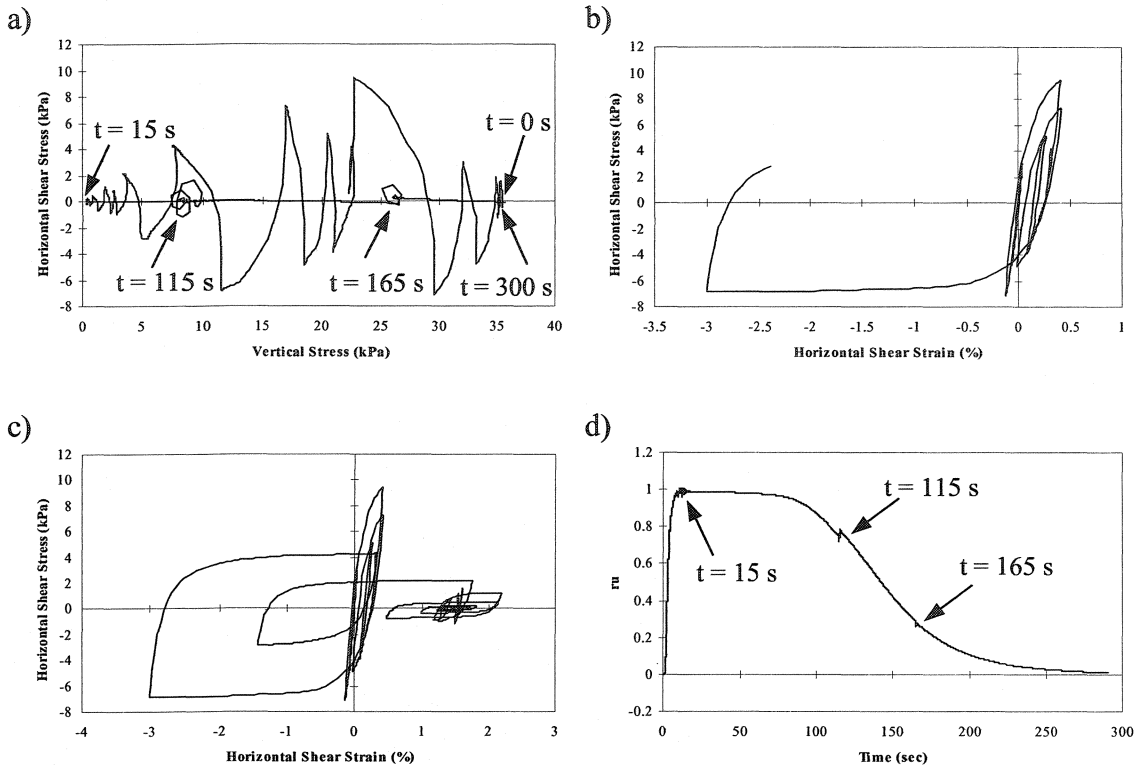

Figure 4-6. Case 1, element B (free field): a) horizontal shear stress vs. vertical stress, b) horizontal shear stress vs. horizontal shear strain, low-strain part, c) horizontal shear stress vs. horizontal shear strain, large-strain part, d) excess pore pressure ratio.

The stress path of element E (Figure 4-5a) starts at a point with some initial static shear stress and ends at a point with reduced (but non-zero) effective vertical stress, with only one significant reversal of shear stress. The final state corresponds to the maximum value of $r_u \approx 0.5$ (Figure 4-5d). However, as shown in Figure 4-5b and Figure 4-5c, this element starts failing, practically under static shear stress after $t \approx 5$ s. The behaviour of element E is characteristic for the predicted behaviour of the entire zone near the slope face: softening (reduction of shear strength) due to some EPWP build-up, accumulation of large shear strains, and eventually, failure under static shear stress. Unlike element E, there are significant shear stress reversals in the stress path of element B and it reaches the state of zero effective stress during shaking (Figure 4-6a). Due to relatively fast dissipation of EPWP (Figure 4-6d), this element regains its strength gradually with the

increase in vertical stress (Figure 4-6a) before retrogression front reaches its location. The moments of the second and third element removals (t = 115 s and 165 s) can be observed as slight perturbations in the predicted stress path and EPWP time-history of element B (Figure 4-6a and Figure 4-6d). Large shear strains do not develop due to absence of static shear stress (Figure 4-6b and Figure 4-6c). There is a slight accumulation of shear strain in element B, which at maximum reaches to a value of about 2% shear strain (Figure 4-6c) and ultimately decreases to a value of about 1.6% by the end of the analysis.

Figure 4-7 shows a comparison between the horizontal shear strength of element F (Figure 4-1) when first removal is done and that when no removal is done. Element F has been selected for this discussion, as it is located on the failure surface in the second stage of retrogression. The removal of the first group of elements at t = 15 s results in a stress redistribution, in the form of the removal of overburden pressure, decrease in vertical effective stress, and thus, decrease in shear strength, which yields to the failure of the second group of elements where element F is located. The element has already experienced some softening due to increase in EPWP (Figure 4-4). This failure mechanism resembles, to some extent, the mechanism of retrogression initiated by failures in the Fraser River Delta as explained by Chillarige et al. (1997a), and mentioned earlier in the literature review.

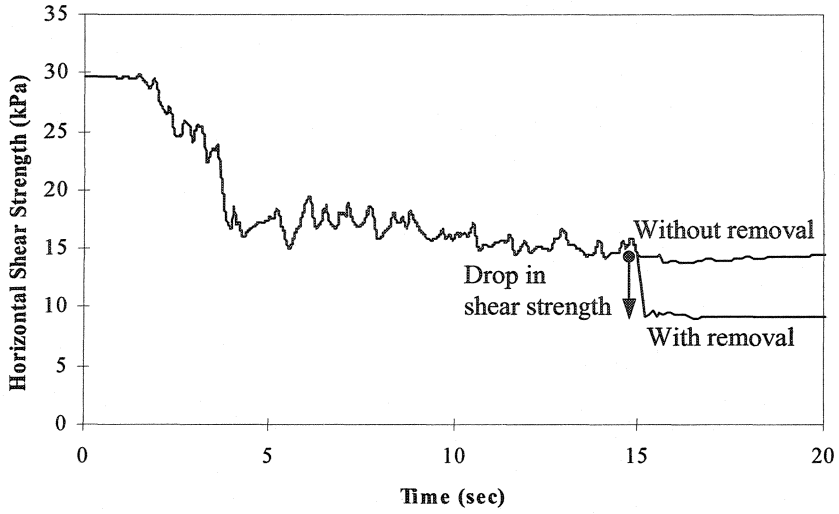

Figure 4-7. Horizontal shear strength of element F with and without removal of the first group at t = 15 s.

The changes in effective stresses and pore pressures due to element removal are calculated by the program based on the partially drained analysis. Those changes are a function of the location of each finite element in the structure. For example, the change in stresses in element B (Figure 4-1) occurring after element removals are shown in Figure 4-6a, and the changes in pore pressure in Figure 4-6d.

The results predicted by the numerical model in terms of EPWP ratio are compared next with the predictions using the simplified procedure of liquefaction analysis (Youd et al., 2001), which is now a standard of practice for evaluating the liquefaction resistance of soils. In the following, the factor of safety against liquefaction is calculated for locations B (free-field) and E (near slope), as shown in Figure 4-1. The simplified procedure is primarily developed for soils under level to gently sloping ground and in shallow depths (up to 10 – 15 m), however, for location E (near slope) the effect of static shear stresses can be incorporated by the correction factor K_α discussed later in more detail. The factor of safety against liquefaction can be calculated as:

$$F_s = \left(\frac{CRR_{7.5}}{CSR}\right) MSF.K_\sigma.K_\alpha \qquad (4\text{-}1)$$

where $CRR_{7.5}$ is cyclic resistance ratio for magnitude 7.5 earthquakes, CSR is cyclic stress ratio induced by earthquake, MSF is the magnitude scaling factor, and K_σ and K_α account for the effects of overburden pressure and static shear stress, respectively.

$CRR_{7.5}$ may in general be obtained from some correlations based on in-situ tests such as SPT, CPT or shear wave velocity. For the initial effective overburden stress at locations B and E, assuming a standard penetration resistance N_{60} = 10 blows/foot for the sand used in this study (Terzaghi et al., 1996), the normalized blow count $(N_1)_{60}$ results as 16 and 20 blows/foot, respectively, which correspond to $CRR_{7.5}$ of 0.18 and 0.23 (Youd et al., 2001).

CSR is calculated as (Seed and Idriss, 1971):

$$CSR = 0.65\frac{a_{\max}}{g}\frac{\sigma_{v0}}{\sigma'_{v0}} r_d \qquad (4\text{-}2)$$

where, $a_{\max}$ is the peak horizontal acceleration at the ground surface, g is the acceleration due to gravity, σ_{v0} and σ'_{v0} are the total and effective vertical overburden stresses at depth in question, and r_d is the stress reduction factor that provides an approximate correction for flexibility of the soil profile. For the submarine slope considered here, since the shear strength of the water above the soil can be neglected, the ratio of total to effective stress is equal to the ratio between saturated and buoyant unit weights, which for this soil is about 2. Using $a_{\max} = 0.3g$ and $r_d = 0.96$ results in $CSR = 0.37$.

Using the concept of equivalent number of uniform stress cycles at $0.65\tau_{max}$ proposed by Seed et al. (1975), the acceleration time-history has about 12.4 equivalent cycles and corresponds to an earthquake of magnitude 7.0. Therefore, using the values recommended by Youd et al. (2001), MSF is approximately equal to 1.2.

K_σ = 1 for both locations B and E because the initial vertical effective stresses are below 100 kPa. $K_\alpha = 1$ at location B (free field), and $K_\alpha = 1.6$ at location E (near slope), after Vaid et al. (2001) and corresponding to a static shear stress ratio $\alpha = \tau_{st} / \sigma'_{v0} = 0.18$, where τ_{st} is the static shear stress, and σ'_{v0} is the initial effective vertical stress.

With the above values, the factors of safety against liquefaction, F_s, predicted according to Eq. (4-1) for locations B and E are 0.58 and 1.18, respectively. Those factors, obtained based on the current state-of-practice, confirm the analysis results that predict liquefaction for location B (zero effective stress with $r_u = 1$), and no liquefaction for location E ($r_u \approx 0.5$).

4.4.2 Case 2: Sand Overlain by Silt layer, Flat Seafloor ($\beta = 0^o$)

The only difference between case 2 and case 1 is that in the top 2.5 m the sand is replaced with a silt layer with a permeability 20,000 times lower (Figure 4-1). Predicted contours of the maximum shear strain (γ_{max}) and the EPWP ratio (r_u) at selected time instants are presented in Figure 4-8. Only the central part of the analysis domain is shown in Figure 4-8. The removal of the first group of elements is performed at t = 15 s, based on the distribution of γ_{max}. This is the same time instant as for case 1 because until t = 15 s contours of $\gamma_{max} > 100\%$ and $r_u > 75\%$ in both cases 1 and 2 are observed to be more or less the same. Five stages of retrogression are predicted in this case. Removed groups of

elements are shown in Figure 4-9. The removal times are: 15, 165, 240, 340, and 390 s, respectively. The extensions of failure in each stage, measured from the slope crest, are approximately equal to 10, 180, 195, 205, and 213 m, respectively, with a total extent of retrogression about four times larger than that predicted for case 1. An explanation for the large difference in the results for cases 1 and 2 is presented hereafter.

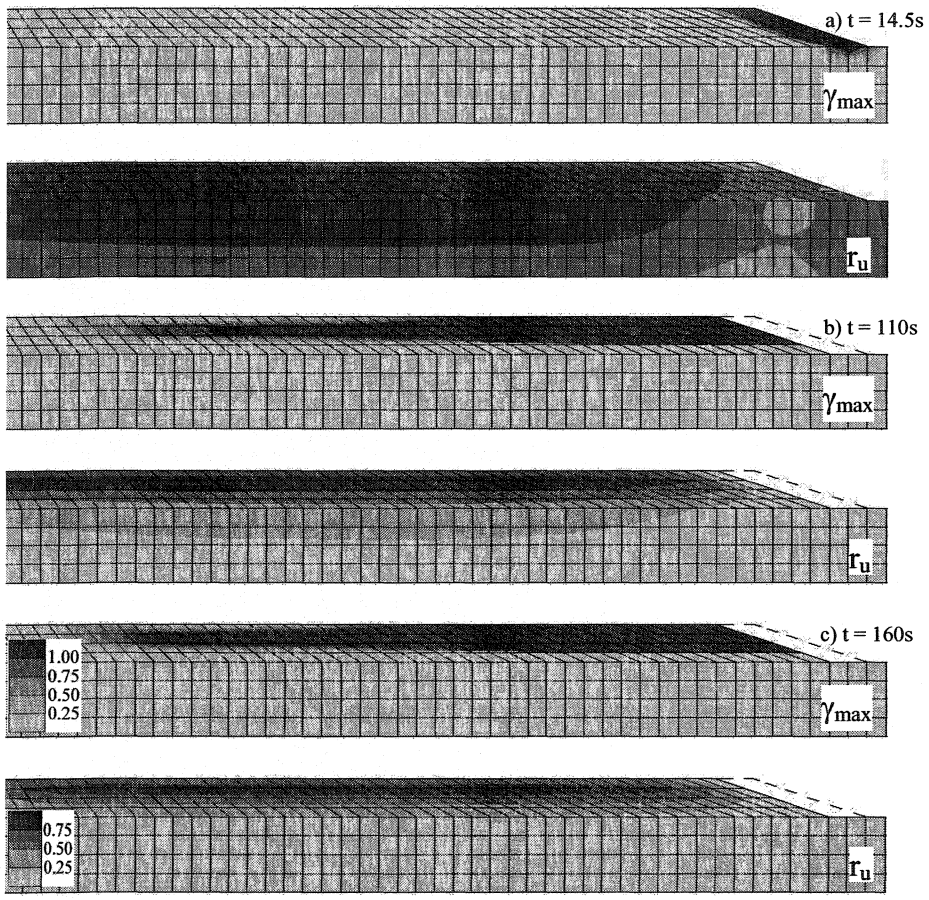

Figure 4-8. Contours of γ_{max} and r_u at selected time instants in case 2. Note that the first and second removal times are t = 15 and 165 s in this analysis.

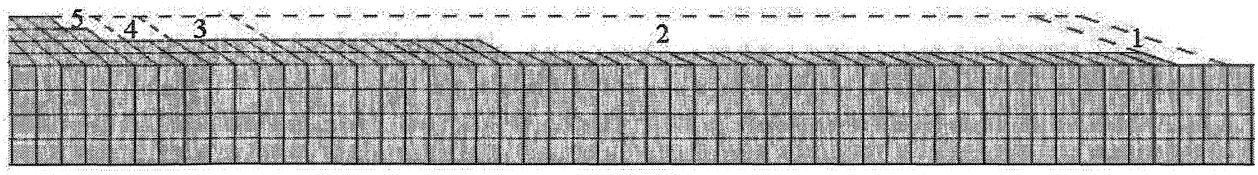

Figure 4-9. Predicted profile at the end of retrogression for case 2, showing the five stages of element removal. Removal times are t = 15, 165, 240, 340, and 390 s.

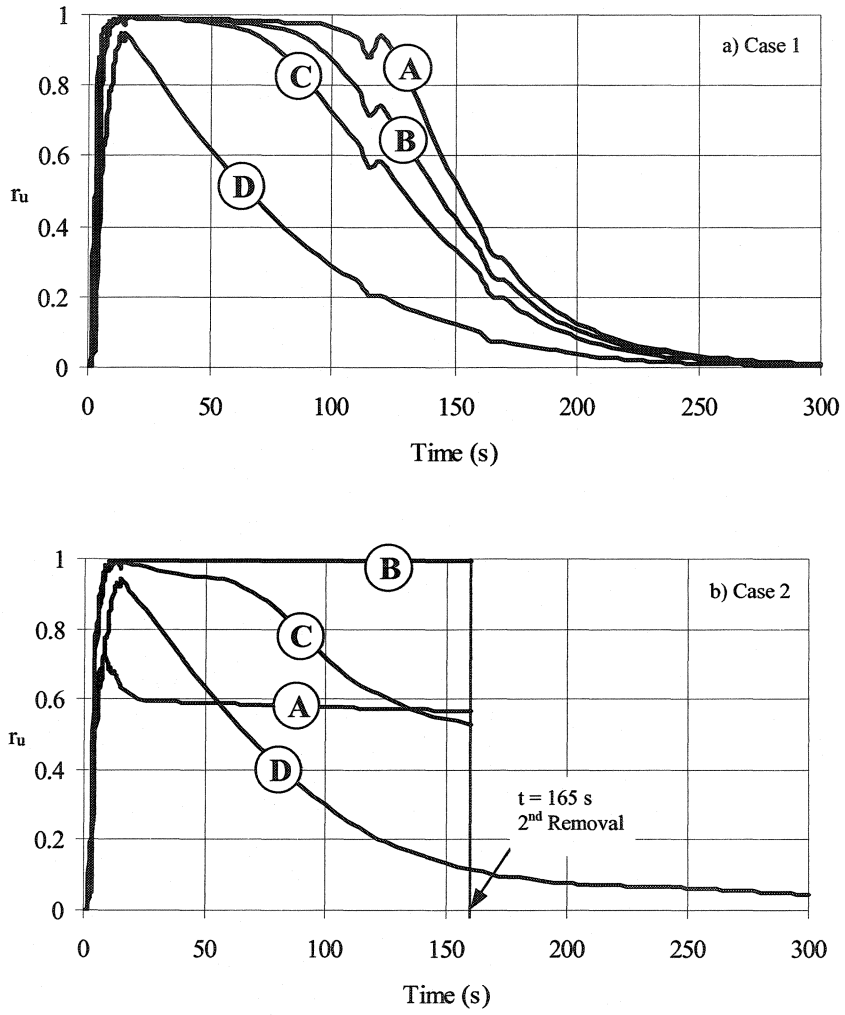

Figure 4-10. Variation of excess pore pressure ratio (r_u) with time and depth in cases 1 and 2. Locations of elements A to D are shown in Figure 4-1. In (b), elements A – C belong to the second group removed at t = 165 s in case 2.

Figure 4-10 and Figure 4-11 show the variation of the EPWP ratio with time for cases 1 and 2, in elements A to D (locations shown in Figure 4-1) for the whole analysis time and during the earthquake only. In case 1 (Figure 4-10a), the dissipation rate is much faster than in case 2 (Figure 4-10b) because vertical seepage is very much slowed down

by the presence of the silt layer. Therefore, although at t = 14.5 s (i.e. very close to the end of shaking) contours of γ_{max} > 100% and r_u > 75% in both cases 1 and 2 are more or less the same (Figure 4-8a and Figure 4-4b), at t = 110 s (before the second removal), the contour of γ_{max} > 100% predicted for case 2 extends over a much greater distance as compared to case 1 (Figure 4-8b & Figure 4-4d).

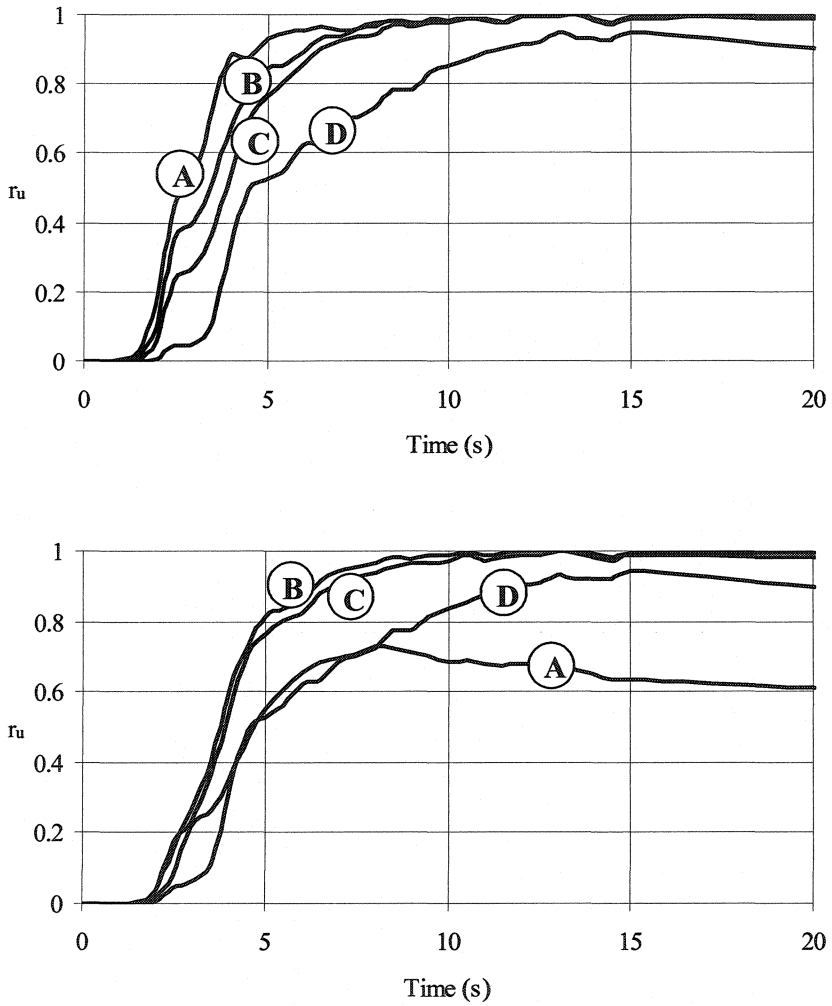

Figure 4-11. Variation of excess pore pressure ratio (r_u) with time and depth in cases 1 and 2 during the earthquake shaking. Locations of elements A to D are shown in Figure 4-1. In (b), elements A – C belong to the second group removed at t = 165 s in case 2.

Figure 4-12 shows the stress path and the shear stress-strain plots for element B (Figure 4-1) in case 2, which belongs to the second group of elements removed at t = 165

s. For element B in cases 1 and 2, the key difference in behaviours is caused by the very low rate of EPWP dissipation in case 2 (Figure 4-10), due to the presence of the less permeable top silt layer. While the stress paths of the both elements during shaking are somewhat similar (compare Figure 4-12a and Figure 4-6a), these paths are completely different after shaking. In case 2, since r_u remains equal to 1 until the removal of this element at t = 165 s (Figure 4-10b), the stress path remains close to the origin, i.e. zero vertical effective stress (Figure 4-12a). Element B undergoes very large shear strains under very small shear stress (Figure 4-12b) due to liquefaction and loss of support.

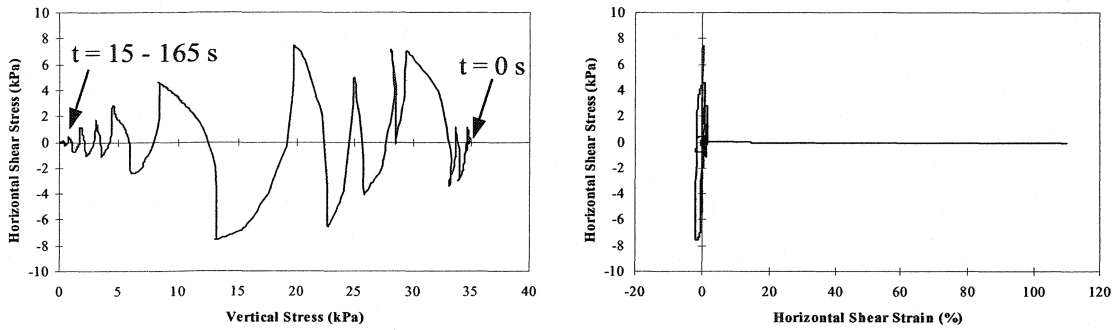

Figure 4-12. Case 2, element B (second removed group): a) horizontal shear stress vs. vertical stress, b) horizontal shear stress vs. horizontal shear strain, low-strain part, c) horizontal shear stress vs. horizontal shear strain, large-strain part, d) excess pore pressure ratio.

4.4.3 Case 3: Uniform Sand, Sloping Seafloor ($\beta = 2^o$)

In this case, the seafloor located to the left of the slope crest (Figure 4-1) is gently sloped at $\beta = 2^o$. Only contours of γ_{max} are shown in Figure 4-13 mainly because the distribution of r_u is roughly similar to that predicted in case 1 and the significant difference lies in the distribution of γ_{max}. It is predicted that a slight increase in the slope of the seafloor results in a substantial increase in the retrogression distance from approximately 40 m to 160 m (only after two stages). It was observed, however, that for this case the retrogression distance is affected by the presence of the left lateral boundary of the analysis domain. For example, in an analysis with the lateral boundary located at

400 m from the slope crest, it was observed that the predicted retrogression distance was approximately 300 m. In this case (both meshes), the second stage of failure occurred in the upper 5 – 7 m of the seafloor, similar to what was predicted in case 2. The second stage of failure is indicative of an infinite slope failure mechanism that occurs in a liquefied layer after loss of support induced by the first stage of retrogression. Thus, the failure extends to a great distance depending on the location of the rigid boundary. In nature, however, such retrogressive failure can be limited by presence of stiffer or denser soil layers or changes in seafloor morphology. Note that if no element removal is done, the numerical model will not predict slope failure beyond the first stage.

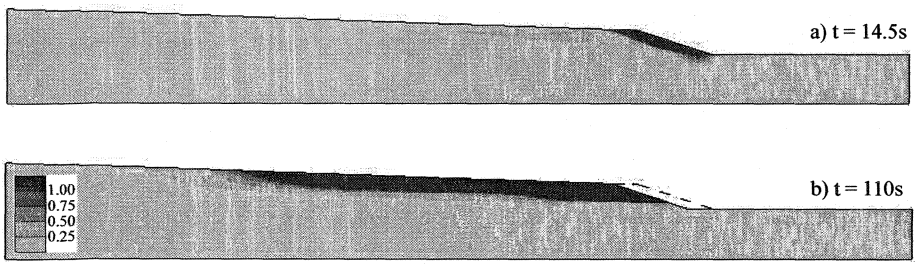

Figure 4-13. Contours of γ_{max} at selected time instants in case 3. Removal time is t = 15 s.

The occurrence of infinite slope failure can be explained based on a simple slope stability analysis as follows. The static factor of safety against sliding for an infinite slope (without seepage) is $F_s = \tan\phi / \tan\beta$, where ϕ is the soil friction angle and β is the slope angle. For $\phi = 31^\circ$ and $\beta = 2^\circ$, the factor of safety is equal to 17.2. After the end of shaking, however, due to the build-up of EPWP, which yields to reduction in effective normal stress, the factor of safety drops significantly. The new factor of safety depends on the value of EPWP ratio, r_u, according to the following equation (e.g. Zangeneh and Popescu, 2003):

$$F_s = \frac{\tan\phi}{\tan\beta}(1 - r_u) \qquad (4\text{-}3)$$

For the geometry and soil characteristics analyzed here, any value of r_u greater than 0.94 results in a value of F_s lower than one and therefore failure. The continuous line in Figure 4-14 shows the distribution of EPWP ratio with depth at the end of shaking, along a vertical line where the elements marked in Figure 4-1 by A to D are located. The depth, above which the EPWP is greater than 0.94, is between 4 and 6 m. It approximately corresponds to the depth to which the contour of γ_{max} > 100% extends (as shown in Figure 4-13b). This is the explanation for predicting an infinite slope failure on a plane parallel to the seabed.

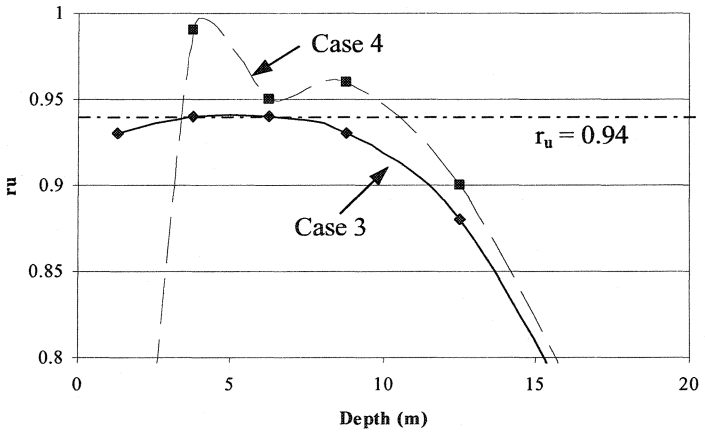

Figure 4-14. Variation of r_u with depth at the end of shaking in cases 3 and 4, and the limit value of r_u required for infinite slope failure.

4.4.4 Case 4: Sand Overlain by Silt Layer, Sloping Seafloor (β = 2°)

The most important observation from this case is that the silt layer again affects the retrogression distance significantly (Figure 4-15). The failure at t = 110 s, extends to greater depth and length (> 200 m) than what was predicted in either case 2 or 3. This is caused by larger values of EPWP that due to the presence of the silt layer cannot dissipate

upwards as they do in case 3. The dashed line in Figure 4-14 shows the distribution of EPWP ratio with depth at the end of shaking. Compared to the continuous line (case 3), r_u is higher in the sand and is greater than 0.94 to a depth of about 10 m. This results in a failure surface that is flatter than the seafloor slope of 2^0, and extends to a greater depth. Again, the predicted retrogression distance is limited by the boundary conditions as discussed for case 3.

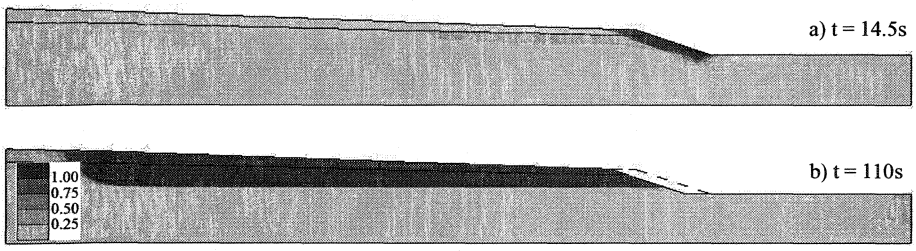

Figure 4-15. Contours of γ_{max} at selected time instants in case 4. Removal time is t = 15 s.

4.4.5 Effect of Mesh Refinement

To assess the effects of finite element mesh size on the numerical results, case 1 (uniform sand and flat seafloor) was re-analyzed using a finer mesh (Figure 4-1b). Some of the analysis results are shown in Figure 4-16 at time instants before each removal and at the end of analysis. The removal times are: 15, 90, 115, and 165 s with extensions of failure approximately equal to 10, 22, 42, 53 m, respectively. A comparison with numerical results obtained for the standard mesh shows that the final extension of failure is approximately equal in the two cases (55 m for the standard mesh vs. 53 m for the fine mesh). There are, however, small differences in the intermediate results. The numbers of retrogression stages are different, i.e. 3 vs. 4, and the shapes of the predicted final (stable) profiles (after end of retrogression) are slightly different, with deeper failure predicted

when using a finer mesh. When using the standard mesh, the depth of failed region in each stage is less than its previous stage, whereas when using the fine mesh, this reduction takes place only after the first stage. Overall, from the results of this limited study, it is deemed that mesh refinement does not affect significantly the analysis results.

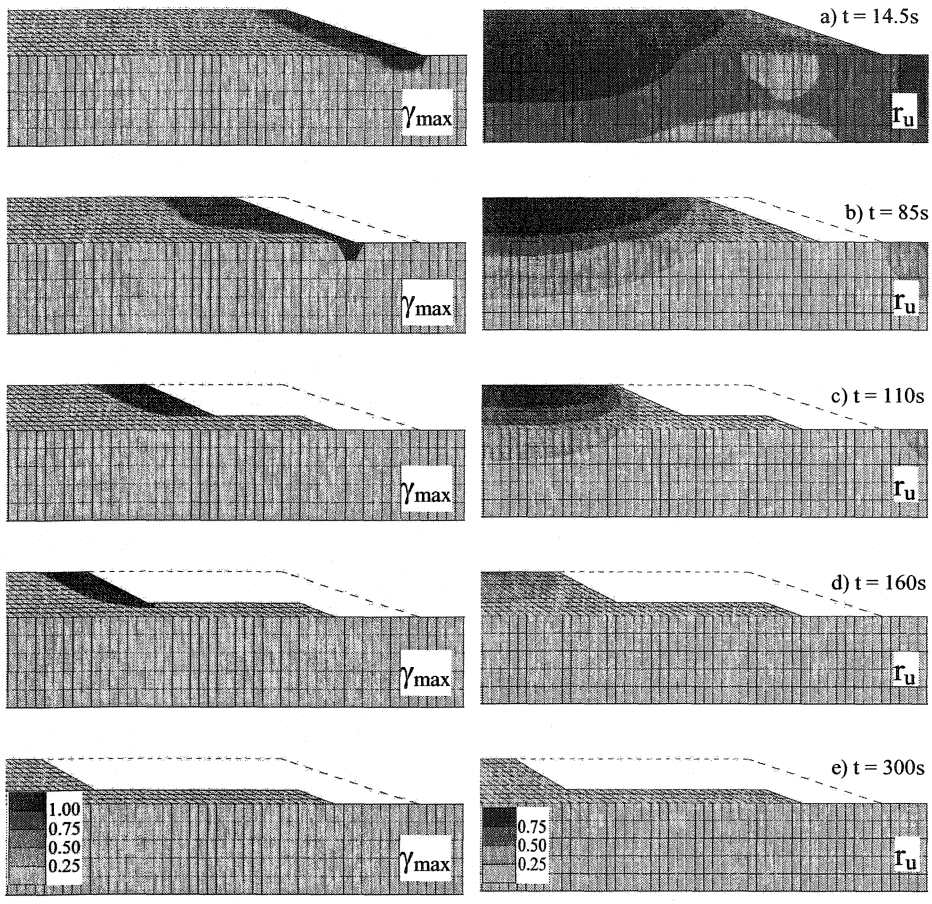

Figure 4-16. Contours of γ_{max} and r_u at selected time instants in case 5. Removal times are t = 15, 90, 115, and 165 s.

To evaluate the effect of mesh refinement on layered soil (Case 2), the variations of r_u with depth in free-field elements (approximately 65m from the slope crest, i.e. where elements A to D are shown in Figure 4-1) at three different time instants are presented in Figure 4-17. As shown, mesh refinement has little effect on the values predicted for the underlying sand material. In the silt layer, however, the difference in predicted r_u closer

to the surface seems to be larger. As r_u should be equal to 0 at the surface, it seems that both lines deviate to some extent from an ideal distribution. Because almost all stages of failure occur in the underlying sand (that is, the failure surface is located in sand) the final results, i.e. extension of retrogression, is found to be the same in both analyses.

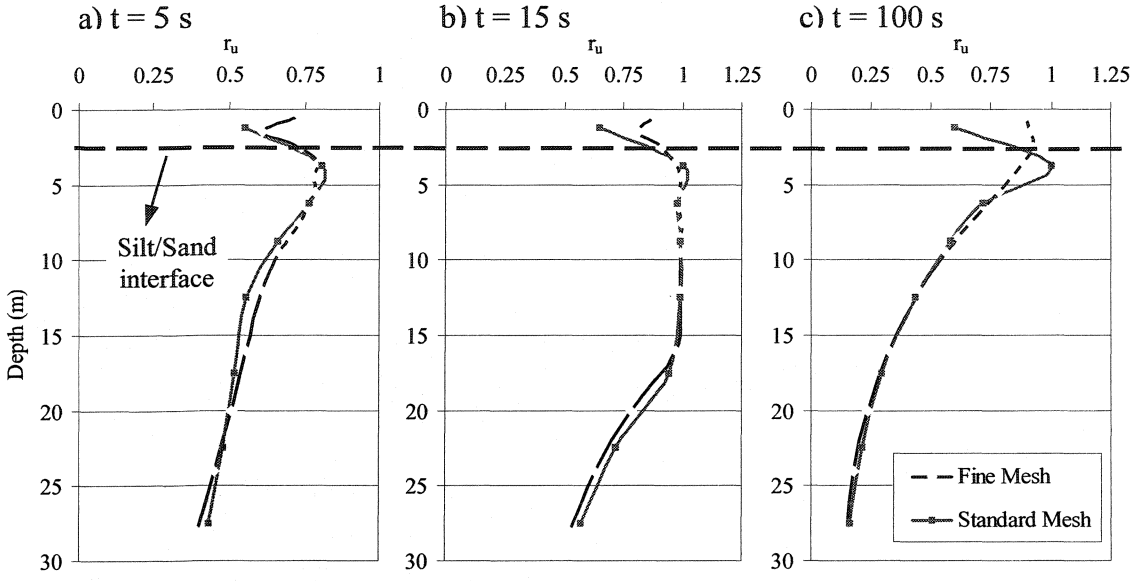

Figure 4-17. Variation of r_u with depth in free-field elements in Case 2 at: a) t = 5 s (during shaking), b) t = 15 s (end of shaking), c) t = 100 s (long after end of shaking), predicted using the fine and standard meshes.

It is shown (e.g. Fiegel and Kutter, 1992; Liu and Dobry, 1993; Kokusho, 1999) that the migration of water due to liquefaction-induced pore pressures lead o formation of a water film underneath a low permeable silt layer. The numerical model used here is not capable of modelling this water film (that can be done perhaps by using an interface element, e.g. Yoshida and Finn, 2000); however, as far as the deformations are concerned, since the program can correctly predict the liquefaction of soil elements below the silt layer, it is in fact predicting presence of a material with almost no shear resistance, be it water or liquefied soil, just below the silt layer. This can be observed

clearly from the predicted features of infinite slope failure for cases 3 and 4, especially in case 4 that the predicted failure surface is deeper and flatter.

4.5 Limitations of the study

An important limitation of the analysis results reported here is caused by the lateral boundary conditions, especially to the left of the slope. Although the boundaries are located at a distance far enough so that they do not affect the distributions of γ_{max} and r_u in the vicinity of the steeper slope, it is obvious that in cases 3 and 4, the extension of the failure is limited by the boundaries of the mesh. Yet, it should be noted that it is quite possible that the site stratigraphy is such that presence of more resistant soil layers can limit the retrogression distance, which somehow resembles the situation considered in this case.

Another significant limitation comes from the assumption that the failed mass completely separates from the deposit and flows away. This does not necessarily always happen. In some failures, the failed mass may remain for a longer period near slope toe as debris accumulation and act as a surcharge or a constraint. In submarine landslides, however, where huge volumes of mass movement are involved, very large run-out distances are observed which implies that such an assumption is valid (see Section 2.2.4)

Finally, there is no quantitative validation of the proposed analysis method. As no complete set of data from a real case history (including morphology and geomechanical properties, geometry of slope failure, and seismic excitation) was available, the only validation of this study is qualitative, coming from evidence of several retrogressive submarine slope failures triggered by seismic events. Such a quantitative comparison with field observations is in particular needed to assess the validity of the proposed

removal criterion. Both the shear strain threshold (γ_{max} > 100%) and the timing for removal have been set somehow arbitrarily in this study. This limitation may be mitigated by comparison with future experimental results.

4.6 Conclusions

It is shown how the retrogressive failure of seafloor, initiated by earthquake, can be simulated using the finite element method. The procedure is explained in four numerical examples that explain a number of different mechanisms of initiation and retrogression of failure. The analyses emphasize the effects of a silt layer and a gently sloping seafloor on the retrogression of slope failure in a sand deposit.

If the presented procedure is not used, i.e. no removal of failed elements is done, the predicted extension of failure will be at least 5 times smaller, and hence, the analysis results will be under-conservative. This difference in predictions, of about one order of magnitude, can vary as a function of soil properties, morphology, seismic acceleration, etc.

It is found that a silt layer and a gentle seafloor slope significantly affect the retrogression distance by increasing it by at least 4 to 5 times as compared to a flat, uniformly sandy seafloor. The element removal was the key feature that allowed relatively more realistic simulations in all cases. The mechanism of initial failure, triggered by the earthquake shaking, is failure under static shear stress while maximum excess pore water pressure (EPWP) ratio near the slope face is well below one, i.e. liquefaction did not occur. After removal, reduction in overburden pressure results in reduction of shear strength, and the initial failure retrogresses back to regions that have already experienced softening because of EPWP build-up. In case of uniform sand, due to

relatively fast rate of dissipation that results in regaining strength for the soil, the extension of retrogression is considerably smaller than for the case where the sand is overlain by a less permeable silt layer. For a gently sloping seafloor, the initial failure causes an infinite slope failure mechanism in the deposit that has lost most of its shear strength due to build-up of pore pressure. The extension of the retrogression can be limited in the field by particular geo-morphological conditions. The predicted infinite slope failure was superficial for uniform sand (failure plane parallel to the seabed) and deeper when a less pervious soil layer was assumed at the seafloor. It also resulted from a limited study that mesh refinement could slightly affect the analysis results with regards to the number of retrogression stages, but not with respect to the predicted extension of failure.

Chapter 5 - THREE-DIMENSIONAL EFFECTS

5.1 Introduction

This Chapter presents a numerical study on three-dimensional (3D) effects in seismic analysis of slopes. The most important objective of this study is to assess the two-dimensional (2D), plane strain simplifying assumption and to set reasonable limits of its applicability. Also, it aims at quantifying the 3D/2D ratios of some predicted quantities related to seismic response of slopes as a function of some influencing factors, most importantly the width to height ratio of the slope.

In the framework of slope stability analysis by factor-of-safety approach, a considerable number of studies have compared the factor of safety obtained from a full 3D analysis (F_{3D}) with the one obtained from a simplified 2D analysis (F_{2D}). The majority of those studies have concluded that $F_{2D} < F_{3D}$ (see Section 2.3.4). These studies typically account for the difference between the 3D and 2D shapes of the failure surface (Figure 5-1), and they show that as the width of the failing soil wedge increases, F_{3D} decreases to a value equal to F_{2D}.

Due to the limitations of the limit equilibrium method when applied to dynamic analysis, results of such studies are not applicable to the seismic analysis of submerged slopes, where potential of liquefaction and other effects of dynamic earthquake loading are significant.

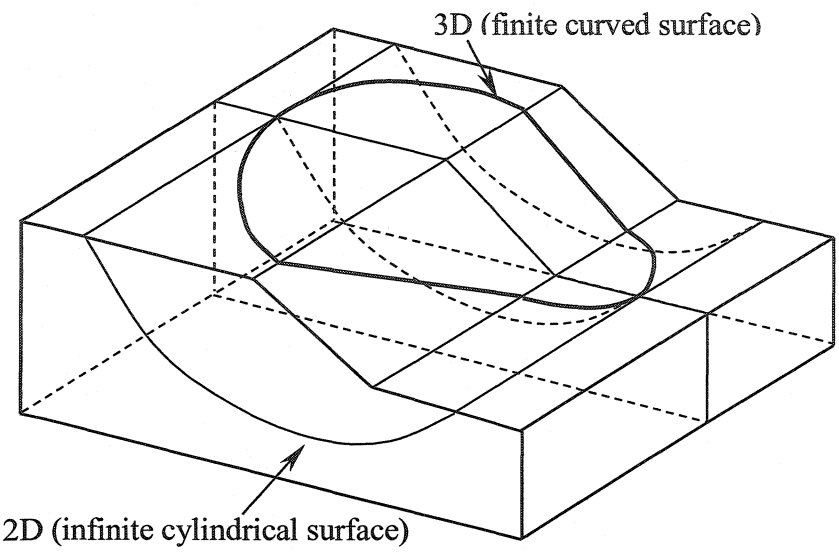

Figure 5-1. 3D (finite curved) versus 2D (infinite cylindrical) assumptions of the shape of failure surface.

In this study, a dynamic, fully coupled Finite Element Method implementing a multi-yield plasticity model (as described in Section 3.4) is used to compare the behaviour of slopes with various width to height ratios and subjected to a range of acceleration levels, as predicted by 3D analyses, with the predicted behaviour of their equivalent 2D configurations. The slope behaviour is indicated by three main responses related to displacement, shear strain, and excess pore pressure ratio. The study includes application of a transmitting boundary condition and its effect compared to an ideal rigid boundary condition.

Response Surface Methodology (Section 2.4) is applied to identify the important factors with significant effects, and to obtain regression models relating the influencing factors and the responses.

5.2 Finite element model

5.2.1 Finite element mesh

The general scheme of the finite element meshes used in this study is shown in Figure 5-2. In addition to the variation of the model width (B), the effect of the finite element discretization (mesh refinement) on the results is also investigated. The cross section of the 3D mesh is either coarse or fine (Figure 5-2b and c). The width of elements in the z-direction (dz) is either 5m or 2m depending on the model width. The slope is 1V:3H, however, through a limited number of analyses, the effect of slope angle changes is also addressed. For the full 3D analyses, due to symmetry of the structure and loading with respect to a plane normal to the z-axis, only half of the mesh is analyzed.

The soil is discretized into eight-node, bilinear, brick finite elements with six degrees of freedom per node, three for solid and three for fluid displacements. Depending on the model width (B) and width of elements in the z-direction, the total number of elements in 3D analysis varies from 2 to 20 times the number of elements in 2D analysis. For the 2D plane-strain analyses, the soil is discretized into four-node, bilinear, quadrilateral finite elements with four degrees of freedom per node, corresponding to vertical and horizontal components of solid and fluid displacements. The coarse and fine meshes have 156 and 372 elements, respectively.

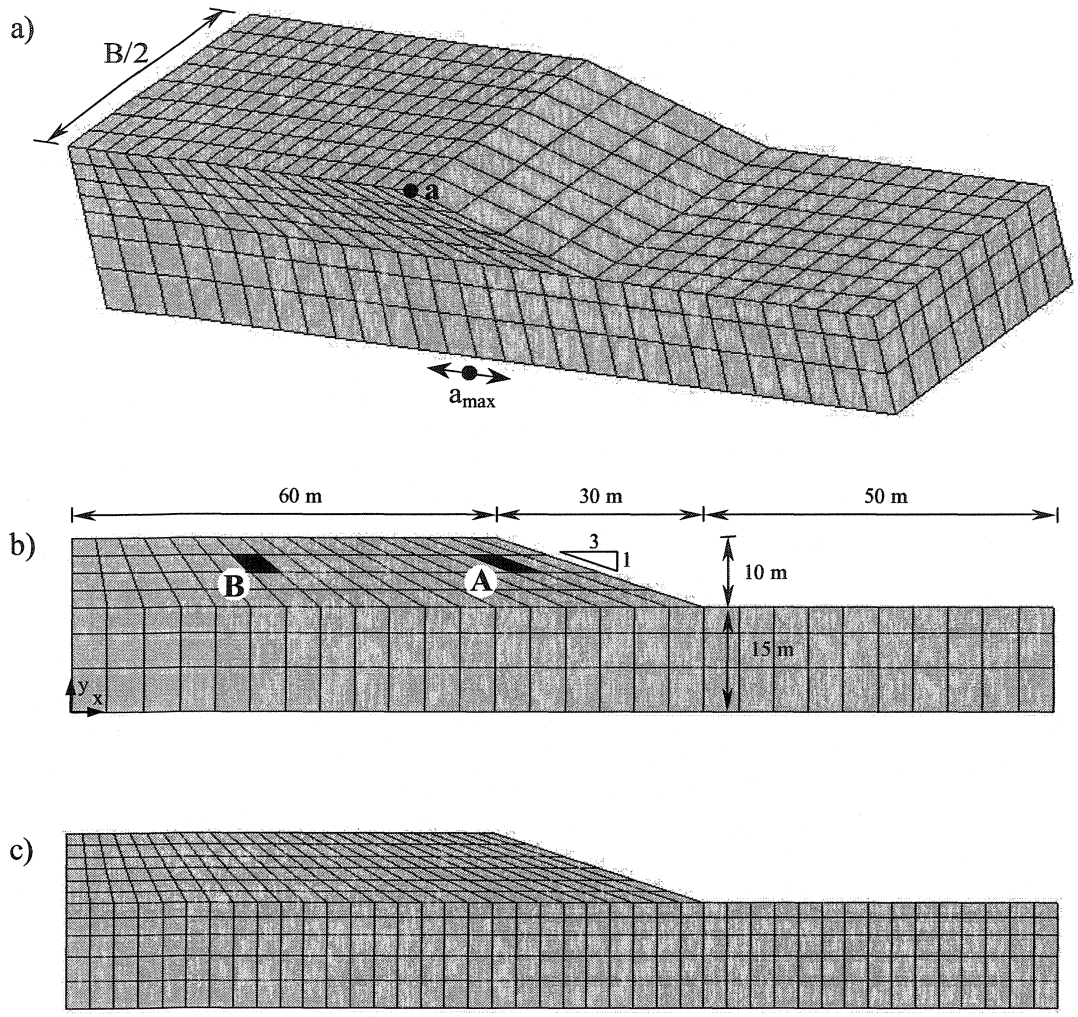

Figure 5-2. The finite element meshes used in this study: a) 3D, b) 2D coarse, and c) 2D fine meshes.

5.2.2 Boundary conditions and earthquake loading

The analysis domain has an idealized shape, especially with regard to the lateral boundaries perpendicular to the face of the slope as they are selected to be vertical and rigid to model presence of a stiff rock. A realistic model would be inclined lateral boundaries (V-shaped valleys) and interface elements with coulomb friction. In this study, it was selected to include the most restrictive boundary condition, which is vertical walls and stick contacts. Inclined boundaries may cause a different behaviour, which may include those effects caused by the reflection of waves towards the surface of the medium

rather than its main body. As it will be discussed later, the effect of the vertical rigid boundary is quite significant in the cases analyzed here, which necessitated the use of a transmitting boundary.

The boundary conditions used in 3D analyses are shown in Figure 5-3. The boundary condition codes are according to the definitions given in Table 5-1 (Prevost, 2002), with the following order: x, y, z components of solid phase motion, and x, y, z components of fluid phase motion. The input acceleration is not applied to the fluid phase on the front and back faces of the model (Figure 5-3) to avoid numerical noise in the response. To simulate impervious boundaries on the front and back faces, the horizontal component of fluid displacement in the x-direction (i.e. the fourth degree-of-freedom) of each node located on those faces is slaved to that of the corresponding node located on the very next vertical plane of nodes. The nodes located at the corners of the model (shown by solid circles in Figure 5-3) have also this type of slaved degrees-of-freedom.

In cases where transmitting boundary conditions are applied to the z = 0 face of the model, the boundary conditions on that face are changed from prescribed acceleration to free movement (code 3 to code 0) and the earthquake acceleration is applied as an incident motion (acceleration) according to the requirements of the finite element code (see Section 3.3.4.1 for details). As such, at nodal points located on the boundary (z = 0 face) and at each time instant, a shear stress is prescribed as a function of the incident (input) motion, nodal displacement, as well as the shear wave speed and the density of the soil deposit.

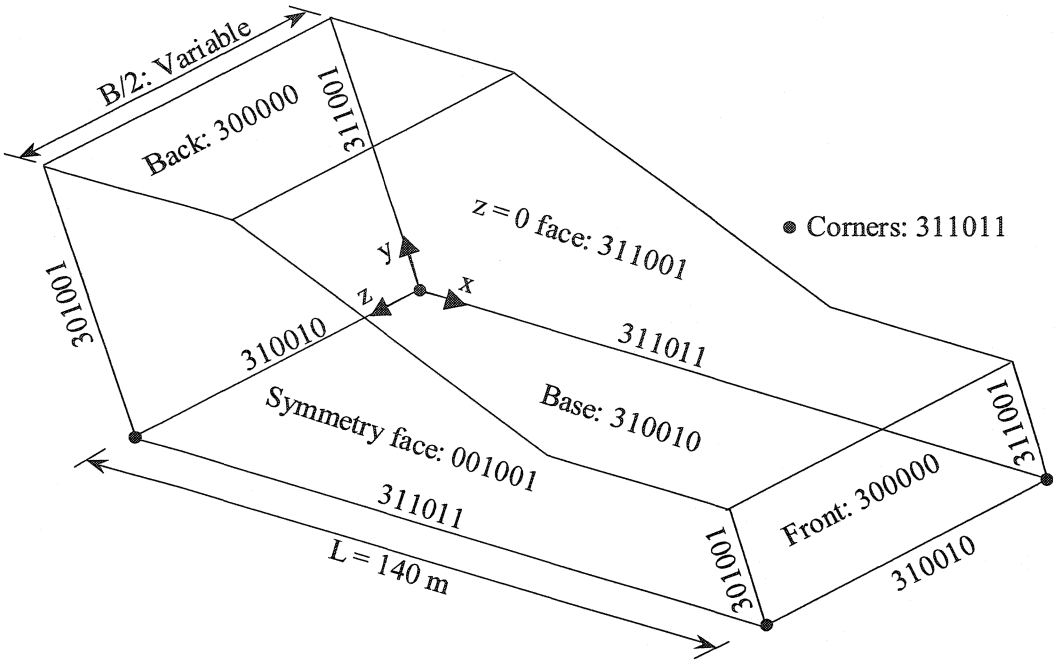

Figure 5-3. Boundary conditions of the 3D model. The boundary condition codes are according to the definitions given in Table 5-1, with the following order: x, y, z components of solid phase motion, and x, y, z components of fluid phase motion.

Table 5-1. Description of boundary condition codes (Prevost, 2002).

Boundary Condition Code	Description
0	Unspecified (i.e., active degree of freedom)
1	Prescribed displacement
3	Prescribed acceleration

As rigid boundaries are assumed for the analysis domain, the earthquake acceleration is applied at the base of the model (y = 0 face) as well as all lateral boundaries, namely x = 0, x = L, and z = 0 faces. The earthquake motion is an acceleration time history generated according to the response spectrum for the soil type 3 (soft to medium clays and sands) recommended by the Uniform Building Code (1994). Figure 5-4 shows the time history scaled to a_{max} = 0.3g. In this study, a_{max} varies from 0.1 to 0.5g. The analysis time is 20 seconds.

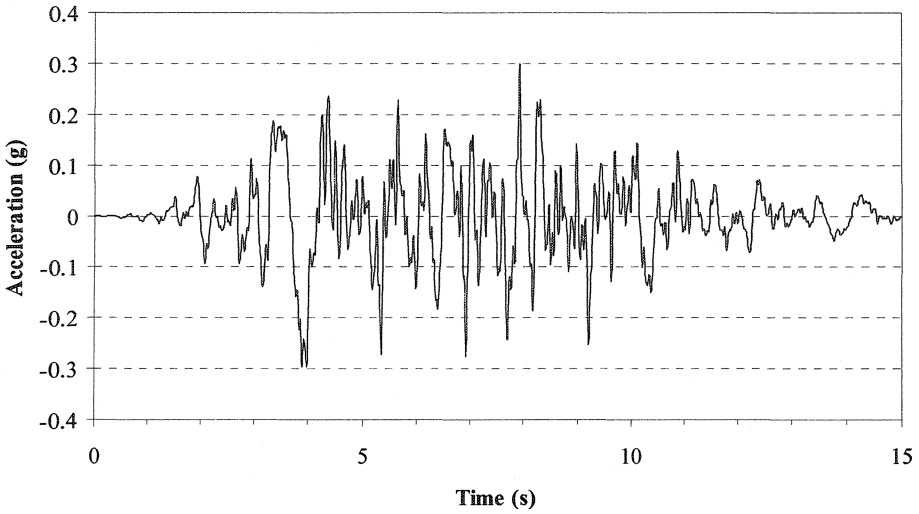

Figure 5-4. Acceleration time history with 0.3g peak ground acceleration (a_{max}).

5.2.3 Material properties

The material properties used in this study (Table 5-2) are estimated based on values reported in the literature for the Fraser River (BC, Canada) sand at D_r = 40%, as described in Chapter 3. A study on the effects of liquefaction strength of the soil is also presented at the end of this Chapter, for a set of updated material properties that were discussed in Chapter 3.

Table 5-2. Material properties.

Soil Property	Symbol	Selected Value (Literature)	Modified Values (UBC tests)
Mass density of solid (kg/m^3)	ρ_s	2720	2710
Porosity	n	0.45	0.45
Low-strain shear modulus (MPa)	G_0	40	47
Poisson's Ratio	ν	0.3	0.3
Reference mean effective normal stress (kPa)	p_0	100	100
Power exponent	n	0.5	0.5
Fluid bulk modulus (MPa)	B_f	2000	2000
Friction angle at failure	ϕ	36	36
Cohesion (kPa)	c	0	0
Maximum deviator strain in compression/extension (%)	ε_{dev}^{max}	5/3	8/7
Dilation angle (phase transformation)	ψ	34	34
Dilation parameter	Xpp	0.2	0.3
Permeability (m/s)	k	$2.3*10^{-4}$	$2.3*10^{-4}$

5.3 Factors and Responses

Results of 2D and 3D analyses are compared to evaluate the applicability of 2D, plane strain simplifying assumption. A number of predicted responses, including displacement, shear strain, and excess pore water pressure ratio, are considered. The comparison is performed in terms of the ratios of those results obtained from 3D analyses, on the plane of symmetry, to those obtained from 2D analyses. Several possible factors are considered in the study. The most important factor is the width to height ratio of the slope (B/H), since with the increase of this ratio, the plane strain assumption becomes valid, given the selected homogeneous material, geometry, and direction of earthquake loading. The effects of B/H are studied for a range of peak ground accelerations. In addition, the influence of mesh refinement on numerical results is also investigated.

The factors are (Figure 5-2): width to height ratio (B/H), maximum acceleration (a_{max}) and mesh size (fine and coarse). These are the selected factors for the main part of the

study; however, effects of some other factors such as slope angle and soil properties are partially investigated, as presented in Sections 5.5.3 and 5.5.4. Another limited study also investigates the 3D effects in case of transverse loading, as described in Section 5.5.5.

The selected responses for comparison are the ratios of 3D to 2D results, predicted at the end of shaking (t = 15s):

1. Displacement: predicted displacement at crest on the plane of symmetry (point 'a' shown in Figure 5-2a),
2. Shear strain index: weighted average (by element area) of predicted maximum shear strain in a zone located on the symmetry plane shown in Figure 5-5a,
3. Excess pore pressure ratio (r_u) index: weighted average (by element area) of the ratio of predicted excess pore pressure to initial vertical effective stress, i.e. $r_u = u_e / \sigma'_{v0}$, in a zone located on the symmetry plane shown in Figure 5-5b.

The ratios (3D/2D) are hereafter referred to as:

1. R_d: 3D/2D crest displacement ratio
2. R_s: 3D/2D shear strain index ratio
3. R_r: 3D/2D r_u index ratio

The selection of elements is based on the typical distributions of maximum shear strain and r_u (see Figure 5-20 to Figure 5-25 discussed later in Section 5.5.1) in a way that the corresponding indices represent the slope performance (deformation, instability, etc.) and that they are not influenced by the lateral boundaries. Although these distributions vary with the peak acceleration, the above definitions of indices and selections of the zones are deemed to represent the extent and severity of failure and/or deformations experienced by the slope.

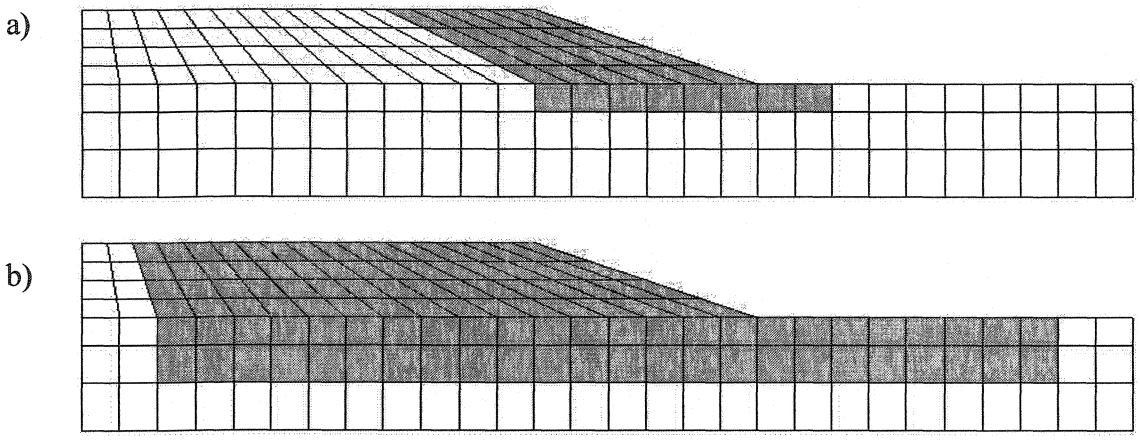

Figure 5-5. Selected elements for calculating: a) shear strain, and b) r_u indices.

5.4 Numerical analysis aspects

5.4.1 Screening by RSM

In the first phase of the analysis, Response Surface Methodology (RSM) is used to screen the significant factors. It is worth emphasizing that the RSM techniques are used only as an efficient tool for identifying the most influential parameters by performing the least number of analyses. Based on the results of the first phase, i.e. screening by RSM, further insight is gained by performing more analyses using only the significant factors to focus on the effects of such factors without spending the computational resources on studying effects of insignificant factors.

The ranges of factors in this phase of the study are: model width (B/H = 2 – 8), maximum acceleration (a_{max} = 0.1 – 0.5g) and mesh size (fine and coarse). Analyses combinations are given in Table 5-3.

Table 5-3. Analyses combinations.

No.	B/H	a_{max}	Mesh
1	2	0.1	Coarse
2	8	0.1	Coarse
3	2	0.5	Coarse
4	8	0.5	Coarse
5	2	0.1	Fine
6	8	0.1	Fine
7	2	0.5	Fine
8	8	0.5	Fine

The RSM analysis shows that B/H and a_{max} are the only factors with significant main effects (Figure 5-6). There is no significant interaction between factors. The fact that the mesh size effect is not significant indicates that the coarse mesh can be used for further analysis with sufficient accuracy and reduced run time.

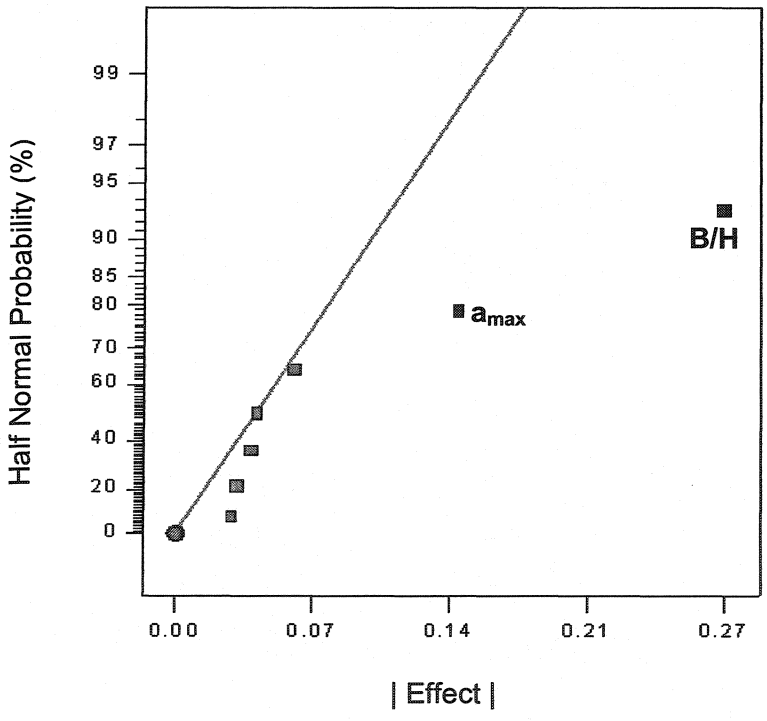

Figure 5-6. Half Normal Probability plot of the effects—a tool for identifying significant effects.

Using the central values of the two significant factors (B/H = 5, and a_{max} = 0.3g) in combination with previous values, the curvature of the response surface is examined. The RSM analysis shows that the curvature of the response surface is significant, especially in terms of model width. In other words, the changes in the responses are highly nonlinear with changes in B/H, and almost linear with changes in a_{max}.

The above results indicate that B/H is the most important factor that needs further study, which is presented in the following sections.

5.4.2 Lateral boundary effects

Figure 5-7 shows the effect of the lateral boundaries on the crest displacement ratio (R_d) for all models with B/2 ranging from 4 to 100 m, that is, for H = 10 m, B/H ranges from 0.8 to 20. The results indicate that R_d has a peak value for certain values of the model width depending on the value of a_{max}. The effect is more pronounced for a_{max} = 0.1g. The same trend can be observed in terms of other responses, i.e. shear strain ratio (R_s) and r_u ratio (R_r).

Also, the same trend can be observed from the predicted deformed shape of the crest (Figure 5-8 to Figure 5-10). Again, the effect of the lateral boundaries is more pronounced for a_{max} = 0.1g.

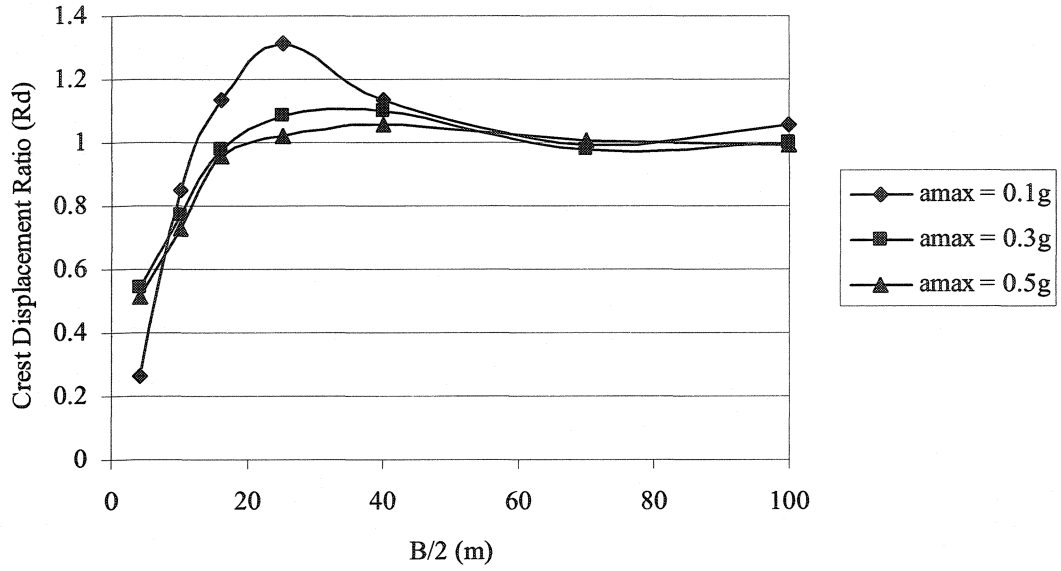

Figure 5-7. Effect of lateral boundaries: Crest displacement ratio for various model widths and a_{max}.

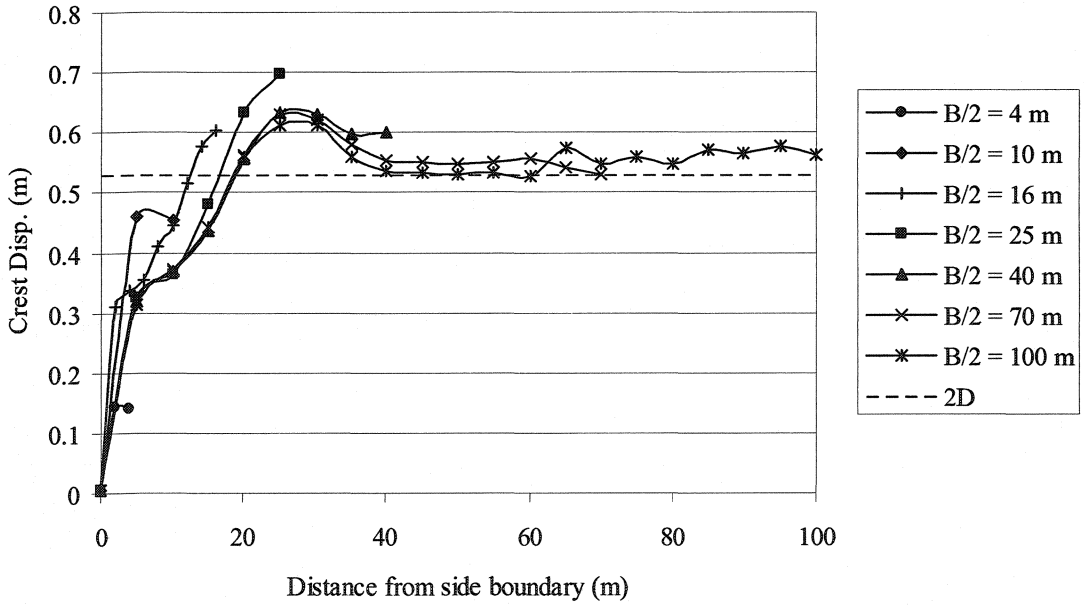

Figure 5-8. Predicted deformed shape of the crest at t = 15 s, for various model widths and a_{max} = 0.1g.

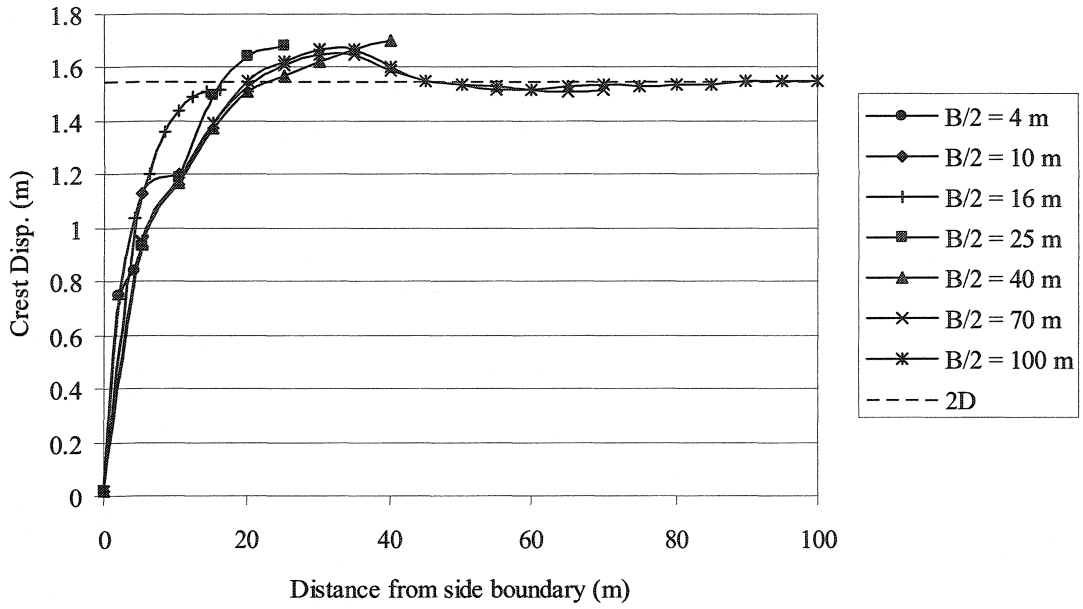

Figure 5-9. Predicted deformed shape of the crest at t = 15 s, for various model widths and a_{max} = 0.3g.

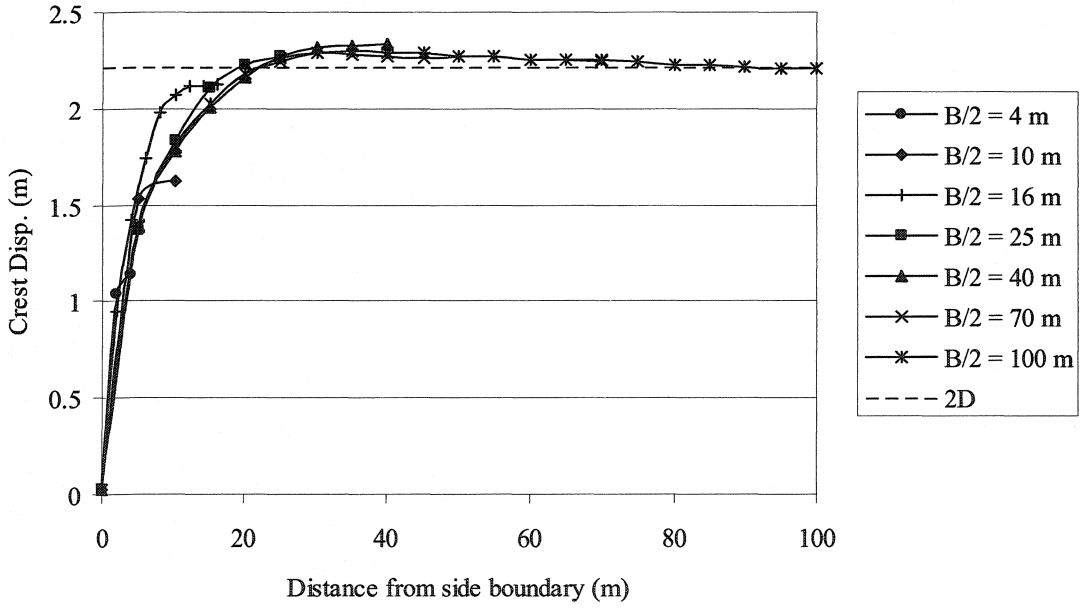

Figure 5-10. Predicted deformed shape of the crest at t = 15 s, for a_{max} = 0.5g.

For the slope analyzed here with H = 10 m, the peak of the crest deformation occurs at a distance of about 25 m from the lateral boundary for a_{max} = 0.1g. This distance slightly increases as the peak acceleration increases. Occurrence of such a peak in crest deformation is believed to be produced by the wave interference phenomenon caused by the reflection of waves from the rigid lateral boundary. The present situation is much more complex owing to all types of wave propagation, more importantly, shear waves (SH-waves) propagating vertically from the base and the longitudinal waves (P-waves) originating from the x = 0 and x = L faces, in addition to those propagating and being reflected horizontally from the z = 0 and z = B faces.

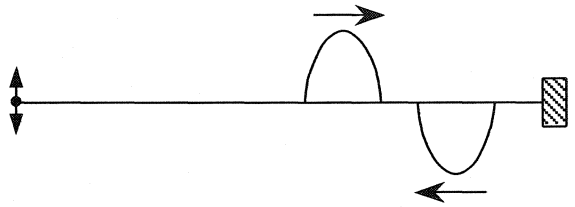

Figure 5-11. Reflection of a single pulse from a fixed end in a rod.

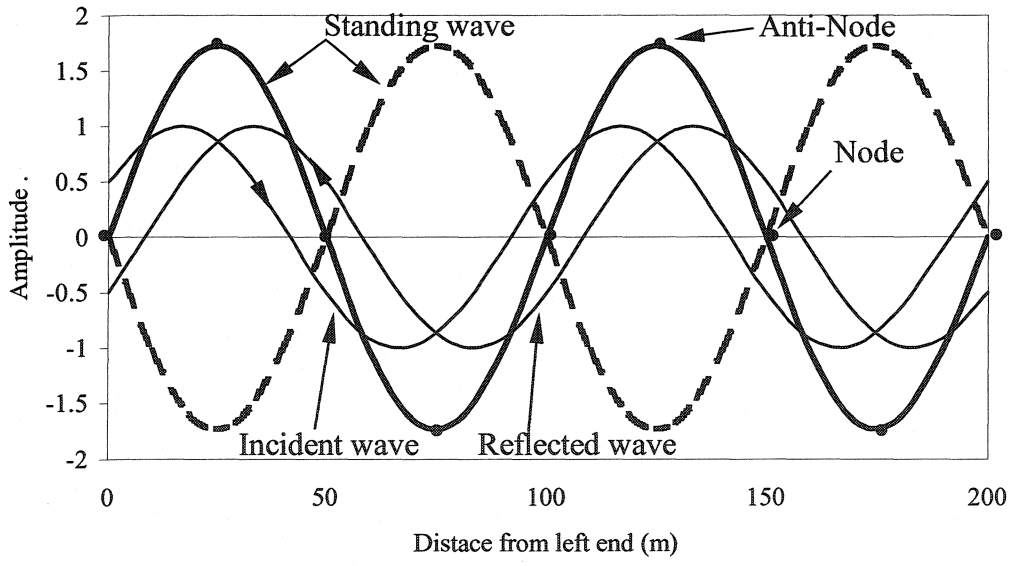

Figure 5-12. Standing wave caused by interference of incident and reflected waves.

Consider a simple, one-dimensional propagation of wave in a rod excited at one end (left) and fixed at the other end (right), as shown in Figure 5-11. The reflected wave from the fixed end is opposite to the incident wave, i.e. a positive single pulse is reflected as a negative one. If the rod is subjected to a sinusoidal wave with period T, and if the wave speed in the rod is C, the wavelength will be $\lambda = CT$. The resultant motion of the two incident and reflected motions can be simply obtained by superimposing the two motions as shown in Figure 5-12, where the rod length is $L = 200$ m, wavelength is $\lambda = 100$ m, and the motions have unit amplitude. In such a circumstance ($L = n\lambda$), a standing wave is generated which results in some certain points of the rod being nodes (with zero displacement) and some as anti-nodes (with maximum displacement) at all times. If the right end is not a reflecting boundary, no interference occurs and all points along the rod will only experience a sinusoidal transient wave, rather than a standing wave.

As noted before, the 3D model of a non-linear material subjected to irregular earthquake loading is much more complex than the above 1D elastic rod subjected to a sinusoidal wave; therefore, no quantitative analogy can be explained for the two cases. Nonetheless, a qualitative analogy, as explained above, indicates that by changing the artificial rigid boundary conditions, which may simulate real conditions in some cases, to some transmitting boundary conditions, the peak in crest deformation can be eliminated.

Furthermore, as it is mentioned in Section 2.3.5.2, the existing transmitting BC formula, including the one implemented in Dynaflow and used here, are all developed for elastic media; and thus, these do not take into account the influence of plastic deformations at the boundary on wave propagation. Nonetheless, it is clear from the

comparisons presented here that even using such transmitting boundaries can reduce significantly the effects of wave interference.

While the results presented in Figure 5-7 to Figure 5-10 seem to reflect the true behaviour of a soil deposit with rigid vertical boundaries, large predicted displacements at a distance of about 25 m from the z = 0 boundary prevents meaningful result analysis in terms of the effect of B/H ratio on 3D vs. 2D results. Moreover, real-life soil deposits are unlikely to include rigid, parallel, vertical boundaries, and therefore, wave reflection/interference phenomenon, such as those simulated here, may not be of interest for practice. Hence, to obtain meaningful results in terms of 3D effects for slopes with different B/H ratios, the wave interference effects have been reduced by using transmitting boundary conditions on the z = 0 face, as described hereafter.

Figure 5-13 presents a comparison between the crest profiles obtained from the models with and without the transmitting boundary conditions. Only results of the model with B/2 = 40 m and a_{max} = 0.1g are shown. As explained in Section 3.3.4.1, the only parameter of the transmitting boundary is ρC, where ρ = mass density, and C = shear wave speed calculated as:

$$C = \sqrt{\frac{G}{\rho}} \qquad (5\text{-}1)$$

where G = shear modulus of the soil skeleton. The shear modulus varies due to softening of the soil with the increase in excess pore pressure. Within liquefied soil, the shear modulus is theoretically zero. An average value is adopted for G equal to half the initial small-strain shear modulus ($G_0/2$) corresponding to an average depth of about 10 m. The resulting value of $(\rho C)_i$ is 2.33 × 10^5 kg/m^2.s. Note that according to Biot's (1956)

theory (see also Richart et al., 1970), the presence of the fluid produces only a minor effect on the shear-wave velocity, as opposed to the important effect it exerts on the dilatational-wave velocity. Richart et al. (1970) also present a graph of measured shear-wave velocity vs. effective confining pressure for dry, drained, and saturated samples of Ottawa sand, in which very small difference can be seen in the values of velocity obtained for the three types of soil at any given effective confining pressure.

Included in Figure 5-13 are also the results of two analyses with ρC ten times larger and smaller than the value assumed in the initial analysis, $(\rho C)_i$. These profiles indicate that by applying the transmitting boundary conditions the peak in the crest displacement profile apparently induced by wave interference is eliminated; however, with the decrease in the value of ρC, the crest displacement on the lateral boundary increases approximately up to the value of displacement on the symmetry face. This displacement close to the boundary has insignificant effect on the crest displacement on the symmetry face (z = B/2), which is less than and very close to the value of the displacements predicted in 2D analysis.

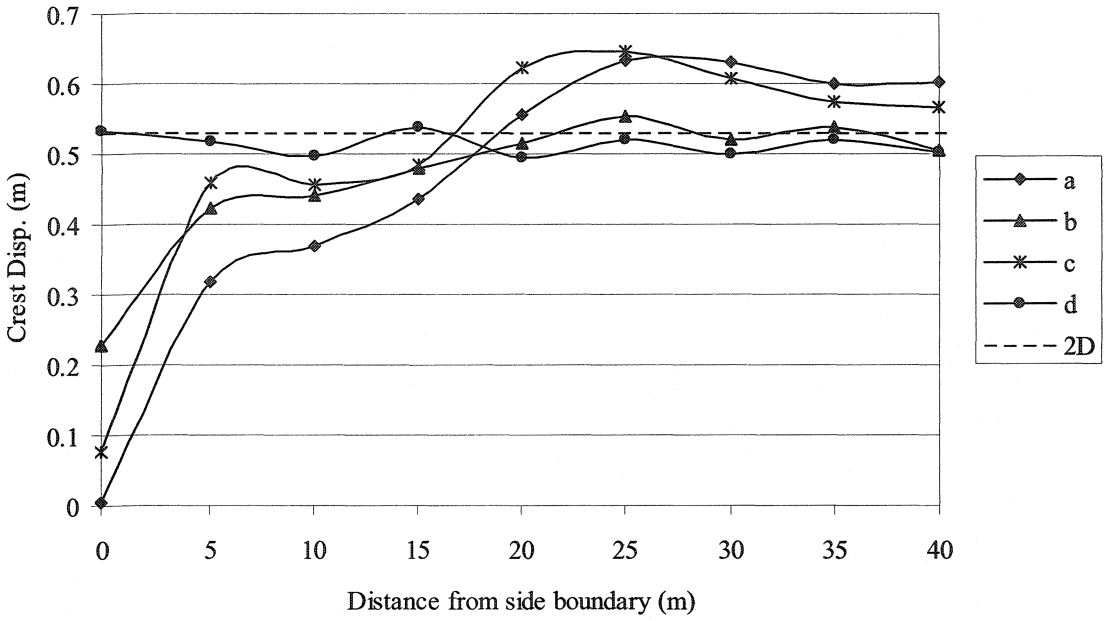

Figure 5-13. Comparison of crest profiles of the models with different boundary conditions (BC) for B/2 = 40 m and a_{max} = 0.1g: a) no transmitting BC; b) with transmitting BC, $\rho C = (\rho C)_i$; c) with transmitting BC, $\rho C = 10 . (\rho C)_i$; d) with transmitting BC, $\rho C = (\rho C)_i / 10$.

Figure 5-14 shows a comparison between crest profiles obtained from 3D analyses with B/2 = 100 m and 2D analysis. Again, the boundary displacement has no significant effect on the crest displacement on the symmetry face (z = B/2). In addition, results of the analyses with all values of B/2 and a_{max} (not shown here) indicate that the crest displacement on the z = 0 face is almost the same for all model widths with the same a_{max}.

It is also expected that the predicted crest displacement on the symmetry face of the 3D model with B/2 = 100 m be very close to the predicted in a 2D analysis. Any small differences may be due to minor numerical problems induced by using a relatively coarse mesh and by having imperfect transmitting boundaries that are expected to occur in the other 3D models with different B/2 values. Therefore, the crest displacement as well as

the shear strain and r_u indices on the symmetry face (z = B/2) of the model with B/2 = 100m is used instead of the 2D result for assessing the 3D effects.

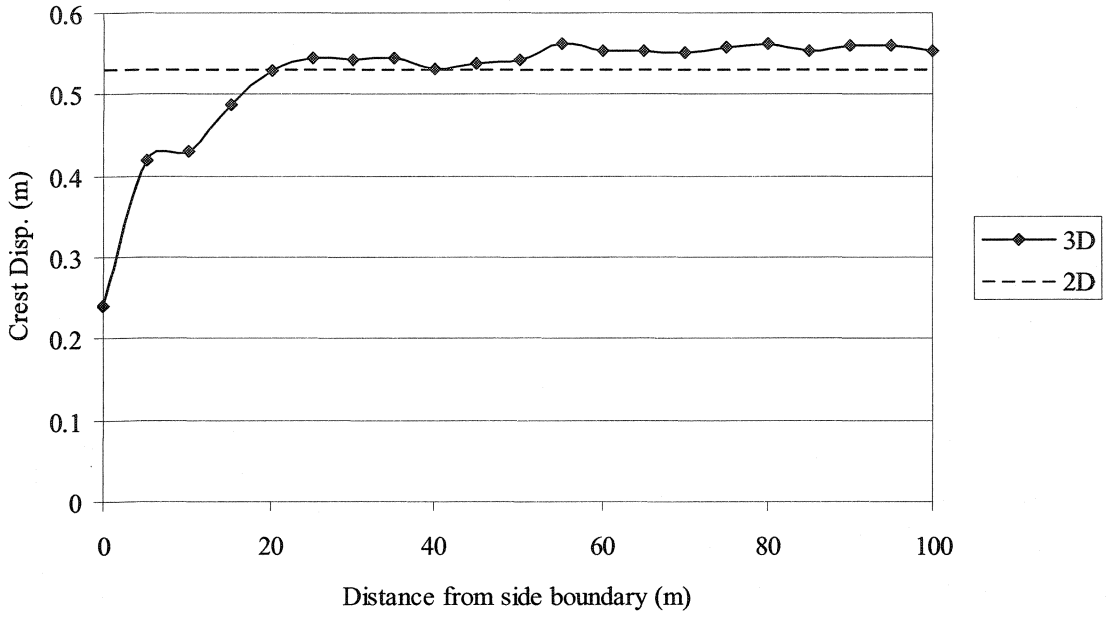

Figure 5-14. Crest profile of the model with B/2 = 100 and transmitting boundaries.

Contours of displacement presented in Figure 5-15 also show the effect of applying the transmitting boundary conditions on eliminating the peak in the crest displacement. The zone with displacement greater than 0.55 m located at a distance of about 20 – 40 m from the z = 0 face in the model with rigid boundaries (Figure 5-15a) is eliminated in the model with transmitting boundaries (Figure 5-15b).

Figure 5-16 presents the typical graph of 3D effects for crest displacement ratio (R_d) obtained for a_{max} = 0.1g. In the following section, the present analysis procedure is used to obtain similar curves for other values of a_{max}.

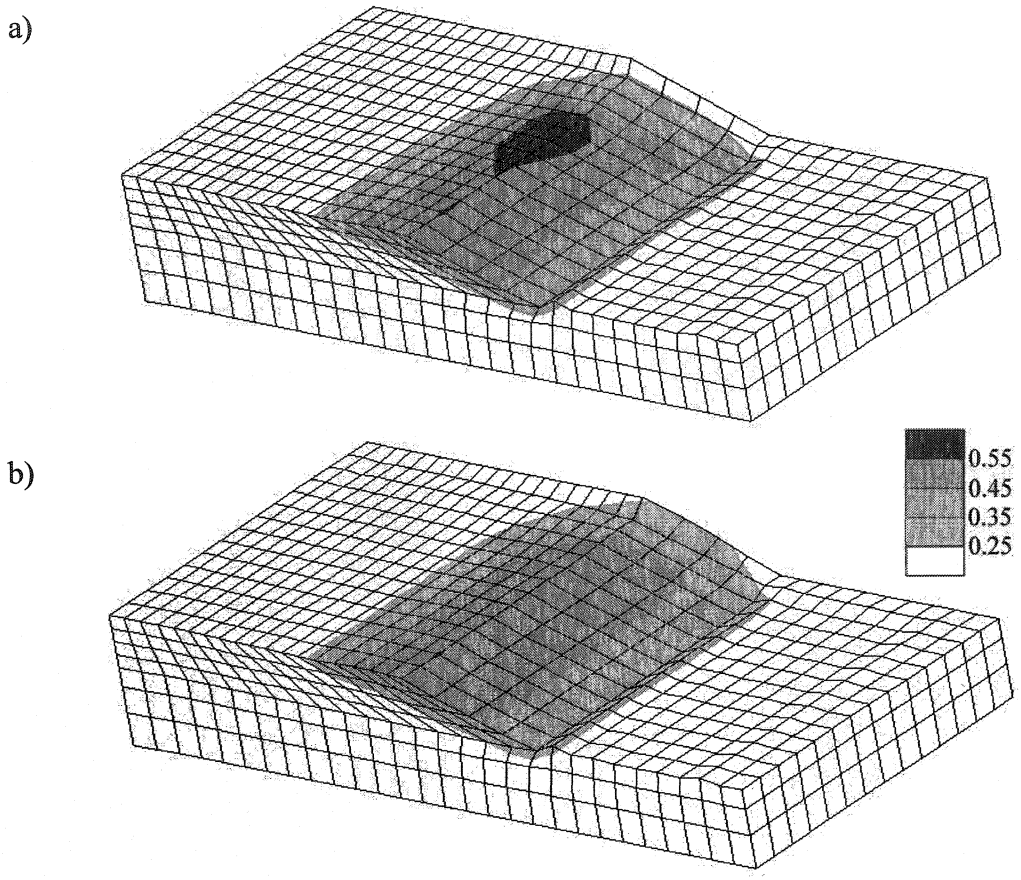

Figure 5-15. Contours of predicted displacement (m): a) without, and b) with transmitting boundary conditions for B/2 = 70 m and a_{max} = 0.1g at t = 15 s. Deformation magnification scale = 10.

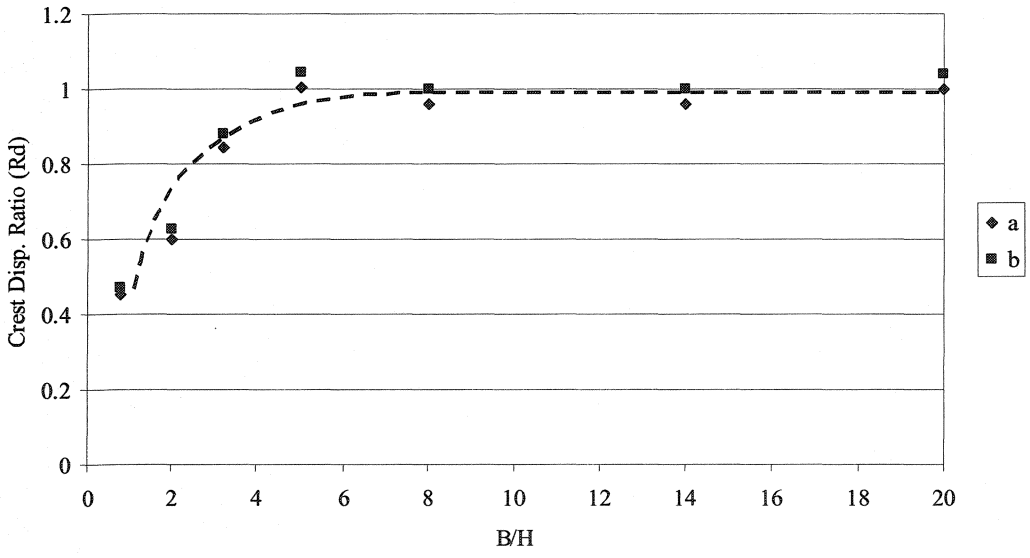

Figure 5-16. Analysis results and a schematic best-fit curve for crest displacement ratio (R_d) for a_{max} = 0.1g: a) using 3D model with B/2 = 100 m, and b) using 2D model.

5.5 Three-Dimensional Effects

5.5.1 Analysis results

Figure 5-17 to Figure 5-25 present contours of predicted displacement, maximum shear strain, and excess pore pressure ratio (r_u) in 3D and 2D models, at t = 15 s. For 3D, the model with B/H = 3.2 is selected. The following points are notable:

1. Displacement contours (Figure 5-17 to Figure 5-19):

Patterns of displacement contours do not vary significantly with varying a_{max}, and they are similar for 2D and 3D models (on the plane of symmetry). In 3D models, maximum values occur on the plane of symmetry at a point between the toe and crest of the slope as indicated by the location of the contour with the highest value. In 2D, as well, maximum values occur between the toe and crest of the slope. This is in accordance with some centrifuge experimental observations (which are closer to 2D configuration) reported by Taboada-Urtuzuastegui et al. (2002).

2. Shear strain contours (Figure 5-20 to Figure 5-22):

Patterns of maximum shear strain contours vary with a_{max} while they are similar for 2D and 3D models (on the plane of symmetry) for the same a_{max}. With the increase in a_{max}, an area of high shear strain initiates near the left and right vertical boundaries, due to the assumed rigid boundaries and perfect stick conditions, and expands near the base of the model.

Additionally, as a_{max} increases, the contours of maximum shear strain on the plane of symmetry in 3D models show lower values below the slope face compared to those in 2D (see Figure 5-20 to Figure 5-22), which indicates that the 3D effect of the lateral boundaries is more significant when a_{max} is higher. This can be more clearly observed

from the graph of variation of shear strain index ratio as a function of B/H and a_{max}, presented and discussed later in Section 5.5.2 (see Figure 5-32). This can be attributed to the fact that the predicted excess pore pressures near the slope face are lower when a_{max} is higher, because of more dilation (as explained later in this Section). More dilation and thus more hardening will result in a stiffer structure and therefore in more significant constraint effect of the lateral boundaries as to lower the shear strains predicted on the plane of symmetry.

3. Excess pore pressure ratio (r_u) contours (Figure 5-23 to Figure 5-25):

Patterns of r_u contours vary significantly with the increase in a_{max}, although in all models the area in the vicinity of the slope has the lowest values of r_u due to static shear stress, while the free-field areas to the left and right of the slope are predicted to liquefy. As indicated by the graphs of shear stress (τ_{xy}) vs. vertical stress (σ_y) of elements A and B (Figure 5-26) located on the plane of symmetry of the model with B/H = 3.2 (see Figure 5-2), the dilation in zones with static shear stress (element A) limits the build-up of excess pore pressure (Figure 5-27), whereas the state of zero effective stress (and r_u = 1) is predicted in the free-field (element B).

With the increase in a_{max}, the depths of the liquefied areas under the flat zones increase and reach the base of the model for a_{max} greater than or equal to 0.3g. Conversely, the larger the a_{max}, the smaller is r_u just below the slope crest. This is due to the fact that, for the soil properties considered in this study, the constitutive model predicts more dilation, and thus, less excess pore water pressure, for elements with static shear stress, when larger load is applied. This is illustrated in Figure 5-28 and Figure 5-29 by comparing the shear stress (τ_{xy}) vs. effective vertical stress (σ_y) and r_u vs. time plots of element A

obtained from the analyses where a_{max} = 0.1g, 0.3g and 0.5g. The stress path of element A is shown in Figure 5-30 in 3D principal stress space, illustrating the contraction/dilation behaviour of this element. When a_{max} is larger the build-up is faster; however, once the phase transformation surface is reached, the larger loading results in larger dilation and thus less pore pressure. Additionally, as indicated by Figure 5-23 and Figure 5-25, for a_{max} = 0.5g, the zone with r_u < 0.25 just below the slope crest extends to the lateral boundary with a greater width near the boundary, whereas for a_{max} = 0.1g, the predicted r_u for the zone below the slope crest is greater than 0.5, both on the plane of symmetry and near the lateral boundary.

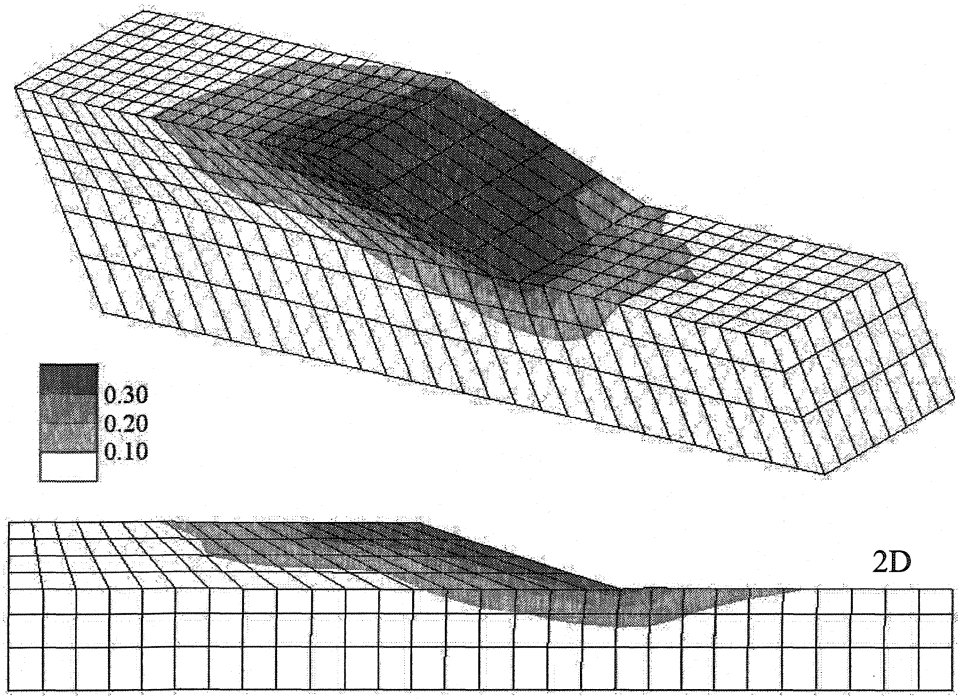

Figure 5-17. Contours of total displacement (m) in 3D (B/H = 3.2) and 2D, at t = 15 s, for a_{max} = 0.1g. Deformation magnification scale is 2.

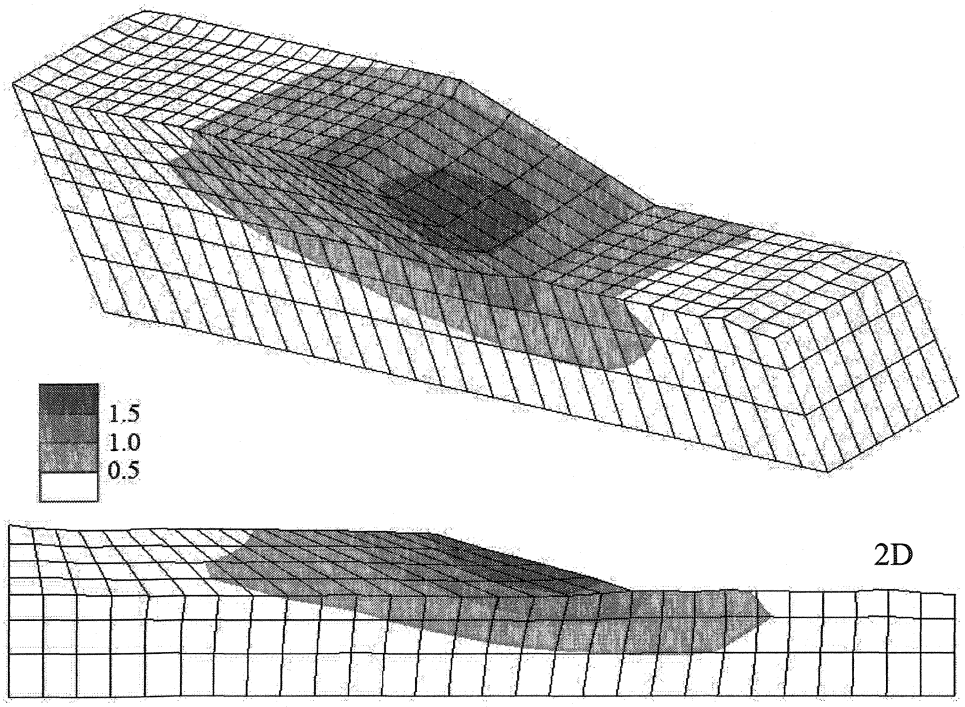

Figure 5-18. Contours of total displacement (m) in 3D (B/H = 3.2) and 2D, at t = 15 s, for a_{max} = 0.3g. Deformation magnification scale is 2.

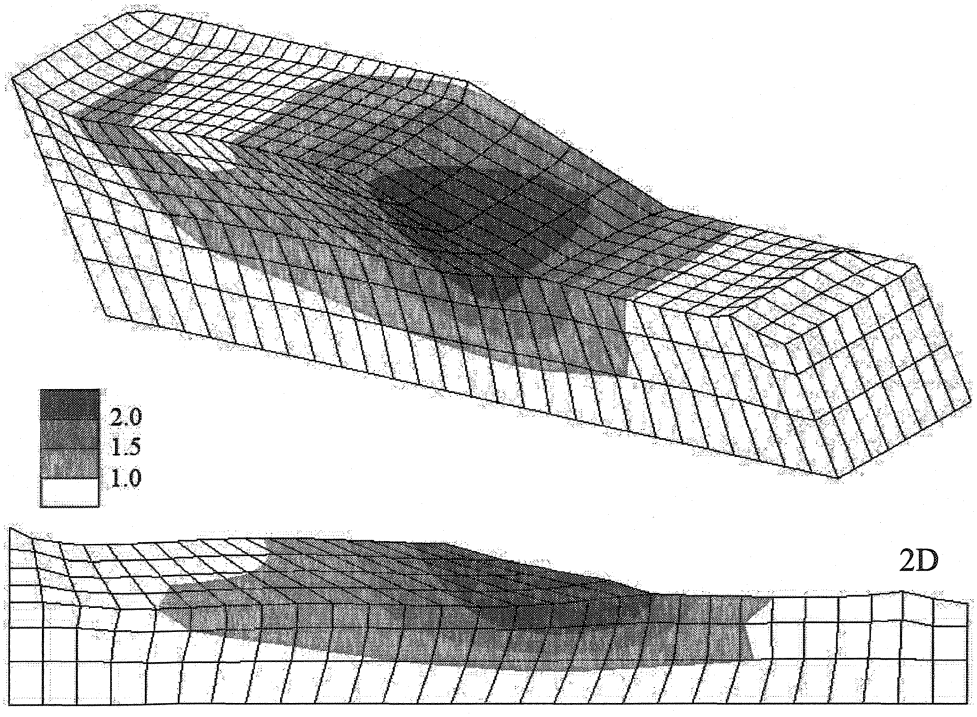

Figure 5-19. Contours of total displacement (m) in 3D (B/H = 3.2) and 2D, at t = 15 s, for a_{max} = 0.5g. Deformation magnification scale is 2.

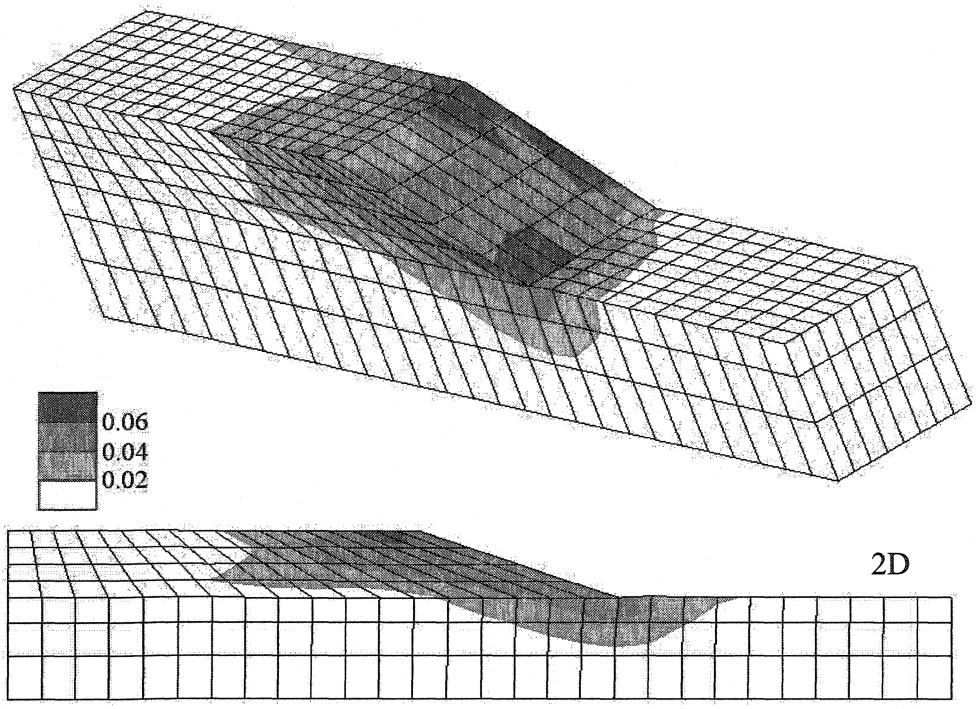

Figure 5-20. Contours of maximum shear strain in 3D (B/H = 3.2) and 2D, at t = 15 s, for a_{max} = 0.1g. Deformation magnification scale is 2.

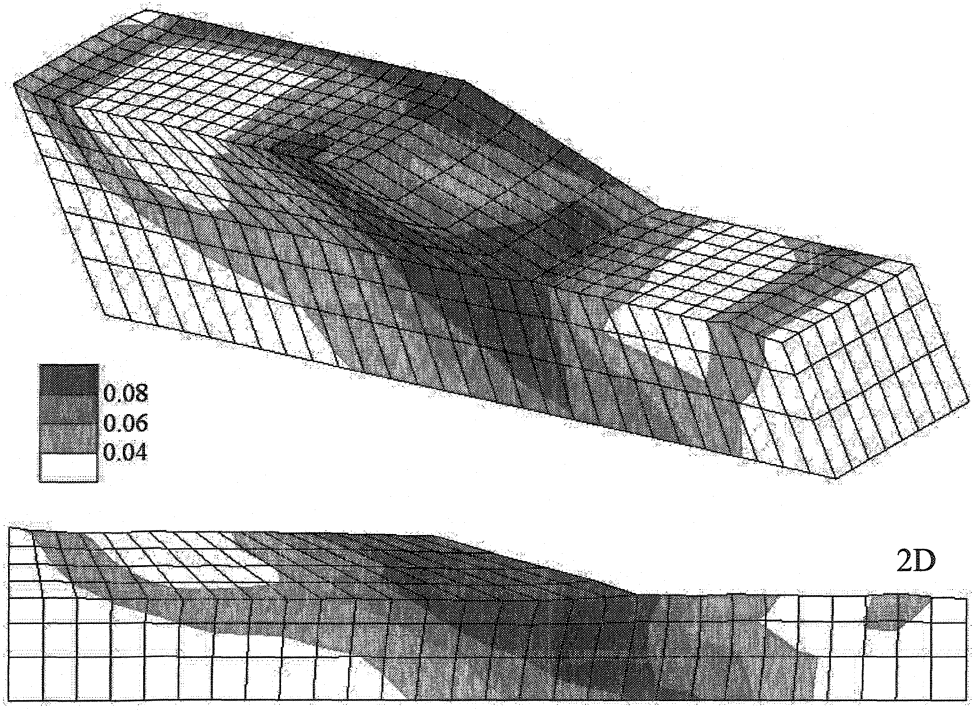

Figure 5-21. Contours of maximum shear strain in 3D (B/H = 3.2) and 2D, at t = 15 s, for a_{max} = 0.3g. Deformation magnification scale is 2.

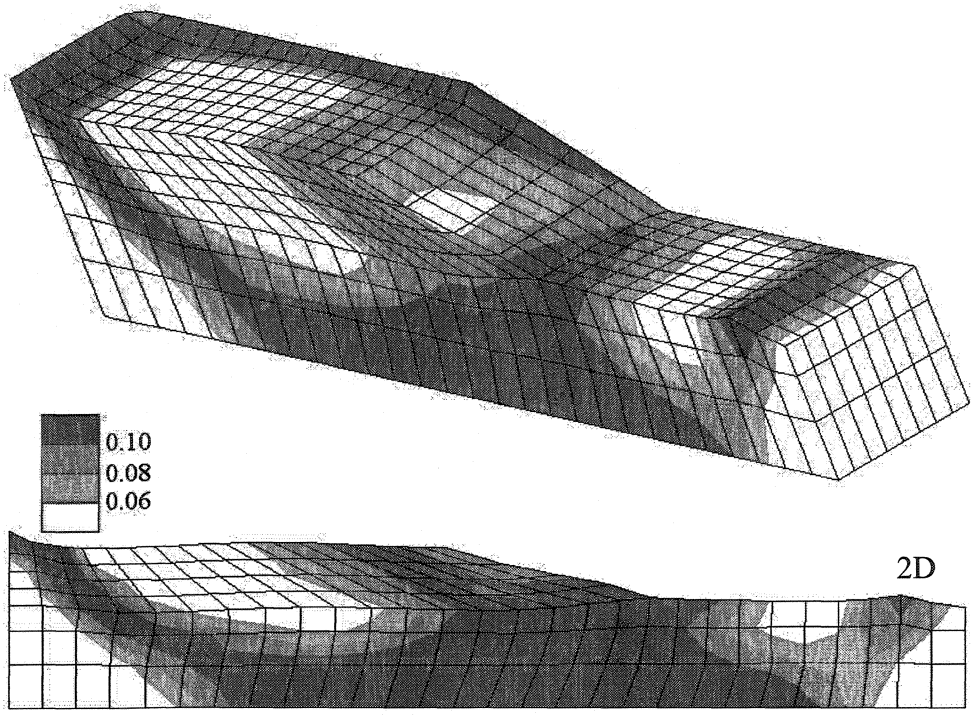

Figure 5-22. Contours of maximum shear strain in 3D (B/H = 3.2) and 2D, at t = 15 s, for a_{max} = 0.5g. Deformation magnification scale is 2.

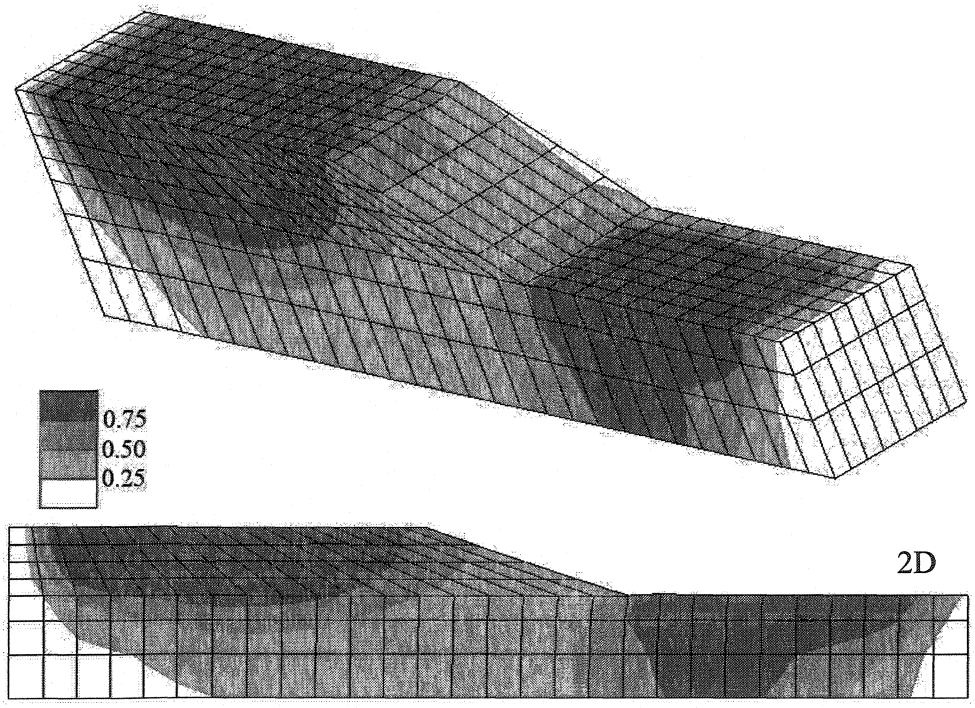

Figure 5-23. Contours of excess pore pressure ratio (r_u) in 3D (B/H = 3.2m) and 2D, at t = 15 s, for a_{max} = 0.1g. Deformation magnification scale is 2.

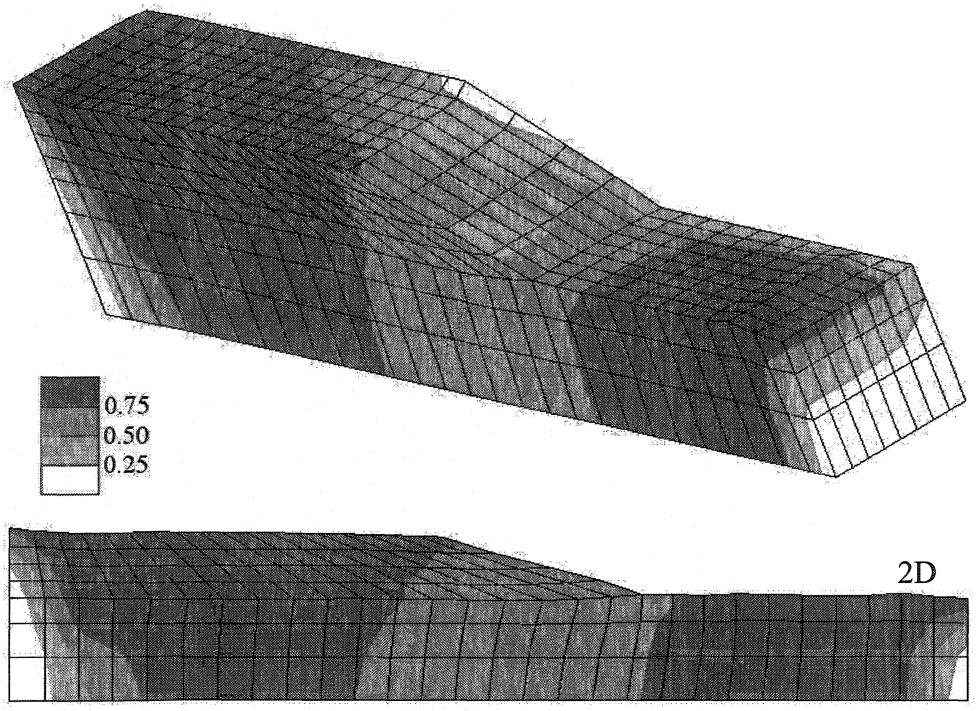

Figure 5-24. Contours of excess pore pressure ratio (r_u) in 3D (B/H = 3.2m) and 2D, at t = 15 s, for a_{max} = 0.3g. Deformation magnification scale is 2.

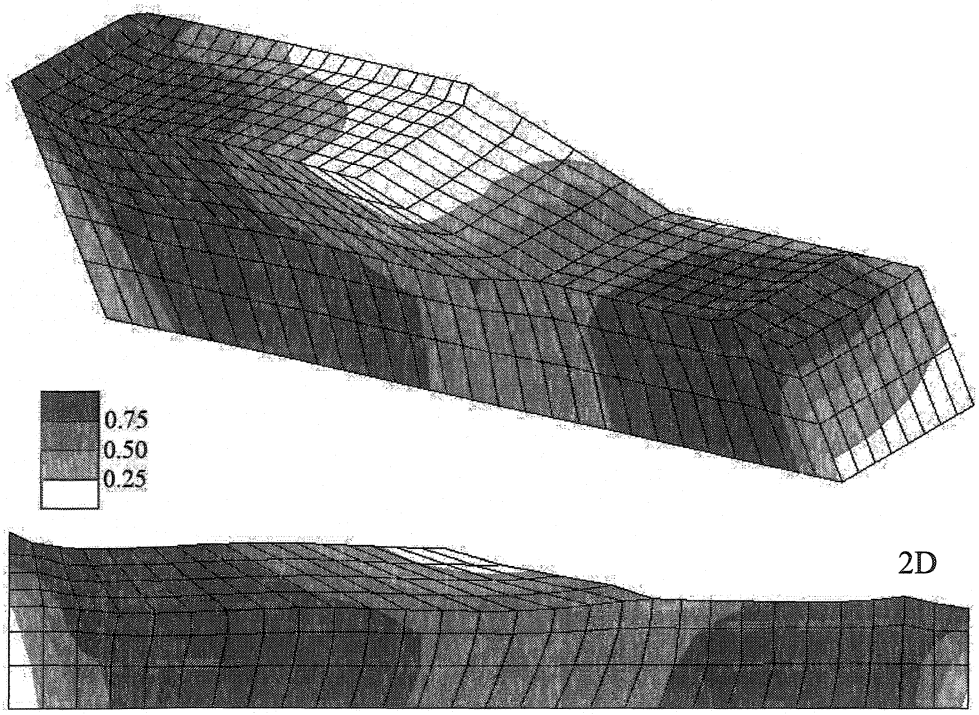

Figure 5-25. Contours of excess pore pressure ratio (r_u) in 3D (B/H = 3.2m) and 2D, at t = 15 s, for a_{max} = 0.5g. Deformation magnification scale is 2.

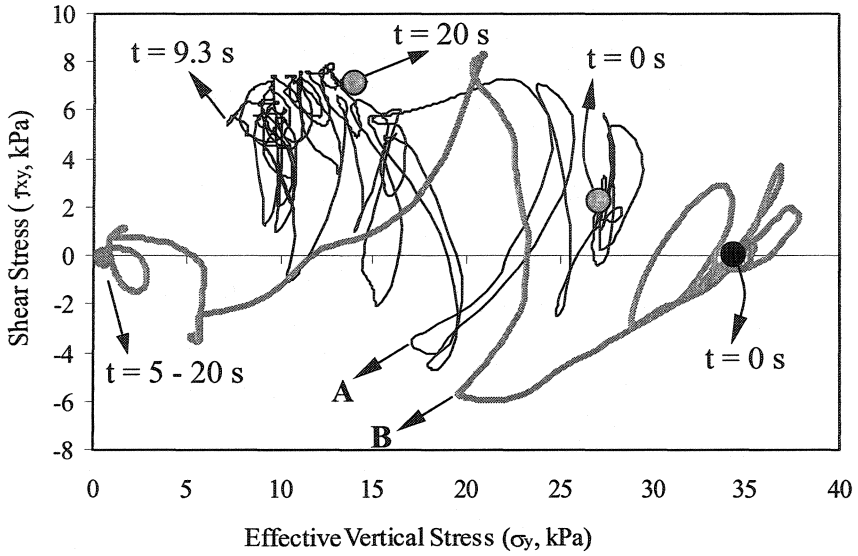

Figure 5-26. Shear stress (τ_{xy}) vs. effective vertical stress (σ_y) for elements A and B, shown in Figure 5-2b, in the model with B/H = 3.2, for a_{max} = 0.1g. Element A is near the slope and element B is in the free-field.

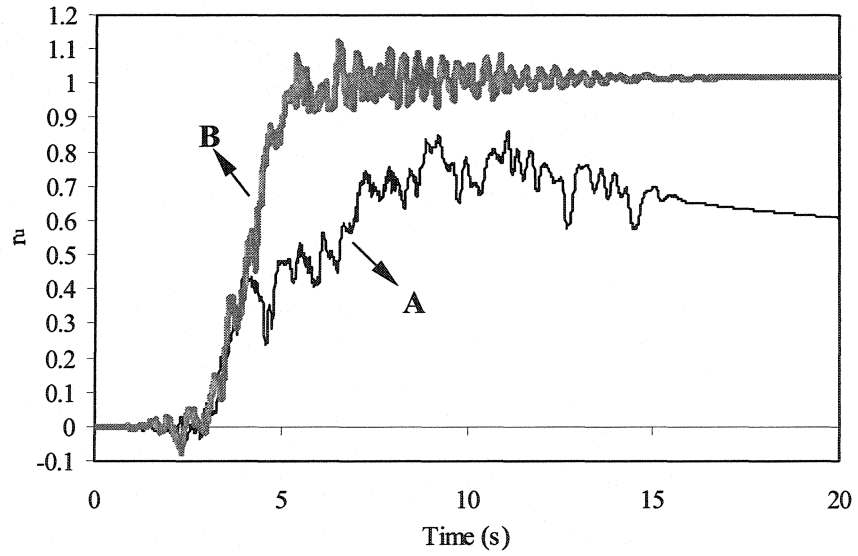

Figure 5-27. Variation of r_u with time for elements A and B shown in Figure 5-2b, in the model with B/H = 3.2, for a_{max} = 0.1g. Element A is near the slope and element B is in the free-field.

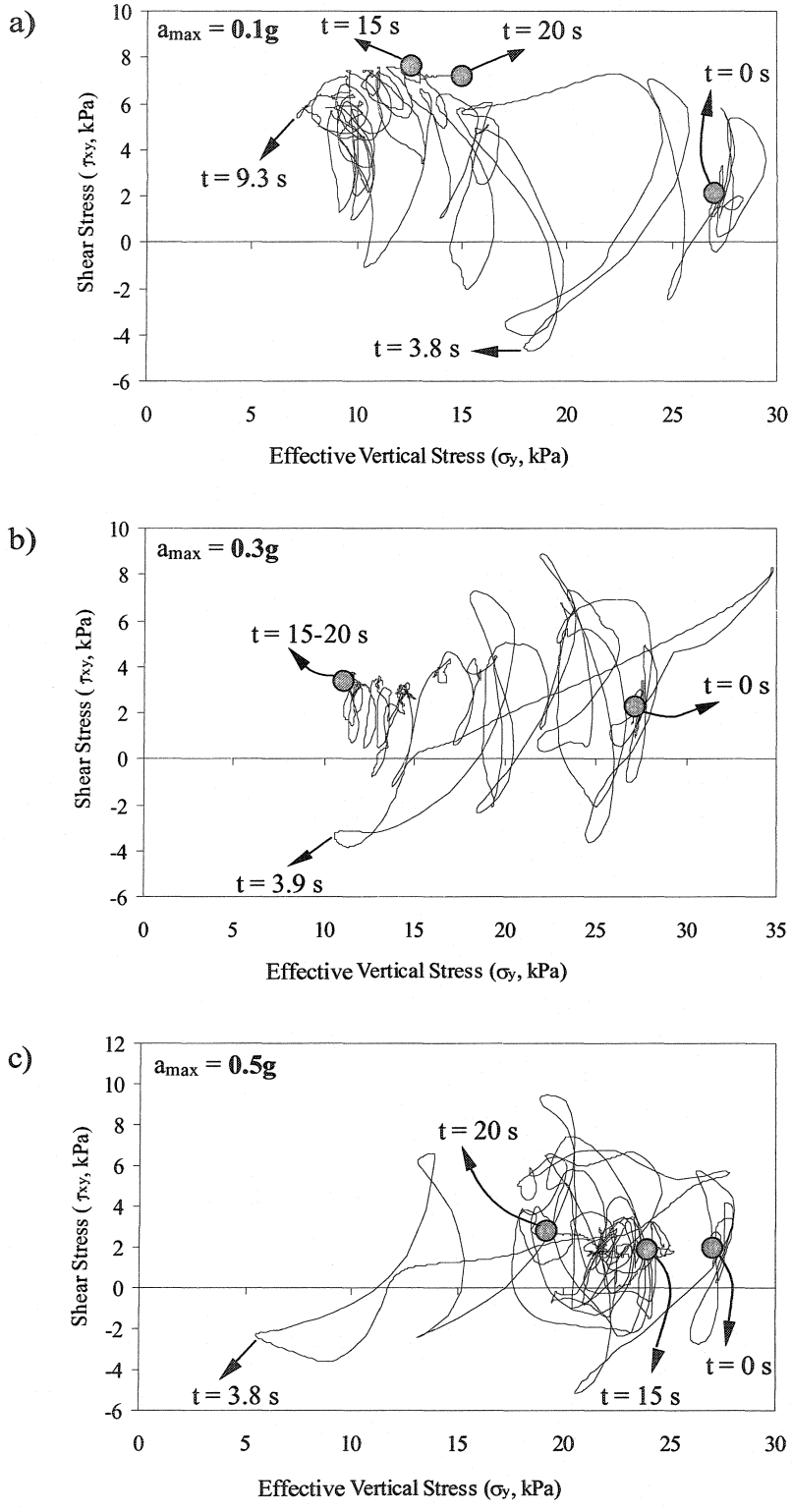

Figure 5-28. Shear stress (τ_{xy}) vs. effective vertical stress (σ_y) for element A (shown in Figure 5-2b) in the model with B/H = 3.2, obtained from the analyses where a_{max} is: a) 0.1g, b) 0.3g, and c) 0.5g.

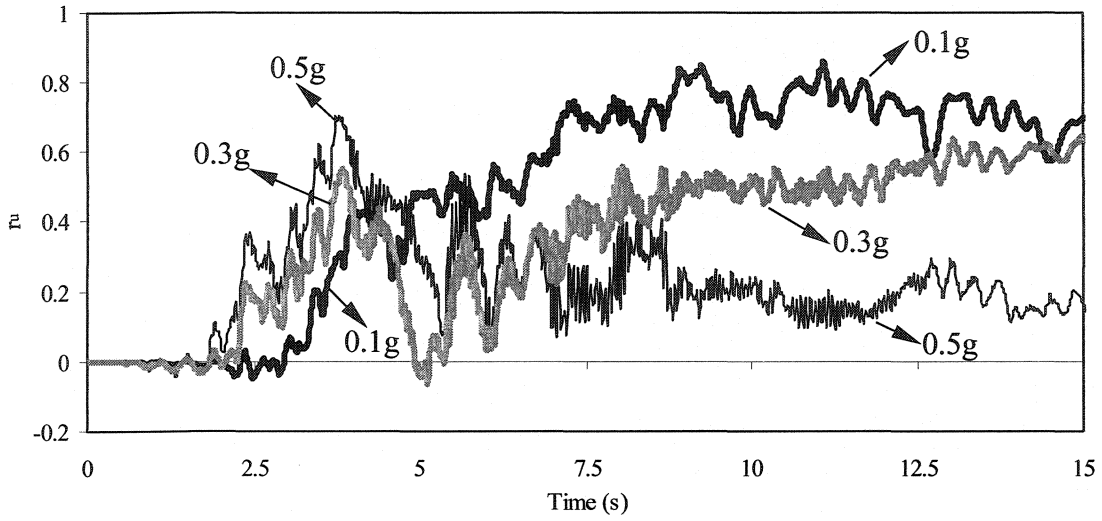

Figure 5-29. Variation of r_u with time for element A (shown in Figure 5-2b), in the model with B/H = 3.2, obtained from the analyses where a_{max} = 0.1g, 0.3 and 0.5g.

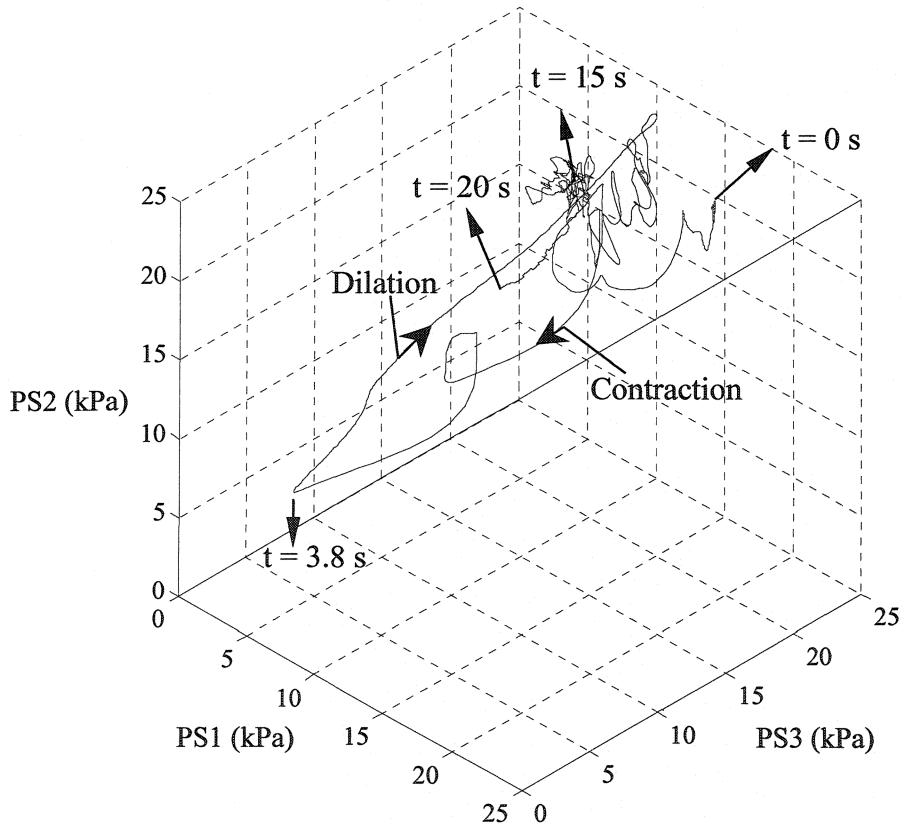

Figure 5-30. Stress path in 3D principal stress space for element A (shown in Figure 5-2b), in the model with B/H = 3.2, obtained from the analysis where a_{max} = 0.5g.

5.5.2 RSM regression models

In this section, the analysis procedure implementing transmitting boundaries, described in the previous sections, is applied to obtain regression models for the curves representing the 3D effects of lateral boundaries on the selected responses (R_d, R_s, R_r) as a function of the model width and a_{max}. The regression models are obtained by means of the RSM analysis to represent the 3D/2D ratios in a format similar to that illustrated in Figure 5-16. Similar to the procedure described earlier, only the two significant factors, i.e. model width to height ratio (B/H) and maximum acceleration (a_{max}), are selected for this study.

Crest displacement ratio (R_d): The curve plotted in Figure 5-31 is best-estimated by the following second-order polynomial regression model. Adjusted and predicted R-squared values are 0.89 and 0.81, which indicate a reasonable goodness-of-fit for the equation.

$$R_d = 0.335 + 0.205(B/H) - 0.016(B/H)^2 \text{ ; for } B/H \leq 6$$

$$R_d = 1.0; \text{ for } B/H > 6 \qquad (5\text{-}2)$$

This equation is in terms of B/H only, not a_{max}, since RSM analysis shows that the factor a_{max} is non-significant.

The regression model is only applicable to B/H < 6, beyond which the ratio is equal to unity because with B/H = 5.88 the above equation results in 1. Also, since in the analyses performed, the smallest value of B/H was 0.8 (corresponding to B/2 = 4 m) extrapolation of the above equation to smaller values should be done with caution as it is apparent that this second-order polynomial does not go to zero with B/H = 0. For the geometry and

assumptions used in this study, these results indicate that a 2D, plane strain analysis can satisfactorily replace 3D analysis if B/H > 6.

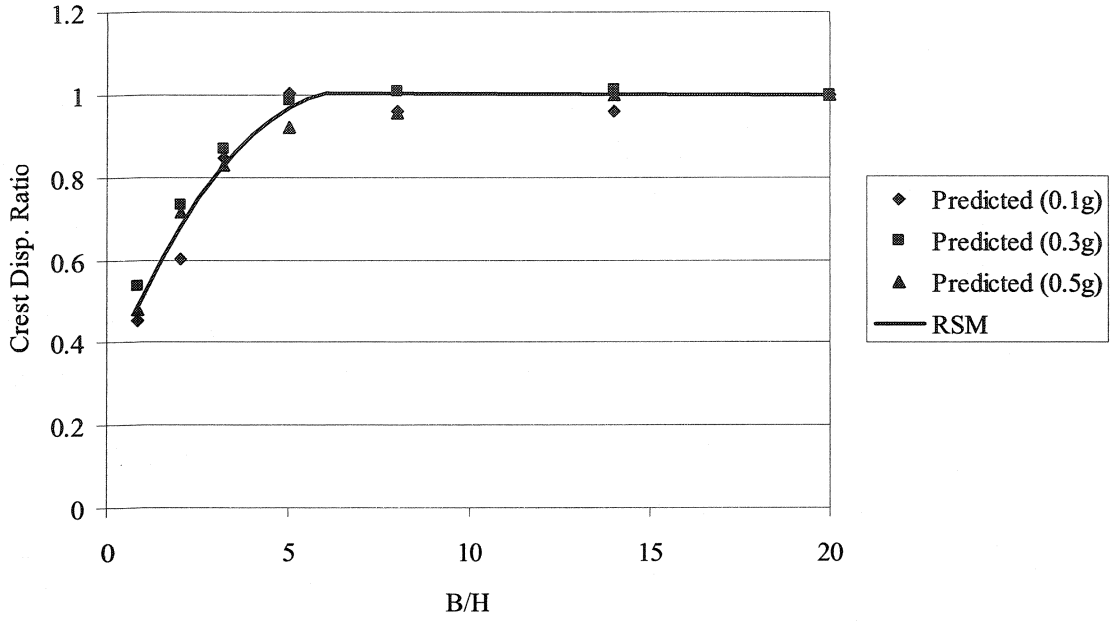

Figure 5-31. Crest displacement ratio (R_d): RSM model and analysis results for all values of a_{max}.

Shear strain ratio (R_s): Both factors B/H and a_{max} and their interaction are significant. The following second-order polynomial regression model represents the recorded results. Both adjusted and predicted R-squared values are equal to 0.97 that shows a very high goodness-of-fit.

$$R_s = 0.605 + 0.144(B/H) - 0.543(a_{max}) - 0.012(B/H)^2 + 0.062(B/H).(a_{max}); \text{ for } B/H \leq 7$$

$$R_s = 1.0; \text{ for } B/H > 7 \qquad (5\text{-}3)$$

Depending on a_{max}, the value of B/H that gives the closest R_s to unity ranges from 6.2 to 7.25; therefore, the B/H $\leq$ 7 limit is given for the above model. In other words, if B/H > 7 the 3D effects in terms of predicted shear strains are negligible. Only one limit is given for the above equation so that its use does not become unnecessarily complicated.

The recorded results and the regression model are shown in Figure 5-32. The response surface (regression model in space) is also presented in Figure 5-33, showing the non-linearity of the response in terms of B/H and its linearity in terms of a_{max}. It should be emphasized that the linearity of the 3D/2D shear strain index *ratio* in terms of a_{max} does not necessarily mean that the shear strain index itself is a linear function of a_{max}; only the ratio of 3D vs. 2D indices resulted to have a linear dependence on a_{max} for the range investigated in this study.

The analysis results show that as a_{max} increases, values of R_s decrease. This decrease is greater when B/H is lower (i.e. there is a positive interaction, in terms of the terminology used in RSM, between a_{max} and B/H). As discussed earlier in Section 5.5.1, this is because the numerical model predicts more dilation when a soil element with static shear stress is subjected to larger loading, which for the soil material analyzed here, results in more pronounced effect of the lateral boundaries. In other words, with increasing a_{max}, 3D effects become more significant.

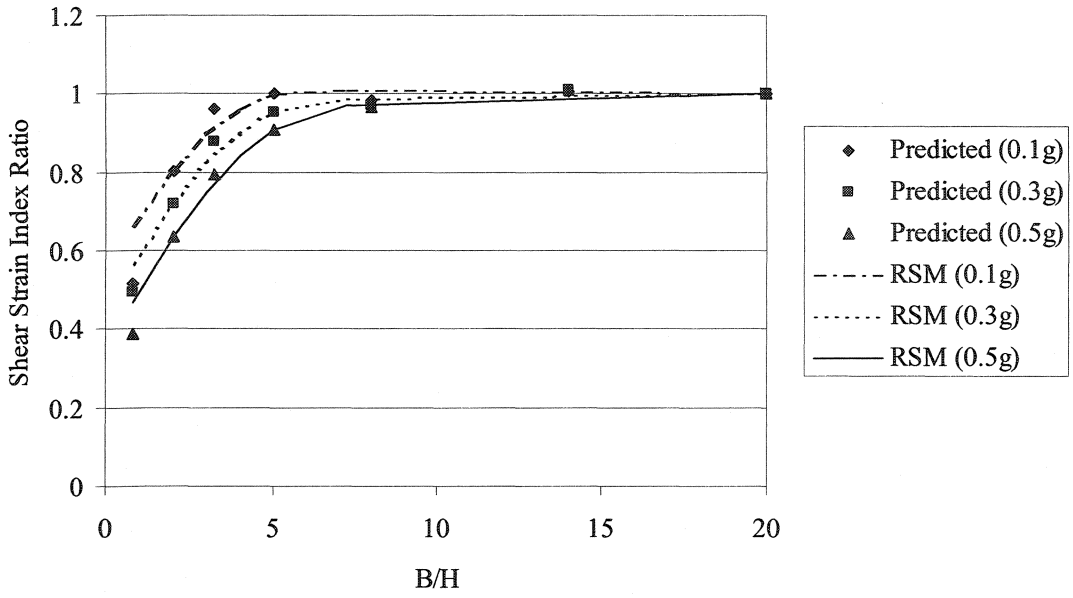

Figure 5-32. Shear strain index ratio (R_s): RSM model and analysis results for all values of a_{max}.

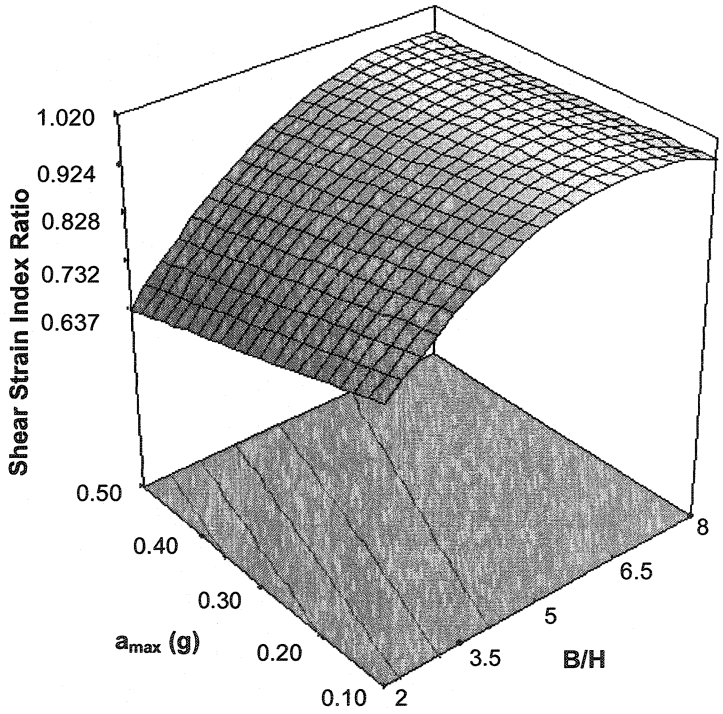

Figure 5-33. 3D presentation of the response surface for shear strain index ratio (R_s).

r_u ratio (R_r): The predicted results shown in Figure 5-34 indicate that, except for the smallest model width (B/H = 0.8), values of R_r (predicted on the symmetry plane) increase with the decrease in model width to a maximum value of 1.1, due to proximity of the lateral boundaries that induce local shearing on a vertical plane. For B/H = 0.8 and a_{max} = 0.3 and 0.5g, R_r is below 1, which is due to the fact that in this model only two rows of elements exist and the lateral boundary condition for the fluid phase affects the excess pore pressures. Setting aside the outlier values (for B/H = 0.8), the following regression model can be obtained (Figure 5-34). Adjusted and predicted R-squared values are 0.96 and 0.83, respectively, which indicate a satisfactory goodness-of-fit.

$$R_r = 1.173 - 0.034(B/H) - 0.406(a_{max}) + 1.75E\text{-}03(B/H)^2 + 0.291(a_{max})^2 + 0.034(B/H).(a_{max}); \text{ for } B/H \leq 6$$

$$R_r = 1; \text{ for } B/H > 6 \qquad (5\text{-}4)$$

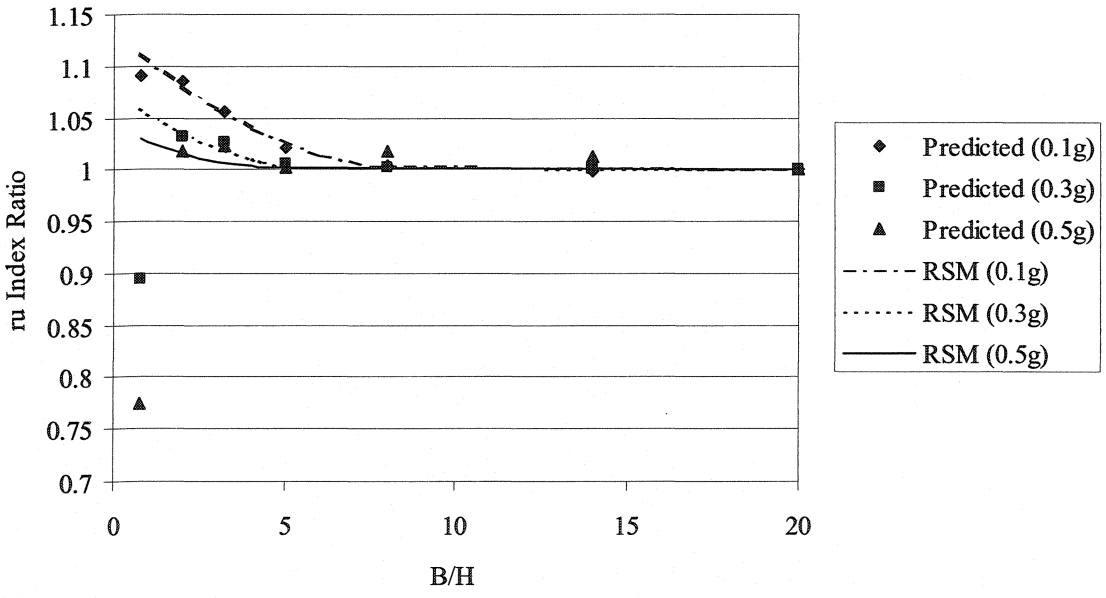

Figure 5-34. r_u index ratio (R_r): RSM model and analysis results for all values of a_{max}.

5.5.3 *Effect of slope angle*

The results presented so far were obtained for a 3H:1V slope. A limited study was performed to evaluate the effect of slope angle. The results obtained for 4H:1V and 2H:1V slopes as well as the 3H:1V slope (with B/H = 2 and 5, and a_{max} = 0.3g) are given in Table 5-4. The values in Table 5-4 indicate that for the cases analyzed here, the slope angle does not significantly influence the results in terms of 3D vs. 2D predictions.

Table 5-4. Effect of slope angle

	B/H = 2			B/H = 5		
Slope	R_d	R_s	R_r	R_d	R_s	R_r
2H:1V	0.74	0.77	1.04	1.00	0.97	1.01
3H:1V	0.73	0.72	1.03	0.99	0.95	1.01
4H:1V	0.73	0.74	1.03	0.99	0.95	1.01

5.5.4 *Updated Material Properties*

For the material properties calibrated based on the new tests performed at the University of British Columbia on the Fraser River sand, i.e. set #2 described in Section 3.6, the ratios R_d, R_s, and R_r for the model with B/H = 3.2 and a_{max} = 0.3g are 0.80, 0.80, and 1.02, respectively. The ratios obtained for the first set of material properties (set #1) were 0.87, 0.88, and 1.03, respectively. The regression models predict these ratios as 0.83, 0.84, and 1.02, respectively. These results indicate that the 3D effects are slightly more significant when updated material properties (set #2) are used. As these properties correspond to a soil with larger dilation parameter (X_{pp} = 0.3 vs. 0.2), although the rate of excess pore water pressure build-up is faster especially for areas with no static shear stress, the amount of dilation that takes place in the zones just below the slope face is

greater. This leads to the same effect explained in Section 5.5.1, where larger acceleration leads to lower pore pressures under the slope and therefore, the constraint effect of the lateral boundaries becomes more pronounced

5.5.5 *Effect of Transverse Loading*

Effect of transverse loading, which cannot be accounted for in a 2D analysis, is partially examined here by performing two analyses. As opposed to the analyses described so far, where due to symmetric loading only half of the structure was included in the analysis, the whole structure is analyzed here. Details of boundary conditions are shown in Figure 5-35. The main differences compared to the previously used boundary conditions (described in Section 5.2.2) are:

1. The earthquake acceleration is applied along the z-direction instead of the x-direction.
2. The planes with transmitting boundary conditions are switched, i.e. in this case, x = 0 and x = L planes have transmitting boundaries. In other words, the planes perpendicular to the direction of loading do not have transmitting boundaries.
3. Nodes with slaved degrees-of-freedom for horizontal fluid motion are now located on the z = 0 and z = B planes and the very next planes of nodes. In this case, the sixth degree-of-freedom (horizontal component of fluid motion in the z-direction) of each node located on those faces is slaved to that of the corresponding node located on the very next vertical plane of nodes.

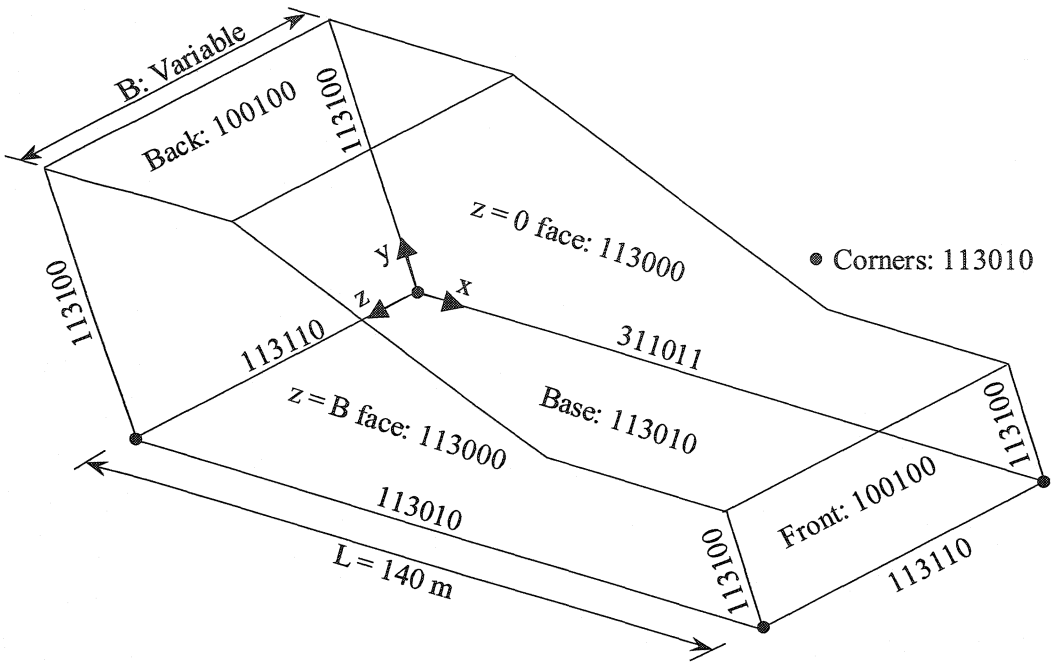

Figure 5-35. Boundary conditions of the 3D model subject to transverse loading. The boundary condition codes are according to the definitions given in Table 5-1, with the following order: x, y, z components of solid phase motion, and x, y, z components of fluid phase motion.

Two structures with B/H = 2 and 8, subject to a_{max} = 0.3g, are analyzed. Figure 5-36 to Figure 5-38 show contours of results, with only one half of the mesh presented (from z = 0 to z = B) so that the distribution of results in depth can be visible. At the selected time instant of t = 15 s that is after the end of shaking, the contours are almost symmetric with respect to the z = B/2 plane.

3D/2D ratios of responses (R_d, R_s, and R_r), as given in Table 5-5, can be calculated assuming that the mesh with B/H = 8 is equivalent to a 2D configuration. Also given in Table 5-5 are the values of these ratios calculated from the regression models presented before.

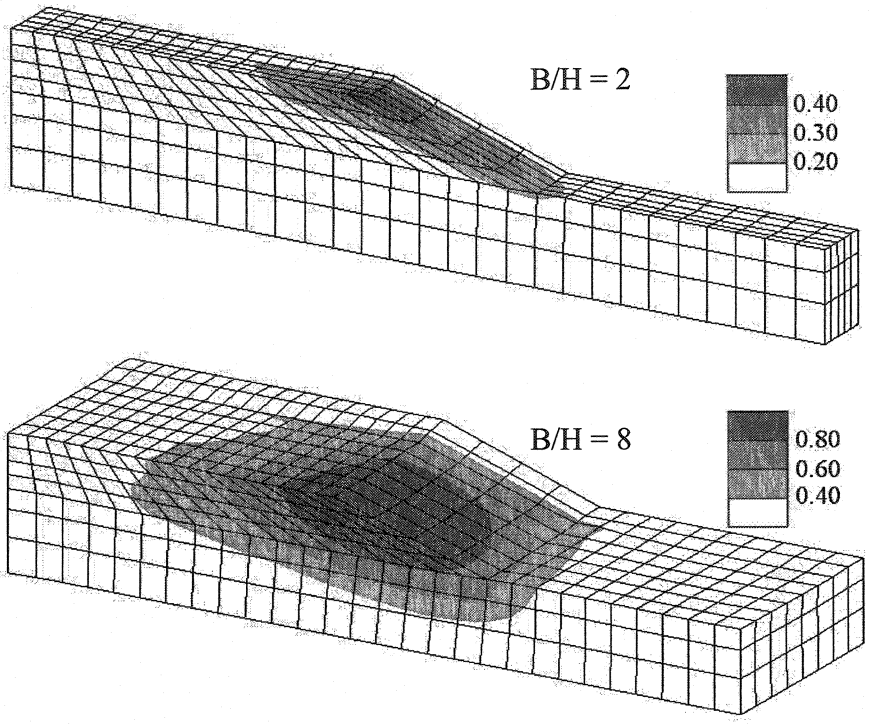

Figure 5-36. Contours of total displacement (m) induced by transverse loading for B/H = 2 and 8, and a_{max} = 0.3g at t = 15 s. Deformation magnification scale is 2.

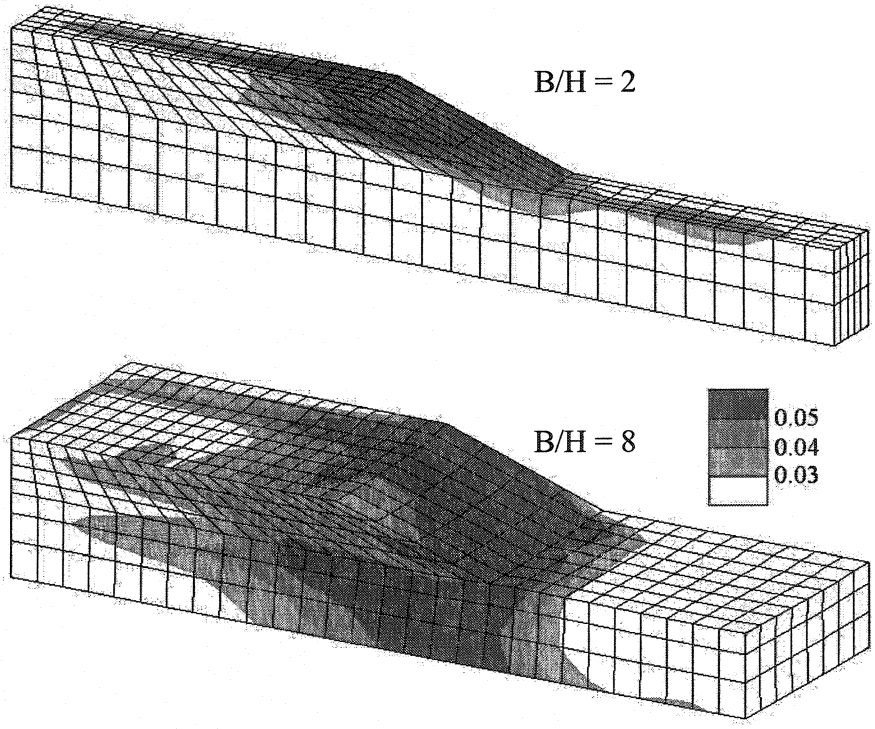

Figure 5-37. Contours of maximum shear strain induced by transverse loading for B/H = 2 and 8, and a_{max} = 0.3g at t = 15 s. Deformation magnification scale is 2.

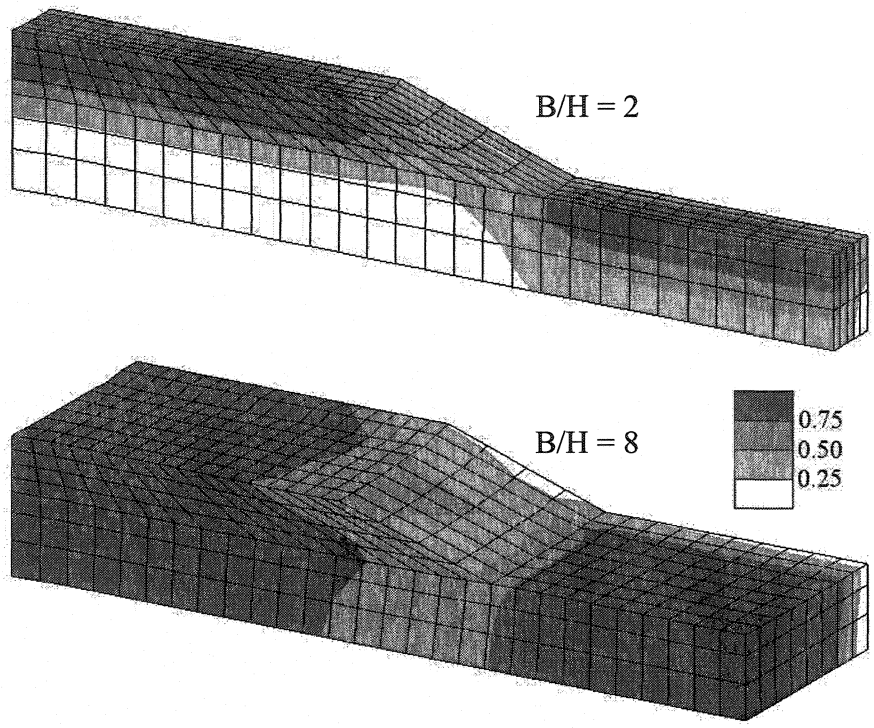

Figure 5-38. Contours of excess pore pressure ratio (r_u) induced by transverse loading for B/H = 2 and 8, and a_{max} = 0.3g at t = 15 s. Deformation magnification scale is 2.

Table 5-5. Comparison between 3D/2D ratios of responses (for B/H = 2, and a_{max} = 0.3g) calculated from cases of parallel and transverse loading.

Loading	R_d	R_s	R_r
Transverse	0.49	0.59	0.75
Parallel	0.68	0.72	1.04

The following points are notable:

1. The large difference between the two groups of ratios obtained from the analyses with transverse and parallel loading, and the fact that the ratios obtained for transverse loading are much lower, indicate that the 3D effects are more significant in the case of transverse loading. In other words, 3D configuration or proximity of the lateral boundaries may have greater importance for transverse loading than for parallel loading. Also, this may raise the question if B/H = 8 can

be considered sufficient for assuming 3D effects of lateral boundaries as insignificant.

2. The predicted displacements are much lower in this case compared to the case of parallel loading, by about 50% (also compare Figure 5-36 with Figure 5-18), which indicates that parallel loading is the critical mode of loading.
3. Shear strains, like displacements, are also lower in this case. Zones with higher shear strains are located near the base of the analysis domain in the case of transverse loading, as opposed to the other case in which those zones stretch from the base to the slope face.
4. In both cases, the predicted r_u below the slope is lower than in other locations in the analysis domain (see Figure 5-38 and Figure 5-24). However, another significant effect of transverse loading is that, in contrast to the case of parallel loading, the predicted r_u in the mesh with lower B/H is lower than that in the one with higher B/H. In other words, the decreasing trend of R_r with increasing B/H, as observed in the case of parallel loading (Figure 5-34), is not observed here for the transverse loading case.

All above conclusions have been made based on the results of a very limited study. More investigations are necessary in this respect.

It is also worth mentioning that the effects of vertical component of earthquake loading may be significant as well. This subject is recommended for a further study.

5.5.6 Comparison with previous studies

As noted in the literature review (Section 2.3.4), according to Duncan (1996), with a few exceptions, most of the 3D slope stability analyses have resulted in higher factors of

safety compared to those resulting from 2D analyses, and 2D deformation analyses have given higher values of displacements, strains and stresses compared to 3D analysis results. None of the studies cited by Duncan (1996) refer to dynamic, effective-stress, non-linear analyses, such as the one performed here.

The results presented here are in general agreement with the previous studies in the sense that the crest displacement and shear strain index predicted in 3D analyses are lower than those predicted in 2D. Excess pore pressure ratios predicted in 3D analyses, in the vicinity of local boundaries, are higher than those predicted in 2D analyses apparently due to local shearing.

Ratios of 3D/2D factors of safety given by previous studies are herein compared to the 3D/2D ratio of the inverse of shear strain index, as explained hereafter. The factor of safety is normally defined as the ratio of the total available shear resistance to the total mobilized shear stress along a postulated failure surface. Because with the increase in the shear stress mobilized on the failure surface the shear strains increase, the factor of safety can be qualitatively related to the inverse of shear strains occurring in the vicinity of the failure surface. In other words, if shear strains are higher, the mobilized shear stresses are also higher and therefore the factor of safety can be assumed to be lower. As the factor of safety is calculated by dividing the existing shear stresses by a limit shear stress (or shear strength), one may divide the existing shear strains by a limit value to normalize the mobilized shear strains with respect to a value corresponding to failure. However, since in this study only the 3D/2D ratio of response is of primary interest, there is no need for such normalization. It should also be mentioned that the shear strain index considered here is calculated over an arbitrarily selected zone close to the slope face (on the plane of

symmetry) and not on a possible failure surface. Moreover, the selection of this index may not be appropriate when large (unlimited) shear strains occur in both 2D and 3D analyses. An index involving shear stresses would give a better image in this situation; however, because in this type of analysis the shear stresses are highly oscillatory, use of such an index is deemed impractical.

It is of course generally possible to calculate the factor of safety using the stress distribution predicted by a finite element solution. As discussed by Krahn (2003), integrating the limit equilibrium analysis with the finite element method overcomes the main shortcoming of the former, namely neglecting the compatibility conditions. As for dynamic loading, the same idea can be applied by using the stress distribution provided by a dynamic finite element analysis. The difference is that the factor of safety for any given failure surface is variable with time.

The procedure that is usually followed for computing the factor of safety from finite-element-calculated stresses consists of the following steps (summarized after Krahn, 2003), assuming that a potential failure mass is divided into a number of slices:

1. Knowing the stress components at Gauss points, projected to and averaged at each nodal point, stress components at any point inside any element can be calculated.

2. Knowing the stress components for the midpoint of the base of each slice, and the inclination of the base line, for a given potential failure surface, the normal and shear stresses at the base of each slice can be calculated.

3. Knowing the normal stress, the available shear resistance for each slice can be calculated.

4. The factor of safety can be calculated by integrating the ratio of available shear resistance vs. mobilized shear stress over the slip surface.

Such calculations involve a great amount of post-processing of the results for this study, especially for 3D analyses, because in addition to performing the above procedure for each case, a search for the critical slip surface that has the minimum factor of safety should be done. Moreover, since the analysis is dynamic, which causes the variation of the factor of safety with time, a time instant at which the factor of safety is minimum for a given failure surface should be found. The shear strain index is used here to avoid the cumbersome procedure described above.

As for quantifying the 3D effects as a function of slope width/height ratio, Figure 5-39 gives a comparison between the results of the present study and a previous study by Arellano and Stark (2000), based on the factor of safety approach to static stability analysis. The shaded area is obtained from the present study from the inverse shear strain index ratio for values of a_{max} = 0.1 to 0.5g. Although the two studies are essentially different (static vs. dynamic, and factor of safety vs. deformation analysis), the results are in the same range. The strong effect of the slope angle shown by the Arellano-Stark curves results from an increase in the area of the vertical sides of the slide mass due to the way the slope geometry was defined in their study (Figure 5-40). In this study, however, since the change in slope angle does not significantly change the area of the lateral boundaries, such an effect resulted less significant.

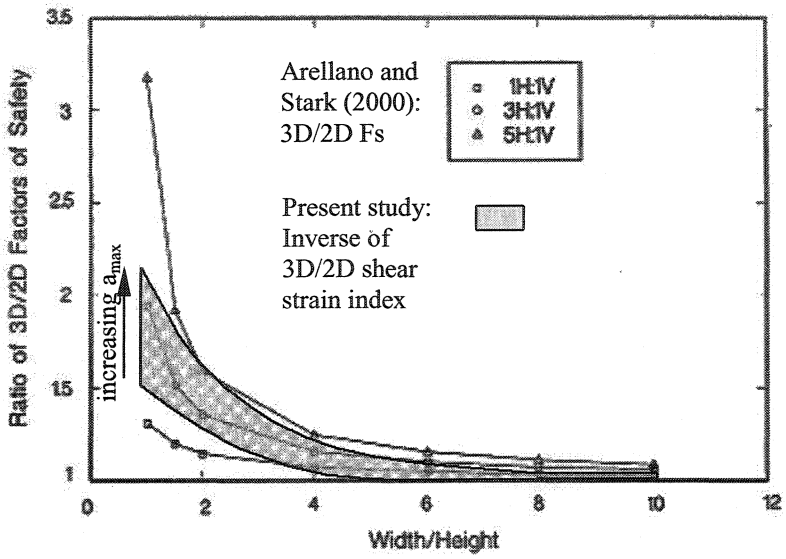

Figure 5-39. Comparison with a previous study (Arellano and Stark, 2000).

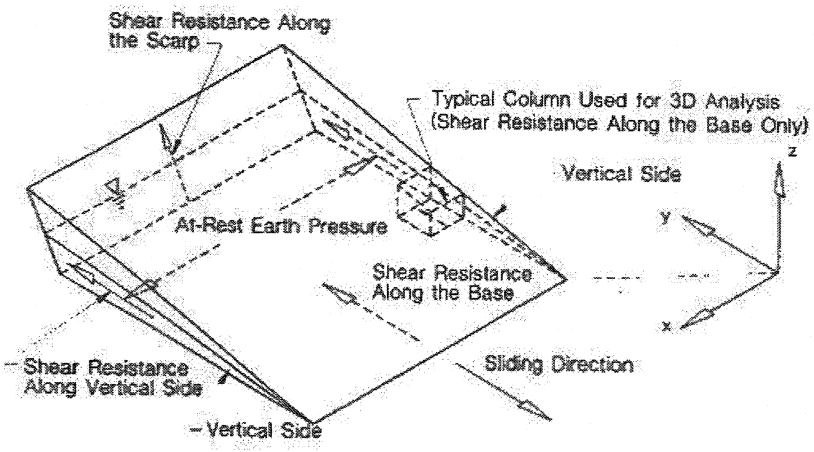

Figure 5-40. 3D Geometry of the slope studied by Arellano and Stark (2000).

Chugh (2003) presents static, finite element-based analysis of the same slope geometry analyzed by Arellano and Stark (2000). It is concluded that for width/height ratios greater than 5, the differences between F_{2D} and F_{3D} tend to lose significance. This value corresponds to a tolerance of about 15%. Based on the same level of tolerance, the present analysis results show that for B/H > 3 – 5 the 2D and 3D results are almost the same. The regression models obtained in this study, however, showed slightly higher limits, about 6 – 7, of very little tolerance is allowed.

Table 5-6 presents selected data from some other studies. The values for the present study are from the regression model obtained for shear strain index ratio with a_{max} = 0.3g. These values are larger than the values from previous factor-of-safety studies, which may be another indication that the 3D effects are more significant in a dynamic analysis than in a static analysis.

Table 5-6. Comparison with some previous studies.

Study	B/H	3D/2D Factor of Safety	Present Study Inverse of 3D/2D shear strain index
Dennhardt and Forster (1985)	0.89	1.2	1.7
Hungr et al. (1989)	2.45	1.2	1.3
Leshchinsky and Huang (1992)	2.00	1.3	1.4

5.6 Conclusion

A comparison is made between the results of three- and two-dimensional seismic analyses of submarine slopes, using dynamic, effective stress, fully coupled, nonlinear finite element analysis. Outcomes of this study provide some quantitative guidelines for geotechnical practice in this particular area of soil dynamics to extrapolate results of less expensive, simplified 2D analyses to more realistic 3D behaviour.

The comparison is in terms of several factors and responses. The factors are model width (or distance between lateral boundaries) normalized as width/height ratio (B/H), maximum acceleration of earthquake (a_{max}), and mesh size (fine/coarse). The responses are ratios of 3D to 2D results, namely, crest displacement, a shear strain index, and an excess pore water pressure ratio (r_u) index. These ratios are referred to as R_d, R_s and R_r, respectively.

The following conclusions can be drawn based on the results of this comparison:

- The study includes application of two types of boundaries, i.e. rigid and transmitting boundaries. In case of rigid (non-transmitting) boundary conditions, a peak in displacement is observed at a certain distance from the lateral boundary, irrespective of the B/H ratio. This peak is eliminated when transmitting boundary conditions are used. While wave reflection is a real phenomenon for the structure analyzed here, its effects had to be minimized to obtain comprehensible results for this study.
- Regression models are provided (see Eqs. (5-2) to (5-4) plotted in Figure 5-31 and Figure 5-34) to relate the responses (R_d, R_s and R_r) and the factors (B/H and a_{max}) for practical extrapolation of 2D analysis results to 3D situation. For example, if the 3D model has a B/H ratio of 2, and the earthquake peak acceleration is 0.2, Eqs. (5-2) to (5-4) indicate that, for the 3D model on the plane of symmetry: 1) crest displacement is about 0.68 of that in the 2D model; 2) shear strains predicted under the slope are on average about 0.76 of that in the 2D model; and 3) excess pore pressures are on average about 8% larger than those in the 2D model. Additionally, for B/H ratio as low as one, the 3D crest displacement and shear strain index are approximately 50% of those predicted in 2D analyses, whereas excess pore pressure is 10% higher in 3D than in 2D analysis.
- The analysis results show that a 2D analysis is sufficiently accurate, i.e. based on a tolerance of about 15%, if the width/height ratio (B/H) of the slope is greater than 3 – 5. This value generally increases with the increase in maximum acceleration of the applied earthquake motion. Moreover, for B/H >

6 – 7, the difference between 3D analysis predictions on the symmetry plane of the slope and 2D analysis predictions was found to be insignificant. The larger values of the limit correspond to larger seismic accelerations.

- The results of this study are also compared with those from some previous studies by comparing the inverse shear strain index ratio ($1/R_s$) with the ratio of 3D/2D factors of safety. The variations of these quantities as a function of B/H are also compared. For example, assuming that the ratio of 3D/2D factors of safety is proportional to $1/R_s$, for a slope with B/H = 2 subjected to a_{max} = 0.2, one may infer from Figure 5-39 that the 3D factor of safety is about 30 – 35% larger than the 2D factor of safety.
- It is found that the peak acceleration (a_{max}) has a significant effect on the shear strain index ratio (R_s): for a constant B/H, R_s is lower for higher a_{max}. This indicates that the 3D effects are predicted to be more significant when a_{max} is larger, which can be attributed to the fact that, for the soil properties assumed here, the constitutive model predicts larger dilation for areas below the slope face (with static shear stress) when larger cyclic load is applied. That is, more dilation results in stiffer soil and thus more pronounced constraint effects of the lateral boundaries.
- For the particular cases analyzed here, with vertical lateral boundaries, it also resulted that the change in slope angle does not affect the 3D/2D ratios mainly because the change in slope angle does not change the area of the lateral boundaries to impose more/less resistance against the deformation on the plane of symmetry.

- It is also found that a soil with slightly lower liquefaction strength and slightly higher dilation parameter (X_{pp}), which is defined in the multi-yield surface constitutive model to control the amount of contraction/dilation during shearing, can have slightly more significant 3D effects, because of the impact the dilatant behaviour under the slope has on the constraint effect of the boundaries.
- A limited study on the effects of transverse loading showed that the 3D effects of lateral boundaries are more significant when the slope is subjected to transverse loading than when it is subjected to seismic loading along the slope direction. For example, the crest displacement on the plane of symmetry of the 3D model with B/H = 2 is about 0.5 of that in the model with B/H = 8, for the case of transverse loading, whereas this ratio is about 0.7 for the case of parallel loading. However, further study is needed in this respect to cover a wider range of B/H.

Chapter 6 - CONCLUDING REMARKS

6.1 Summary and Conclusions

A large amount of evidence is now available on submarine slope failures. These failures can be triggered by several phenomena including earthquakes. Soil liquefaction is one of the most important phenomena associated with seismically induced submarine slope failures. Correct prediction of dynamic effects of earthquakes on saturated soil deposits requires the correct simulation of dynamic soil behaviour and accounting for 3D effects. In this research, a more rigorous analysis is used which considers the observed dynamic soil behaviour aspects.

To study two important features of submarine slope failures, i.e. retrogression of failures and three-dimensional effects, two- and three-dimensional (2D and 3D) seismic analyses of submarine slopes are performed using a numerical method, employing: (1) a multi-yield surface plasticity soil constitutive model, and (2) solid-fluid coupled-field analysis. The numerical model is implemented in the finite element program Dynaflow.

The main purposes of the analyses carried out in this research are to provide quantitative and qualitative assessments of those features, i.e. retrogression of slope failures and three-dimensional effects, for geotechnical practice, as well as enhancing understanding of the mechanisms involved. The simulation of retrogression aims at drawing the attention to the importance of accounting for this effect in evaluating the potential hazards for off-shore structures. The comparisons made between the 2D and 3D responses of slopes is believed to be useful for deciding whether expensive, time-consuming, full 3D analyses are necessary in a practical situation.

In Chapter 3, the constitutive model parameters required for the analyses have been obtained for two types of sand, namely, Nevada and Fraser River sands:

- The Nevada sand properties are the basis for the soil properties used in the analysis of retrogressive failures (Chapter 4). They are based on the laboratory tests performed in the framework of the VELACS project (VErification of Liquefaction Analysis by Centrifuge Studies), conducted in early 1990's. One of the VELACS centrifuge tests, which represents an infinite submarine slope inclined at a 2^{o} angle, is used to validate the numerical model and selected soil parameters. This verification along with the more comprehensive studies performed by Popescu and Prevost (1993a, 1993b, 1995) indicate that the numerical model used in this study can accurately predict seismic behaviour of liquefiable soils.
- Fraser River sand properties were inferred from the literature and used in the study of 3D effects (Chapter 5). Upon the completion of some recent laboratory tests at UBC as part of an ongoing research project (Earthquake Induced Damage Mitigation from Soil Liquefaction), a set of updated material properties were also estimated and then used in the study.
- A procedure is used for calibration of some soil parameters of Fraser River sand based on liquefaction strength analysis. The procedure uses Response Surface Methodology, for efficient estimation of a set of parameters that produces the best-fit curve for the data recorded in laboratory cyclic simple shear tests. The liquefaction strength curve, i.e. the plot of cyclic stress ratio vs. number of cycles to liquefaction, is the basis for this calibration.

In Chapter 4, an algorithm for finite element simulation of retrogressive failures is introduced and used in a comprehensive study of this phenomenon; and some limitations of the study are discussed. The method uses the element removal capabilities of the finite element program to model a soil mass that fails and then flows away, causing upper parts of slope to fail retrogressively due to loss of support. To better understand the mechanisms involved, idealized geometries and soil layering configurations are analyzed, leading to the following conclusions:

- It is found that the extension of failure increases significantly because of both a gentle slope of the seafloor and/or presence of a silt layer. The effects of a shallow silt layer (with much lower permeability than sand) and of a gently sloping seafloor (with a 2^{o} angle to horizontal) on the extension of retrogression in a sandy seabed are explained through predicted stress paths and soil shear strength before and after a soil failure.
- Retrogression distances for all cases as well as the removal times are addressed. For example, for the soil materials considered here, when the seafloor located to the back of the slope (1H:3V, 10 m height) is flat, presence of a superficial silt layer increases the retrogression distance from about 50 m to about 200 m.
- For a slightly sloping seabed located to the back of a potentially unstable slope, it is found that a retrogressive failure of a theoretically infinite extension can occur. The mechanisms of such failures are explained and the depths of failure surfaces predicted by the finite element program are compared with the result of a simple analysis. In this study, presence of the artificial boundaries of the

analysis domain limits the extension of failure. However, in a natural slope, such a mechanism (infinite failure) can be limited by natural changes in material properties, soil stratigraphy, and so on.

- The effect of mesh refinement is also assessed to be insignificant.

In Chapter 5, a numerical study on 3D effects in seismic analysis of slopes is presented. Assessment of the 3D effects or the differences between 3D and 2D analyses results has been the subject of many studies, where either the factor-of-safety (Fs) or the deformation analysis approach has been used. The majority of them have concluded that 2D results are more conservative than 3D ones: 3D factor of safety is usually greater than the 2D one, and displacements or strains in 3D are lower than in 2D. Since the 2D analyses are based on the plane strain assumption that is valid when the width of the slope is very large compared to its height, some studies (e.g. Arellano and Stark, 2000) have presented comparisons of the results as a function of slope width/height ratio (B/H).

Similarly in this study, limits of applicability of the 2D plane strain assumption are assessed for the seismic analysis of submarine slopes. This is done by comparing the results of 2D and 3D analyses, with 3D models having different widths. The width/height ratios (B/H) of the 3D models are variable so that a limit value can be found, above which the approximate 2D response is sufficiently close to the exact 3D response. The study also accounts for some other factors such as peak acceleration of the earthquake record, mesh refinement, and slope angle.

To compare the results, seismic response of the slope in both 2D and 3D cases is determined in terms of three different quantities, namely: slope crest displacement, a shear strain index indicating an average shear strain developed in a selected zone near the

face of the slope, and an excess pore water pressure ratio (r_u) index indicating an average value of r_u developed in a selected zone of the analysis domain. Results of 3D analysis are taken from the plane of symmetry of the model. It is concluded that:

- Use of a transmitting boundary condition for the lateral boundaries of the 3D model is necessary to alleviate some of the effects of a fixed, rigid boundary so that the seismic shear wave reflection effects and consequently the wave interference phenomena are reduced.
- Regression models presented in this study, providing the ratios of 3D/2D responses as a function of width/height ratio and maximum acceleration of earthquake can be used in practical applications to extrapolate 2D analysis results to 3D situations.
- A 2D analysis can replace the time-consuming, expensive 3D analysis with no significant modification (for a tolerance of about 15%) if width/height ratio (B/H) of the slope is larger than 3 – 5 (depending upon the type of response), with larger values corresponding to larger seismic accelerations.
- The effect of earthquake peak acceleration is found significant as to cause more dilation in the zones below the slope, and therefore, more pronounced effects of the lateral boundaries.
- Influence of a few other factors, such as slope angle and slight change in material properties, are found (by limited number of analysis) to be insignificant or slightly significant.

- The 3D effects are found to be more significant when slope is subjected to transverse loading than when it is subjected to parallel loading, yet further study is needed to quantify those effects in this case.

6.2 Future Work

For future work, based on the procedures introduced and explained in this thesis, it is recommended to:

1. Further validate the numerical model predictions based on the results of centrifuge tests that are ongoing under NSERC sponsorship (see e.g. http://www.civil.ubc.ca/liquefaction);
2. Extend the area of applicability by addressing a larger range of soil types and slope geometries.
3. Use results of laboratory soil tests and geophysical investigations (such as advanced 3D seismic profiling of seabed), which will be published in near future in the framework of projects such as COSTA-Canada (http://www.costa-canada.ggl.ulaval.ca/english.html), to re-calibrate the soil parameters and study the effects of retrogression and 3D configuration for locations of interest such as Fraser River Delta, Grand Banks, etc.
4. Extend the analysis of 3D effects to account for combined loading, i.e. parallel, transverse, and vertical loading all included.

Overall, it is sincerely hoped that all the attempts made for this research can be useful for future practical applications as well as theoretical enhancement.

REFERENCES

Adam, M., Pflanz, G., Schmid, G. (2000). "Two- and three-dimensional modelling of half-space and train-track embankment under dynamic loading." Soil Dynamics and Earthquake Engineering, 19 (8): 559 – 573.

AEA Technology (1999). "CFX-4.3: Flow Solver User Guide." Oxford, AEA Technology.

Andersen, A., and Bjerrum, L. (1967). "Slides in subaqueous slopes in loose sand and silt." Marine Geotechnique, ed., Richards, A. F., Urbana, Illinois, 221 – 239.

Anderson, M. G., and Richards, K. S. (1987). Slope Stability, Geotechnical Engineering and Geomorphology. John Wiley & Sons. New York.

Ang, H.S., and Newmark, N.M. (1972). "Development of a transmitting boundary for numerical wave motion calculations." Report 2631, Defense Atomic Support Agency, Apr.

Arellano, D. and Stark, T.D. (2000). "Importance of three-dimensional slope stability analyses in practice." Slope Stability 2000, ASCE, Geotechnical Special Publication No. 101, 18 – 32.

Arulanandan, K., and Scott, R.F., editors (1993). "Proc. Int. Conf. on Verif. Numerical Procedures for the Analysis of Soil Liq." Problems, Vol. 1, Balkema, Rotterdam.

Arulanandan, K., and Scott, R.F., editors (1994). "Proc. Int. Conf. on Verif. Numerical Procedures for the Analysis of Soil Liq." Problems, Vol. 2, Balkema, Rotterdam.

Arulmoli, K., Muraleetharan, K.K., Hosain, M.M., and Fruth, L S. (1992). "VELACS laboratory testing program, soil data report." The Earth Technology Corporation, Irvine, California, Report to the National Science Foundation, Washington D.C.

Atkinson, J. H. (1981). Foundations and Slopes. McGraw-Hill, London

Azizian, A. and Popescu, R. (2001). "Backanalysis of the 1929 Grand Banks submarine slope failure." Proceedings, 54th Canadian Geotechnical Conference, Calgary, Alberta, Canada, Vol. 2, 808 – 815.

Baybutt, P., Cox, D.C., Kurth, R.E. (1981). "Methodology for uncertainty analysis of light water reactor meltdown accident consequences." Topical report form BCL to NRC.

Beaty, M., and Byrne, P.M. (1998). "An effective stress model for predicting liquefaction behaviour of sand." Geotechnical Earthquake Engineering and Soil Dynamics III, eds., P. Dakoulas, M.Yegian, and R Holtz, ASCE, Geotechnical Special Publication, 75 (1), 766 – 777.

Been, K., and Jefferies, M.G. (1985). "A state parameter for sands." Geotechnique, 35(2), 99 – 112.

Been, K., Conlin, B.H., Crooks, J.H.A., Fitzpatrick, S.W., Jefferies, M.G., Rogers, B.T., and Shinde, S. (1987). "Discussion: Back analysis of the Nerlerk berm liquefaction

slides." Can. Geotech. J., 24, 170 – 179. Original paper by Sladen et al. (1985), Can. Geotech. J., 22, 579 – 588.

Been, K., Jefferies, M.G., and Hachey, J. (1991). "The critical state of sands." Geotechnique, 41(3): 365 – 381.

Belloti, R., Ghionna, V., Jamiolkowski, M., Lancellotta, R., and Manfredini, G. (1986). "Deformation characteristics of cohesionless soils from in-situ tests." In Use of In-Situ Tests in Geotechnical Engineering, S.P. Clemence, editor, 47 – 73.

Bielak, J. and Christiano, P. (1984). "On the effective seismic input for non-Linear soil-structure interaction systems." Earthquake Engineering and Structural Dynamics, Vol. 12, 107 – 119.

Biot, M.A. (1962). "Mechanics of deformation and acoustic propagation in porous media." Journal of Applied Physics, 33(4), 1482 – 1498.

Bishop, A. W. (1955). "The use of the slip circle in the stability analysis of slopes." Geotechnique, 5(1), 7 – 17.

Bjerrum, L. (1954). "Geotechnical properties of Norwegian marine clays." Géotechnique, 4, 49 – 69.

Boe, R., Hovland, M., Instanes, A., Rise, L., and Vasshus, S. (2000). "Submarine slide scars and mass movements in Karmsundet and Skudenesfjorden, southwestern Norway: morphology and evolution." Marine Geology, 167, 147 – 165.

Box, G. E. P., and Draper, N. R. (1987). Empirical Model-Building and Response Surfaces. John Wiley & Sons, New York.

Box, G. E. P., and Wilson, K. B. (1951). "On the experimental attainment of optimum conditions." Journal of the Royal Statistical Society B, 13, 1 – 45.

Bugge, T., Befring, S., Belderson, R.H., Eidvin, T., Jansen, E., Kenyon, N.H., Holtedhal, H., and Sejrup, H.P. (1987). "A giant three-stage submarine slide off Norway." Geo-Marine Letters, 7, 191 – 198.

Byrne, P.M., and McIntyre, J. (1994). "Deformations in granular soils due to cyclic loading." Proc. Settlement '94, A.T. Yeung and G.Y. Felio, editors, College Station, Texas, 1864 – 1896.

Byrne, P. M., Park, S., Beaty, M., Sharp, M., Gonzalez, L., and Abdoun, T. (2003), "Numerical modelling of liquefaction and comparison with centrifuge tests." Submitted to Canadian Geotechnical Journal.

Byrne, R. J., Kendall, J., and Brown, S. (1992). "Cause and mechanism of failure, Kettleman Hills landfill B-19, Phase IA." Proc., Stability and Performance of Slopes and Embankments – II, ASCE, Vol. 2, 1188 – 1215.

Carson, M.A., and Lajoie, G. (1981). "Some constraints on the severity of landslide penetration in sensitive deposits." Geog. Phys. et Quat., XXXV, 301 – 316.

Castro, G. (1975). "Liquefaction and cyclic mobility of saturated sands." Journal of Geotechnical Engineering, ASCE, 101(GT6), 551 – 569.

Cavounidis, S. (1987). "On the ratio of factors of safety in slope stability analysis." Geotechnique, London, 37(2), 207 – 210.

Chaney, R.C., and Fang, H.Y. (1991). "Liquefaction in the coastal environment: an analysis of case histories." Marine Geotechnology, 10, 343 – 370.

Chang, C.J., Chen, W.F., and Yao, J.T.P. (1984). "Seismic displacement in slopes by limit analysis." Journal of Geotechnical Engineering, ASCE, 110(7), 860 – 874.

Chen, A.T.F. (1985). "Transmitting boundaries and seismic response." Journal of Geotechnical Engineering, ASCE, 111(2), 174 – 180.

Chen, R. H., and Chameau, J. L. (1983). "Three-dimensional limit equilibrium analysis of slopes." Geotechnique, London, 33(1), 31 – 40.

Chen, W. F. (1975). Limit Analysis and Soil Plasticity. Elsevier, New York.

Chen, W. F., and Baladi, G. Y. (1985). Soil Plasticity: Theory and Implementation. Elsevier, Amsterdam.

Chen, W.F., Han, D.J. (1988). Plasticity for Structural Engineers. Springer-Verlag, New York.

Chen, Z., and Morgenstern, N. R. (1983). "Extensions to the generalized method of slices for stability analysis. Canadian Geotechnical Journal, 20(1), 104 – 119.

Chillarige, A.V., Morgenstern, N.R., Robertson, P.K., and Christian, H.A. (1997a). "Seabed instability due to flow liquefaction in the Fraser River delta." Canadian Geotechnical Journal, 34, 520 – 533.

Chillarige, A.R.V., Robertson, P.K., Morgenstern, N.R. and Christian, H.A. (1997b). "Evaluation of the in situ state of Fraser River sand", Can. Geotech. J., 34: 510 –519.

Chugh, A. K. (2003). "On the boundary conditions in slope stability analysis." Int. J. Numer. Anal. Meth. Geomech., 27: 905–926.

Clark, J.I., and Guigne, J.Y. (1988). "Marine geotechnical engineering in Canada." Canadian Geotechnical Journal, 25, 179 – 198.

Clayton, J., and Engquist, B. (1977). "Absorbing boundary conditions for acoustic and elastic wave equations." Bull. Seismological Society of America, 67, 1529 – 1541.

Cohen, M., Jennings, P.C. (1983). "Silent boundary methods for transient analysis." In: Computational Methods for Transient Analysis, Vol. 1, Belytschko, T. and Hughes, T.J.R., eds., 301 – 360.

Cornell, J. A. (1990). "How to apply response surface methodology." The ASQC Basic References in Quality Control: Statistical Techniques, Vol. 8, ASQC, Wisconsin.

COSTA-Canada, (2000): http://www.costa-canada.ggl.ulaval.ca/english.html

Cotecchia, V. (1987). "Earthquake-prone environments." In: Slope Stability, eds., Anderson, M.G., and Richards, K.S., John Wiley & Sons, New York, 287 – 330.

Cox, D. C., and Baybutt, P. (1981). "Methods of uncertainty analysis: A comparative survey." Risk Analysis, 1(4), 251 – 258.

Cremonini, M, Christiano, P. and Bielak, J. (1988). "Implementation of effective seismic input for soil structure interaction systems." Earthquake Engineering and Structural Dynamics, Vol. 16, 615 – 625.

Dafalias, Y.F. (1994). "Overview of constitutive models used in VELACS." Proc. Int. Conf. on Verification of. Numerical Procedures for the Analysis of Soil Liquefaction Problems, K. Arulanandan and R.F. Scott, editors, Vol. 2, Balkema, Rotterdam,1293 – 1303.

Dafalias, Y.F., and Popov, E.P. (1975). "A model of nonlinearly hardening materials for complex loading." Acta Mechanica, 21, 173 – 192.

Dafalias, Y.F., and Herrmann, L. R. (1982). "Bounding surface formulation of soil plasticity." Soil Mechanics—Transient and Cyclic Loads, G. N. Pande and O. C. Zienkiewics, editors, Wiley, New York, 253 – 282.

Das, B.M. (1998). Principles of Geotechnical Engineering. PWS-KENT.

De Blasio, F. V., Issler, D., Elverhøi, A. C., Harbitz, B., Bryn, P., and Lien, R. (2003). "Dynamics and material properties of the giant Storegga slide as suggested by numerical simulations." First International Symposium on Submarine Mass Movements and Their Consequences, eds., Locat, J., and Mienert J., 223 – 230.

Dennhardt, M., and Forster, W. (1985). "Problems of three-dimensional slope stability." Proc., 11th. Int. Conf. Soil Mechanics and Foundation Engineering, 427 – 431.

Deodatis, G. (1996). "Non-stationary stochastic vector processes: seismic ground motion applications." Probabilistic Engineering Mechanics, 11:149 – 168.

Design-Expert®, http://www.statease.com

Di Maggio, F. L., and Sandler, I. S. (1971). "Material model for granular soils." ASCE, EM Division, Vol. 97, 935 – 950.

Dobry, R. and Taboada, V.M. (1994). "Possible lessons from VELACS model No. 2 results." Proc. Int. Conf. on Verification of. Numerical Procedures for the Analysis of Soil Liquefaction Problems, K. Arulanandan and R.F. Scott, editors, Vol. 2, Balkema, Rotterdam. 1341 – 1352.

Downing, D. J., Gardner, R. H., and Hoffman, F. O. (1985). "An examination of response-surface methodologies for uncertainty analysis on assessment models." Technometrics, 27(2), 151 – 163.

Duncan, J. M. (1996). "State-of-the-art: limit equilibrium and finite element analysis of slopes." J. Geotech. Geoenv. Engrg., ASCE, 122(7), 577 – 596.

Duncan, J. M., and Chang, Y. C. (1970). "Nonlinear analysis of stress and strain in soils." ASCE, SM5, 96, 1629 – 1653.

Duncan, J. M., and Stark, T. D. (1992). "Soil strength from back analysis of slope failures." Proc., Specialty Conf. Stability and Performance of Slopes and Embankments-II, ASCE, Berkeley, CA, June, Vol.1, 890 – 904

Edwards, B.D., Lee, H.J., and Field, M.E. (1995). "Mudflow generated by retrogressive slope failure, Santa Barbara basin, California continental borderland." J. Sedimentary Research, A65, 1, 57 – 68.

Elgamal, A., Yang, Z., Parra, E. (2002). "Computational modeling of cyclic mobility and post-liquefaction site response." Soil Dynamics and Earthquake Engineering, 22, 259 – 271.

Engquist, B., and Madja, A. (1977). "Absorbing boundary conditions for the numerical simulation of waves." Math. Comp., 31(139), 629 – 651.

Fiegel, G.L., and Kutter, B.L., (1992). "Liquefaction mechanism for layered soil." J. Geotech. Eng., ASCE, 120(4), 737 – 755.

Finn, W.D.L. (1982). "Dynamic response analyses of saturated sand." Soil Mechanics—Transient and Cyclic Loads, G. N. Pande and O. C. Zienkiewics, editors, Wiley, New York, 105 – 131.

Finn, W.D.L. (1990). "Seismic analysis of embankment dams." Dam Engineering, 1(1), 59 – 75.

Finn, W.D.L. (2000). "State-of-the-art of geotechnical earthquake engineering practice." Soil Dynamics and Earthquake Engineering, 20, 1 – 15.

Finn, W.D.L. (2002). "State of the art for the evaluation of seismic liquefaction potential." Computers and Geotechnics, 29, 329 – 341.

Finn, W.D.L., and Yogendrakumar, M. (1989). "TARA-3FL: Program for analysis of liquefaction induced flow deformations." Dept. of Civil Engr., Univ. of British Columbia, Vancouver, BC.

Finn, W.D.L., M. Yogendrakumar, N., Yoshida, and Yoshida, H. (1986). "TARA-3: A program for non-linear static and dynamic effective stress analysis." Soil Dynamics Group, Univ. of British Columbia, Vancouver, BC.

Firestone, M. et al. (1997). "Guiding principles for Monte Carlo Analysis." Risk Assessment Forum, U.S. Environmental Protection Agency, Washington, D.C.

Fredlund, D. G. and Krahn, J. (1977). "Comparison of slope stability methods of analysis." Canadian Geotechnical J., 14(3), 429 – 439.

Gardner, J.V., Hughes Clarke, J.E., Mayer, L.A., Kleiner, A., and Paton, M. (1999a). "Mapping a continental shelf and slope in the 1990s: A tale of three multibeams." Shallow Water Survey Conference Proceedings, Sydney, CDROM, 11pp. http://www.omg.unb.ca/omg/papers/Gardner.pdf

Gardner, J.V., Prior, D.B., and Field, M.E. (1999b). "Humboldt Slide—a large shear-dominated retrogressive slope failure." Marine Geology, 154, 323 – 338.

Griffiths, D. V., and Lane, P. A. (1999). "Slope stability analysis by finite elements." Geotechnique 49(3), 387 – 403.

Griffiths, D.V. and Prevost, J.H. (1990). "Stress-strain curve generation from simple triaxial parameters." Num. Analyt. Meth. Geomech., 14, 587 – 594.

Grozic, J.L.H. (1999). "The behaviour of loose gassy sand and its susceptibility to liquefaction." Ph.D. thesis, University of Alberta, Canada.

Grozic, J.L.H., Robertson, P.K., and Morgenstern, N.R. (2000). "Cyclic liquefaction of loose gassy sand." Canadian Geotechnical Journal, 37: 843 – 856.

Gu, W.H., Morgenstern, N.R., and Robertson, P.K. (1993). "Progressive failure of the lower San Fernando dam." Journal of Geotechnical Engineering, ASCE, 119, 333 – 348.

Gu, W.H., Morgenstern, N.R., and Robertson, P.K. (1994). "Postearthquake deformation analysis of Wildlife site." Journal of Geotechnical Engineering, ASCE, 120, 274 – 289.

Hampton, M.A., Lee, H.J., and Locat, J. (1996). "Submarine landslides." Reviews of Geophysics, 34(1), 33 – 59.

Hansen, A. (1984). "Landslide hazard analysis." In: Slope Instability, eds., Brundsen, D., and Prior, D.B., Wiley, 523 – 602.

Harder, L.F., and Jr. Boulanger, R.W., (1997). "Application of K_σ and K_α correction factors." Proc., NCEER Workshop on Evaluation of Liquefaction Resistance of Soils, National Center for Earthquake Engrg. Research, SUNY at Buffalo, 167 – 190.

Hardin, B.O. (1978). "The nature of stress-strain behaviour for soils." Proceedings, ASCE Geotechnical Engineering Division Specialty Conference on Earthquake Engineering and Soil Dynamics, Vol. 1, 3 – 90.

Hardin, B.O. and Richard, F.E. (1963). "Elastic wave velocities in granular soils." ASCE J. Soil Mech. and Found. Div., 89(SM1), 33 – 65.

Haug, M.D., Sauer, E.K., and Fredlund, D.G. (1976). "Retrogressive slope failures near Saskatoon." Proc., 29th. Canadian Geotechnical Conference, Vancouver, pp. II-66 to II-83.

Hayashi, H., M. Honda, and Yamada, T. (1992). "Modeling of nonlinear stress strain relations of sands for dynamic response analysis." Proc., 10th World Conf. on Earthquake Engr., Madrid, Balkema, Rotterdam, vol. 11, 6819 – 6825.

Howie, J.A., Shozen, T., and Y.P. Vaid (2002). "Effect of ageing on stiffness of very loose sand." Canadian Geotechnical Journal, 39, 149 – 156.

Hughes Clarke, J.E. (1996). "Are you really getting full bottom coverage? A collection of thoughts and images." Ocean Mapping Group, UNB, http://www.omg.unb.ca/~jhc/coverage_paper.html

Hungr, O., Salgado, F.M., and Byrne, P.M. (1989). "Evaluation of a three-dimensional method of slope stability analysis." Canadian Geotechnical Journal, 26(4), 679 – 686.

Ishibashi, I., and Zhang, X. (1993). "Unified dynamic shear moduli and damping ratios of sand and clay." Soils and Foundations, 33, 1, 182 – 191.

Ishihara, K. (1996). Soil Behavior in Earthquake Geotechnics. Oxford Engineering Science Series, No 46.

Issler, D., De Blasio, F. V., Elverhøi, A., Ilstad, T., Bryn, P. and Lien, R. (2003). "Issues in the assessment of gravity mass flow hazard in the Storegga area off the western Norwegian coast." First International Symposium on Submarine Mass Movements and Their Consequences, eds., Locat, J., and Mienert J., 231 – 238.

Itasca Consulting Group Inc., FLAC (Fast Lagrangian Analysis of Continua), http://www.winternet.com/~icg/flac.html

Iwan, W.D., (1967). "On a class of models for the yielding behaviour of continuous and composite systems." Journal of Applied Mechanics, Trans. ASME, 34(E3), 612 – 617.

Jeremic, B. (2000). "Finite element methods for 3D slope stability analysis." Slope Stability 2000, ASCE, 224 – 238.

Justo, J.L., and Saura, J. (1983). "Three-dimensional analysis of Infiernillo dam during construction and filling of the reservoir." Int. J. for Numerical and Analytical Methods in Geomechanics, 7, 225 – 243.

Kausel, E. (1985). "Local transmitting boundaries." Journal of Engineering Mechanics, ASCE, 114(6), 1011 – 1027.

Keane, C.M., and Prevost, J.H. (1989). "An analysis of earthquake data observed at the Wildlife Liquefaction Array Site, Imperial County, California." Proceedings, 2nd US-Japan Workshop on Liquefaction., Large Ground Deformations and Effects on Lifelines, New York: 39 – 53.

Kokusho, T. (1999). "Water film in liquefied sand and its effect on lateral spread." J. Geotech. Engrg., ASCE, 125(10), 817 – 826.

Krahn, J. (2003). "The 2001 R.M. Hardy Lecture: The limits of limit equilibrium analyses." Canadian Geotechnical Journal, 40, 643 – 660.

Kvalstad, T.J., Gauer, P, Kaynia, A.M., Nadim, F., Bryn P. (2002). "Slope Stability at Ormen Lange." International Conference on Offshore Site Investigation and Geotechnics, 'Diversity and Sustainability', London, UK.

Lai, T., Elgamal, A., Kutter, B.L., and Wilson, D.W. (2002). "Three-dimensional modeling for site seismic response in laminated and rigid centrifuge containers." Physical Modelling in Geotechnics, ICPMG '02, eds., R. Phillips, P.J. Guo, and R. Popescu, Balkema, 189 – 194.

Lefebvre, G., Duncan, J. M., and Wilson, E. L. (1973). "Three-dimensional finite element analysis of dams." J. Soil Mech. and Found. Div., ASCE, 99(7), 495 – 507.

Lemke, R.W. (1967). "Effects of the earthquake of March 27, 1964, at Seward, Alaska." U.S. Geological Survey Prof. Pap., 542-E, 43 pp.

Leroueil, S., Locat, J., Vaunat, J., Picarelli, L., Lee, H., and Faure, R. (1996). "Geotechnical characterization of slope movements." Proc., 7th. Internationsla Symposium on Landslides, Trondheim, Norway.

Leshchinsky, D. (1990). "Slope stability analysis: generalized approach." J. Geotech. Engrg., ASCE, 116(5), 851 – 867.

Leshchinsky, D., and Huang, C. C. (1992). "Generalized three-dimensional slope-stability analysis." J. Geotech. Engrg., ASCE, 118(11), 1748 – 1764.

Liao, Z.P., and Wong, H.L. (1984). "A transmitting boundary for the numerical simulation of elastic wave propagation." Soil Dynamics and Earthquake Engineering, 3(4), 174 – 183.

Lindman, E.L. (1973). "On getting all of the waves out of the box." Proc., 6th Conf. on Numerical Simulation of Plasmas, Lawrence Berkeley laboratory, Berkeley, Calif., 42 – 45.

Liu, L. and Dobry, R. (1993). "Centrifuge earthquake modelling of liquefaction and its effect on shallow foundations." Department of Civil and Environmental Engineering, RPI, New York.

Locat, J., and Lee, H.J. (2002). Submarine landslides: advances and challenges. Canadian Geotechnical Journal, 39(1), 193 – 212. Also: Keynote Lecture, 8th International Symposium on Landslides, Cardiff, UK, 1 – 30, 2000.

Locat, J., Bornhold, B., Byrne, P., Hart, B., Hughes-Clarke, J., Konrad, J.M., Lee, H., Leroueil, S., Long, B., Mosher, D., Piper, D., Phillips, R., Popescu, R., and Thomson, R. (2001). "COSTA-Canada, A Canadian contribution to the study of continental slope stability: An overview." Proceedings, 54th Canadian Geotechnical Conference, Calgary, Vol. 2, 730 – 737.

Lye, L.M. (2002). "Design of Experiments in Civil Engineering: Are we still in the 1920's?" Annual Conference of the Canadian Society for Civil Engineering, GE069, 1 – 10.

Lye, L.M. (2003). "Some applications of statistical design of experiment methodology in Civil Engineering." Annual Conference of the Canadian Society for Civil Engineering, GCD-115, 1 – 10.

Lysmer, J., and Kuhlemeyer, R.L. (1969). "Finite dynamic model for infinite media." Journal of Engineering Mechanics Division, ASCE, 95(EM4), 859 – 877.

Lysmer, J., and Waas, G. (1972). "Shear waves in plane infinite structures." J. Eng. Mech. Div., ASCE, 98(EM1), 85 – 105.

Martin, H.L. (1978). "A three-dimensional analysis of the Storvass dam." Int. J. for Numerical and Analytical Methods in Geomechanics, 2, 3 – 17.

Martin, G.R., Finn, W.D.L., and Seed, H.B. (1975). "Fundamentals of liquefaction under cyclic loading." Journal of Geotechnical Engineering, ASCE, 101(GT5).

Mayne, P.W. and Holtz, R.D. (1985). "Effect of principal stress rotation on clay strength." Proceedings, 11th Int. Conf. Soil Mechanics and Foundation Engineering, San Francisco, Vol. 2, 579 – 582.

Mitchel, R.J., and Markell, A.R. (1974). "Flowsliding in sensitive soils." Canadian Geotechnical Journal, 11, 11 – 31.

Montgomery, D. C. (1997). Design and Analysis of Experiments. John Wiley & Sons, New York.

Montgomery, D.C., Peck, E.A., and Vining, G.G. (2000). Introduction to Linear Regression Analysis, 3rd ed. New York, John Wiley.

Moran, K. (1993). "Offshore site investigations on Canadian continental margins." 4th. Canadian Conference on Marine Geotechnical Engineering, Vol. 3, 977 – 997.

Morgenstern, N. R., and Price, V. R. (1965). "The analysis of the stability of general slip surfaces." Geotechnique, 15, 79 – 93.

Morin, P., and Dawe, C.R. (1986). "Geotechnical properties of two deep sea marine soils from Labrador Sea area." Proc., Third Canadian Conference on Marine Geotechnical Engineering, St. John's, Nfld., Vol. 1, 117 – 137.

Mosher, D.C., Monahan, P.A., and Barrie, J.V. (2001). "Submarine failures in the Strait of Georgia, British Columbia: Landslides of the 1946 Vancouver Island Earthquake." Proceedings, 54th Canadian Geotechnical Conference, Calgary, Vol. 2, 744 – 75.

Mroz, A., (1967). "On the description of anisotropic workhardening." J. Mech. Phys. Solids, 15, 163 – 175.

Mulder, T. and Cochonat, P. (1996). "Classification of offshore mass movements." J. Sedimentary Research A, 66, 43 – 57.

Myers, R. H., and Montgomery, D. C. (1995). Response Surface Methodology: Process and Product Optimization Using Design Experiments. John Wiley & Sons, New York.

Nakase, A., and Kamei, T. (1988). "Undrained shear strength of remolded marine clays", Soils and Foundations, Vol. 28(1), 29 – 40.

Nave, C. R. (2000). HyperPhysics. Georgia State University, http://230nsc1.phy-astr.gsu.edu/hbase/hph.html

Newmark, N.M. (1965). "Effects of earthquakes on dams and embankments." 5th Rankine Lecture, Geotechnique, 15(2), 137 – 160.

Noorany, I. (1984). "Phase relationships in marine soils." J. of Geotechnical Engineering, ASCE, 110(4), 539 – 543.

Noorany, I. (1989). "Classification of marine sediments." J. of Geotechnical Engineering, ASCE, 115(1), 23 – 37.

Phillips, R. (2001). "Simulating submarine slope instability initiation using centrifuge model testing." Proc., 54th. Canadian Geotechnical Society Conf., 802 – 806.

Piper, D.J.W., Cochonat, P., and Morrison, M.L. (1999). "The sequence of events around the epicentre of the 1929 Grand Banks earthquake: initiation of debris flows and turbidity current inferred from sidescan sonar." Sedimentology, 46, 79 – 97.

Piper, D.J.W., Cochonat, P., Ollier, G., Le Dreezen, E., Morrison, M.L., and Baltzer, A. (1992). "Evolution progressive d'un glissement rotationnel en un courant de turbidité: cas du séisme de 1929 des Grands Bancs (Terre Neuve)." Académie des Sciences (Paris), Comptes Rendus, V. 314, Série II, 1057 – 1064.

Popescu, R. (1995). "Stochastic Variability of Soil Properties: Data Analysis, Digital Simulation, Effects on System Behavior." Ph.D. Thesis, Princeton University, Princeton, NJ.

Popescu, R. (2001). "A method for seismic evaluation of embankment dams." Canadian Dam Association Annual Conference, Fredericton, NB.

Popescu, R. (2002). "Finite element assessment of the effects of seismic loading rate on soil liquefaction." Canadian Geotechnical Journal, 39(2), 331 – 344.

Popescu, R. and Prevost, J.H. (1993a). "Centrifuge validation of a numerical model for dynamic soil liquefaction." Soil Dynamics and Earthquake Engineering, 12, 73 – 90.

Popescu, R. and Prevost, J.H. (1993b). "Numerical class 'A' predictions for models no. 1, 2, 3, 4a, 4b, 7, 11 and 12." Proc. Int. Conf. on Verif. of Numerical Procedures for the Analysis of Soil Liquefaction, Arulanandan and Scott ed., Balkema, Rotterdam, Vol. 1, 1105 – 1207.

Popescu, R. and Prevost, J.H. (1995). "Comparison between VELACS numerical 'class A' predictions and centrifuge experimental soil test results." Soil Dynamics and Earthquake Engr., 14(2), 79 – 92.

Popescu, R., Prevost, J.H., Ohbo, N., and Hayashi, K. (1992). "Numerical simulations of soil liquefaction." In Proceedings of the 4th US-Japan Workshop on Liquefaction, Large Ground Deformations, and Effects on Lifelines, 269 – 282.

Popescu, R., Prevost, J.H. and Deodatis, G. (1998). "Seismic Analysis of a Wharf Seawall". In Proceedings of the Structural Engineers World Congress (SEWC), San Francisco, CA.

Popescu, R., Deodatis, G., and Prevost, J.H. (2000). "PRISM—a strong motion database." In Proceedings of the 53rd Canadian Geotechnical Conference. Canadian Geotechnical Society, Vol. 2, 825–832.

Potts, D. M., and Zdravkovic, L. (1999). Finite Element Analysis in Geotechnical Engineering. Vol. I: Theory, Vol. II: Application. Thomas Telford, London.

Poulos, H.G. (1988). Marine Geotechnics. Unwin Hyman, London.

Poulos, S.J. (1981). "The steady state of deformation." Journal of Geotechnical Engineering, ASCE, 107(5), 553 – 562.

Prevost, J.H. (1977). "Mathematical modeling of monotonic and cyclic undrained clay behaviour." Int. J. Numerical Methods in Geomechanics, 1(2), 195 – 216.

Prevost, J.H. (1985). "A simple plasticity theory for frictional cohesionless soils." Soil Dynamics and Earthquake Engineering, 4(1), 9 – 17.

Prevost, J.H. (1993). "Nonlinear dynamic response analysis of soil and soil-structure interacting systems." Soil Dynamics and Geotechnical earthquake Engineering, P. Seco e Pinto, editor, Balkema, Rotterdam.

Prevost, J.H., (1998). "Recent Developments in Constitutive Models for Geomechanics." Proceedings, 12th Engineering Mechanics, ASCE, La Jolla, California, 1–6.

Prevost, J.H. (2002). "Dynaflow—A nonlinear transient finite element analysis program." Version 2002, Release 01.A., Dept. of Civil Engrg. & Operation Research, Princeton Universtiy, Princeton, NJ. First Release, 1981. http://www.princeton.edu/~dynaflow/description_df.htm

Prevost, J.H. and Keane, C.M. (1989). "Shear stress-strain curve generation from simple material parameters." Journ. Geotechnical Engr., 116(8), 1255 – 1263.

Prevost, J.H. and Popescu, R. (1996). "Constitutive Relations for Soil Materials." Electronic J. of Geotechnical Engr., http://geotech.civen.okstate.edu/ ejge/ppr9609/index.htm.

Prevost, J.H., Abdel-Ghaffar, A.M., and Lacy, S.J. (1985). "Nonlinear dynamic analysis of an earth dam." ASCE, J. Geotechnical Engrg., 111(7), 882 – 897.

Prior, D.B., and Coleman, J.M. (1978). "Disintegrative retrogressive landslides on very-low-angle subaqueous slopes." Mississippi delta. Marine Geotechnology, 3: 37 – 60

Prior, D.B. and Coleman, J.M. (1984). "Submarine slope instability." In Slope Instability, eds., Brundsen, D., and Prior, D.B., Wiley, 419 – 445.

Prior, D.B., Bornhold, B.D., Coleman, J.M., and Bryant, W.R. (1982). "Morphology of a submarine slide, Kitimat Arm, British Columbia." Geology, 10, 588 – 592.

Rack, F.R., et al. (2000). "Tomorrow's Technology Today. A survey of emerging trends in non-destructive measurements for the geosciences." Interim report of the IMAGES standing committee on "New Technologies in Sediment Imaging", http://joiscience.org/t3_report/t3_report.html

Richart, F.E., J.R. Hall and R.D. Woods (1970). Vibrations of Soils and Foundations, Prentice-Hall.

Robertson, P.K., and Wride, C.E. (Fear) (1998). "Evaluating cyclic liquefaction potential using the cone penetration test." Canadian Geotechnical Journal, 35, 442 – 459.

Roesset, J.M., and Ettouney, M.M. (1977). "Transmitting boundaries: a comparison." International Journal for Numerical and Analytical Methods in Engineering, 1(2), 151 – 176.

Roscoe, K. H., and Burland, J. B. (1968). "On the generalized stress strain behaviour of wet clay." Eng. Plasticity, Cambridge University Press, 535 – 609.

Roscoe, K. H., and Schofield, A.N. (1963). "Mechanical behaviour of an idealized wet clay." 2nd ECSMFE, Wiesbaden, Vol. I, 47 – 54.

Roscoe, K.H., Schofield, A.N., and Wroth, C.P. (1958). "On the yielding of soils." Geotechnique, 8, 22 – 53.

Sasitharan, S., Robertson, P.K., Sego, D.C., and Morgenstern, N.R. (1993). "Collapse behaviour of sand." Canadian Geotechnical Journal, 30, 569 – 577.

Scott, R.F. (1985). "Plasticity and constitutive relations in Soil Mechanics." J. Geotechnical Eng., ASCE, 111(5), 563 – 605.

Sedov, L. I. (1993). Similarity and Dimensional Methods in Mechanics. 10th ed., Translated by A. G. Volkovets, CRC Press, Boca Raton.

Seed, H.B. (1968). "Landslides during earthquakes due to soil liquefaction." J. Soil Mechanics and Foundations Division, ASCE, 94: 1053 – 1122.

Seed, H.B. (1987). "Design problems in soil liquefaction." Journal of Geotechnical Engineering, ASCE, 113(8), 827 – 845.

Seed, H.B. and Idriss, I.M. (1971). "Simplified procedure for evaluating soil liquefaction potential." Journal of Geotechnical Engineering, ASCE, 97(9), 1249 – 1273.

Seed, H.B., and Peacock, W.H. (1971). "Test procedures for measuring soil liquefaction characteristics." Journal of Soil Mechanics and Foundation Engineering, ASCE, 97(SM8): 1099 – 1119.

Seed, R.B., and Harder, L.F. (1990). "SPT-based analysis of cyclic pore pressure generation and undrained residual strength." Proc. of the Memorial Symposium for H.Bolton Seed, BiTech Publications.

Shahabi, A.A., Das, B.M., and Tarquin, A.J. (1984). "An empirical relation for coefficient of permeability of sands." In Proc., 4th. Australia-New Zeeland Conf. on Geomechanics, Vol. 1, 54 – 57.

Shibata, T., and Teparaksa, W. (1988). "Evaluation of liquefaction potentials of soils using cone penetration tests." Soils and Foundations, 28(2), 49 – 60.

Simo, J.C. and Ortiz, M. (1985). "A unified approach to finite deformation elastoplastic analysis based on the use of hyperelastic constitutive equations." Comp. Meth. Appl. Mech. Engr., 49, 221 – 245.

Simons, H.A., Randolph, M.F., (1986). "Comparison of transmitting boundaries in dynamic finite element analyses using explicit time integration." International Journal for Numerical and Analytical Methods in Geomechanics, 10, 329 – 342.

Sivathayalan, S. and Vaid, Y.P. (2002). Influence of generalized initial state and principal stress rotation on the undrained response of sands." Can. Geotech. J. 39: 63–76.

Skempton, A.W., and Hutchinson, J.N. (1969). "Stability of natural slopes and embankment foundations, State-of-the-art Report." Proc., 7th. Int. Conf. Soil Mech. Found. Eng., Mexico City, Vol. 2, 291 – 335.

Sladen, J.A., D'Hollander, and R.D., Krahn, J. (1985a). "The liquefaction of sands—a collapse surface approach." Canadian Geotechnical Journal, 22, 564 – 578.

Sladen, J.A., D'Hollander, R.D., Krahn, J., and Mitchell, D.E. (1985b). "Back analysis of the Nerlerk berm liquefaction slides." Can. Geotech. J., 22, 579 – 588.

Smith, W.D. (1974). "A non-reflecting plane boundary for wave propagation problems." J. of Computational Physics, 15, 492 – 503.

Stark, T. D., Eid, H. T. (1998). "Performance of three-dimensional slope stability methods in practice." J. Geotech. Geoenv. Engrg., ASCE, 124(11), 1049 – 1060.

Stark, T.D., and Olson, S.M. (1995). "Liquefaction resistance using CPT and field case histories." J. Geotech. Engrg., ASCE, 121(12), 856 – 869.

Steedman, R.S., Madabhushi, S.P.G., and Chan, A.H.C. (1989). "Use of Compound Parabolic Collectors in the modelling of semi-infinite soil media." Cambridge University Technical Report, CUED/D – SOILS/TR226.

Taboada-Urtuzuastegui, V.M., Martinez-Ramirez, G., Abdoun, T. (2002). "Centrifuge modeling of seismic behaviour of a slope in liquefiable soil." Soil Dynamics and Earthquake Engineering, 22, 1043 – 1049.

Terzaghi, K. (1956). "Varieties of submarine slope failures." Proc., 8th. Texas Conf. Soil Mech. Found. Eng., 1 – 41.

Terzaghi, K., Peck, R.B, and Mesri, G. (1996). Soil Mechanics in Engineering Practice. Third Edition, John Wiley & Sons, New York.

UBC (Uniform Building Code, 1994). International Conference of Building Officials, ICBO, Whittier, CA, Vol. 2.

Urgeles, R., Locat, J., Lee, H., Martin, F., and Konrad, J.M. (2001). "The Saguenay Fjord: Integrating marine geotechnical and geophysical data for spatial slope stability hazard analysis." Proceedings, 54th Canadian Geotechnical Conference, Calgary, Alberta, Canada, Vol. 2, pp. 768 – 775.

Vaid, Y.P. and Chern, J. C. (1985). "Cyclic and monotonic undrained response of saturated sands," Advances in the Art of Testing Soils Under Cyclic Conditions, ASCE, 120 – 147.

Vaid, Y.P. and Eliadorani, A. (2000). "Undrained and drained (?) stress strain response." Can. Geotech. J., 37:1126–1130.

Vaid, Y.P., and Sivathayalan, S. (1996). "Static and cyclic liquefaction potential of Fraser Delta sand in simple shear and triaxial tests." Can. Geotech. J. 33: 281–289.

Vaid Y.P., Sivathayalan S, Stedman D. (1999). "Influence of specimen-reconstituting method on the undrained response of sand.", ASCE Geotechnical Testing J., GTJ9909, 22(3), 187 – 196.

Vaid, Y.P., Stedman, J.D. and Sivathayalan, S. (2001). "Confining stress and static shear effects in cyclic liquefaction." Can. Geotech. J., 38: 580–591.

Valanis, K.C. and Read, H.E. (1982). "A new endochronic plasticity model for soils." in Soil Mechanics—Transient and Cyclic Loads, eds., Pande, G.N., and Zienkiewics, O.C., Wiley, 1982, 375 – 417.

Williams, J.P., and Aurora, R.P. (1982). "Case study of an integrated geophysical and geotechnical site investigation program." Offshore Technology Conference, OTC 4168, Vol. 1, 11 – 25.

Wolf, J.P., and Song, C. (1996). "Finite-Element Modelling of Unbounded Media." John Wiley & Sons.

Yoshida, N. and Finn, W.D.L. (2000). "Simulation of liquefaction beneath an impermeable surface layer." Soil Dynamics and Earthquake Engineering, 19, 333 – 338.

Yoshimine, M., Robertson, P.K., and Wride (Fear) C.E. (1999). "Undrained shear strength of clean sands to trigger flow liquefaction." Can. Geotech. J., 36(5), 891 – 906.

Youd, T.L., Idriss, I.M., Andrus, R.D., Arango, I., Castro, G., Christian, J.T., Dobry, R., Finn, W.D.L., Harder , L.F., Hynes, M.E., Ishihara, K., Koester, J.P., Liao, S.S.C., Marcuson, W.F., Martin, G.R., Mitchell, J.K., Moriwaki, Y., Power, M.S., Robertson, P.K., Seed, R.B., and Stokoe, K.H. (2001). "Liquefaction Resistance of Soils: Summary report from the 1996 NCEER and 1998 NCEER/NSF workshops on Evaluation of liquefaction resistance of soils." Journal of Geotechnical and Geoenvironmental Engineering, ASCE, 127(10): 817 – 833.

Yu, S. H., Salgado, R., Sloan, S. W., and Kim, J. M. (1998). "Limit analysis versus limit equilibrium for slope stability." J. Geotech. and Geoenv. Engrg., ASCE, 124(1), 1 – 11.

Zangeneh, N. and Popescu, R. (2003). "Displacement analysis of submarine slopes using enhanced Newmark method." First International Symposium on Submarine Mass Movements and Their Consequences, eds., Locat, J., and Mienert J., Nice, France, 193 – 202.

Zangeneh, N., Azizian, A., Lye, L., and Popescu, R. (2002). "Application of Response Surface Methodology in numerical geotechnical analysis." Proceedings, 55th Canadian Geotechnical Conference, 321 – 329.

Zienkiewics, O. C., Humpheson, C., and Lewis, R. W. (1975). "Associated and non-associated viscoplasticity and plasticity in soil mechanics." Geotechnique, 25, 671 – 689.

Zienkiewics, O. C., and Taylor, R. L. (1989). The Finite Element Method. Vol. I: Basic Formulation and Linear Problems. Vol. II: Solid and Fluid Mechanics, Dynamics and Non-Linearity. McGraw-Hill, UK.